Design Optimization of Savonius and Wells Turbines

Dissertation
zur Erlangung des akademischen Grades

Doktoringenieur
(Dr.-Ing.)

von **M.Sc. Mohamed Hassan Ahmed Mohamed**
geb. am 15. July 1974 in Kairo, Ägypten

genehmigt durch die Fakultät für Verfahrens- und Systemtechnik
der Otto-von-Guericke-Universität Magdeburg

Gutachter:

Prof. Dr.-Ing. Dominique Thévenin
Prof. Dr.-Ing. Christian Oliver Paschereit
Prof. Dr.-Ing. Zbigniew A. Styczynski

Promotionskolloquium am: 14.04.2011

I would like to dedicate this thesis

TO

MY PARENTS

TO

My wife **DALIA** and my children **SAMA** and **AHMED**

TO

My sisters **SOMIA** and **ASMAA**

AND TO

My brothers **IBRAHIEM** and **AHMED**

Acknowledgment

Firstly, I would like to express my thankfulness and gratitude to my country **Egypt** for the financial support during my research. Without that, I was not able to work and search here in Germany.

I am greatly indebted to my supervisor **Prof. Dr. Ing. Dominique Thévenin**. I am extremely grateful for his support, invaluable guidance and for his continuing help even before I came to Germany. I also wish to thank him for providing a wonderful work atmosphere and facilities.

I am also grateful to **Dr. Elemér Pap** for his valuable suggestions and help. I am very grateful to **Dr. Gábor Janiga** for his great help. I acknowledge the efficient support of **Matthias Lind** concerning all experimental measurements.

I always feel lucky to be with so many excellent researchers. Thanks are due to all colleagues of my institute, who were always quite helpful during my stay.

I would like to thank my colleague **Dr. Hemdan Shalaby** for his great help and his valuable advices about the life in Magdeburg during starting time.

Finally, my sincere thanks go to my wife **Dalia** who offered her invaluable support to help me during this long education journey.

M. Mohamed
Magdeburg, Germany
1. October 2010

Abstract

Research and development activities in the field of renewable energy have been considerably increased in many countries recently, due to the worldwide energy crisis. Wind energy is becoming particularly important. Although considerable progress have already been achieved, the available technical design is not yet adequate to develop reliable wind energy converters for conditions corresponding to low wind speeds and urban areas. The Savonius turbine appears to be particularly promising for such conditions, but suffers from a poor efficiency. The present study considers improved designs in order to increase the output power of a classical Savonius turbine. It aims at improving the output power of the Savonius turbine as well as its static torque, which measures the self-starting capability of the turbine. In order to achieve both objectives, many designs have been investigated and optimized by placing in an optimal manner an obstacle plate shielding the returning blade. The geometry of the blade shape (skeleton line) has been optimized in presence of the obstacle plate. Finally, frontal guiding plates have been considered and lead to a superior performance of Savonius turbines. The optimization process is realized by coupling an in-house optimization library (OPAL, relying in the present case on Evolutionary Algorithms) with an industrial flow simulation code (ANSYS-Fluent). The target function is the output power coefficient. Compared to a standard Savonius turbine, a relative increase of the power output coefficient by 58% is finally obtained at design point. The performance increases throughout the useful operating range. The static torque is found to be positive at any angle, high enough to obtain self-starting conditions.

Considering now ocean's and sea's energy, the Wells turbine is one of the technical systems allowing an efficient use of the power contained in waves with a relatively low investment level. It consists of a self-rectifying air flow turbine employed to convert the pneumatic power of the air stream induced by an Oscillating Water Column into mechanical energy. On the other hand, standard Wells turbines show several well-known disadvantages: a low tangential force, leading to a low power output from the turbine; a high undesired axial force; usually a low aerodynamic efficiency and a limited range of operation due to stall. In the present work an optimization process is employed in order to increase the tangential force induced by a monoplane and two-stage Wells turbine using symmetric airfoil blades as well as by a two-stage Wells turbine using non-symmetric airfoil blades. The automatic optimization procedure in this part of the work is again carried out by coupling the in-house optimization library OPAL with

the industrial CFD code ANSYS-Fluent. This multi-objective optimization relying on Evolutionary Algorithms takes into account both tangential force coefficient and turbine efficiency. Detailed comparisons are finally presented between the optimal designs and the classical Wells turbine using symmetric airfoils, demonstrating the superiority of the proposed solutions. The optimization of the airfoil shape lead to a considerably increased power output (+12%) and simultaneously to an increase of efficiency throughout the full operating range.

Zusammenfassung

Aufgrund der weltweiten Energiekrise wurden die Anstrengungen in Forschung und Entwicklung im Bereich der erneuerbaren Energien in den letzten Jahren in vielen Ländern erheblich erhöht. Dabei nimmt die Windenergie eine zunehmend wichtige Rolle ein. Obwohl bereits erhebliche Fortschritte erzielt wurden, ist das zur Verfügung stehende technische Design noch nicht ausreichend angepasst, um zuverlässige Windenergieanlagen für Bedingungen mit vergleichbar geringen Windgeschwindigkeiten und städtischen Gebieten zu entwickeln. Die Savonius-Turbine scheint besonders vielversprechend für solche Bedingungen zu sein, leidet aber unter einem schlechten Wirkungsgrad. Die vorliegende Studie betrachtet verbesserte Designs, um die Ausgangsleistung einer klassischen Savonius Turbine zu erhöhen. Diese zielt sowohl auf die Verbesserung der Leistung der Savonius-Turbine als auch auf die Steigerung des statischen Drehmoments, welches für die Selbst-Startfähigkeit der Turbine bestimmend ist. Um beide Ziele zu erreichen, wurde eine Vielzahl von Entwürfen untersucht und optimiert, wobei in optimaler Weise ein Leitblech zur Abschirmung des rückkehrenden Turbinenblattes positioniert wurde. Die Geometrie des Turbinenblattes (Skelett-Linie) wurde in Anwesenheit des Leitblechs optimiert. Dies führte schließlich zu einer gesteigerten Leistung der Savonius Turbine. Die Optimierung wurde durch die Kopplung einer hauseigenen Optimierungsbibliothek (OPAL im vorliegenden Fall auf Evolutionären Algorithmen basierend) mit einem industriellen Strömungssimulations Code (ANSYS-Fluent) realisiert. Hierbei ist der Ausgangsleistungskoeffizient die Zielfunktion. Im Vergleich zu einer Standard-Savonius Turbine ist eine relative Erhöhung des Ausgangsleistungskoeffizienten um 58% am Auslegungspunkt erreicht worden. Die Leistung steigt im gesamten Betriebsbereich. Das statische Drehmoment erweist sich in jedem beliebigen Winkel positiv und ist hoch genug, um die Selbst-Startbedingung der Turbine zu erfüllen.

Betrachtet man nun die Wasserkraft, so ist die Wells-Turbine eines der technischen Systeme, welches eine effiziente Nutzung der Energie in Wellen unter Aufwendung relativ geringer Investitionskosten ermöglicht. Diese besteht aus einer sich selbst richtenden Luftstrom Turbine, welche die durch eine oszillierende Wassersäule eingebrachte pneumatische Energie des Luftstroms in mechanische Energie in Form von Rotation umwandelt. Auf der anderen Seite zeigen Standard Wells-Turbinen mehrere bekannte Nachteile: eine geringe Tangentialkraft, was zu einer geringen Leistung der Turbine führt, eine hohe unerwünschte axiale Kraft, eine geringe aerodynamische Effizienz und einen begrenzten Betriebsbereich durch Strömungsabriss. In der vorliegenden Arbeit wurde ein Optimierungsprozess eingesetzt, um die Tangentialkraft zu erhöhen,

welche durch eine zweistufige Wells-Turbine mit symmetrisch profilierten Schaufeln, sowie durch eine zweistufige Wells-Turbine mit nicht-symmetrisch profilierten Schaufeln induziert wird. Das automatische Optimierungsverfahren in diesem Teil der Arbeit wird wiederum durch die Kopplung der hauseigenen Optimierungsbibliothek OPAL mit dem industriellen CFD-Code ANSYS-Fluent durchgeführt. Diese Mehrzieloptimierung unter Berufung auf Evolutionäre Algorithmen berücksichtigt sowohl den Tangentialkraftkoeffizienten als auch den Wirkungsgrad der Turbine. Abschließend werden detaillierte Vergleiche zwischen den optimalen Designs und der klassischen Wells-Turbine mit symmetrischen Profilen präsentiert, welche die Überlegenheit der vorgeschlagenen Lösungen veranschaulichen. Die Optimierung der Tragflächenform führte zu einer beachtlich gesteigerten Leistung (+12%) und gleichzeitig zu einer Erhöhung der Effizienz über den gesamten Betriebsbereich.

Contents

Nomenclature

Roman symbols

A	Projected area of rotor (DH), m^2
B	Rotor pitch of Wells turbine, m
b	Blade span of Wells turbine, m
c	Airfoil blade chord, m
C_A	Total pressure difference coefficient
C_p	Power coefficient ($P/[1/2\rho AU^3]$)
C_m	Torque coefficient ($T/[\rho R^2 HU^2]$)
C_{ms}	Static torque coefficient ($T_s/[\rho R^2 HU^2]$)
C_T	Tangential force coefficient
D	Turbine diameter of Savonius turbine (2R), m
D_t	Turbine diameter of Wells turbine, m
d	Blade chord ($2r$) of Savonius turbine, m
Δp_0	Total pressure difference, Pa
F_D	Drag force, N
F_L	Lift force, N
F_T	Tangential force, N
F_X	Axial force, N
f^*	Wave frequency, Hz
H	Blade height, m
h	Hub to tip ratio for Wells turbine
G	Gap ratio
g_w	Gap width for the three-blade Savonius turbine, m
L_d	Deflector length, m
L_o	Obstacle length, m
N	Rotational speed of rotor, rpm
P	Output power ($2\pi NT/60$), W
Q	Volumetric flow-rate, m^3/s

R	Tip radius of Savonius turbine, m
r_t	Tip blade radius, m
r_h	Hub blade radius, m
r	Blade radius of semi-cylindrical Savonius blade, m
s	Blade solidity
T	Output torque, Nm
T_s	Static torque quantifying self-starting capability, Nm
t	Airfoil max. half thickness, m
U	Mean wind velocity in axial direction, m/s
u_t	Tip blade speed of Wells turbine, m/s
v_A	Axial air velocity, m/s
w	Relative velocity, m/s
z	Number of blades of Wells turbine

Greek symbols

α	Angle of incidence, (°)
β	Obstacle angle, (°)
η	Aerodynamic efficieny
γ	Deflector angle, (°)
γ_b	Setting blade angle, (°)
ϕ	Flow coefficient
ρ	Density, kg/m³
θ	Rotor angle, (°)
ω	Angular speed, 1/s

List of Tables

List of Figures

Chapter 1

Introduction

Life is nothing but a continuous process of energy conversion and transformation. The accomplishments of civilization have largely been achieved through the increasingly efficient and extensive harnessing of various forms of energy to extend human capabilities and ingenuity. Energy is similarly indispensable for continued human development and economic growth. Providing adequate, affordable energy is essential for eradicating poverty, improving human welfare, and raising living standards world-wide. And without economic growth, it will be difficult to address environmental challenges, especially those associated with poverty. But energy production, conversion, and use always generate undesirable by-products and emissions at least in the form of dissipated heat. Energy cannot be created or destroyed, but it can be converted from one form to another. Although it is common to discuss energy consumption, energy is actually transformed rather than consumed. What is consumed is the ability of oil, gas, coal, biomass, or wind to produce useful work. In this thesis, only conversion of selected renewable energy sources has been investigated.

1.1 Renewable energy

Unlike fossil fuels, which are exhaustible, renewable energy sources regenerate and can be sustained indefinitely. The five renewable sources used most often are: Biomass (including wood and wood waste, municipal solid waste, landfill gas, biogas, ethanol, and biodiesel), Hydropower (including tidal, water potential and ocean wave energy), Geothermal, Wind and Solar energy.

The use of renewable energy is not new. More than 150 years ago, wood, which is one form of biomass, supplied up to 90% of our energy needs. Today, we are looking again at renewable sources to find new ways to use them to help meet our energy needs (see Fig. 1.1).

In 2006, about 18% of global final energy consumption came from renewable energies, with 13% coming from traditional biomass, which is mainly used for heating, and 3% from hydroelectricity. New renewables (small hydropower installations, modern biomass, wind, solar, geothermal, and biofuels) accounted for another 2.4% and are growing very
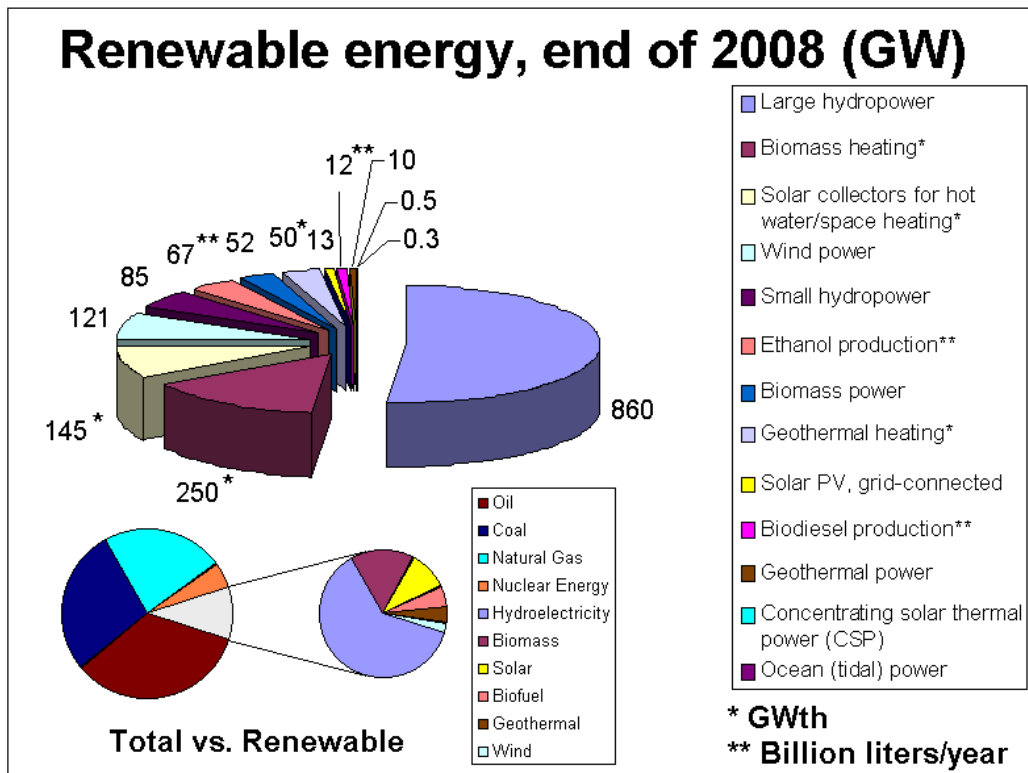
Figure 1.1: 2008 worldwide renewable energy sources. Source: [12].

rapidly [11]. The share of renewables in electricity generation is around 18%, with 15% of global electricity coming from hydroelectricity and 3.4% from new renewables.

The European policy concerning the use of electricity from renewable energy sources aims at a 20% share of renewable energy in the European energy system. In summer 2010, the governments of the member states are to submit national plans to the European Commission. Some countries have already developed national targets. In Denmark, the governments long-term policy aims at achieving a 30% share of energy from renewable energy sources in 2020 [79].

While most renewable energy projects and production is large-scale, renewable technologies are also suited to small off-grid applications, sometimes in rural and remote areas, where energy is often crucial in human development.

Some renewable energy technologies are criticized for being intermittent or unsightly, yet the renewable energy market continues to grow. Climate change concerns, coupled with high oil prices, peak oil, and increasing government support, are driving increasing renewable energy legislation, incentives and commercialization. New government spending, regulation and policies helped the renewable energy industry weather the 2009 economic crisis better than many other sectors [65].

In the past, renewable energy has generally been more expensive to produce and use than fossil fuels. Renewable resources are often located in remote areas, and it is

expensive to build power lines to the cities where the electricity they produce is needed. The use of renewable sources is also limited by the fact that they are not always available; cloudy days reduce solar power; calm days reduce wind power; and droughts reduce the water available for hydropower.

1.1.1 Some properties of renewable energy

Renewable energy is in principle a clean, emission free power generation technology. Some important properties of renewable energy conversion can be summarized as follows:

- Greenhouse effect

  First, renewable energy conversion produces no carbon dioxide (the main potential greenhouse gas) during operation, and only minimal quantities during the manufacture of its equipment and construction. By contrast, fossil fuels such as coal, gas and oil are major emitters of carbon dioxide.

- Air pollution

  Renewable energy also has a positive effect on the quality of the air we breathe. The combustion of fossil fuels produces sulphur dioxide and nitrogen oxide, both serious sources of pollution. These gases are the main components of the "acid rain" effect - killing forests, polluting water courses and corroding the stone facades of buildings; not to mention the human health effects.

- Water

  Another consideration of renewable energy deployment concerns water. In an increasingly water-stressed world, renewable energy conversion uses virtually none of this most precious of commodities in its operation. Most conventional technologies, from mining and extraction to fuel processing and plant cooling measure their water use in millions of liters per day. Other environmental effects resulting from the range of fuels currently used to generate electricity include the landscape degradation and dangers of fossil fuel exploration and mining, the pollution caused by accidental oil spills and the health risks associated with radiation produced by the routine operation and waste management of the nuclear fuel cycle. Exploiting renewable sources of energy, reduces these risks and hazards.

- Environmental impact

  Renewable energy is arguably the cleanest electricity generation technology, but, like any other industry, does have environmental impacts. The construction and operation, often in rural areas, raises issues of visual impact, noise and the potential effects on local ecology and wildlife. Most of these issues are addressed during consultation with local authorities. Since the early days of this relatively young industry, significant improvements have been made with regards to the siting of wind farms and the design of turbines, for instance.

1.1.2 A few numbers

Renewable energy resources include solar energy, geothermal energy, energy from the wind or waves, energy from tides and energy from biomass [42]. Only these relevant for the present thesis are now discussed.

- **Solar energy**

  Every year the Earth receives about 300,000,000,000,000,000,000,000,000 kJ of energy from the sun. Some energy is absorbed by green plants and used to make food by photosynthesis. So ultimately, the sun is the source of most energy resources available to us, including fossil fuels. The two energy sources considered in the present work (wind and waves) are indirectly a result of sun radiation: solar energy drives processes in the atmosphere that cause the wind and waves [42].

- **Wind energy**

  When the earth is irradiated by the sun the ground absorbs some of this radiation. This heated ground warms the air above it. Hot air rises in what are called convection currents. The uneven heating of the earth's surface causes winds.

  For example, if the sun's rays fall on land and sea, the land heats up more quickly. This results in the air above the land moving upwards more quickly than that over the sea (hot air rises). As a result the colder air over the sea will rush in to fill the gap left by the rising air. It is processes like these that give rise to high and low pressure areas, and thus to winds.

  Wind energy is non-polluting and is freely available in many areas. Wind turbines are becoming more efficient. The cost of the electricity they generate is falling. Large balancing areas and aggregation benefits of large areas help in reducing the variability and forecast errors of wind power as well as in pooling more cost effective balancing resources [41]. There are already several power systems and control areas coping with large amounts of wind power [115], like in Denmark, Germany, Spain, Portugal and Ireland that have integrated 9-20 % of wind energy (of yearly electricity demand).

  However, the disadvantages of wind energy exist as well. To be efficient, wind turbines need to be linked together in wind farms, often with 20 turbines or more. This looks unsightly, and can be noisy. The wind farms also need to be sited reasonably close to populations so that the electricity generated can be distributed. Another disadvantage is that winds are intermittent and do not blow all the time [42].

  In this thesis, one turbine used to convert wind energy is extensively optimized in order to improve the output power.

- **Wave energy**

  Waves are caused by the action of winds on the sea. Waves can be many meters in height and contain a great deal of energy. This energy can be harnessed to

drive turbines that generate electricity. Wave energy collectors are of two main types. The first type directs waves into man-made channels, where the water passes through a turbine that generates electricity. The second type uses the up and down movement of a wave to push air.

For example, the Limpet shoreline wave energy concept has been commissioned in December 2000 on the Island of Islay, off the west coast of Scotland. It is intended to enable Islay to replace fossil fuels and become self-sufficient through renewable energy. The waves feed indirectly a pair of counter-rotating Wells turbines, each of which drives a 250 kW generator, giving a theoretical peak power of 500 kW [24].

Waves' energy is non-polluting, wave turbines are relatively quiet to operate and do not affect wildlife. However, some disadvantages exist: the turbines can be unsightly; wave heights vary considerably, so they would not produce a constant supply of energy. In this work, the Wells turbine used to convert wave energy into mechanical energy is investigated and optimized to increase its efficiency.

1.1.3 Future of renewable energy

The worldwide energy demand is continuously growing and, according to the forecasts of the International Energy Agency, it is expected to rise by approx. 50% until 2030. Currently, over 80% of the primary energy demand is covered by fossil fuels. Although their reserves will last for the next decades, they will not be able to cover the worldwide energy consumption in the long run. In view of possible climatic changes due to the increase in the atmospheric CO_2-content as well as the conceivable scarcity of fossil fuels, it becomes clear that future energy supply can only be guaranteed through increased use of renewable energy sources. With energy recovery through renewable sources like sun, wind, water, tides, geothermal or biomass the global energy demand could be met many times over; currently, however, it is still inefficient and too expensive in many cases to take over significant parts of the energy supply.

Renewable energies have long since emerged from their much ridiculed niche existence and established a firm place in the energy mix. Their further expansion is certain now that the European Union has laid down ambitious and binding targets. These state that by 2020 renewable energies are to account for as much as 20% of Europe's energy consumption. These targets focus attention not only on the electricity sector, but also on the use of renewable energy sources in heat production and in the transport sector [67].

Due to the usual adaptation reactions on the markets, it is foreseeable that prices for fossil fuels will rise, while significantly reduced prices are expected for renewable energies. Already today, wind, water and sun are economically competitive in some regions. However, to solve energy and climate problems, it is not only necessary to economically utilize renewable alternatives to fossil fuels, but also to optimize the whole value added chain of energy, i.e., from development and conversion, transport and storage up to the consumers' utilization.

Innovation and increases in efficiency in conjunction with a general reduction of energy consumption are urgently needed in all fields to reach the targets within the

given time since the world population is growing and striving for more prosperity [26] (see Fig. 1.2).
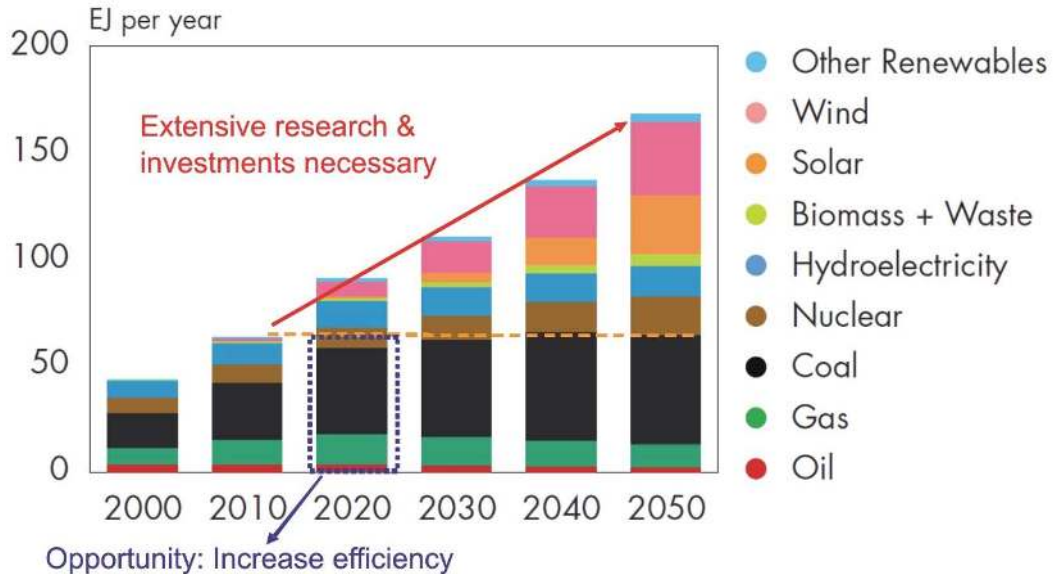
Figure 1.2: 2008 worldwide renewable energy sources [26].

1.2 Scope of the Thesis

The optimization of renewable energy turbomachines is a completely new topic. While gas turbine have been for instance considered extensively, turbomachines used for wind and wave energy conversion are still at a very basic stage. The aim of this thesis is to investigate and optimize two such devices. Therefore, the specific objectives of this work are:

1. **Savonius turbines** (wind energy conversion)

   - Study the impact of an obstacle shielding partially the returning blade(s) and optimize the position and angle of this obstacle as well as the shape of the blades under the effect of this obstacle.

   - Investigate the impact of a deflector installed simultaneously with the obstacle (frontal guiding plates) to redirect the flow toward the advancing blade(s) and optimize the position and angle of these guiding plates as well as the shape of the blades under the effect of these plates.

   - Optimize the performance of the full turbine considering either two or three three blades.

   - At the end, a considerably improved design must be available.

2. **Wells turbine** (wave energy conversion)

- Study a modified Wells turbine consisting of non-symmetric airfoils, taking into account the mutual interaction between the blades.
- Optimize the blade shape of monoplane Wells turbine and obtain new, non-standard airfoils with a higher performance.
- Optimize the shape of the airfoil for a two-stage, modified Wells turbine using non-symmetric airfoils.
- Obtain the optimal shape of the airfoil for a two-stage Wells turbine using symmetric airfoils.
- At the end, a considerably improved design must be available.

1.2.1   Conclusions and outline

This chapter provides a brief introduction to renewable energy conversion and its importance for human life. In chapter 2, wind and wave energy conversion are discussed in details, followed by a discussion of the Savonius turbine and Wells turbine, which are the main topic of this work. Chapter 3 illustrates the employed optimization technique. A literature review of the performance of Savonius and Wells turbines is presented in chapter 4 including previous attempts to improve the performance of both turbines. The numerical methods are introduced in chapter 5, including the coupling between the flow solver and the optimizer (OPAL). All the results of the optimization are presented in chapter 6 for Savonius turbine and chapter 7 for Wells turbine, comparing the new designs with the classical ones. The thesis ends with conclusions and suggestions for future work in chapter 8.

Chapter 2

Basic concepts

2.1 Introduction

The utilization of renewable energy sources is not at all new; in the history of mankind renewable energies have for a long time been the primary possibility of generating energy. This only changed with industrial revolution when lignite and hard coal became increasingly important. Later on, also crude oil gained importance. Offering the advantages of easy transportation and processing, crude oil has become one of the prime energy carriers applied today. As fossil energy carriers were increasingly used for energy generation, at least by the industrialized countries, the application of renewable energies decreased in absolute and relative terms; besides a few exceptions, renewable energies are of secondary importance with regard to overall energy generation. Yet, the utilization of fossil energy carriers involves a series of undesirable side effects which are less and less tolerated by industrialized societies increasingly sensitized to possible environmental and climate effects at the beginning of the 21st century. This is why the search for environmental, climate-friendly and socially acceptable, alternatives suitable to cover the energy demand has become increasingly important. Also with regard to the considerable price increase for fossil fuel energy on the global energy markets in the last few years, not only in Europe, high hopes and expectations are placed on the multiple possibilities of utilizing renewable sources of energy. Considering this background, the present chapter aims at presenting the physical and technical principles for using wind and wave energy.

2.2 Wind energy conversion

Solar radiation induces the movement of the air masses within the atmosphere of the earth. Of the total solar radiation incident on the outer layer of the atmosphere, approximately 2.5% are utilized for the atmospheric movement. This leads to a theoretical overall wind power of approximately 4.3 10^{15} W. The energy contained in the moving air masses, which for example can be converted into mechanical and electrical energy by wind mills and turbines, is therefore a secondary form of solar energy. The aim of

the following discourse is to show the main basic principles of the supply in wind energy and to discuss its supply characteristics [53].

Wind power is growing at the rate of 30% annually, with a worldwide installed capacity of 157,900 megawatts (MW) in 2009 [12]. It is widely used in Europe, Asia, and the United States. The measured wind speeds can be analyzed and the annual mean value can be calculated. If the yearly mean wind velocity is averaged over various years, areas of similar wind speeds can be identified. Figure 2.1 shows these values on a worldwide scale referring to 10 m above ground.
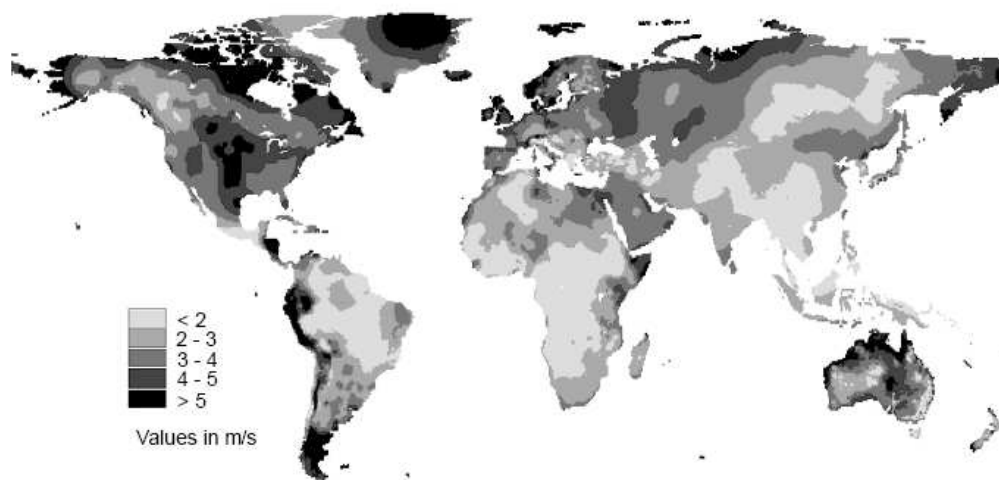
Figure 2.1: Distribution of yearly annual mean values of the wind speed for 10 m above ground worldwide [53].

Wind energy converters harness the kinetic energy contained in flowing air masses. In the following, the fundamental physical principles of this type of energy conversion are explained. Most modern wind energy converters are equipped with rotors to extract wind power, and consist of one or several rotor blades. The extracted wind power generates rotation and is thereby converted into mechanical power at the rotor shaft. Mechanical power is taken up at the shaft in the form of a moment at a certain rotation and is transfered to a machine (such as a generator). The entire wind power station thus consists of a wind energy converter (rotor), a mechanical gear and a generator. It is physically impossible to technically exploit the entire wind energy, as in this case air flow would come to a standstill; air would fail to enter the swept rotor area, and wind power would no longer be available. There are two different physical principles to extract power from wind. The airfoil drag method is based on the wind drag force incident on a wind-blown surface. The second principle, also referred to as aerodynamic or airfoil lift principle, which is based on flow deviation inside the rotor is at present predominantly applied for wind energy conversion. Both principles are outlined throughout the following sections to explain the main differences. The implementation of an innovative aerodynamic control technique in wind turbines is a point under extensive investigation

since the conventional wind turbine blade technology is reaching its limits. Almost all the effort of the wind turbine industry in the field of aerodynamics is related to the development of blades which offer better performance, increased reliability and faster control of larger wind turbines [78]. A discussion on the maximum achievable wind power output by means of an ideal wind energy converter follows.

2.2.1 Horizontal axis turbines

These are the standard turbines used at present. According to the lift principle, wind is deviated to generate peripheral force inside the rotor (Fig. 2.2). For high-speed propeller-type converters, rotor blades are mostly designed according to the wing theory.

Figure 2.2: Horizontal axis wind turbine.

The airfoil cross-section at radius r is set at a local blade pitch angle ϑ with respect to the rotor plane of rotation (Fig. 2.3). The axial free stream velocity v_a in the rotor plane and the tangential speed $u = r\omega$ at the radius of the blade cross-section combine to form a resultant flow velocity v_r. Together with the airfoil chord line, it forms the local aerodynamic angle of attack α. For the benefit of those readers unfamiliar with aerodynamics, the difference between the aerodynamic angle of attack α and the blade pitch angle ϑ should be noted: the angle of attack is an aerodynamic parameter and the blade pitch angle is a design parameter. The two angles are often confused, making it more difficult to understand the aerodynamic relationships. Linking the relationships of fluid mechanics for the momentum of the axial flow and of the radial flow components of the rotating wake with the formulations for the aerodynamic forces at the blade

element allows the flow conditions at the blade element to be determined so that the local aerodynamic lift and drag coefficients can be calculated.

The calculation of the balance of forces includes not only the pure airfoil drag but also other drag components which derive from the spatial flow around the rotor blade. In particular, the flow around the blade tip, a result of the pressure difference between the top and the underside of the blade, produces the so-called free tip vortices. The resultant drag is called induced drag, a function of the local lift coefficient and the aspect ratio (slenderness) of the blades. The higher the aspect ratio, i.e., the more slender the blades, the lower the induced drag. These blade tip losses are introduced as additional drag components, as are the hub losses which are the result of vortices in the wake of the flow around the hub. They are derived from a complex vortex model of the rotor flow [37]. With several semi-empirical approaches for these vortex losses, the blade element theory provides the distribution of aerodynamic forces over the length of the blade. This is usually divided into two components: one in the plane of rotation of the rotor, the tangential force distribution; and one at right angles to it, the thrust distribution. Integrating the tangential force distribution over the rotor radius provides the driving torque of the rotor and, with the rotational speed of the rotor, the rotor power or power coefficient, respectively. Integrating the thrust distribution yields the total rotor thrust for instance to the tower. Referred to the power rating of the air stream, the simple momentum theory by Betz provides the ideal peak power coefficient of 0.593 which is independent of the tip speed ratio. Taking into consideration the angular momentum in the rotor wake shows that the power coefficient becomes a function of the tip speed ratio (see later section 2.2.3). It is only when the tip speed ratios become infinitely high that the power coefficient approaches Betz's ideal value. Introducing the aerodynamic forces acting on the rotor blades, and particularly the aerodynamic drag, further reduces the power coefficient; in addition, the power coefficient now exhibits an optimum value at a certain tip speed ratio. The aerodynamic rotor theory based on the momentum theory and on the blade element theory, yields the real rotor power curve with good approximation. Nevertheless, it should be kept in mind that the momentum theory as well as the blade element model include several simplifications, which limit their validity to a disc-shaped wind energy converter. Sometimes, the momentum theory is therefore called "disc actuator theory" [37].

2.2.2   Vertical axis turbines

The oldest design of wind rotors features rotors with a vertical axis of rotation. At the beginning, however, vertical-axis rotors could only be built as pure drag-type rotors (see the idea of drag turbines in Fig. 2.4).

The Savonius rotor, which can be found as simple ventilator on some railroad carriages or delivery vans, and the cup anemometer used to measure wind velocity are well-known examples of rotors with a vertical axis of rotation. It was only recently that engineers succeeded in developing vertical-axis designs, which could also effectively utilize aerodynamic lift. The design proposed in 1925 by the French engineer Darrieus, in particular, has been considered as a promising concept for modern wind turbines. As
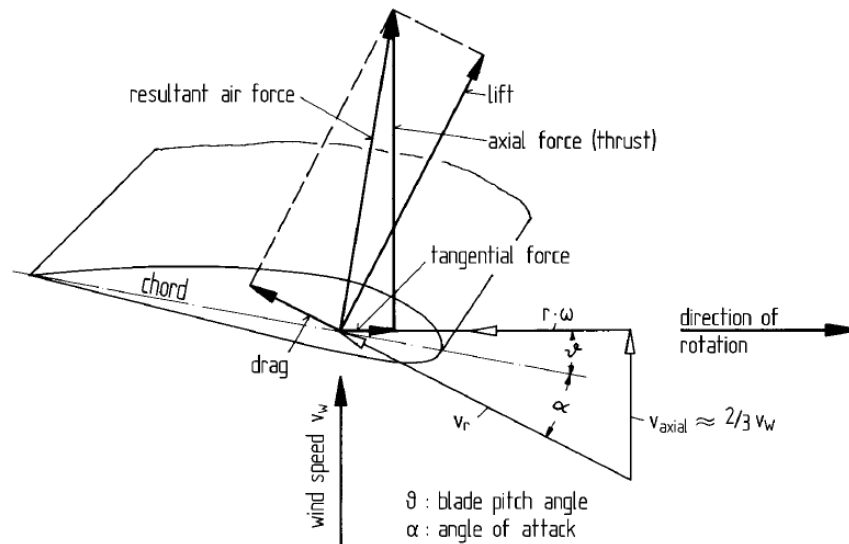
Figure 2.3: Flow velocities and aerodynamic forces at the airfoil cross-section of a blade element [53].

is the case with horizontal-axis rotors, Darrieus rotors are preferably built with two or three rotor blades. The specific advantages of vertical axis turbine concepts are that their basically simple design includes the possibility of housing mechanical and electrical components, gearbox and generator at ground level, and that there is no yaw system. This is countered by disadvantages such as low tip-speed ratio, inability to self-start and not being able to control power output or speed by pitching the rotor blades. A variation of the Darrieus rotor is the so-called H-rotor. Instead of curved rotor blades, straight blades connected to the rotor shaft by struts are used. Attempts were made particularly in the UK, in the US and in Germany to develop this design to commercial maturity. H-rotors of a particularly simple structure, with the permanently excited generator integrated directly into the rotor structure without intermediary gear-box, were developed by a German manufacturer up until the beginning of the nineties but the development was stopped then since there was no economic success in sight. Occasionally, the Savonius design is still used for small, simple wind rotors, especially for driving small water pumps. It is not suitable for electricity-generating wind turbines due to its low tip-speed ratio and its comparatively low power coefficient.

Altogether, it can be said that wind rotors with vertical axes and among these primarily the Darrieus rotor and Savonius rotor, might still have a large potential for development and optimization. Whether the basic advantages of these designs can prevail over their disadvantages and whether it will become a serious rival to the horizontal-axis rotors cannot be foreseen for the long-term. In any case, this will still require a relatively long period of development. In half of this thesis, the development and optimization of
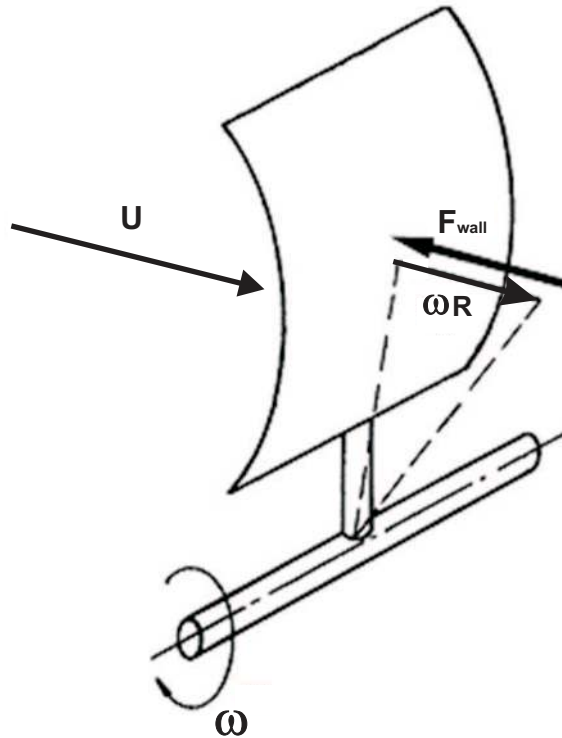
Figure 2.4: Flow conditions and drag force for vertical axis turbines [53].

a new concept based on a Savonius turbine is the target.

2.2.3   Betz limit

The main component of a wind turbine is the energy converter, which transforms the kinetic energy contained in the moving air into mechanical energy. For an initial discussions of basic principles, the exact nature of the energy converter is irrelevant. The extraction of mechanical energy from a stream of moving air with the help of a disk-shaped, rotating wind energy converter follows its own basic rules. The credit for having recognized this principle is owed to Albert Betz. Between 1922 and 1925, Betz published writings in which he was able to show that, by applying elementary physical laws, the mechanical energy extractable from an air stream passing through a given cross-sectional area is restricted to a certain fixed proportion of the energy or power contained in the air stream. Moreover, he found that optimal power extraction could only be realized at a certain ratio between the flow velocity of air in front of the energy converter and the flow velocity behind the converter. Although Betz's "momentum theory", which assumes an energy converter working without losses in a frictionless airflow, contains simplifications, its results are still used for performing first calculations in practical engineering. But its true significance is founded in the fact that it provides a common physical basis for the understanding and operation of wind energy converters of various

designs. For this reason, the following pages will provide a summarized mathematical derivation of the elementary momentum theory by Betz.

2.2.3.1 Betz's momentum theory

The kinetic energy of an air mass m moving at a velocity U can be expressed as:

$$E = \frac{mU^2}{2} \tag{2.1}$$

Considering a certain cross-sectional area A, through which the air passes at velocity U, the volume flow rate Q (m/s^3) flowing through during a time unit, the so-called volume flow rate, is:

$$Q = AU \tag{2.2}$$

and the mass flow rate with the air density ρ is:

$$\dot{m} = \rho AU \tag{2.3}$$

The equations expressing the kinetic energy of the moving air and the mass flow yield the amount of energy passing through cross-section A per unit time. This energy is physically identical to the power P in (W):

$$P = \frac{\rho AU^3}{2} \tag{2.4}$$

The question is how much mechanical energy can be extracted from the free-stream airflow by an energy converter? As mechanical energy can only be extracted at the cost of the kinetic energy contained in the wind stream, this means that, with an unchanged mass flow, the flow velocity behind the wind energy converter must decrease. Reduced velocity, however, means at the same time a widening of the cross-section, as the same mass flow must pass through it. It is thus necessary to consider the conditions in front of and behind the converter (Fig. 2.5). Here, U_1 is the undelayed free-stream velocity, the wind velocity before it reaches the converter, whereas U_2 is the flow velocity behind the converter. Neglecting any losses, the mechanical energy, which the disk-shaped converter extracts from the airflow corresponds to the power difference of the air stream before and after the converter:

$$P = \frac{\rho AU_1^3 - \rho AU_2^3}{2} \tag{2.5}$$

Maintaining the mass flow (continuity equation) requires that:

$$\rho A_1 U_1 = \rho A_2 U_2 \tag{2.6}$$

Thus,

$$P = \frac{\dot{m}}{2}(U_1^2 - U_2^2) \tag{2.7}$$
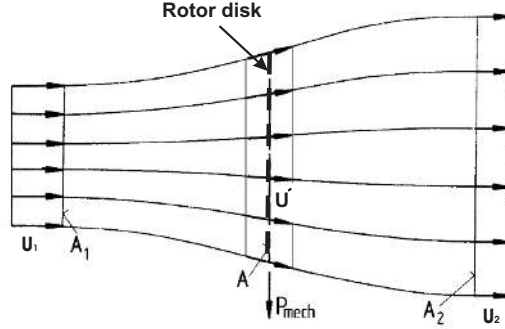
Figure 2.5: Flow conditions due to the extraction of mechanical energy from a free-stream air flow, according to the elementary momentum theory.

From this equation it follows that, in purely formal terms, power would have to be at its maximum when U_2 is zero, namely when the air is brought to a complete standstill by the converter. However, this result does not make sense physically. If the outflow velocity U_2 behind the converter is zero, then the inflow velocity before the converter must also become zero, implying that there would be no more flow through the converter at all. As could be expected, a physically meaningful result consists in a certain numerical ratio of U_2/U_1 where the extractable power reaches its maximum. This requires another equation expressing the mechanical power of the converter. Using the law of conservation of momentum, the force which the air exerts on the converter can be expressed as:

$$F = \dot{m}(U_1 - U_2) \tag{2.8}$$

According to the principle of "action equals reaction", this force, the thrust, must be counteracted by an equal force exerted by the converter on the airflow. The thrust, so to speak, pushes the air mass at air velocity U', present in the plane of flow of the converter. The power required for this is:

$$P = FU' = \dot{m}(U_1 - U_2)U' \tag{2.9}$$

Thus, the mechanical power extracted from the air flow can be derived from the energy or power difference before and after the converter, on the one hand, and, on the other hand, from the thrust and the flow velocity. Equating these two expressions yields the relationship for the flow velocity U':

$$\frac{\dot{m}}{2}(U_1^2 - U_2^2) = \dot{m}(U_1 - U_2)U' \tag{2.10}$$

Thus, the flow velocity in the converter plane is equal to the arithmetic mean of U_1 and U_2.

$$U' = \frac{(U_1 + U_2)}{2} \tag{2.11}$$

The mass flow thus becomes:

$$\dot{m} = \rho A U' = \frac{\rho A (U_1 + U_2)}{2} \tag{2.12}$$

The mechanical power output of the converter can be expressed as:

$$P = \frac{\rho A (U_1^2 - U_2^2)(U_1 + U_2)}{4} \tag{2.13}$$

In order to provide a reference for this power output, it is compared with the power of the free-air stream which flows through the same cross-sectional area A, without mechanical power being extracted from it. This power was:

$$P_o = \frac{\rho A U_1^3}{2} \tag{2.14}$$

The ratio between the mechanical power extracted by the converter and that of the undisturbed air stream is called the "power coefficient" C_p:

$$C_p = \frac{P}{P_o} = \frac{\frac{\rho A (U_1^2 - U_2^2)(U_1 + U_2)}{4}}{\frac{\rho A U_1^3}{2}} \tag{2.15}$$

After some re-arrangement, the power coefficient can be specified directly as a function of the velocity ratio U_2/U_1:

$$C_p = \frac{P}{P_o} = \frac{1}{2} \left[1 - \left(\frac{U_1}{U_2} \right)^2 \right] \left[1 + \left(\frac{U_1}{U_2} \right) \right] \tag{2.16}$$

The power coefficient, i.e., the ratio of the extractable mechanical power to the power contained in the air stream, therefore, now only depends on the ratio of the air velocities before and after the converter. If this interrelationship is differentiated to get the maximum value of the power coefficient it can be obtained that the power coefficient reaches a maximum at a certain velocity ratio with $U_2/U_1 = 1/3$. The maximum "ideal power coefficient" C_p becomes

$$\boxed{C_{p(max)} = \frac{16}{27} = 0.593} \tag{2.17}$$

Betz was the first to derive this important value and it is, therefore, frequently called the "Betz factor". Knowing that the maximum, ideal power coefficient is reached at $U_2/U_1 = 1/3$, the flow velocity U' in the rotor plane becomes:

$$U' = \left(\frac{2}{3} \right) U_1 \tag{2.18}$$

It is worthwhile to recall that these basic relationships were derived for an ideal, frictionless flow (for the effect of the friction, see for instance [77]), and that the result was obviously derived without having a close look at the wind energy converter. In real
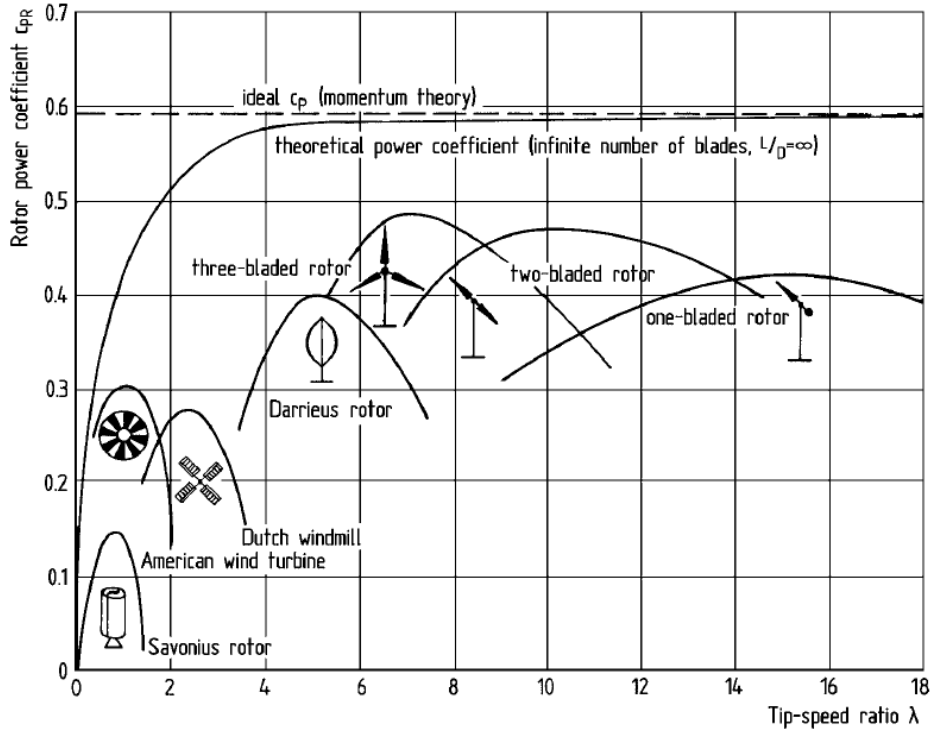
Figure 2.6: Power coefficients of wind rotors of different designs [37].

cases, the power coefficient will always be smaller than the ideal Betz value, as shown in Fig. 2.6. The essential findings derived from the momentum theory can be summarized in words as follows:

- The mechanical power which can be extracted from a free-stream airflow by an energy converter increases with the third power of the wind velocity.

- The power increases linearly with the cross-sectional area of the converter traversed; it thus increases with the square of its diameter.

- Even with an ideal airflow and lossless conversion, the ratio of extractable mechanical work to the power contained in the wind is limited to a maximum value of 0.593. Hence, only less than 60% of the wind energy of a certain cross-section can be converted into mechanical power.

- When the ideal power coefficient achieves its maximum value ($C_p = 0.593$), the wind velocity in the plane of flow of the converter amounts to two thirds of the undisturbed wind velocity and is reduced to one third behind the converter.

2.2.4 Principle operation of standard Savonius turbines

In half of this thesis, optimizing of a Savonius wind turbine will be considered.

The choice of a wind turbine is obviously based on its performance in connection with the local wind conditions. To support the discussion, a comparison between the characteristics of the main conventional wind turbines is shown in Fig. 2.6.

Figure 2.6 gives the power coefficient C_p, ratio of the aerodynamic power of the turbine to the power of the incident wind, as a function of the speed ratio λ. This speed ratio λ is also called velocity coefficient and is equal to the ratio of the tip peripheral speed to the wind velocity. The power coefficient is directly linked to the global efficiency of a wind machine. The curves in Fig. 2.6 show that the fast running horizontal axis wind machines (two- or three-bladed airscrew) have incontestably the best efficiencies. Consequently, theses machines are nowadays systematically chosen for the equipment of large-area wind sites. On the other hand, the Savonius rotor, which is a slow-running vertical axis wind machine ($\lambda \simeq 1.0$) has a rather poor efficiency: $C_p \simeq 0.15$ to 0.2 at best [68]. Nevertheless, it can present some advantages for specific applications, in particular due its simplicity, and resulting robustness and low cost. And there is room for improvement!

S.J. Savonius initially developed the vertical axis Savonius rotor in the late 1920s. The concept of the Savonius rotor is based on cutting a cylinder into two halves along the central plane and then moving the two half cylinders sideways along the cutting plane, so that the cross-section resembles the letter S [36] (Fig. 2.7).
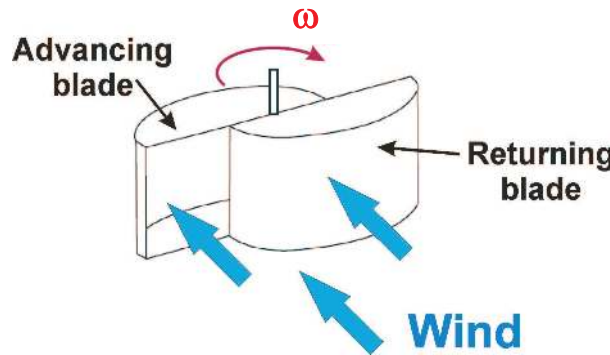
Figure 2.7: Conventional Savonius rotor.

2.2.5 Performance of a Savonius turbine

Using the notations of Fig. 2.8, the velocity coefficient is defined as:

$$\lambda = \omega R / U \qquad (2.19)$$

For a Savonius rotor of height H, a wind of incoming velocity U, the mechanical power P and the mechanical torque on the axis of a Savonius turbine can respectively be written as follows:

$$C_p = \frac{P}{\rho R H U^3} \qquad (2.20)$$
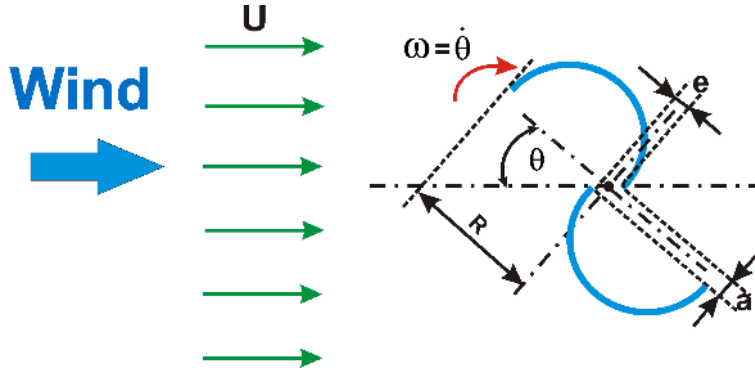
Figure 2.8: Schematic description and main parameters characterizing a Savonius rotor.

and

$$C_m = \frac{T}{\rho R^2 H U^2} \tag{2.21}$$

where C_p and C_m are respectively the power coefficient and the torque coefficient. In the following sections, a rotor is called a *conventional Savonius rotor* if the geometrical parameters a and e Fig. 2.8 are respectively equal to 0 and $d/6$. This reference configuration of the rotor has been extensively studied by many groups (see citations in [70] and next chapter). This conventional design will be the starting point for the optimization process described in later chapters.

2.3   Wave energy conversion

Let us switch to the second focus of this document: wave energy conversion with optimized Wells turbines. Very large energy fluxes can be found in deep water sea waves. The power in the wave is proportional to the square of the amplitude and to the period of the motion. Therefore, the long period ($\approx$10 s) and large amplitude ($\approx$2 m) waves have considerable interest for power generation, with energy fluxes commonly averaging between 50 and 70 kW per meter width of oncoming wave.

The possibility of generating electrical power from these deep water waves has been realized for many years, and there are countless ideas for machines to extract the power.

The utilization of the sea wave was rarely considered on a practical scale prior to 1973. However, a great deal of research has been conducted since 1973, the year of so-called oil crisis [5].

In recent years interest has revived, particularly in Japan, Britain and Scandinavia, so the research and small-scale development has progressed to the stage of commercial construction for power extraction. As with all renewable energy supplies, the scale of operation has to be determined and present trends support moderate power generation levels at about 1 MW from modular devices about 50 m wide across the wavefront. Such devices should be economic to replace diesel-generated electricity, especially on islands [134].

2.3.1 Wave energy potential

There is a large amount of ongoing work on wave energy due to a broad availability (Fig. 2.9), which cannot be done justice in a brief overview. For ease of presentation, the activities will be divided between the technologies suitable for deployment on the shoreline, near the shore and offshore [133].

Wave power levels are approximate and given as kW/m of wave front
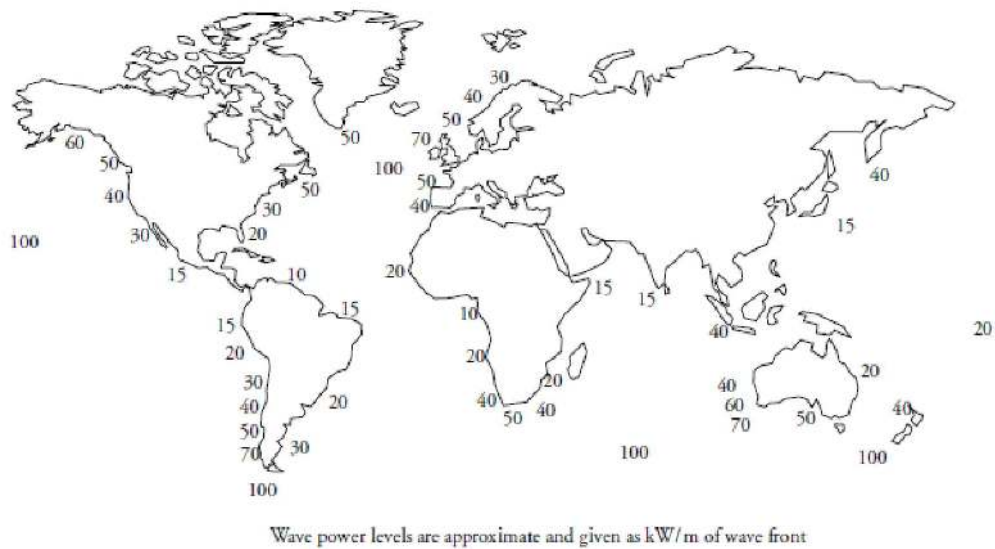
Figure 2.9: Approximate global distribution of wave power levels in kW/m of wave front [133].

- Shoreline devices

  These devices are fixed to or embedded in the shoreline itself, which has the advantage of easier maintenance and/or installation. In addition these would not require deep water moorings or long lengths of underwater electrical cable. However, they would experience a less powerful wave regime.

- Near shore devices

  The main prototype device for moderate water depths (i.e., < 20 m depth) is the OSPREY developed by Wavegen. This is a 2 MW system, with provision for addition of a 1.5 MW wind turbine. Since there could be environmental objections to large farms of wind or wave energy devices close to the shore, this system aims to maximize the amount of energy produced from a given amount of near shore area.

- Offshore devices

  This class of device exploits the more powerful wave regimes available in deep water (> 40 m depth) before energy dissipation mechanisms have had a significant effect.

However, it is important to appreciate the many difficulties facing wave power developments. It was summarized by Twidell and Weir [134] as follows:

1. Wave patterns are irregular in amplitude, phase and direction. It is difficult to design devices to extract power efficiently over this wide range of variables.

2. There is always probability of extreme gales or hurricanes producing waves of freak intensity. The structure of the power devices must be able to withstand this.

3. Wave periods are commonly from 5 up to 10 sec (frequency $\cong$0.1 Hz). It is extremely difficult to couple this irregular slow motion to electrical generators requiring about 500 times greater frequency.

Many attempts have been made to construct such devices and efficiently match variable natural conditions, extract the wave power and withstand the listed difficulties. Some of these devices being developed are placed underwater, anchored to the ocean floor, while others ride on top of the waves. The following section gives an idea of the most famous mechanism to convert the wave energy to mechanical energy, called Oscillating Water Column mechanism (OWC).

2.3.2 Oscillating Water Column (OWC) principle

One of the many extraction systems proposed in recent years, the oscillating water column device, provides the simplest and possibly the most reliable means of converting slow irregular wave motion into high speed rotational movement required for electrical power generation.

The device is essentially a caisson rested on sea bottom with a large submerged opening at the front and a small nozzle at the ceiling (Fig. 2.10). An air turbine coupled to an electric generator is connected to the nozzle. The water column within the lower half of the caisson is caused to oscillate vertically by incident waves through the opening, and it induces the compression and expansion of air mass within the upper half of the caisson as shown in Fig. 2.10. The air motion generates a high-velocity flow through the nozzle, which activates the air turbine and generates electricity [73]. The wave power is thus converted into air power in the air chamber of the wave power-extracting caisson.

OWC wave power extractors can be quite easily fitted to a vertical breakwater, because the latter is mostly built with a large concrete caisson rested on the foundation. A combination of OWC wave power extractor and breakwater is also attractive from the viewpoint of economical feasibility of wave power extraction, because the construction cost of the total system can be jointly born by the accounts for power generation and harbor protection.

2.3.3 Wells turbines

Serious research on wave-energy extraction methods began in several countries during the 1970's. Dr. Wells, a former professor of civil engineering at Queen's university of
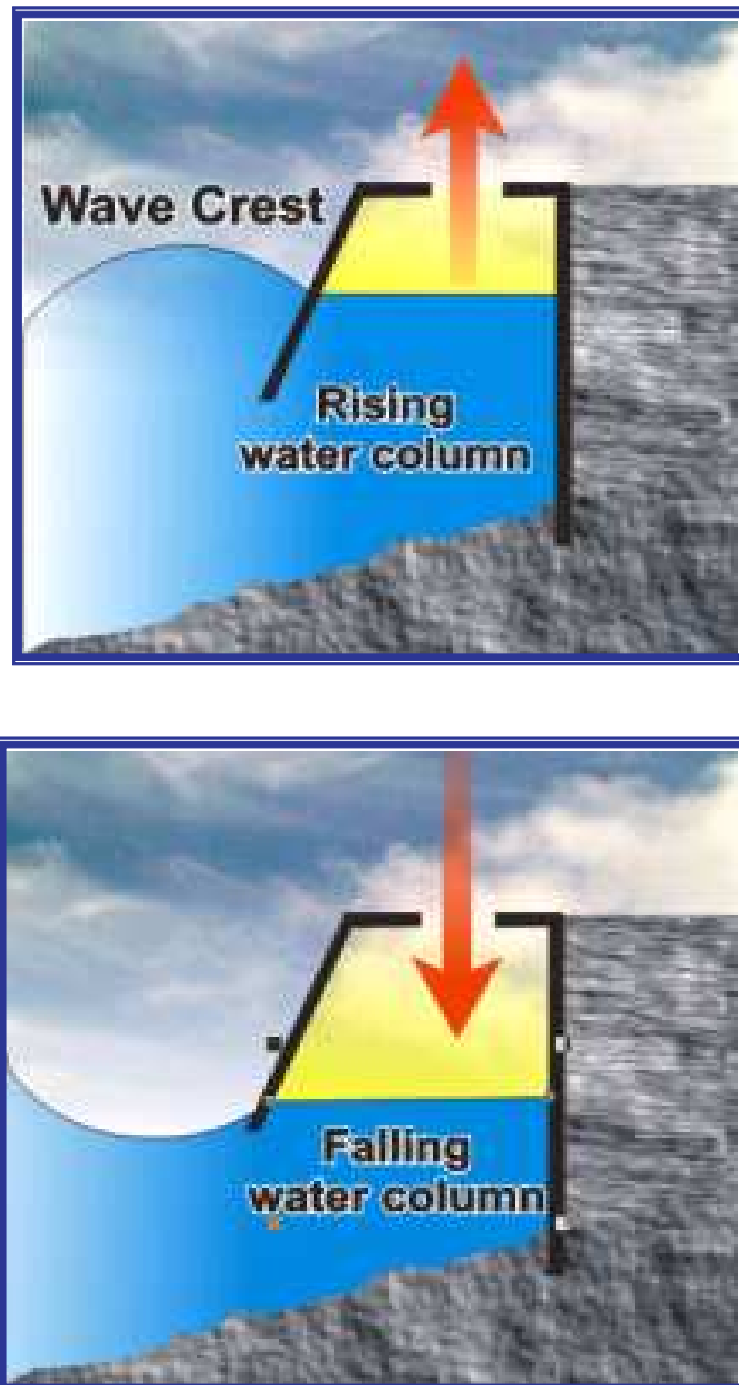
Figure 2.10: The wave motion in the OWC device [73].

Belfast, proposed in 1976 a form of self-rectifying axial flow air turbine as a device suitable for wave energy conversion using the oscillating water column. In its simplest form the air turbine rotor consists of several symmetrical airfoil blades positioned around a hub. Because of its simple and efficient operation, the Wells turbine has been widely

applied for ocean waves energy absorption. Therefore, it has been subjected to a considerable amount of research and development in many counties. In the next chapter, the state of the art of Wells turbines used as converter for wave energy will be proposed.

2.3.4 Operation of Wells turbines

Most research programs attempting to gain energy from waves depend on the OWC as converter mechanism [7, 22, 25, 75, 137]. The water wave energy is converted to pneumatic energy in the air, which passes periodically across a self-rectifying, axial air flow turbine. The first prototype was constructed in UK in 1988. This device is located on the Isle of Islay, one of the southern islands in the Inner Hebrides and depends on a Wells turbine as final converter [15, 16, 84, 138].

The turbine itself consists in a number of symmetric airfoils set around the hub radially at 90° stagger angle, with the chord plane normal to the axis of rotation (Fig. 2.11). According to the standard airfoil concept, if the airfoil is set at an angle of attack α in a fluid flow, it will generate a lift force F_L normal to the free stream and a drag force F_D in the direction of the free stream. These lift and drag forces can be combined to get the tangential force F_T and the axial force as shown in Fig. 2.12. For a symmetrical airfoil as considered in [84, 86, 88, 90, 92, 97], the direction of tangential force, F_T is the same for both positive and negative values of angle of attack ($\pm\alpha$) as shown in Fig. 2.12.
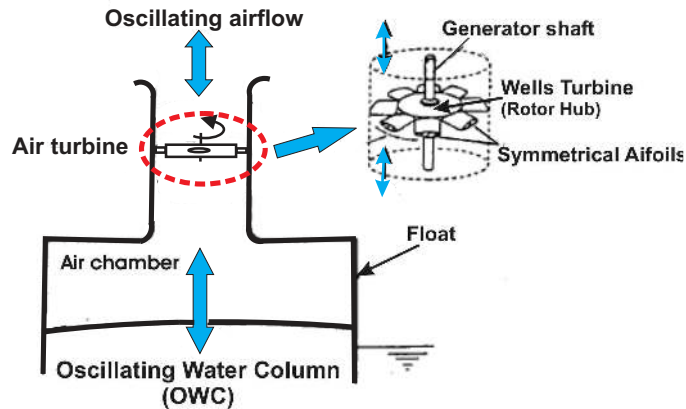
Figure 2.11: Wells turbine in state of upward and downward air flow.

2.3.5 Wells turbine performance

If such symmetric airfoil blades are positioned around an axis of rotation, they will rotate in the tangential force direction regardless of the direction of airflow, as shown in Fig. 2.12. The force F_T is responsible for the torque and consequently the blade power,

while the axial force F_A results in an axial thrust along the axis of the rotor, which has to be absorbed by the bearings. This leads to a unidirectional device rotation for an alternating airflow without the need for non-return valve. The tangential force F_T and the axial force F_A shown in Fig. 2.12 can be obtained from:
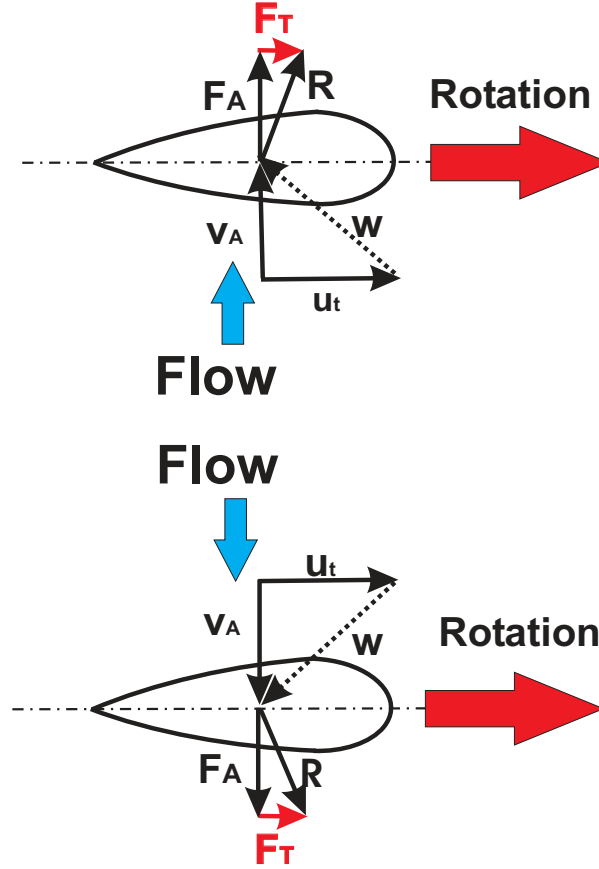
Figure 2.12: Axial and tangential forces acting on a Wells turbine.

$$F_T = F_L \sin(\alpha) - F_D \cos(\alpha) \tag{2.22}$$

$$F_A = F_L \cos(\alpha) + F_D \sin(\alpha) \tag{2.23}$$

The running characteristics under steady flow conditions are usually characterized by the tangential force coefficient C_T, axial force coefficient C_A and efficiency η with flow coefficient ϕ. The tangential force coefficient C_T and the axial force coefficient C_A are calculated as :

$$C_T = F_T / \left[(1/2)\rho \left(v_A^2 + u_t^2 \right) zbc \right] \tag{2.24}$$

$$C_A = \Delta p_0 \pi r_t^2 / \left[(1/2)\rho \left(v_A^2 + u_t^2 \right) zbc \right] \tag{2.25}$$

where $u_t = \omega r_t$ is the peripheral velocity, ω is the rotor angular velocity and r_t is the tip radius (Fig. 2.13). Furthermore, v_A is the axial velocity normal to the plane of rotation,
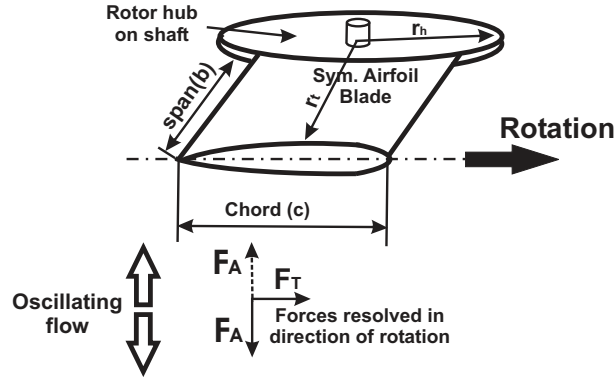
Figure 2.13: Main geometrical parameters of a Wells turbine.

z is the number of blades, b is the blade span, c is the blade chord (see Fig. 2.13) and Δp_0 is the total pressure difference across the rotor.

The non-dimensional variables expressing the performance of a Wells turbine are function of the aerodynamic force coefficients that are in turn function of several parameters, as given by [84, 92]:

$$(C_T, C_A) = f(\phi, s, h, AR, \tau, \tau_c, T_u, f^*, Re, blade\ profile\ shape) \qquad (2.26)$$

where, $\phi = v_A/u_t$ is the flow coefficient, s is the rotor solidity, h is the hub to tip ratio (r_h/r_t), AR is the aspect ratio (b/c), c is blade chord, b is blade span, τ is the blade thickness, τ_c is the tip clearance ratio, T_u is the turbulence level, f^* the frequency of wave motion and the Reynolds number Re.

2.4 Conclusions

After having introduced all needed concepts and notations, its is now time to analyze the state of the art for both systems considered in this thesis: Savonius turbine (wind energy) and Wells turbine (wave energy).

Chapter 3

Literature Review

Due to the growing significance of wind and wave energy conversion, a wealth of publications can be found for the systems considered in this thesis. The present chapter is again divided in two parts. The present state of Savonius turbines is first considered, before reviewing the literature on Wells turbines.

3.1 Savonius turbine

Savonius turbines show inherent drawbacks compared to conventional wind turbines: mainly a low efficiency and poor starting characteristics. Therefore, many authors have tried to identify the best principles of operation and to improve the characteristics of Savonius turbines.

3.1.1 Experimental investigations of Savonius turbines

Some studies have been carried out in wind tunnels, using controlled conditions. Other consider free-space experiments. Generally, the global performance of a rotor, identical to or derived from the conventional Savonius rotor, is presented in such studies, but without realizing any detailed, quantitative parametric study. Sometimes, some visualizations of the flow in and around the rotor are proposed, but with a poor description of the physical phenomena. Such publications are of very limited scientific or technological interest and are therefore not included here.

Beyond issues associated with intellectual properties, this lack of quantitative information is sometimes associated to the complexity of the flow in and around wind turbines. In particular for Savonius turbines, the resulting flow conditions are highly unsteady. Furthermore, boundary layer separation is an essential aspect for the efficiency of the system. As a consequence, detailed aerodynamic studies are rare and often do not allow the prediction of the energetic behavior of the rotor. However, some publications [10, 27, 31, 51] are of higher quality and give a precise description of the aerodynamics of the conventional Savonius rotor, mainly obtained by pressure measurements on the paddles.

Further articles describe an extensive experimental study in a wind-tunnel to evaluate the importance of geometrical parameters on the Savonius rotor performance. Through the corresponding rotor power output coefficient versus the tip speed ratio, the influence of each blade geometry parameter is investigated. Such parametric studies already lead to geometrical configurations with a considerable increase in the rotor performance efficiency [30, 39, 54, 128, 142].

The flow in and around a Savonius rotor has also been studied using flow visualization experiments in combination with the measured pressure distributions on the blade surfaces. It is observed that the flow separation regions on the blade surfaces are fairly reduced by the rotation effect (compare Fig. 3.1 and 3.2). Similarly, the flow through the overlap is weakened by the appearance of resisting flow. The former contributes to the torque production of the rotating rotor while the latter acts as a resistance. These phenomena, together with the flow stagnation region on the front side of the rotor, contribute to the power producing mechanism of the Savonius rotor [4, 29].
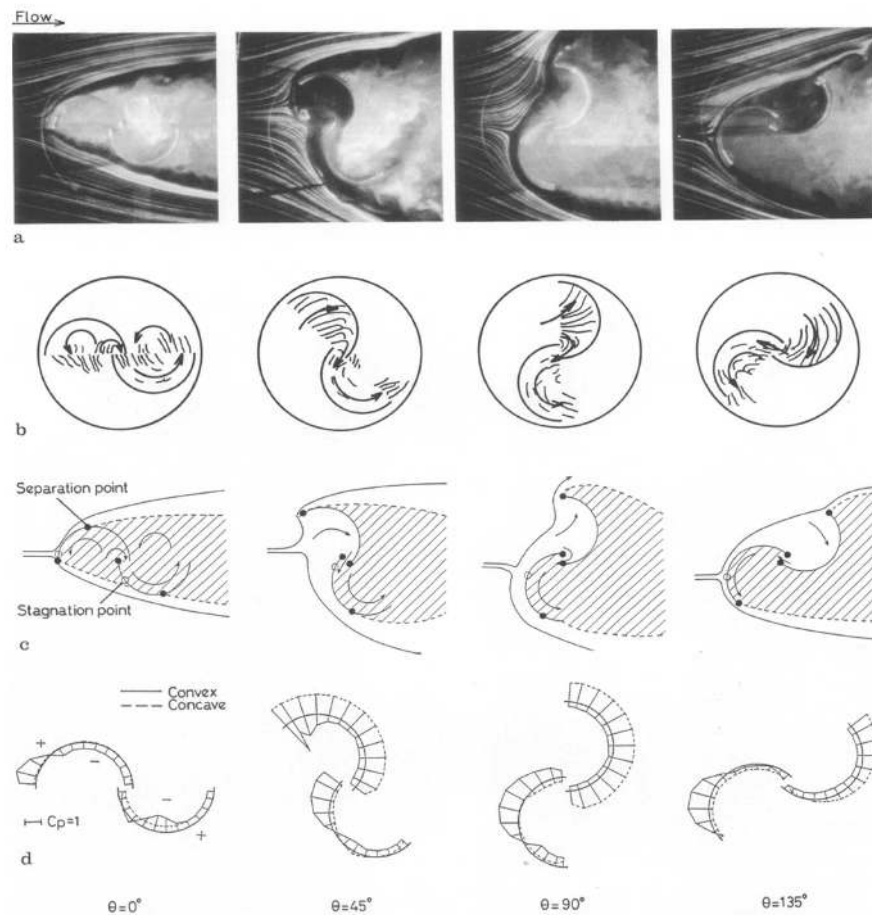
Figure 3.1: Flow in and around a non-rotating Savonius rotor ($\lambda = 0$); a: visualized flow field; b: flow inside the rotor; c: flow model; d: surface pressure distribution [29].
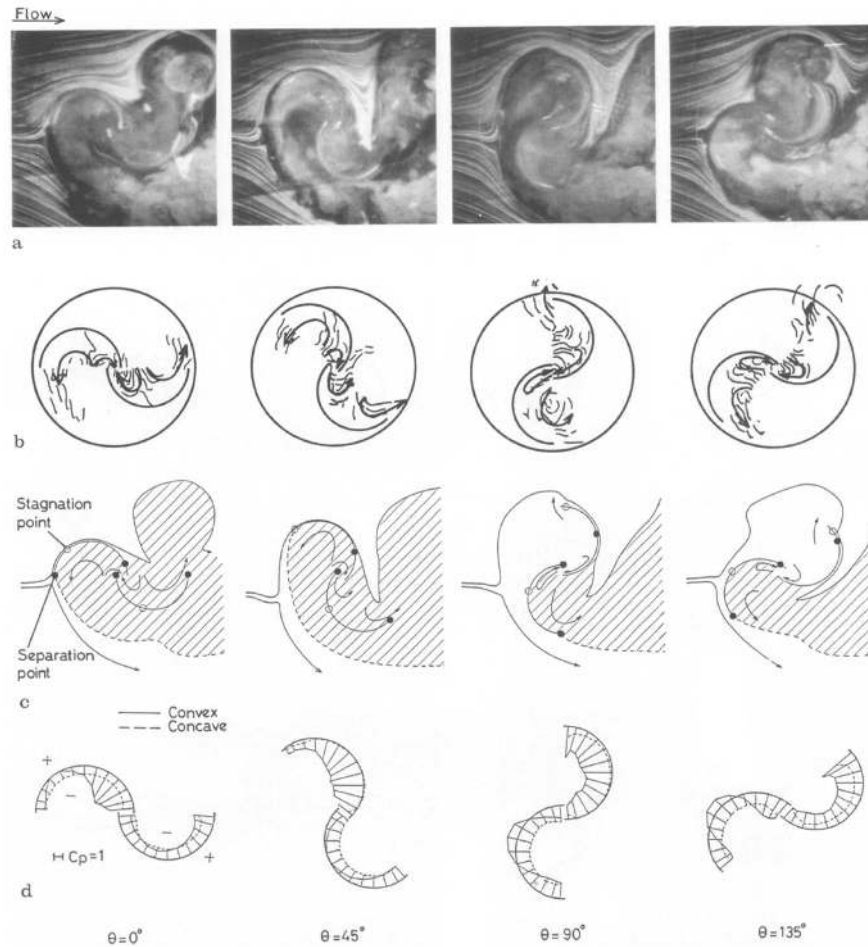
Figure 3.2: Flow in and around a Savonius rotor in rotation ($\lambda = 0.9$); a: visualized flow field; b: flow inside the rotor; c: flow model; d: surface pressure distribution [29].

Significant features observed here are the downward movement of the separation point (Fig. 3.2c) and the relative decrease in the pressure coefficient on the convex side of the advancing blade (Fig. 3.2d). These phenomena can be caused by the occurrence of a Coanda-like flow pattern (Fig. 3.2a) on the convex side, which appears clearly at small rotor angles of $\theta = 0°$ to $45°$. The attached flow on the convex side tends to separate at large rotor angles ($\theta = 90°$ to $135°$), which is due to the outward flow motion at the tip of the advancing blade. This flow is induced by the pressure gradient distributed over the concave side of the advancing blade. The injected flow grows into a vortex circulating in the rotating direction of the rotor, which increases in size downstream. It is considered that the attached flow patterns of the rotating rotor contribute to the rotating torque of the rotor, as is expected from the pressure distributions (Fig. 3.2d). On the other hand, a relative decrease in the stagnation torque is expected here in comparison with the non-rotating rotor (Fig. 3.1), since the relative velocity is decreased on the advancing blade and is increased on the returning one. In addition, the stagnation point moves to the

center of the blade due to the rotation effect. It can be seen that the pressure coefficients are decreased overall by the effect of circulation produced by the rotor rotation. Such a circulation is a steady phenomenon. In comparison with the non-rotating rotor, the flow through the overlap is reduced here by the production of resisting flow. This flow is expected to reduce the pressure recovery effect on the back side of the returning blade, which is supported by the measured pressure distributions near the overlap.

3.1.2 Numerical investigations of Savonius turbines

Numerical simulations have also been carried out on this kind of rotors. These studies include static or dynamic modelling. Nevertheless, most results suffer from a too crude description of the rotor. A few of these papers [23, 28, 49] used the discrete vortex method to predict the flow around a pair of coupled Savonius rotors. They suggested that the reason why so few numerical studies had been successful was due to the complexity of the flow pattern about the rotor and to the separation of the flow from the blade surfaces.

Usually, wind sites are equipped today with fast-running horizontal axis wind turbines of the airscrew type, associated to a high efficiency. Some articles point out that the choice of a wind turbine must not be based only on high efficiency and proposed a comparative criterion adapted to the comparison of a horizontal axis wind turbine with a vertical axis wind turbine: the L-σ criterion. This criterion consists in comparing wind turbines which intercept the same front width of wind, by allocating them a same reference value of the maximal mechanical stress on the blades or the paddles. On the basis of this criterion, a quantitative comparison points to a clear advantage of the Savonius rotors, because of their lower angular velocity, and provides some elements for the improvement of their rotor [71]. The results show that the power per unit length provided by the considered Savonius rotor is about four times as high as that provided by a fast-running two bladed airscrew. The American windmill and the Savonius rotor have comparable values of their associated power per unit length. A favorable factor to obtain a high power per unit length is consequently a low angular velocity. In terms of the ease of setting up, and the potential for improvement in efficiency, the Savonius rotor should be preferred to all other considered configurations following [71].

Flow fields around rotating Savonius rotors have been also simulated by solving the two-dimensional incompressible Navier-Stokes equations [95]. The results show a good agreement with experimental performance for the following points: the torque grows weaker in inverse proportion to the tip speed ratio; a gap between the rotor buckets is effective in increasing maximum power. These calculations have been realized using a static approximation (the rotor is supposed to be fixed whatever the wind direction) and also a dynamic calculation; in this second case, the velocity coefficient was equal to 1.0 (nominal working point in accordance with Fig. 2.6). These calculations are continued until the residual values (variations in certain chosen parameters, e.g., velocity in the wind direction), have all dropped below 10^{-3} (criterion for convergence). From our experience, this is a relatively weak and perhaps insufficient criterion.

A separate study has been carried out to verify the model accuracy, comparing a

static simulation and a dynamic one. To do so, a static simulation of the flow around the conventional Savonius rotor ($e/d = 1/6$; $a = 0$; no central shaft) has allowed to determine the pressure distribution on the paddles. Then the static torque has been calculated as a function of the wind velocity angle θ (Fig. 2.8). These numerical results were compared to experimental data. The simulations give satisfactory results since the differences between the experimental data and the numerical simulations are always below 10%, except for angles θ around 0° and 180° where an instability of the torque is observed (Fig. 3.3, [68]).
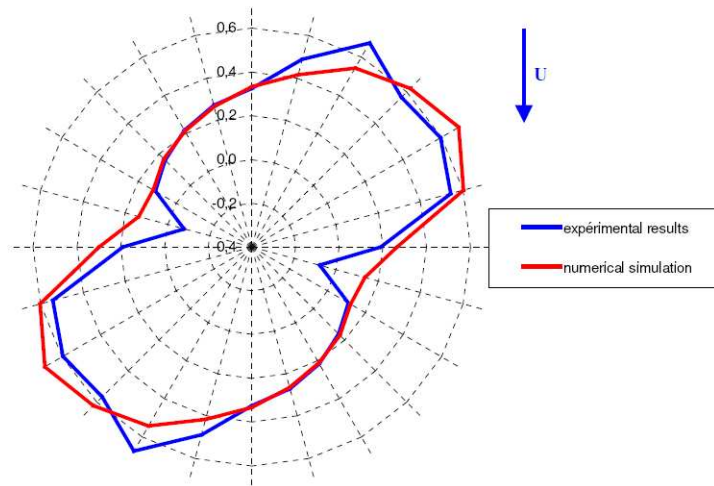
*Figure 3.3: Static torque coefficient of a Savonius rotor (*Re $= 1.56 \, 10^5$*) [68].*
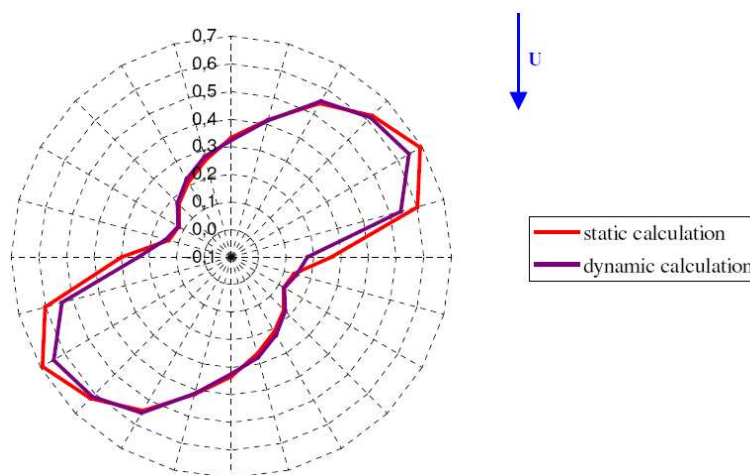
*Figure 3.4: Dynamic torque coefficient of a Savonius rotor (*Re $= 1.56 \, 10^5, \lambda = 1$*) [68].*

In a second step, a dynamic calculation (rotating turbine) has been carried out for the same value of the Reynolds number: Re$= 1.56 \, 10^5$, setting the velocity coefficient

equal to 1.0. The torque coefficient C_m has been evaluated by calculating the average value of the torque on a whole revolution of the rotor. The results are compared to the ones given with the static calculation. The difference between the two curves generally does not exceed 2% whatever the angle θ (Fig. 3.4). This is clearly in contradiction with the experimental studies discussed previously (see again Fig. 3.1 and 3.2), and must therefore be considered with caution. The simulated flows have been analyzed by visualizing relative velocity, vorticity, pressure, etc. The behavior of the shed vortices has been observed carefully, and it has been clarified that the shed vortices have a large effect on the resulting flow fields and on the global performance [49, 50, 70].

3.1.3 Methods to improve Savonius turbine performance

Several propositions can be found in the literature to improve the performance of conventional Savonius rotors.

3.1.3.1 Deflector plate

Attempts to improve the performance of a S-shaped Savonius rotor by using a deflecting plate placed in front of the rotor have been documented. Using a deflecting plate placed on the retreating side of the blade it has been observed that the power coefficient can be increased relatively by about 20% [27, 43].

3.1.3.2 Double and three steps Savonius rotor

When considering only the starting torque, it can be seen that, for some directions of the wind velocity, the starting torque of the standard Savonius configuration would be so low that the rotor could not start alone. It is the reason why many authors have chosen to use a double-step (see Fig. 3.6) and three-step Savonius rotor, where the upper and the lower paddle pairs are set at 90° to each other (double step), respectively at 120° for the three step rotor. The double-step and three-step rotors are said to be slightly superior to the corresponding single-step turbine (conventional Savonius rotor) in self-starting, but lower for both torque and power characteristics [38, 68].

3.1.3.3 Guide vanes

In order to decrease the torque variation of the standard Savonius rotor and to improve its starting capability, a new type of Savonius turbine, using three stages with 120 degree bucket phase shift between the adjacent stages with and without guide vanes, has also been investigated [39].

The results indicate that the static torque coefficient of the one stage turbine without guide vanes is periodic with a cycle of 180 degrees (depending on the number of stages) and that its variation is very large. The lower values of static torque are observed in the ranges of $\theta = 140° - 170°$ and $320° - 350°$. Guide vanes can be used to increase the static torque and decrease its fluctuation. But, unlike the static characteristic, the dynamic effect depends on the wind speed, so that the maximum values of C_m and C_p
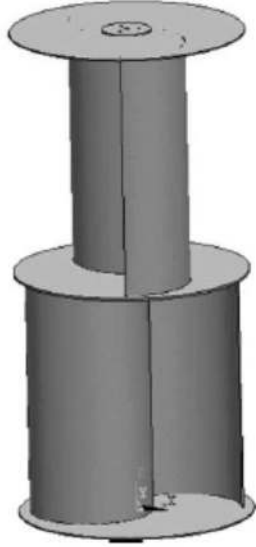
Figure 3.5: Double-step Savonius rotor [68].

of the three-stage rotor are much smaller than those of the one-stage rotor. The guide
vanes increase the dynamic torque coefficient for small λ values ($0 < \lambda < 0.3$), but lead
to a decrease in the torque for larger values ($\lambda > 0.3$).

Recently, one study was published concerning the three bucket Savonius rotor [36].
Unfortunately, the authors rely on an erroneous formulation to compute the rotor power
and torque. They consider:

$$P_{rotor} = (1/2\rho A V_1^2)u \tag{3.1}$$

and

$$T = 60 P_{rotor}/2\pi N \tag{3.2}$$

where V_1 is the test-section inlet air velocity and u is the tip peripheral blade velocity.
As a consequence the computed power is the power available in the incoming wind and
not the mechanical power of the turbine. Consequently, the results are not analyzed
further.

3.1.3.4 Twisted-blade Savonius rotor

Another investigation aims at exploring the feasibility of a twisted-bladed Savonius
rotor for power generation (Fig. 3.6). A twisted blade integrated within a three-bladed
rotor system has been tested in a low speed wind-tunnel, and its performance has
been compared with conventional semi-circular blades (corresponding to a twist angle
of 0°). Performance analysis has been made on the basis of starting characteristics, static
torque and rotational speed. Experimental evidence shows the potential of the twisted
blade rotor in terms of smooth running, higher efficiency and self-starting capability
as compared to that of the conventional rotor [94, 98]. Semicircular blades correspond

to zero twist angle. By increasing this angle, the performance of the Savonius rotor is increased in its performance as shown in Fig. 3.7. It is also shown that a larger twist angle is preferable for a lower wind velocity in order to produce maximum power and better starting characteristics. A twist angle $\alpha = 15°$ gives optimum performance at low airspeeds of $U = 6.5$ m/s in terms of starting acceleration and maximum no-load speed. Such blades shows a maximum of $C_p = 13.99$ at tip speed ratio of $\lambda = 0.65$ (i.e., at $U = 8.23$ m/s), whereas the semicircular blade $\alpha = 0°$ shows a $C_p = 11.04$ at $\lambda = 1$.
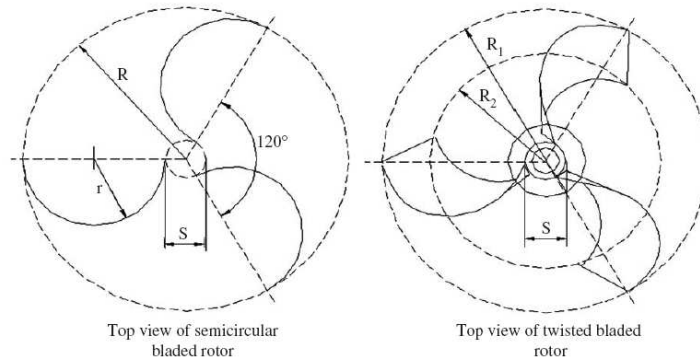
Figure 3.6: Twisted-blade Savonius Rotor [98].
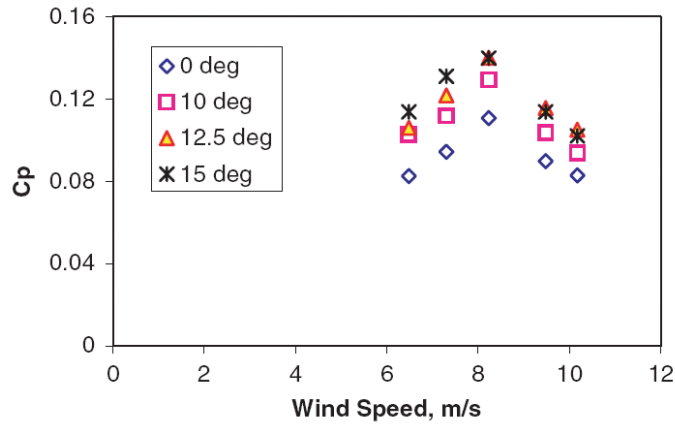
Figure 3.7: Power coefficient for twisted-blade Savonius rotor [98].

3.1.3.5   Savonius rotor using a guide-box tunnel

This publication aims at improving and adjusting the output power of a Savonius rotor under various wind power. A guide-box tunnel is employed as the appropriate device to achieve this purpose. The guide-box tunnel is like a rectangular box used as wind passage, in which a test rotor is included as shown in Fig. 3.8. The area ratio between

the inlet and exit of the guide-box is variable in order to adjust the inlet mass flow rate or input power. At first, experiments have been conducted to find the configuration that would provide the best relative performance. The experiments measure the static torque of the fixed rotor at any phase angle and the dynamic torque under rotation.

Figure 3.9 shows that the maximum rotor rotational speed is obtained for a guide-box area ratio between 0.3 and 0.7. The resulting value of the output power coefficient of the rotor with guide-box tunnel using an area ratio of 0.43 increases considerably (by a factor 1.5 using three blades; by a factor 1.23 using two blades) compared to the conventional design without guide-box (Fig. 3.9). The optimum spacing ratio between the rotor tip and the side walls of the guide-box tunnel is around 1.4. The resulting increase in performance seems promising, but the guide-box of course increases considerably the system complexity [48].
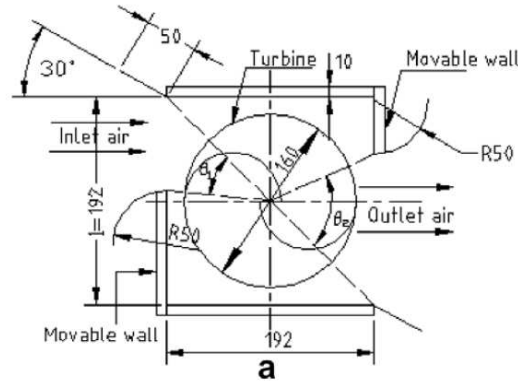
Figure 3.8: Savonius rotor using a guide-box tunnel [48].

3.1.3.6 Modified Savonius rotor

The conventional Savonius rotor is made from two vertical half-cylinders running around a vertical axis. A modified rotor (Fig. 3.10) has also been proposed, which is just a modification of the Savonius rotor, using now three geometrical parameters: the main overlap e, the secondary overlap e', and the angle β between the paddles. The characteristic curve of such a rotor (values of the static torque coefficient C_m vs. wind angle) are presented in Fig. 3.11.

The results are relatively encouraging, since the new rotor induces maximal values of the static torque much higher than those obtained with the conventional rotor. Nevertheless, it also introduces low and negative values of the torque, with a large angular variation. Overall, the mean value of the torque is increased: $C_m = 0.48$, i.e., 60% more than for the conventional rotor. Further studies are necessary to refine the analysis.
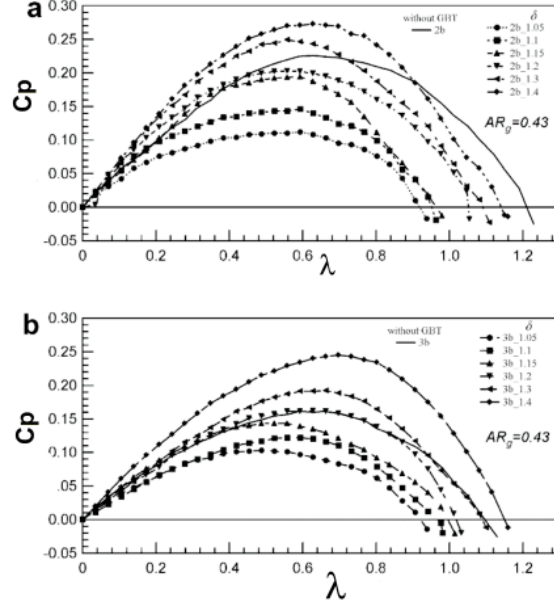
Figure 3.9: Power coefficient of Savonius rotor using a guide-box tunnel [48].

Table 3.1: Summary of Savonius turbine main modifications

Design	Gain	Description	Comments
Deflector Plate	20%	Not verificated	No details since 1992
Multi-Steps	Good self-starting	For same aspect ratio	Lower C_p by 30%
Guide Vanes	Depends on wind speed	Bad for large λ	Good stability
Twisted-blade	$\simeq 27\%$	High cost	Good self-starting capability
Guide-Box Tunnel	50% (3 blades)	Complex design	Not practical
Modified Savonius	60%	Large vibrations	Not practical

3.1.4 Summary of Savonius turbine review

All the research projects discussed in the present review have tried to understand and improve the performance (torque and efficiency) of the Savonius turbine, considering either the conventional geometry or slight modifications. All the improvements have been tested manually, by means of a tedious trial-and-error analysis. Such studies are going on. All proposed modifications have been summarized and discussed in Table 3.1. It can be finally concluded that:

- There is a renewed interest for Savonius turbines in recent years, as shown in Fig. 3.12;

- Depending on the retained definition, their efficiency can be indeed considered as quite high [71];
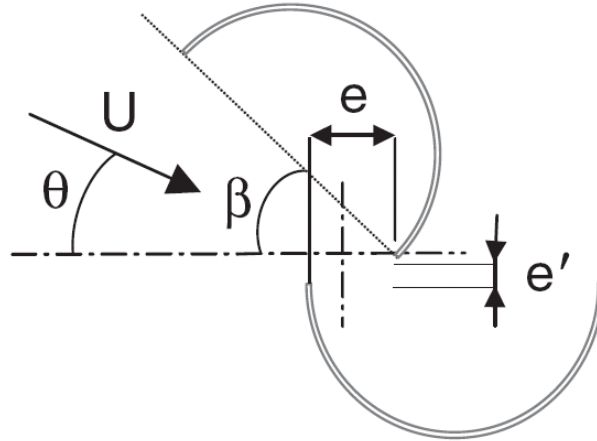
Figure 3.10: Modified Savonius Rotor [69].
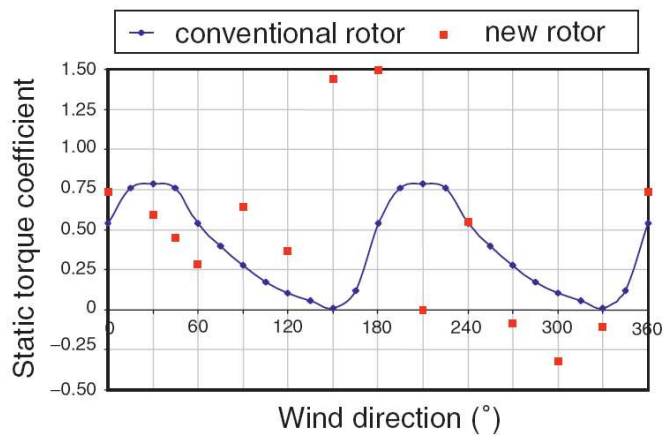
Figure 3.11: Static torque for the modified Savonius rotor ($\theta = 90°$, $\beta = 45°$, $e/d = 1/6$) [69].

- Contradictory observations can be found in the literature, both qualitatively and quantitatively. Therefore, the results presented in this review must all be considered with great caution;

- Many small modifications and improvements have been proposed in the literature to improve global efficiency or some specific characteristics (e.g., self-starting conditions) as summarized in Table 3.1 ;

- Nevertheless, a real optimization of the system has not been realized up to now and would therefore be very interesting. This will be the subject considered in later chapters of this thesis.
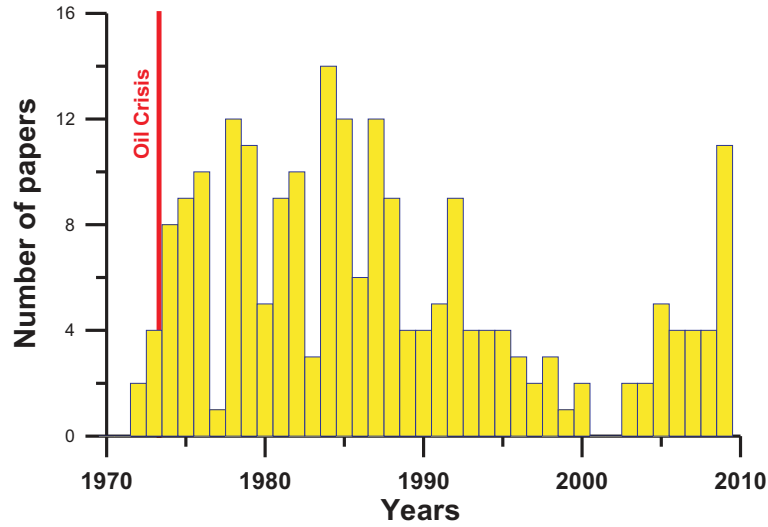
Figure 3.12: Savonius turbine publication statistics in international journals and conferences.

3.2   Wells Turbine

Let us switch now to the second configuration discussed in this work.

3.2.1   Performance parameters of Wells turbine

Many papers cited in the literature [9, 21, 63, 141] concern the principle of operation and factors controlling the performance of Wells turbines both experimentally and theoretically. The performance of Wells turbine includes the power output, the pressure drop across the rotor, the turbine efficiency and the operating range of the turbine.

Here, we should note that the performance of the wave power converter depends on the energy absorption efficiency of the OWC, which is closely related to the pressure difference across the turbine, as well as to the turbine efficiency. An unidirectional airflow test rig [82] constructed to investigate experimentally the effect of the flow coefficient ϕ, on both the pressure drop coefficient and the efficiency of a monoplane turbine and in same time a theoretical investigation was made, at $h = 0.62$ for two values of rotor solidity ($s = 0.5$ and $s = 0.75$). The results indicated that, a linear relationship between the pressure drop across the turbine and the flow coefficient ϕ, exists, for both low or high rotor solidity. It also indicated that the blade efficiency for blade profile NACA 0021 increases with the flow coefficient up to a certain value, and then decreases. This is due to separation of the flow around the turbine blades. In the next sections we will discuss in details the different parameters affecting the performance of Wells turbines.

3.2.1.1   Solidity

The solidity of the turbine, $s = zc/\pi r_t(1 + h)$ (see Fig. 3.13) is a measure of airflow blockage within the turbine. It is also a measure of the mutual interaction between the blades and is an important design variable that affects the self-starting of the turbine [82, 90, 97, 93, 118, 140]. In Fig. 3.14 the efficiency, η is normalized with respect to the corresponding two dimensional single airfoil efficiency, η_o. The results indicate that at small values of solidity, its impact is small. To obtain self-starting capability of the turbine at hub to tip $h = 0.6$, $s > 0.51$ is needed in [89] but only $s > 0.45$ in [73]. The reduction in efficiency for a Wells turbine at high solidity is due to increased kinetic energy losses at the exit associated with swirl. In addition, there could be significant three dimensional effects near the hub where, at high solidity, the blades are close to each other and may interact with the boundary layer on the hub. These interactions lead to endwall losses on the surface of the hub and also on the blade surfaces near the hub. These effects are compounded by the fact that the blades near the hub are always at a larger incidence that at the tip. In this work, solidity is constant and equal to 0.67, which corresponds to a number of blades equal to 8. This solidity value has been retained since it has been proved in a number of studies to be highly suitable for Wells turbines (for instance [106, 110]).
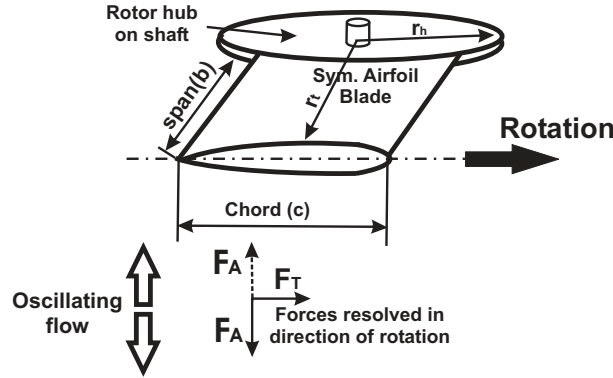
Figure 3.13: Axial and tangential forces acting on a Wells turbine.

3.2.1.2   Hub-to-tip ratio

The effect of the hub to tip ratio ($h = d_h/d_t$ or r_h/r_t, see Fig. 3.13) was studied in several papers [82, 90, 97]. The results indicated that the efficiency for different profiles decreases with increasing the hub to tip ratio. From our personal experience the effect of hub to tip ratio on the turbine efficiency is rather complex. This is due to the interaction between the blades in hub region, which leads to higher incident angles locally. Therefore, the stall occurs earlier in hub region than in the tip region. Admittedly based on small-scale tests, publications suggest that values of $h \approx 0.6$ are recommended for optimal design.
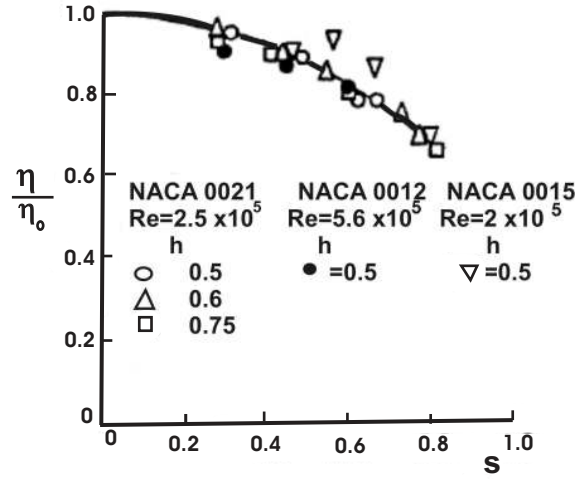
Figure 3.14: Solidity effect on the efficiency [82, 92, 97].

3.2.1.3   Aspect ratio

The aspect ratio, $AR = span(b)/chord(c)$, influences the turbine efficiency and flow ratio at which the turbine stalls, as can be seen in Fig. 3.15. The data shown here are from experiments conducted at a fixed hub to tip ratio and fixed solidity where the variation in the aspect ratio was obtained by varying the chord length. This means that Re= wc/ν changed during the test. Therefore, there is a certain influence of the Reynolds number on this data. These results, again limited to small-scale tests, suggest that aspect ratio and Reynolds number play a dominating effect on the efficiency. The primary effect of reducing the aspect ratio is to increase the efficiency by delaying stall, associated with the positive effect obtained on the blades due to increased mass flow through the tip [82, 97]. The effect of aspect ratio is however not clear in this study due to varying Reynolds number.

3.2.1.4   Reynolds number

A Wells turbine is very sensitive to the Reynolds number (Re= wc/ν) like all conventional turbomachines, due to the impact of Reynolds number on the aerodynamic around the airfoils of the turbine and to its contribution to stall [97].

3.2.1.5   Tip clearance

The tip clearance ratio ($\tau = tip\ clearance/chord(c)$) is a very important parameter for the performance of turbomachines. Several groups studied the effect of tip clearance on stall and efficiency of the Wells turbine.The results indicated that decreasing the tip clearance advances the stall point but increases the efficiency of the turbine, due to the reduced leakage losses. On the other hand, if the turbine has a large tip clearance, it
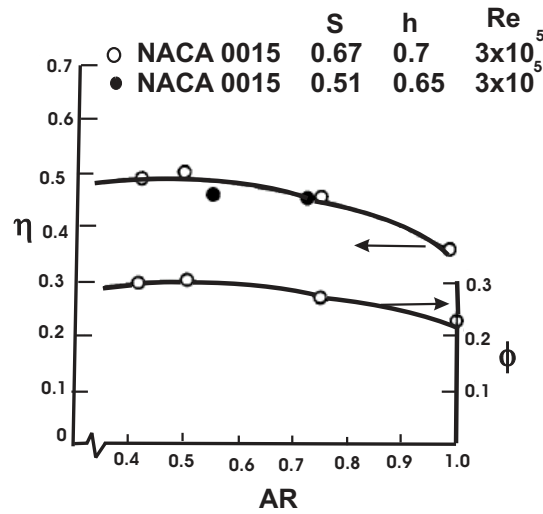
Figure 3.15: Aspect ratio effect on the efficiency [82, 92, 97].

operates without stall. There is no significant advantages to increase tip clearance above 2%. Therefore, the recommended tip clearance is $\tau \leq 2\%$ [45, 46, 82, 97].

3.2.1.6   Inlet turbulence

Turbomachines are sensitive to the inlet flow conditions, such as distortion of velocity profile and turbulence levels. Increase in turbulence levels can alter boundary layer development by advancing transition of the boundary layer and delaying stall. The performance of turbomachines can be improved by increasing the turbulence level at the inlet up to 3% [82, 97]. Experimental results indicate that the performance of the Wells turbine improves with an increase in turbulence but a significant increase in turbulence levels is required to produce any appreciable improvement in performance. As a whole the Wells turbine is less sensitive to inlet turbulence compared to most conventional turbomachines.

3.2.1.7   Blade shape

The airfoil thickness is very important because it determines the aerodynamics around the airfoil, the stall point and the turbine weight. The effect of airfoil thickness on the aerodynamic performance can not be separated from the effect of the Reynolds number, since they contribute together to separation on the airfoil. The published results indicated that NACA 0021 airfoil profiles (21% thickness) lead to the best performance for conventional Wells turbines [93]. Thick airfoil blades are advantages to improve self starting characteristics of the turbine [46, 91, 129, 130, 135].

3.2.2   Unsteady flow effect on the performance of Wells turbine

It is generally accepted that the airflow frequency in a wave energy device is so small ($f^* < 1\ Hz$) that dynamic effects are negligible. All the results shown above are based on quasi-steady assumptions or experiments conducted in unidirectional airflow test rigs. Some groups studied Wells turbine under oscillating flow (unsteady considers). The results indicated a hysteretic effect on the force coefficients (Fig. 3.16). The hysteretic effects are caused by asymmetry in the boundary layer development on the blade surfaces and oscillating motion of the wake, the extent of which can be appreciable at low Reynolds numbers [82, 85, 97] (Fig. 3.17).

Dynamic stall is a process resulting from a series of events, which involves a hysteresis loop in the airfoil lift curve and account for a higher maximum lift force than that achieved in the static curve, during a cycle of pitching motion. Helicopter, turbine and windmill blades may all be affected by this phenomenon, which increases forces and moments applied to the blade and its root, and reduces fatigue life. But the loop of hysteretic curve of the dynamic stall is different from the one of Wells turbine. So, the mechanism of the hysteretic characteristics of Wells turbine is still unclear [47, 57].

The flow structure around the blade of Wells turbines has been checked by some researchers. Figure 3.18 shows the illustration of the flow structure obtained by numerical simulation [61, 62]. At high angles of attack, a separation vortex (2) appears on the blade suction surface on the hub side and reduces blade circulation, because of the excessive angle of attack near the hub. A strong downward flow (4) is induced by the separation vortex near the trailing edge. It brings about the clockwise vortical wake flow (3a), which enlarges the flow separation on the adjacent blade suction surface (3b) [58, 59, 104, 103].

The intensity of the vortical flow varies in the accelerating and the decelerating flow process. In the accelerating flow stroke, as the blade circulation increases, vortices opposite to the blade circulation are shed from the trailing edge. The stronger vortices are shed at a larger radius because the blade circulation increases more than at a smaller radius.

Then, the clockwise trailing vortices are generated. Therefore, the clockwise vortical flow is intensified by these vortices. In the decelerating flow process where the blade circulation decreases, the shed vortices are in the same direction of the blade circulation. They form counterclockwise trailing vortices, which suppress the vortical wake flow. Since the stronger vortical wake flow enlarges the separation on the suction surface of the adjacent blade, the performance in the accelerating flow process becomes lower than in the decelerating flow process [103]. This effect can be reduced by decreasing the solidity (Fig. 3.18). This observation can be explained, since the vortical wake flow enlarging flow separation becomes more distant from the blade suction surface for the case of low solidity [103].
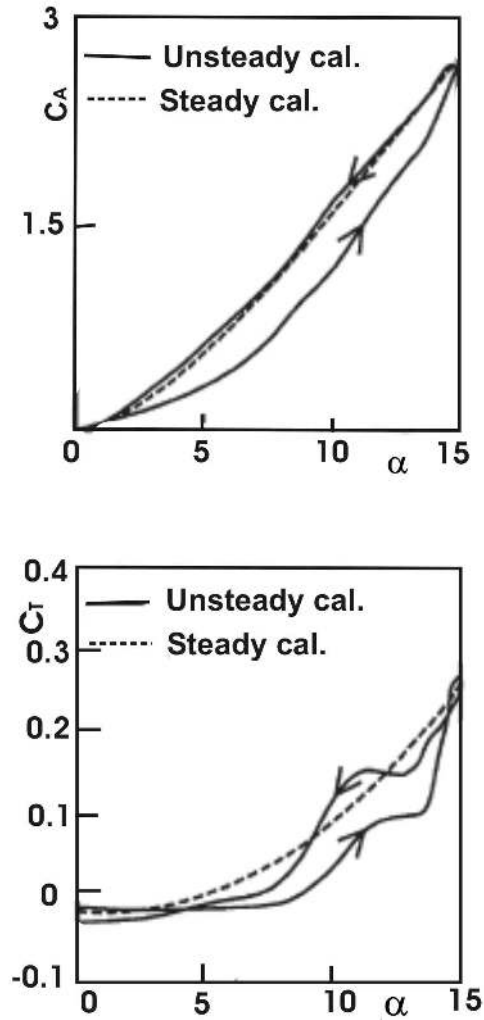
Figure 3.16: Effect of unsteady flow on Wells turbine performance [103].

3.2.3 Methods to improve Wells turbine performance

Due to the drawbacks of Wells turbine, like low efficiency, bad starting capability at low solidity and low output power, many researchers tried to suggest some ideas to improve the performance, like installing guide vanes [87, 111, 117], or improving profiles [127], as discussed in the next section.
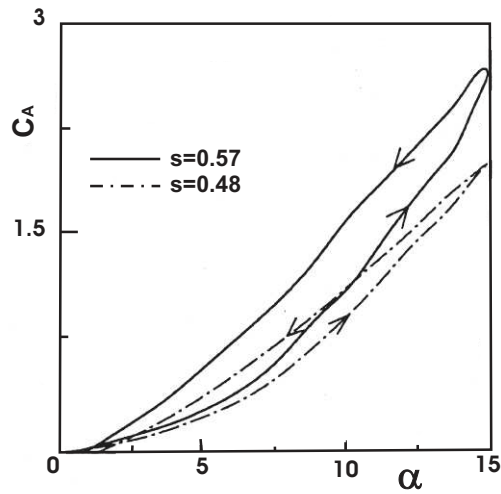
Figure 3.17: Effect of solidity on the hysteretic behavior [103].
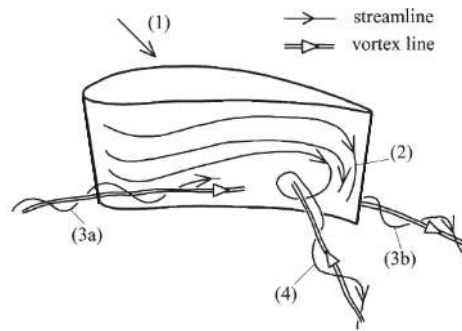
Figure 3.18: Illustration of the flow structure in blade suction side [103].

3.2.3.1 Guide vanes installation

Many papers [13, 33, 105, 109, 110, 112, 116, 121, 122] have demonstrated the usefulness of 2D and 3D (twisted) guide vanes. The effect of guide vanes (Fig. 3.19) has been investigated experimentally and theoretically by testing a model under steady flow conditions. It is found that the running and starting characteristics of the Wells turbine with guide vanes are superior to those without guide vanes (Fig. 3.20).

The results indicated in particular that the three dimensional guide vanes (variable angles along the vane span) providing a constant rotor blade angle of attack with radius lead to the best characteristics and are therefore recommended.

3.2.3.2 Self-pitch-controlled blades

Experimental investigations were performed by model testing of the rotor with fixed blades under steady flow conditions [32, 44, 56, 60, 99, 100, 101, 106, 120]. The turbine
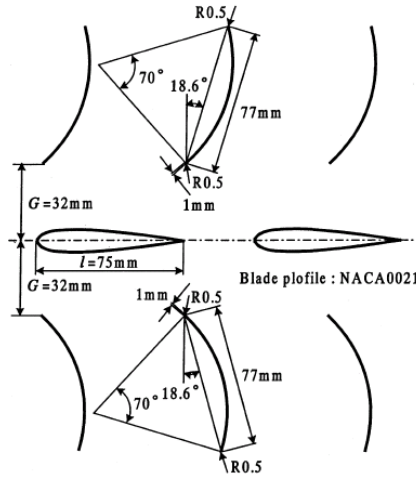
Figure 3.19: Installation of guide vanes [106].
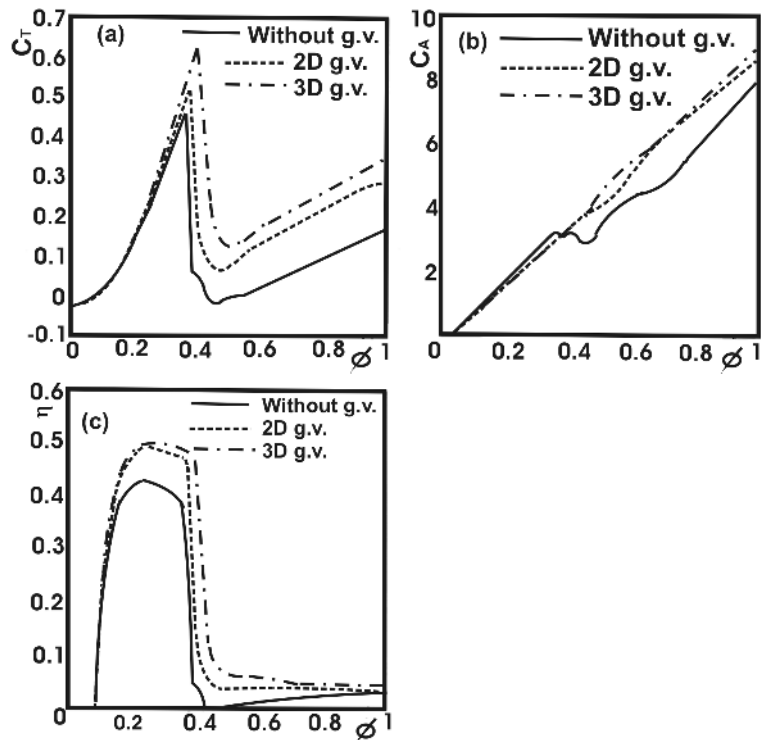
Figure 3.20: Guide vanes effect on the turbine performance [105].

blade is set on the hub by a pivot located near the leading edge that enables it to oscillate between two prescribed setting angles of $\pm\gamma_b$ (Fig. 3.21). As an airfoil set at a certain angle of incidence experiences a pitching moment M about the pivot, the turbine blades

can flip by themselves between $+\gamma_b$ and $-\gamma_b$ according to the flow direction. Therefore, higher torque and efficiency are obtained for high flow coefficients, while performance decreases for lower flow coefficient. The results indicated that the operating range improved when increasing setting angle. since the incidence angle ($\theta = \alpha - \gamma_b$) decreased. On the other hand, the torque improved only in the high operating range compared with conventional Wells turbine ($\gamma_b = 0$).
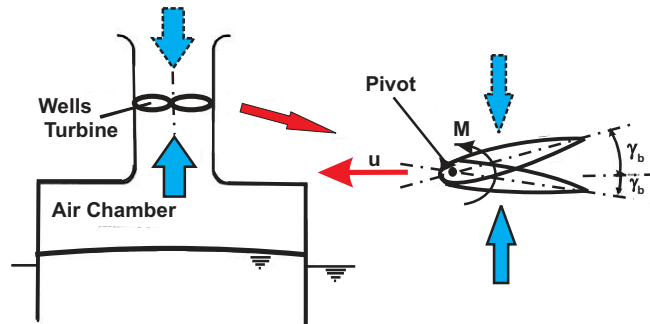
Figure 3.21: Principle of using self-pitch-controlled blades [106].

3.2.3.3 Lean blade (blade swept)

Experimental research on different types of rotor blades has been conducted recently to improve the aerodynamic performance of the Wells turbine, using lean blade (swept blade) as shown in Fig. 3.22 for two different airfoils (NACA 0015 and HSIM-15-262123-1576, Fig. 3.23), which can operate with wider operating range [108] and acceptable power output and efficiency. A numerical study indicated that the comparison between standard NACA 0015 unswept blade turbine rotor and the swept one by 30° is very difficult for small flow coefficients. For high flow coefficients, however, the swept one is better in term of efficiency. However, the results are poor concerning power output. On the other hand, the airfoil HSIM-15-262123-1576 is better than both unswept and swept standard NACA 0015. Therefore, the rotor blade geometry has a remarkable influence on the turbine performance. Some rotor geometries give a considerably wider range of flow rates for high efficiency and acceptable power output. Others have higher peak efficiency but a narrower range of flow rates [8, 102, 126, 136].

3.2.3.4 End plate

The effect of end plate (Fig. 3.24) on the turbine characteristics has been investigated experimentally for different plate sizes (a/c) by model testing under steady flow conditions and compared with the classical Wells turbine [119, 123, 124, 125], without end plate. Experiments indicate that the best geometry corresponds to $a/c = 0.033$. The effectiveness of the end plate has been checked by using CFD to get the optimal position of the plate.
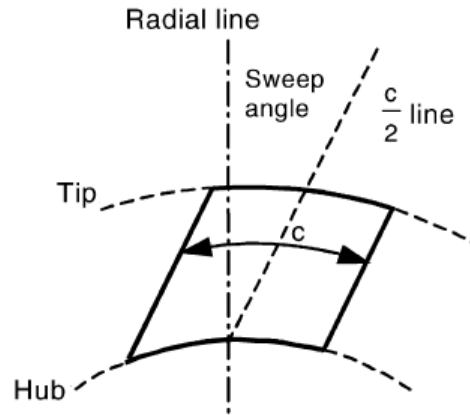
Figure 3.22: Swept blade (lean blade) [8].
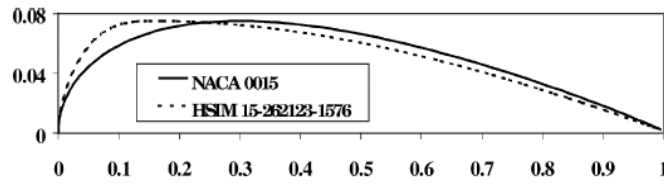
Figure 3.23: NACA 0015 and HSIM 15-262123-1576 blades [8].

The forward type case shows the highest tangential force coefficient, while the backward type has the lowest value. On the other hand, the values of forward type and middle type are almost the same concerning axial force coefficient, C_A. Globally, the highest efficiency was for the forward type position, leading to wider operating range and higher turbine performance.

3.2.4   Multi-plane Wells turbine

In wave energy devices, where the available pressure drop is higher than a monoplane could accommodate, multi-plane turbine must be used. Several investigations studied the performance of multi-plane Wells turbine and are reviewed in this section [14, 55, 80].

3.2.4.1   Two-stage Wells turbine (biplane turbine)

All the previous theoretical and experimental results for the flow field around a Wells turbine rotor indicate that a considerable amount of exit kinetic energy is lost with the swirl component of the flow velocity, at least in the absence of guide vanes. This kinetic energy can be partly recovered by using a second stage of blades. Two-stage Wells turbine have been already investigated experimentally and theoretically [34], but considering only symmetric airfoils, as shown in Fig. 3.25.
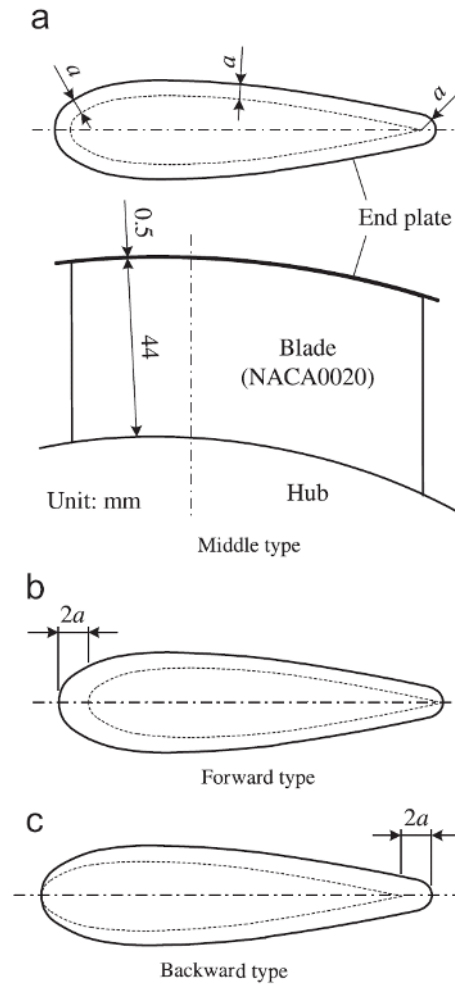
Figure 3.24: Rotor blade with end plate: (a) Middle type; (b) Forward type; (c) Backward type [124].

3.2.4.2 Two-stage contra-rotating Wells turbine

The first commercial wave power station (capacity of 500 kW), called LIMPET (Land Installed Marine Pneumatic Energy Transmitter) in UK is constructed with a two-stage contra-rotating Wells turbine [6]. In this configuration, the two rotors are installed as in Fig. 3.26.

Some researchers studied this configuration and made a comparison with the conventional biplane Wells turbine [17, 18, 24, 83]. Small-scale experiments on the contra-rotating Wells turbine have been conducted using constant flow wind-tunnels. The turbine tip diameters for these tests were 0.2 and 0.59 m, respectively, with nominal Mach numbers of 0.2 and 0.23 and Reynolds numbers of $3 \ 10^5$ and $6.5 \ 10^5$, respectively. The results indicated that a contra-rotating Wells turbine is aerodynamically more efficient than the biplane Wells turbine and operate without stalling over wider flow rates
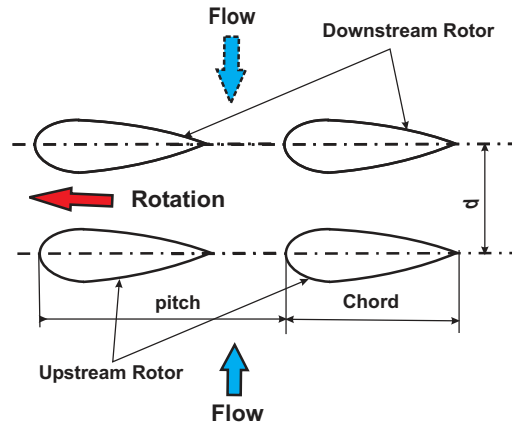
Figure 3.25: Two stage (biplane) Wells turbine.
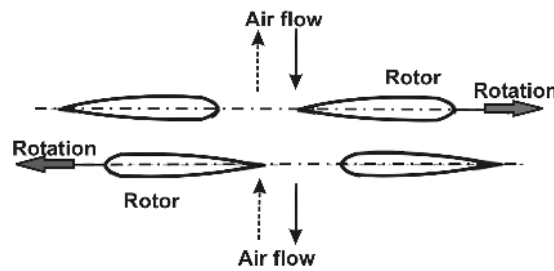
Figure 3.26: Contra-rotating Wells turbine [107].

than the biplane turbine. They concluded also that the downstream rotor must rotate at higher speed than the upstream to achieve some improvement. The performance of the contra-rotating Wells turbine installed in the LIMPET wave power station was compared to the predicted performance from theoretical analysis and model tests [24]. Figure 3.27 gives the non-dimensional turbine torque against flow coefficient for both rotors during both the intake and exhaust strokes. During exhaust, the results indicate that the LIMPET turbine stalls at approximately the same flow coefficient as the constant-flow model, but that the torque at stall is reduced by approximately 25% for the exhaust stroke and 46% for the intake stroke. In addition to comparing exhaust and intake it is also interesting to consider the relative performance of either rotor shown in Fig. 3.27. During exhaust there is no measurable difference in stall between the rotors. However, on intake, the downstream rotor has a noticeably higher torque coefficient at stall condition.

Figure 3.28 shows a plot of the LIMPET turbine efficiency with flow coefficient during the intake and exhaust, together with turbine efficiency derived from constant flow model tests. During exhaust, at low flow coefficients, the LIMPET turbine appears to have a higher efficiency than in constant flow model tests. This is possibly due to
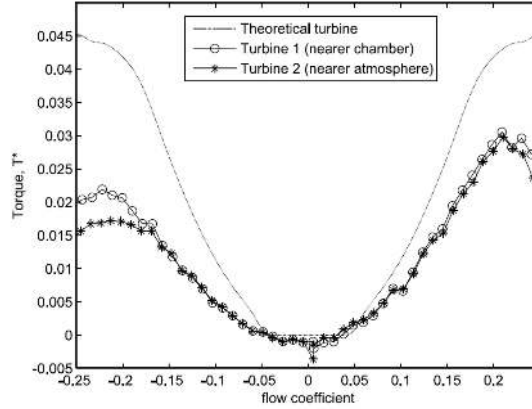
Figure 3.27: Torque coefficients for both LIMPET Rotors during intake and exhaust [24].

a lower drag coefficient at higher Reynolds numbers. However, measurement errors are magnified at low torques and flow coefficients, so the data in this region should be viewed cautiously. However, the early onset of stall experienced by the LIMPET turbine reduces the peak efficiency of the turbine to approximately 52%, whilst simultaneously reducing its effective operating range. During intake, a higher flow coefficient is required for the turbine lift force to overcome the drag force due to relatively smaller torques being generated for the same flow coefficients. Smaller turbine torques during intake cause a smaller increase in turbine efficiency with flow coefficient, resulting in a peak efficiency of only approximately 42%.
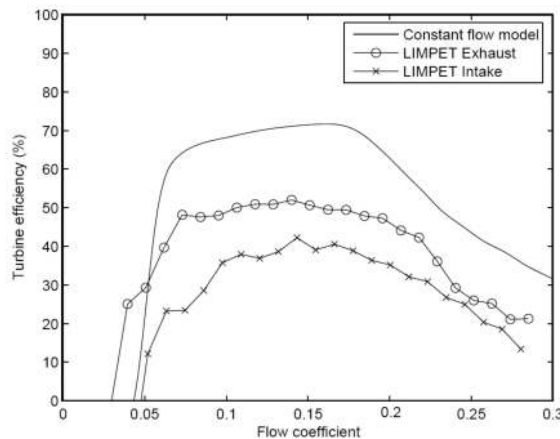
Figure 3.28: Comparison of LIMPET and constant flow model turbine efficiencies [24].

This study concluded that the contra-rotating Wells turbine finally has a lower efficiency than a biplane or monoplane Wells turbine with guide vanes. In addition, a contra-rotating Wells turbine requires an additional generator (or a gearbox to re-

verse the direction of rotation of one rotor), making it more complex and expensive to implement than biplane and monoplane Wells turbines. Consequently, unless the performance of contra-rotating Wells turbines can be significantly improved, they are not recommended over other Wells turbine variants. Obviously, contradictory information are found in the literature concerning contra-rotating configurations highlighting the need for further studies.

3.2.5 Summary of Wells turbine review

All the studies discussed in the present review have tried to understand and improve the performance of the Wells turbine, considering either the conventional geometry or slight modifications. All the improvements have been tested manually, by means of a tedious trial-and-error analysis. Such studies are going on. All proposed modifications have been summarized and discussed in Table 3.2. It can be finally concluded that:

Table 3.2: Main modifications allowing to improve the performance of Wells turbines

Design	Gain	Description and Comments
Contra-rotating [14]	Improve efficiency by $\simeq 5\%$	Double shaft, complex
Pitch setting [106]	Improve efficiency by $\simeq 7\%$	For positive small angles, complex
Guide vanes [33]	Improve efficiency by $\simeq 5\%$	Smaller operating range
End plate [124]	Improve efficiency by $\simeq 5\%$	Only for $0.2 \leq \phi \leq 0.25$
Multi-stage * [81]	Wider operating range	Reduce efficiency by $\simeq 10\%$
Multi-stage ** [74]	Improve efficiency by $\simeq 2\%$	Small parameter space

*Symmetric airfoils **Non-Symmetric airfoils
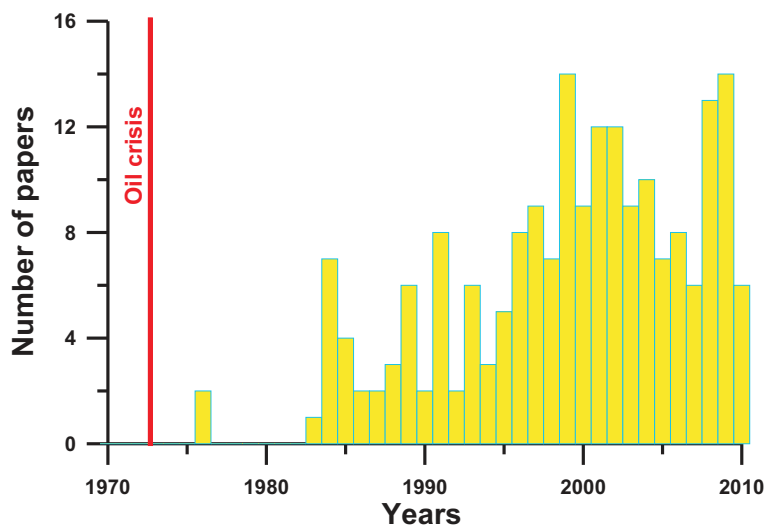
Figure 3.29: Wells turbine publication statistics in international journals and conferences.

- There is a renewed interest for Wells turbines in recent years, as shown in Fig. 3.29;

- Contradictory observations can be found in the literature, both qualitatively and quantitatively. Therefore, the results presented in this review must all be considered with great caution, in particular concerning the contra-rotating design ;

- Many small modifications and improvements have been proposed in the literature to improve global performance, as summarized in Table 3.2;

- Nevertheless, a real optimization of the system has not been realized up to now and would therefore be very interesting. This will be the subject considered in later chapters of this thesis.

3.3   Conclusions

In spite of many published studies, it still seems possible to increase considerably the performance of both Savonius and Wells turbines by relying on modern computational methods, as demonstrated in later chapters. The needed methodology for this purpose is described in the next two chapters.

Chapter 4

Optimization

4.1 Introduction

Optimization pervades the fields of science, engineering, and business. In physics, many different optimal principles have been enunciated, describing natural phenomena in the fields of optics or classical mechanics. Statistics treats various principles termed "maximum likelihood," "minimum loss," and "least squares," and business makes use of "maximum profit," "minimum cost," "maximum use of resources," "minimum effort," in its efforts to increase profits. A typical engineering problem can be posed as follows: A process can be described by representative equations (or perhaps solely by experimental data). You have a single performance criterion in mind such as maximum efficiency or minimum cost. The goal of optimization is to find the values of the variables in the process that yield the best value of the performance criterion. A trade-off usually exists. Typical problems in engineering process design or plant operation have many (possibly an infinite number) of solutions. Optimization is concerned with selecting the best among the entire set by efficient quantitative methods, thanks to computers and associated software, which make the necessary computations feasible and cost effective. To obtain useful information using computers, however, requires (1) a critical analysis of the process or design, (2) insight about what the appropriate performance objectives are (i.e., what is to be accomplished), (3) use of past experience, sometimes called engineering judgment [35], and (4) suitable methods and algorithms.

Until recently, the denomination "optimization" was mostly used in the engineering literature to describe a trial-and-error, manual procedure (undoubtedly related to optimization, but in a very minimalist sense), at the difference of a real, mathematical optimization. This is now changing rapidly. In the present project, mathematical optimization will be considered to obtain the optimal shape geometry. Hence, for us, optimization means "the design (or operation) of a system or process to make it as good as possible in some defined sense". As a consequence, the best possible solution constrained by appropriate conditions should be ideally found, and not simply a "better" one [132]. Another definition is given by [2], which states that optimization is the process of obtaining the "best", if it is possible to measure and change what is "good" or "bad". The definition in [96] is that the optimization theory is a body of mathe-

matical results and numerical methods for finding and identifying the best candidate from a collection of alternatives without having to explicitly enumerate and evaluate all possible alternatives.

In practice, one wishes the "most" or "maximum" (e.g., salary) or the "least" or "minimum" (e.g., expenses). Therefore, the word "optimum" is taken to mean "maximum" or "minimum" depending on the circumstances; "optimum" is a technical term which implies quantitative measurement and is a stronger word than "best" which is more appropriate for everyday use. Likewise, the word "optimize", which means to achieve an optimum, is a stronger word than "improve". A computer is the perfect tool for optimization as long as the idea or variable influencing the idea can be input in electronic format. The process of optimization lies at the root of engineering, since the classical function of the engineer is to design new, better, more efficient, and less expensive systems as well as to devise plans and procedures for the improved operation of existing systems. The power of optimization methods to determine the best case without actually testing all possible cases comes through the use of a modest level of mathematics and at the cost of performing iterative numerical calculations using clearly defined logical procedures or algorithms implemented on computing machines.

4.2   Optimization uncertainty

For practical problems, optimization does not deliver a "solution truth" because of the uncertainty that exists in the mathematical and physical representation of the process or the data used to model it. Engineers have to use their own judgment in applying optimization techniques to problems that have considerable uncertainty associated with them, both from the standpoint of accuracy and from the fact that operating parameters are not always static. In some cases, it may be possible to carry out a first analysis via deterministic optimization and then add on stochastic features to the analysis to yield quantitative predictions of the degree of uncertainty. Whenever the model of a process is idealized and the input and parameter data only known approximately, the optimization results must be treated judiciously. They can provide for instance upper limits on expectations. Another way to evaluate the influence of uncertain parameters in optimal design is to perform a sensitivity analysis. It is possible that the optimum value of a process variable is unaffected by certain parameters (low sensitivity); therefore, having precise values for these parameters will not be crucial to finding the true optimum [35]. Furthermore, optimization can only deliver accurate results when the quality of a specific design can be measured accurately. For our problem, this issue will be considered in the next chapter.

4.3   How can we achieve optimization?

Most real-life problems have several solutions and occasionally an infinite number of solutions may be possible. Assuming that the problem at hand admits more than one solution, optimization can be achieved by finding the best solution of the problem in

terms of some performance criterion. Several general approaches to optimization are available, as follows:

- Analytical methods

- Graphical methods

- Experimental methods

- Numerical methods

Analytical methods are based on the classical techniques of differential calculus. In these methods the maximum or minimum of a performance criterion is determined by finding the values of parameters $x_1, x_2, ..., x_n$ that cause the derivatives of $f(x_1, x_2, ..., x_n)$ with respect to $x_1, x_2, ..., x_n$ to assume zero values. The problem to be solved must obviously be described in mathematical terms before the rules of calculus can be applied. The method need not entail the use of a digital computer. However, it cannot be applied to highly nonlinear problems or to problems where the number of independent parameters exceedingly grows.

A graphical method can be used to plot the function to be maximized or minimized if the number of variables does not exceed a few. If the function depends on only one variable, say, x_1, a plot of $f(x_1)$ versus x_1 will immediately reveal the maxima and/or minima of the function. Similarly, if the function depends on only two variables, say, x_1 and x_2, a set of contours can be constructed. A contour plot, like a topographical map of a specific region, will reveal readily the peaks and valleys of the function. Unfortunately, the graphical method is of limited usefulness since in most practical applications the function to be optimized depends on many variables.

The optimum performance of a system can sometimes be achieved by direct experimentation. In this method, the system is set up and the process variables are adjusted one by one and the performance criterion is measured in each case. This method may lead to optimum or near optimum operating conditions. However, it can lead to unreliable results since in certain systems, two or more variables interact with each other, and must be adjusted simultaneously to yield the optimum performance criterion.

The most important general approach to optimization is based on numerical methods (real optimization). In this approach, iterative numerical procedures are used to generate a series of progressively improved solutions to the optimization problem, starting with an initial estimate for the solution. The process is terminated when some convergence criterion is satisfied. For example, when changes in the independent variables or the performance criterion from iteration to iteration become insignificant. Numerical methods can be used to solve highly complex optimization problems of the type that cannot be solved analytically. Furthermore, they can be readily programmed on digital computers. The discipline encompassing the theory and practice of numerical optimization methods has come to be known as mathematical programming [2], covering:

- Linear programming

- Integer programming

- Quadratic programming

- Nonlinear programming

- Dynamic programming

Each one of these branches of mathematical programming is concerned with a specific class of optimization problems. The differences among them will be illustrated in the nest sections.

4.4 Structure of optimization problems

Although the application problems discussed in the previous section originate from radically different sources and involve different systems, at their root they have a remarkably similar form. All five can be expressed as problems requiring the minimization of a real-valued function $f(x)$ of an N-component vector argument $x = (x_1, x_2, ..., x_N)$ whose values are restricted to satisfy a number of real-valued equations $h_k(x) = 0$, a set of inequalities $g_j(x) \geq 0$, and the variable bounds $x_i^{(U)} \geq x_i \geq x_i^{(L)}$. In subsequent discussions we will refer to the function $f(x)$ as the objective function, to the equations $h_k(x) = 0$ as the equality constraints, and to the inequalities $g_j(x) \geq 0$ as the inequality constraints. For our purposes, these problem functions will always be assumed to be real valued, and their number will always be finite. Optimization then means:

$$
\begin{array}{lll}
\text{Minimize or maximize} & f(x) & \\
\text{Subject to} & h_k = 0 & k = 1, ..., K \\
& g_x \geq 0 & j = 1, ..., J \\
& x_i^{(U)} \geq x_i \geq x_i^{(L)} & i = 1, ..., N
\end{array}
$$

This general problem is called the constrained optimization problem. The problem in which there are no constraints, that is, unconstrained optimization problem, would correspond to

$$J = K = 0$$

and

$$x_i^{(U)} = -x_i^{(L)} = \infty \quad i = 1, ..., N$$

but it is almost never found in engineering.

Optimization problems can be classified further based on the structure of the functions f, h_k, and g_j and on the dimensionality of x. Unconstrained problems in which x is a one-component vector are called single-variable problems and form the simplest. Constrained problems in which the function h_k and g_j are all linear are called linearly constrained problems. This subclass can further be subdivided into those with a linear objective function f and those in which f is nonlinear. The category in which all problem functions are linear in x includes problems with continuous variables, which are called linear programs, and problems in integer variables, which are called integer programs. Problems with nonlinear objective and linear constraints are sometimes called linearly constrained nonlinear programs. This class can further be subdivided according to the particular structure of the nonlinear objective function. If $f(x)$ is quadratic, the problem is a quadratic program; if it is a ratio of linear functions, it is called a fractional linear program; and so on. Subdivision into these various classes is worthwhile because the special structure of these problems can be sometimes efficiently exploited in devising solution techniques [2]. Note that, in all this document, only direct optimization is considered. Possibilities offered by inverse design (based on solving the adjoint problem) are not discussed.

4.5   Types of mathematical programming

Several branches of mathematical programming were enumerated in Section 4.3. Each one of these branches consists of the theory and application of a collection of optimization techniques that are suited to a specific class of optimization problems. The differences among the various branches of mathematical programming are closely linked to the structure of the optimization problem and to the mathematical nature of the objective and constraint functions.

4.5.1   Linear programming (LP)

If the objective and constraint functions are linear and the variables are constrained to be positive, optimization can be readily achieved by using some powerful LP algorithms.

4.5.2   Integer programming (IP)

In certain linear programming problems, at least some of the variables are required to assume only integer values. This restriction renders the programming problem nonlinear and more complex.

4.5.3   Quadratic programming (QP)

If the constraints are linear and the objective function is quadratic, such an optimization problem is said to be a quadratic programming (QP) problem.

4.5.4 Nonlinear programming (NP)

In nonlinear programming problems, the objective function and usually the constraint functions are nonlinear. This is the most general branch of mathematical programming and, in effect, LP and QP can be considered as special cases of nonlinear programming. The choice of an optimization algorithm depends on the mathematical behavior and structure of the objective function. Rarely, the objective function is a well behaved nonlinear function and all that is necessary is a general purpose, robust, and efficient algorithm. For many applications, however, specialized algorithms exist which are more efficient or more robust [19]. This is clearly the case for the problems considered in the present thesis.

4.5.5 Dynamic programming (DP)

In some applications, a series of decisions must be made in sequence, where subsequent decisions are influenced by earlier ones. In such applications, a number of optimizations have to be performed in sequence and a general strategy may be required to achieve an overall optimum solution.

4.6 Requirements for optimization

To apply the mathematical results and numerical techniques of optimization theory to real engineering problems, it is necessary to clearly delineate the boundaries of the engineering system to be optimized, to define the quantitative criterion on the basis of which candidates will be ranked to determine the "best", to select the system variables that will be used to characterize or identify candidates, and to define a model that will express the manner in which the variables are related. This composite activity constitutes the process of formulating the engineering optimization problem. Good problem formulation is the key to the success of an optimization study [96].

4.6.1 Defining the system boundaries

Before undertaking any optimization study, it is important to clearly define the boundaries of the system under investigation. They serve to isolate the system from its surroundings, because, for purpose of analysis, all interactions between the system and its surroundings are assumed to be frozen. Nonetheless, since interactions always exist, the act of defining the system boundaries is the first step in the process of approximating the real system. In many situations it may turn out that the initial choice of boundary is too restrictive. To fully analyze a given engineering system, it may be necessary to expand the system boundaries and to include other subsystems that strongly affect the operation of the system under study.

4.6.2 Performance criterion

Given that we have selected the system of interest and have defined its boundaries, we next need to select a criterion on the basis of which the performance or design of the system can be evaluated, so that the best design or set of operating conditions can be identified. There is a considerable choice in the precise definition of such a criterion: minimum production time, maximum production rate, minimum energy utilization, maximum torque, minimum weight, and so on.

4.6.3 Independent variables

The third key element in formulating a problem for optimization is the selection of the independent variables that are adequate to characterize the possible candidate designs or operating conditions of the system. There are several factors to be considered in selecting the independent variables. First, it is necessary to distinguish between variables whose values are amenable to change and variables whose values are fixed by external factors, lying outside the boundaries selected for the system in question. Furthermore, it is important to differentiate between system parameters that can be treated as fixed and those that are subject to fluctuations influenced by external and uncontrollable factors. Clearly, variations in these key system parameters must be taken into account in the formulation of the problem. Second, it is important to include in the formulation all the important variables that influence the operation of the system or affect the design definition. For instance, if in the design of a gas storage system we include the height, diameter, and wall thickness of a cylindrical tank as independent variables but exclude the possibility of using a compressor to raise the storage pressure, we may well obtain a very poor design. For the selected fixed pressure, we would certainly find the least-cost tank dimensions. However, by including the storage pressure as an independent variable and adding the compressor cost to our performance criteria, we could obtain a design with a much lower overall cost because of a reduction in the required tank volume. Thus, the independent variables must be selected so that all important alternatives are included in the formulation. Finally, another consideration in the selection of variables is the level of detail to which the system is considered. While it is important to treat all key independent variables, it is equally important not to obscure the problem by the inclusion of a large number of fine details of subordinate importance. A good rule is to include only those variables that have a significant impact on the composite system performance criterion.

4.6.4 System model

Once the performance criterion and the independent variables have been selected, the next step in problem formulation is to assemble the mathematical and physical models that describe the manner in which the problem variables are related and the way in which the performance criterion is influenced by the independent variables. In principle, optimization studies may sometimes be performed by experimenting directly with the

real system. Thus, the independent variables of the system or process may be set to selected values, the system operated under those conditions, and the system performance index evaluated using the observed performance. The optimization methodology would then be used to predict improved choices of the independent variable values and the experiments continued in this fashion. In practice, most optimization studies are carried out with the help of a representation of the real system, called a model. Models are typically used in engineering design because they offer the cheapest and fastest way of studying the effects of changes in key design variables on system performance. For flow optimization the Navier-Stokes equations constitute the natural model.

4.7   Optimization methods

In this work we consider methods that iteratively produce estimates of x^* (optimum solution), that set of design variables that causes $f(x)$ to take on its optimum value. The methods that have been devised for the solution of this problem can be classified into three broad categories [96] based on the type of information that must be supplied by the user:

- Direct-search methods, which use only function values;

- Gradient methods, which require estimates of the first derivative of f;

- Second-order methods, which require estimates of the first and second derivatives of f.

No single method can be expected to uniformly solve all problems with equal efficiency. For instance, in some applications available computer storage is limited; in others, function evaluations are very time consuming; in still others, high accuracy in the final solution is desired. In many applications it is either impossible or very time consuming to obtain the derivatives. For our problem, it is almost impossible and extremely time consuming to estimate the function derivatives. Furthermore, function evaluations rely again on computer-based simulations, and are therefore noisy and of limited accuracy. As a consequence, only Genetic Algorithms (a stochastic direct methods) are discussed further.

4.8   Evolutionary Algorithms

Evolutionary Algorithms (EA) are computer programs that attempt to solve complex problems by mimicking the processes of Darwinian evolution (e.g., [76]). In an EA a number of artificial creatures search over the space of the problem. They compete continually with each other to discover optimal areas of the search space. It is hoped that over time the most successful of these creatures will evolve to describe the optimal solution. The artificial creatures in EAs, known as individuals, are typically represented by fixed length strings or vectors. Each individual encodes a single possible solution to

the problem under consideration. For example, in order to construct an EA to search the conformation space of a molecule, each angle of rotation around a flexible bond could be encoded as a real number. Concatenating these numbers gives a string which can be used within an EA. Thus, each individual would encode a specific set of torsion angles. EAs manipulate pools or populations of individuals. The EA is started with an initial population of size N comprising random or quasi-random individuals. Every individual is then assigned a fitness value. To generate a fitness score the individual is decoded to produce a possible solution to the problem. The value of this solution is then calculated using the fitness function. Population members with high fitness scores therefore represent better solutions to the problem than individuals with lower fitness scores. Following this initial phase the main iterative cycle of the algorithm begins. Using mutation (perturbation) and recombination operators, the N individuals in the current population produce n children according to a survival probability ratio. The n children are assigned fitness scores. A new population of N individuals is then selected from the N individuals in the current population and the n children. This new population becomes the current population and the iterative cycle is repeated. The survival of the fittest is employed and individuals compete against each other. The selection is applied either when choosing individuals to become parent of children or when choosing individuals to form a new population. There have been three main independent implementation instances of EAs: Genetic Algorithms (GAs), first developed by Holland (1975) and thoroughly reviewed by Goldberg (1989); evolution strategies (ESs), developed in Germany by Rechenberg (1973) and Schwefel (1981); and evolutionary programming (EP), originally developed by L. J. Fogel et al.(1966) and subsequently refined by D. B. Fogel (1995). Each of these three algorithms has been proved capable of yielding approximately optimal solutions given complex, multi-modal, non-differential, and discontinuous search spaces. In the present project, only GA have been employed and therefore described now.

4.8.1   Genetic Algorithm (GA)

This is the most popular type of EA. One seeks the solution of a problem in the form of strings of numbers, by applying operators such as recombination and mutation [114]. A path through the components of the GA is shown as a flowchart in Fig. 4.1. Each block in this "big picture" overview is discussed in detail in what follows.

The canonical GA encodes the problem within binary string individuals. Nowadays, real or double-precision representations are mostly used for engineering problems. Evolutionary pressure is applied in the steps of the iterations, where the stochastic technique of roulette wheel parent selection is used to pick parents for the new population. The concept is as follow:

1. A population of N random or quasi-random individuals is initialized

2. Fitness scores are assigned to each individual
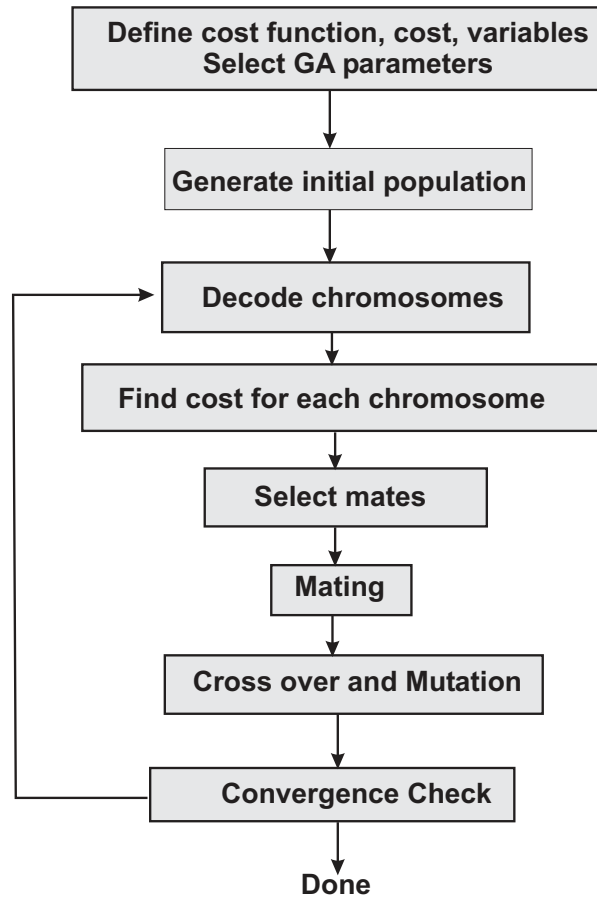
Figure 4.1: Flowchart of a Genetic Algorithm.

3. Using roulette wheel parent selection $N/2$ pairs of parents are chosen from the current population to form a new population.

4. With probability Pc (crossover), children are formed by performing crossover on the $N/2$ pairs of parents. The children replace the parents in the new population.

5. With probability Pm (mutation), mutation is performed on the new population.

6. The new population becomes the current population.

7. If the termination conditions are satisfied exit, otherwise go to step 3.

In Fig. 4.2, selection based on roulette is expained using a trivial example with a population of ten individuals. Each individual is assigned a sector of a roulette wheel that is proportional to its fitness and the wheel is spun to select a parent.

While selection is random and any individual has the capacity to become a parent, selection is clearly biassed towards fitter individuals. Parents are not required to be unique and, in each iteration, fit individuals may produce many offsprings. From a
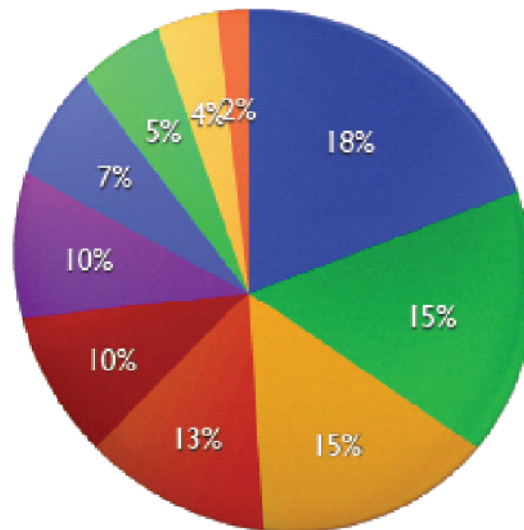
Figure 4.2: Example of selection based on the roulette-wheel for ten individuals.

population of size N, $N/2$ pairs of parents are chosen. These parents initiate a new population. With probability Pc each pair is recombined using the crossover operator to produce a pair of children. This cut and splice operator is illustrated in Fig. 4.3.
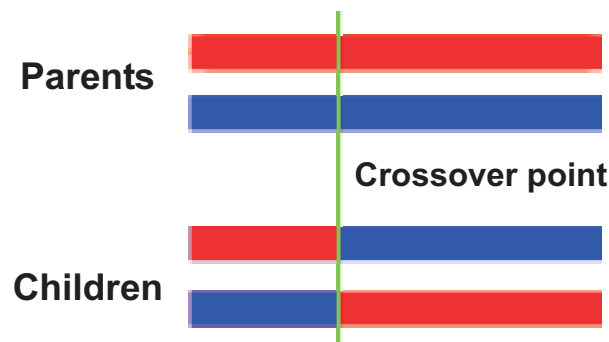
Figure 4.3: Example of crossover.

A cross point is selected at random. Each child is identical to one parent before the cross point and identical to the other after the cross point. The child individuals then replace their parents in the new population. Following crossover, mutation is applied to all or some individuals in the new population. The probabilities of mutation and crossover, Pm and Pc are parameters of the algorithm and must be set by the user. With probability Pm, each bit on every string is inverted or modified. The new population then becomes the current population and the cycle is repeated until some termination criteria are satisfied. The algorithm typically runs for some fixed number of iterations, or until convergence is detected within the population.

Many GAs applied to real world problems bear only a passing resemblance to the canonical GA, and GAs are best viewed as a paradigm for evolutionary search, rather than a specific algorithm. The binary encoding is often inappropriate for many problems and may be extended to non-binary representations. Successful GAs have used integer string individuals or even more general representations such as tree and matrix structures. Specialized crossover operators have been devised to handle unusual encodings. In order to increase program effectiveness hybrid GAs mix problem-specific operations with crossover and mutation. Selection pressure is defined as the relative probability that the fittest individual in the population will be chosen as a parent relative to an individual of average fitness. Too high a selection pressure and a GA will rapidly converge to a suboptimal solution. While encouraging search, a low selection pressure can result in a GA taking an inordinate time to converge. In order to control selection pressure within a GA fitness values are often rescaled when applying roulette wheel parent selection. One problem with a canonical GA is that there is no guarantee that good individuals will survive from one iteration to the next. Not all algorithms produce an entirely new population at each iteration. An elitist strategy involves copying the best individuals unchanged from the current population to the new population, as done in the present work. In a steady-state GA, each iteration involves the application of one crossover or mutation operator and only one or two new individuals are added to the population, usually replacing the worst individuals. As a whole, GAs have proved to be the most popular EAs. They provide an efficient a simple framework for attempting to solve complex search problems and have been widely applied.

4.8.2 Advantage and disadvantage of Genetic Algorithm

Some of the advantages of a GA include that it

- Optimizes with continuous or discrete variables,

- Does not require any derivative information,

- Simultaneously searches from a wide sampling of the cost surface,

- Deals with a large number of variables,

- Is well suited for parallel computers,

- Optimizes variables with extremely complex cost surfaces (they can jump out of a local minimum),

- Provides a list of optimum variables, not just a single solution,

- Works with numerically generated data, experimental data, or analytical functions.

These advantages produce stunning results when traditional optimization approaches fail miserably. Of course, the GA is not the best way to solve every problem. For instance, the traditional methods have been tuned to quickly find the solution of a well

behaved convex analytical function of only a few variables. For such cases the calculus-based methods by far outperform the GA, quickly finding the minimum while the GA is still analyzing the costs of the initial population. However, many realistic problems do not fall into this category.

4.9   Conclusions

For the optimization problem considered in this work:

- Function evaluations rely on a complex computation with a limited accuracy,

- Concurrent objectives will be considered,

- Local minima are often expected,

- Results for non optimal configurations may be nevertheless interesting,

- Parallel computers are available.

For all these reasons, GA appears to be ideally suited and will always be used in what follows. Now, it is essential to compute the cost function as efficiently and accurately as possible. This is the subject of the next chapter.

Chapter 5

Numerical methods and algorithms

5.1   Introduction

Accurate computer simulations of fluid flows involve a wide range of issues, from grid generation to turbulence modelling to the applicability of various simplified forms of the Navier-Stokes equations. Many of these issues are not addressed at all in this thesis, like acoustics or reacting flows [3]. Instead, we focus on selected numerical issues, with emphasis on finite-volume solutions of the Navier-Stokes equations, coupled with optimization to improve wind and wave energy turbines. We present in this chapter a foundation for developing, analyzing, and understanding such methods.

5.2   CFD & Optimization

Computational Fluid Dynamics (CFD) deals with the numerical analysis of complex flows. Despite impressive progress in recent years, CFD remains an imperfect tool in the comparatively mature discipline of fluid dynamics, partly because electronic digital computers have been in widespread use for only thirty years or so. The Navier-Stokes equations, which govern the motion of a Newtonian viscous fluid were formulated well over a century ago. The most straightforward method of attacking any fluid dynamics problem is to solve these equations for appropriate boundary conditions. Analytical solutions are few and trivial and, even with today's supercomputers, numerically exact solution of the complete equations for the three-dimensional, time-dependent motion of turbulent flow is prohibitively expensive except for basic research studies in simple configurations at low Reynolds numbers. Therefore, the straightforward approach is still impracticable for engineering purposes. Moreover, CFD will be considered for optimization in this work.

Optimization methods allowing to identify a constrained, best possible solution have been known for a long time, but have not permeated all engineering disciplines yet. Concerning more specifically fluid dynamics, the first applications of optimization are found for aeronautical problems, in particular to improve wing profile and flight properties (typically, reduce drag). This is a problem with a high added-value and involves only

the basic equations of fluid dynamics (Euler or Navier-Stokes equations, depending on the investigated properties). This explains why most available books and articles dealing with optimization relying on evaluations obtained by Computational Fluid Dynamics concern such situations. Even then, the number of such books and review articles remains quite limited [132]. In our group, a considerable experience is available concerning such mathematical optimization relying on evaluations based on Computational Fluid Dynamics. We therefore employ our own optimization library, OPAL (for OPtimization ALgorithms), containing many different optimization techniques. Different CFD solvers (in-house codes, ANSYS-Fluent, ANSYS-CFX) have been coupled in the past with this optimizer. It has already been employed successfully to improve a variety of applications like for instance heat exchangers [40] or burners [52].

5.3 Computational procedure

The optimization procedure can only deliver the right solution, if all evaluations relying on Computational Fluid Dynamics indeed lead to an accurate flow description. From the literature it is known that an accurate CFD simulation of the flow around a Savonius turbine or Wells turbine is a particularly challenging task, mainly due to its highly time-dependent nature and to the fact that flow separation plays an important role for the efficiency of the system. It is therefore necessary to check the full CFD procedure with great care. Afterwards, the resulting methodology must be validated.

5.3.1 Pre-process: geometry & grid generation

Note first that both problems considered in this thesis are indeed two-dimensional in space, allowing an easier representation and discretization. The flow is time-dependent for Savonius turbine, while a steady solution is sufficient for Wells turbine.

5.3.1.1 Savonius turbine: size of computational domain

The appropriate size of the computational domain has first been investigated. It must be indeed checked that this size does not impact the results of CFD. A computational domain of increasing dimensions (square domain of size $2L \times 2L$, suitably normalized by the rotor radius R, see Fig. 5.1) has been considered in the CFD computation. It is easy to notice from Fig. 5.1 that the three smaller domains are associated with a large variation of the torque coefficient. On the other hand, the remaining three (larger domains) lead to a nearly constant value, with a relative variation of the output quantity below 1.1%. This demonstrates that the computational domain should extend at least over 20 times the rotor radius in each direction. In a smaller domain, the boundary conditions influence the flow results in an inappropriate manner. Finally, the domain marked in Fig. 5.1 has been retained for all further Savonius computations in this work.
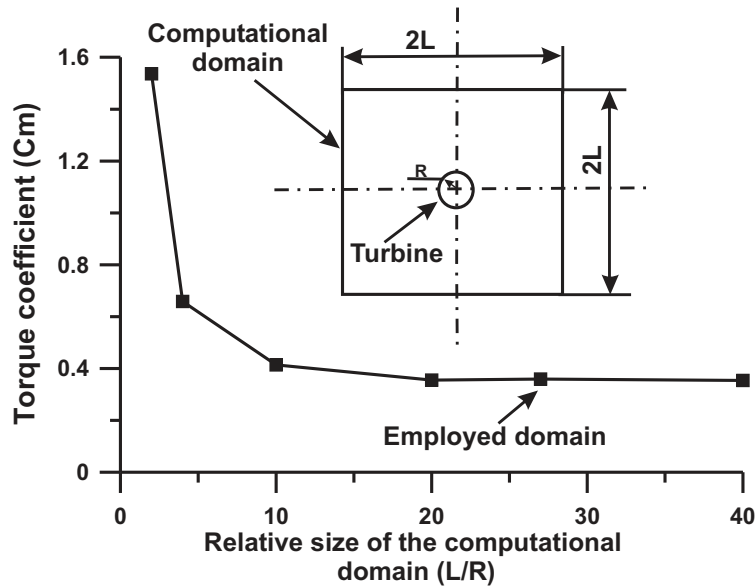
Figure 5.1: Size of the computational domain and impact on the torque coefficient

5.3.1.2 Savonius turbine mesh independence

Several different two-dimensional grids of increasing density and quality, composed of 5 400 up to 120 000 cells, have been tested for a conventional two-blade Savonius turbine with obstacle and deflector plates, using a representative example of the target solutions. It is easy to notice from Fig. 5.2 that the five coarsest grids are associated with a large variation of the torque coefficient. On the other hand, all remaining grids employing more than 80 000 cells lead to a relative variation of the output quantity below 1.3%. Since the cost of a CFD evaluation obviously increases rapidly with the number of grid cells, the intermediate grid range between 85 000 and 100 000 cells has been retained for all further results shown in the present work concerning Savonius turbines.

5.3.1.3 Wells turbine: size of computational domain

The mutual interaction between the blades constrains the size of the computational domain (Fig. 5.3) since only a single blade is considered. The appropriate size of the computational domain has been selected in the spanwise direction by using constant solidity and periodic boundary condition for both sides of the domain. In the axial direction recommendation from the literature have been implemented ($s = 0.67$, see section 3.2.1.1).

5.3.1.4 Wells turbine mesh independence

Corresponding results are shown in Fig. 5.4. Several different two-dimensional grids of increasing density and quality, composed of 12 200 up to 108 000 cells, have been tested for the baseline, non-symmetric blade configuration NACA 2421. All other parameters
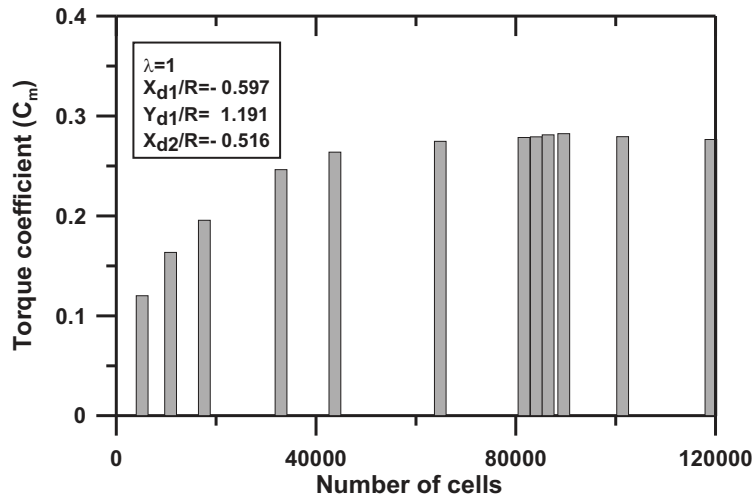
Figure 5.2: Grid-independence study for the torque coefficient
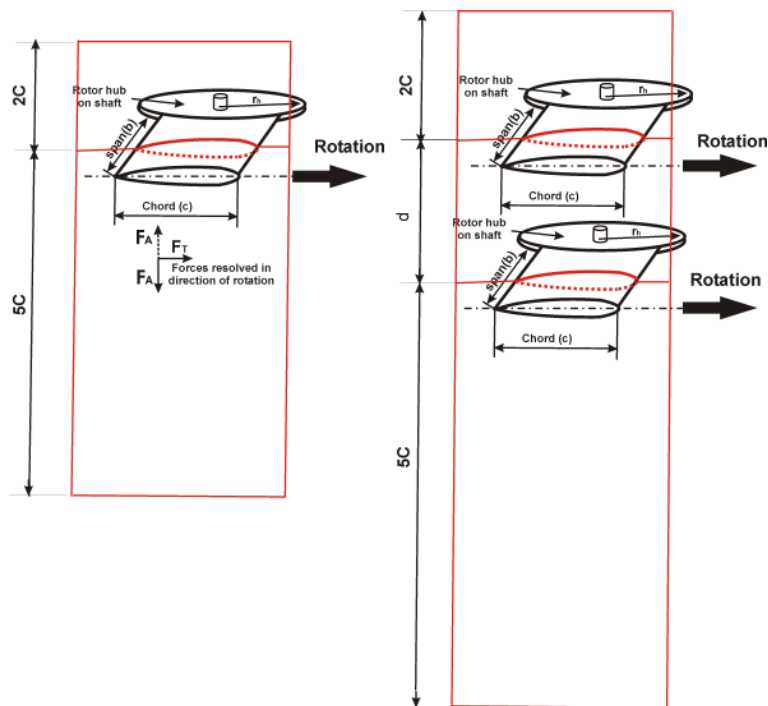
Figure 5.3: Size of the computational domain around monoplane and two-stage Wells turbines

of the CFD are unchanged. It is easy to notice that the six coarsest grids are associated with a large variation of the objective functions (here, the tangential force coefficient is represented). On the other hand, all remaining grids employing more than 53 000 cells lead to a variation of the target variables smaller than 1.5%. Therefore, the intermediate

grid range between 55 000 and 80 000 cells is retained for all further results shown in the present work for Wells turbine, depending on the type (one or two stages).
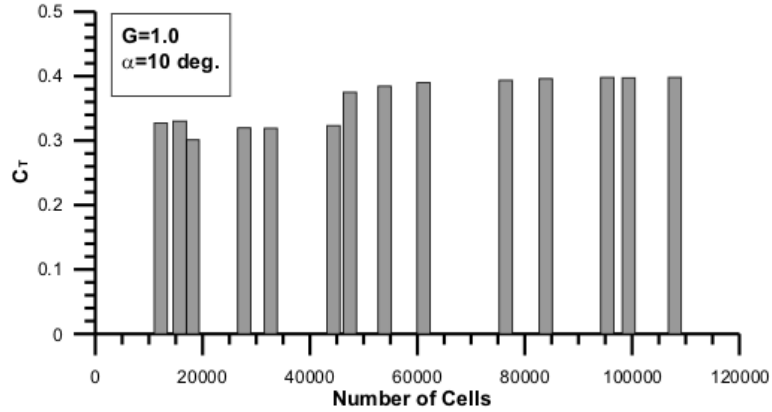
Figure 5.4: Grid-independence study for the tangential force coefficient

5.3.2 Numerical solution of the flow field

5.3.2.1 Why Fluent?

From all CFD codes available in our group, ANSYS-Fluent has finally been retained. Fluent is the world's leading commercial supplier of Computational Fluid Dynamics software and services. Fluent enables engineers to simulate fluid flow, fluid machines, heat and mass transfer, and a host of related phenomena involving turbulent, reacting, and multi-phase flows. Many researchers have used Fluent for simulating Savonius turbines [1, 69, 70] and Wells turbine [9, 103, 130, 131] in the past. Therefore, Fluent has a capability to predict the performance of such turbines. Other commercial tools do not show any noticeable advantage. Open-source CFD codes like OpenFOAM are definitely cheaper but of limited numerical efficiency when considering a moving mesh or using parallel computers [139]. Fluent is already coupled to our own optimization library and has been finally selected as CFD solver for this study.

5.3.2.2 Model validation and selection for Savonius turbine

All flow simulations presented in this work rely on the software ANSYS-Fluent version 6.3. The unsteady Reynolds-Averaged Navier-Stokes equations are solved using the SIMPLE (Semi-Implicit Method for Pressure-linked Equations) algorithm for pressure-velocity coupling. The flow variables and all turbulent quantities are discretized in a finite-volume formulation using a second-order upwind scheme. The unsteady flow is solved by using the Sliding Mesh Model (SMM).

The full numerical procedure and in particular the employed turbulence model have been validated by comparison with published experimental results for conventional Savonius turbines (two-blade and three-blade Savonius rotor of [38] and [48], respectively).

The influence of the turbulence model is shown in Fig. 5.5 and Fig. 5.6. These results demonstrate the excellent agreement obtained between CFD and experiments for the target function, C_p, when using the Realizable $k - \varepsilon$ turbulence model. The employed computational procedure thus appears suitable to predict the performance of the turbine in the investigated range of operation and is now kept for all further simulations of Savonius turbines.
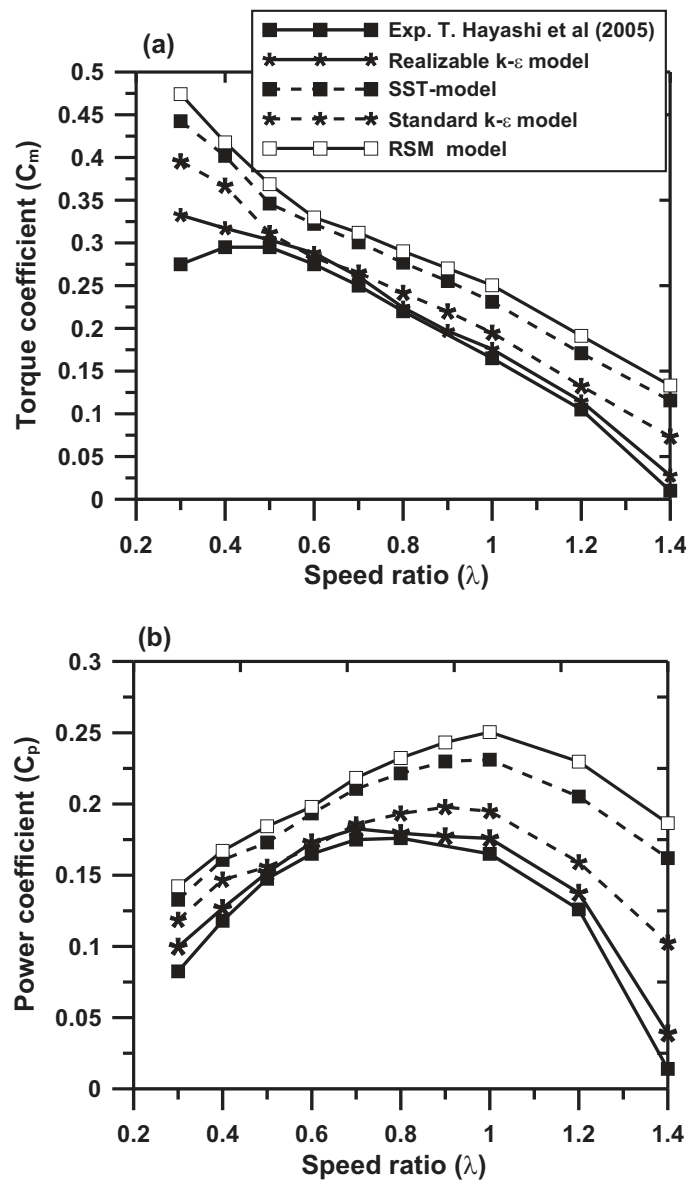
Figure 5.5: Validation of computational model: a) torque coefficient, b) power coefficient, both compared to published experimental results for a two-blade conventional Savonius turbine [38]
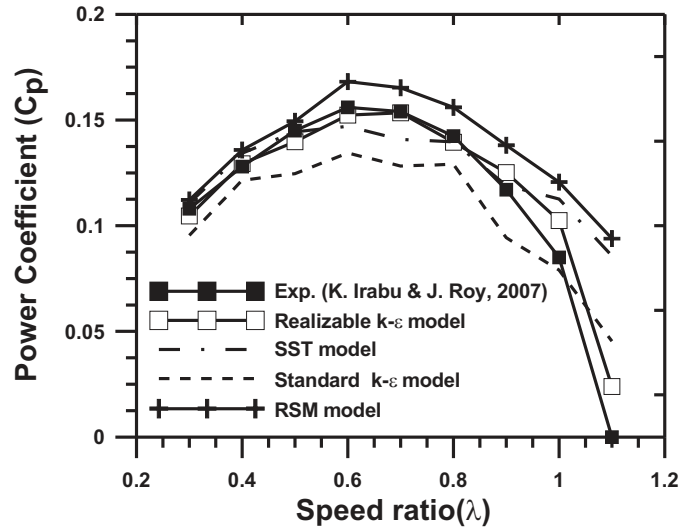
Figure 5.6: Validation of computational model: power coefficient compared to experimental results for a three-blade Savonius turbine [48]

5.3.2.3 Model validation and selection for Wells turbine

The full numerical model and in particular the employed turbulence model have been again validated by comparison with published experimental results for a standard, mono-plane Wells turbine at a flow Reynolds number Re= $2.4 \ 10^5$ using the chord as characteristic length. Published studies usually consider a range Re= $1 \ 10^5$ to Re= $5 \ 10^5$, since this corresponds to realistic conditions for employing a Wells turbine. Solidity is assumed constant and equal to $s = 0.67$ following [110], which corresponds to a number of blades equal to 8. The influence of the turbulence model is shown in Fig. 5.7. These results demonstrate again the excellent agreement obtained between CFD and experiments for this standard configuration, in particular when using the Realizable k-ε turbulence model. This model thus appears suitable to predict the performance of the turbine in the later investigated range of operation (flow coefficient varying from $\phi = 0.08$ to 0.25) and is now kept for all further simulations. For both turbines, Reynolds-Stress Model (RSM) leads to a considerably longer computing time but surprisingly to a worse agreement than the k-ε models. This is probably due to the low turbulence level and to a larger influence of the inflow turbulence boundary conditions, which are not properly characterized in the experiments. Inlet boundary conditions for the RSM model have been implemented using different possibilities, prescribing either k and ϵ or the turbulence intensity together with a length scale. Nevertheless, it has been impossible to obtain a better agreement. Therefore, the RSM model appears to be unappropriate for such configurations, associated with a low but unknown inflow turbulence level.
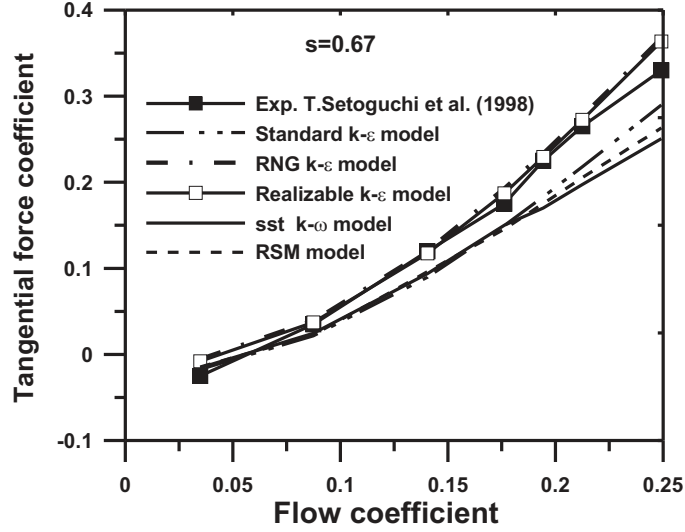
Figure 5.7: Influence of the turbulence model on the tangential force coefficient, compared to experimental results for a monoplane Wells turbine [107]

5.3.2.4   Realizable $k - \epsilon$ turbulence model

As explained in the previous sections, the realizable k-ϵ turbulence model developed by Shih et al. [113] has always been retained. This model contains a new transport equation for the turbulent dissipation rate. Also, a critical coefficient of the model, C_μ , is expressed as a function of mean flow and turbulence properties, rather than assumed to be constant as in the standard model. This allows the model to satisfy additional mathematical constraints on the normal stresses, consistent with the physics of turbulence (realizability). The concept of a variable is also consistent with experimental observations in boundary layers. The Realizable k-ϵ model usually provides improved results for swirling flows and flows involving separation when compared to the standard k-ϵ model.

- **Transport equations:**

$$\frac{\partial}{\partial t}(\rho k) + \frac{\partial}{\partial x_j}(\rho\, k\, u_j) = \frac{\partial}{\partial x_j}\left[\left(\mu + \frac{\mu_t}{\sigma_k}\right)\frac{\partial k}{\partial x_j}\right] + P_k + P_b - \rho\,\epsilon - Y_M + S_k \quad (5.1)$$

$$\frac{\partial}{\partial t}(\rho\epsilon) + \frac{\partial}{\partial x_j}(\rho\,\epsilon\, u_j) = \frac{\partial}{\partial x_j}\left[\left(\mu + \frac{\mu_t}{\sigma_\epsilon}\right)\frac{\partial \epsilon}{\partial x_j}\right] + \rho\, C_1\, S\,\epsilon - \rho\, C_2\,\frac{\epsilon^2}{k + \sqrt{\nu\,\epsilon}} + C_{1\,\epsilon}\frac{\epsilon}{k}C_{3\epsilon}P_b + S_\epsilon$$
$$(5.2)$$

where

$$C_1 = \max\left[0.43, \frac{E}{E+5}\right], \qquad E = S\frac{k}{\epsilon}, \qquad S = \sqrt{2S_{ij}\, S_{ij}} \qquad (5.3)$$

where S is the modulus of the mean rate of strain tensor.

In these equations, P_k represents the generation of turbulence kinetic energy due to the mean velocity gradients, calculated as follows:

$$P_k = \mu_t S^2 \tag{5.4}$$

P_b is the generation of the turbulence kinetic energy due to buoyancy, negligible for our applications:

$$P_b = \beta g_i \frac{\mu_t}{Pr_t} \frac{\partial T}{\partial x_i} \tag{5.5}$$

where Pr_t is the turbulent Prandtl number for energy and g_i is the component of the gravitational vector in the ith direction. The default value of Pr_t is 0.85.

The cofficient of thermal expansion, β is defined as:

$$\beta = -\frac{1}{\rho} (\frac{\partial \rho}{\partial T})_P \tag{5.6}$$

- **Modelling turbulent viscosity**

$$\mu_t = \rho \, C_\mu \, \frac{k^2}{\epsilon} \tag{5.7}$$

While C_μ is constant in the standard k-ϵ model, in the Realizable k-ϵ model this coefficient is calculated as follows:

$$C_\mu = \frac{1}{A_0 + A_s \frac{kU^*}{\epsilon}} \tag{5.8}$$

$$U^* = \sqrt{S_{ij} \, S_{ij} + \tilde{\Omega}_{ij} \, \tilde{\Omega}_{ij}} \tag{5.9}$$

$$\tilde{\Omega} = \Omega - 2\epsilon_{ijk} \, \omega_k \tag{5.10}$$

and

$$\Omega = \overline{\Omega}_{ij} - \epsilon_{ijk} \, \omega_k \tag{5.11}$$

where $\overline{\Omega}_{ij}$ is the mean rate of rotation viewed in a rotating reference frame with the angular velocity ω_k. The model constants A_0 and A_s are given by:

$$A_0 = 4.04, \quad A_s = \sqrt{6} \cos \phi \tag{5.12}$$

where

$$\phi = \frac{1}{3} \, \arccos(\sqrt{6} \, W) \tag{5.13}$$

$$W = \frac{S_{ij} \, S_{jk} \, S_{ki}}{\tilde{S}} \tag{5.14}$$

$$\tilde{S} = \sqrt{S_{ij} \; S_{ij}} \tag{5.15}$$

$$S_{ij} = \frac{1}{2} \left(\frac{\partial u_j}{\partial x_i} + \frac{\partial u_i}{\partial x_j} \right) \tag{5.16}$$

- **Model Constants**

$$C_{1\epsilon} = 1.44, \qquad C_2 = 1.9, \qquad \sigma_k = 1.0, \qquad \sigma_\epsilon = 1.3 \tag{5.17}$$

5.3.3 Post-Processing: analysis of results

5.3.3.1 Moment calculation for Savonius turbines

The unsteady flow is solved by using the Sliding Mesh Model. Since many different configurations must be evaluated during the optimization, the computing time associated with one single CFD computation must be kept acceptable. Three complete revolutions are always computed, using an appropriate, constant value of the time-step; the first revolution is only used to initiate the correct flow solution, while the flow properties (in particular the power coefficient C_p and the torque coefficient C_m) are obtained by averaging the results during the last two revolutions. This combination (1 revolution for initializing the flow + 2 revolutions to compute the target function) has been kept throughout. The moment coefficient C_m and the power coefficient C_p are calculated according to Eqs. (2.20) and (2.21), respectively.

We have checked separately the influence of the number of revolutions on the computed turbine performance for the optimal design (Fig. 5.8), by continuing the CFD simulation. After 10 revolutions, the average power coefficient reaches a constant value. The absolute difference in C_p between this value and the one obtained after only three revolutions equals 0.024. This is an estimation of the uncertainty associated with the considered optimization process. This inherent uncertainty is very small compared to the range of C_p explored during the optimization and is thus deemed acceptable. It amounts to only 6% of the pressure coefficient associated with the optimal design. The influence of the number of revolutions on the estimation of C_p by CFD has been also investigated systematically in a separate project [139], confirming the present findings. Only three revolutions have been thus computed for each Savonius design in order to reduce the needed computational time.

5.3.3.2 Forces calculation for Wells turbines

When an airfoil is set at an angle of incidence α in a fluid flow, it will generate a lift force F_L normal to the free stream and a drag force F_D in the direction of the free stream. These lift and drag forces can then be combined to get the tangential force F_T and the axial force F_A (Fig. 2.12). The corresponding force coefficients are the tangential force coefficient C_T and the axial force coefficient C_A, respectively which are calculated according to Eqs. (2.24) and (2.25). Together with the turbine efficiency, C_T will be the objective function for the optimization.
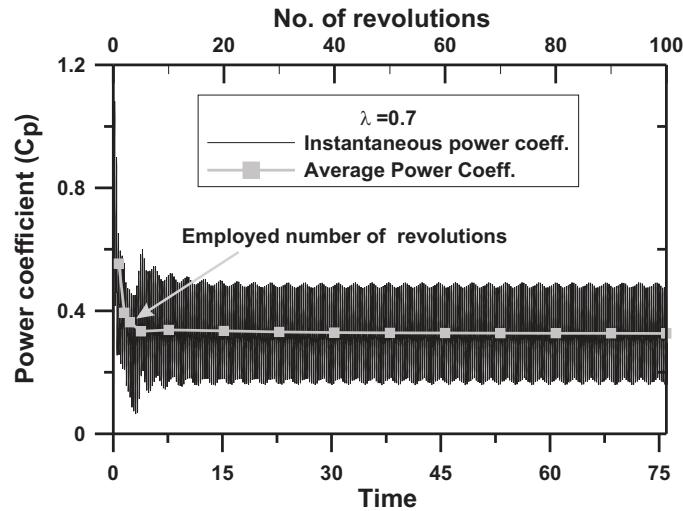
Figure 5.8: Influence of the number of revolutions on the instantaneous and on the average power coefficient C_p computed by CFD for the optimum design shown later.

5.4 CFD/Optimization coupling

A fully automatic optimization finally takes place, using OPAL (decision-maker for the configurations to investigate), the commercial tool Gambit for geometry and grid generation (including quality check) and the industrial CFD code ANSYS-Fluent to compute the flow field around the turbines. As a result of the CFD computation the objective function(s) is determined, and stored in a result file. The procedure is automated using journal scripts (to restart Gambit, Fluent) and a master program written in C (Algorithm 5.5.1), calling all codes in the right sequence as shown in Fig. 5.9. By checking the values stored in the result file, OPAL is able to decide how to modify the input parameters before starting a new iteration. The fully coupled optimization procedure is a complex task, which has been described in detail in previous publications [40, 52, 132].

Algorithm 5.4.1

```
/* Block 1 − Generate input file */
begin
  sprintf( filename, "input.dat");
  if ( !( f_input := fopen(path, "w") ) )
                                          Open the input-file for the simulation.
    then
        printf( "Cannot write file %s !", path );
        exit;                                       Error opening the input-file.
  fi
  comment: Create the header of the input file.
  fprintf( f_input, "$DesignVariable1 = %le",
```
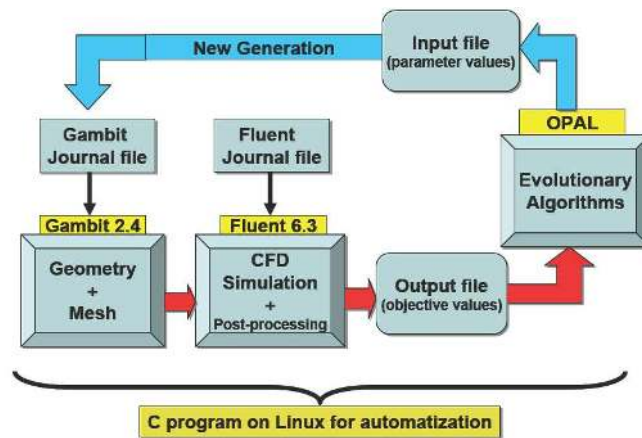
Figure 5.9: Schematic description of optimizer (OPAL) and CFD code coupling.

$DesignVariable1$);
fprintf(f_input, "$DesignVariable2 = %le",
$DesignVariable2$);
fclose(f_input);   **Close the input-file.**
end
/* Block 2 – Perform the simulation */
begin system("rm -f old_results.dat");   **Remove the previous result.**
  comment: Call the simulation tool.
  system("fluent 2ddp -g -i journal_file.jou");
end
/* Block 3 – Import the result(s) of the simulation */
begin
  if (!(f_result := fopen("Result.dat", "r")))
                                                       Open the result file.
    then
        ErrorVariable := 1;   **Error reading the result file.**
        continue;
        if
          fscanf(f_result,"%le", &Drag);   **Read the objective value.**
          fclose(f_result);   **Close the result file.**
        end

Many types of files have to be prepared in order to start optimization process, as follows:

- **Fluent journal file (fluent.jou)**

In this file, all the steps needed for CFD have been coded by text interface as script file. For example, a statement like "de bc vi 3 y y n 10 n 0.9902 n -0.13917 y n 0.49 n 4.9" means "define boundary-conditions of the velocity inlet (zone number 3), the velocity specification method is magnitude and direction with absolute reference frame and constant value. The inlet velocity value equal 10 m/s with constant X-component of the flow direction equal 0.9902 and constant Y-component equal -0.13917. The Inlet turbulent specification method is k and ε with constant values equal 0.49 and 4.9, respectively". This procedure is then repeated for every step in fluent sequence.

- **Gambit journal file (gambit.jou)**

  By the same method, a file is also constructed for geometry and grid generation. However, in our cases, this file has been built from two sub-files (head and tail). Since this work considers shape optimization, the tail file describes the body and contains all geometry steps. The values of all parameters describing the geometry are placed in the head file at the beginning of each optimization iteration.

- **Optimization parameters file (*.tcl)**

  In this file, all the optimization parameters have been implemented, containing number of generations, population size, mutation rate, crossover probability and so on (Table 5.1). Beside these parameters, all constrains of each optimization parameter have been defined in this file.

Further, files have been constructed during the optimization, as:

- Input file (*.in)

  This file contains the values of the optimization parameters for every generation.

- Fluent output file (fluent.out)

  with this file, we can follow the convergence of the CFD solution for every configuration during evaluation.

- Output file (Result.dat)

  The output file includes all the objective results for every tested configuration. Results are stored in this file after every generation.

5.5 Optimization parameters

5.5.1 Savonius turbine: single objective optimization

The design variables considered for the optimization will be described in the next chapter, since many different cases have been optimized in this work. For this purpose, different parameters are considered in each configuration, which, together, are sufficient to fix clearly the geometry of this specific case. The objective function considers only

one output of the simulation (single objective optimization), that should be maximized as far as possible: the output power coefficient C_p. The parameters of the GA are listed in Table 5.1.

Table 5.1: Parameters of the Genetic Algorithm

Parameter	*Value*
Population size of the first generation, N	20 to 30
Number of generations	N_g
Survival probability	50%
Average probability	33.3%
Crossover probability	16.7%
Mutation probability	100%
Mutation magnitude	30%[a] (i.e. ±15%)

[a]This value is multiplied by 0.8 at each generation. For example the mutation magnitude is only 4% (±2%) after 10 generations. Mutation magnitude must be decreased during the optimization process to stabilize the population.

The number of generations N_g will be varied, depending on the number of free parameters, since there is a very strong relation between the number of parameters, the population size and the efficiency of the Genetic Algorithm (computing time and solution quality) [20].

5.5.2 Wells turbine: multi-objective concurrent optimization

The central goal when designing an improved Wells turbine is to achieve high efficiency and high power output (i.e., high tangential force coefficient). The objective function hence contains simultaneously two outputs of the simulation (multi-objective concurrent optimization), that should both be maximized as far as possible: the tangential force coefficient C_T; and the turbine efficiency η , which is inversely proportional to the axial force coefficient, and is defined for a negligible density change as:

$$\eta = \frac{F_T \, u_t}{\Delta p_0 \, Q} \tag{5.18}$$

with Q the volumetric flow-rate through the turbine.

The design variables again depend on the specific problem considered and will be listed in Chapter 7. The parameters of the GA are given in Table 5.1.

5.6 Conclusions

All the tools required for the optimization have been now developed and validated. The final analysis can be started, beginning with the Savonius turbine.

Chapter 6

Savonius turbine: single-objective optimization

6.1   Introduction

As already discussed in section 3.1.3, both two-blade and three-blade Savonius turbines have been proposed and constructed. The three-blade configuration should be in particular advantageous to obtain good self-starting conditions. At the beginning of this project, a small company contacted us with a modified, three-blade design without gap, called in what follows GW-turbine. We will start by considering and optimizing this specific configuration, before comparing with the standard (but optimized) three-blade Savonius turbine. At the end of the chapter, the best overall solution, involving indeed only two blades, will be fully optimized, yielding very promising results.

6.2   Optimal GW-turbine: modified three-blade Savonius turbine without gap

6.2.1   Performance of the original GW-turbine

A modified design, a three-blade rotor without passage in between has been proposed by a small company, in an effort to improve the performance compared to the conventional system (Fig. 6.1).

Three issues must be specifically investigated in this case:

1. is it possible to improve the performance by changing the shape of the blade (not being semi-cylindrical any more)?

2. is it possible to improve the performance by employing a deflector nose in front of the turbine?

3. is it possible to improve the performance by using mobile parts for the returning blade, thus reducing drag by "opening" the returning blade?
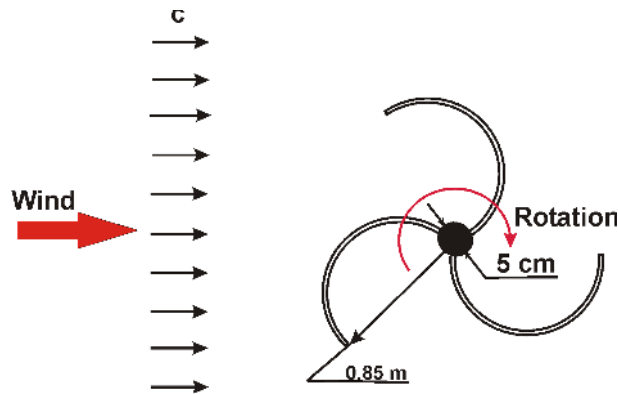
Figure 6.1: Schematic shape of the GW-turbine

We begin by considering the newly proposed design compared to the conventional turbine.
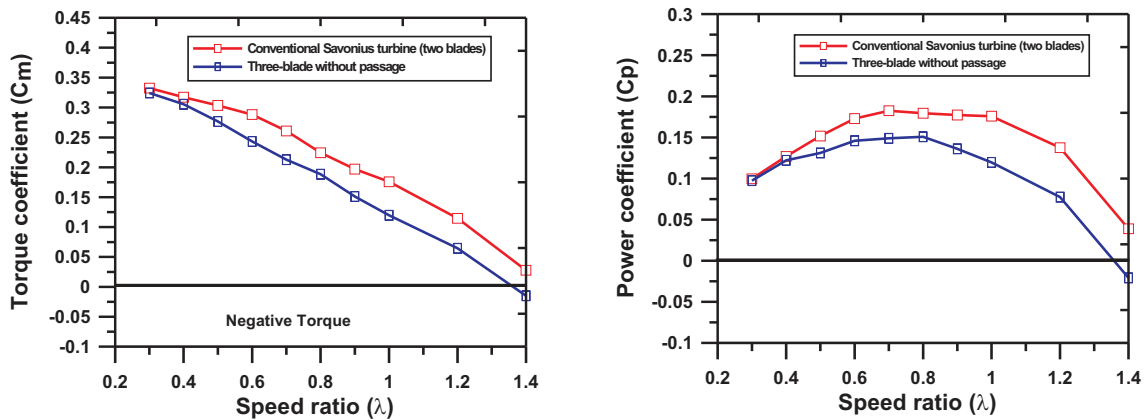
Figure 6.2: Performance comparison between the GW-turbine and the conventional, two-blade Savonius rotor.

Figure 6.2 shows the comparison between the GW-turbine (denoted "three blades without passage") and the conventional Savonius turbine performance. Unfortunately, it appears clearly from these first comparisons that the new design systematically leads to a poorer performance, both from the point of view of power coefficient and of torque coefficient. For very low values of λ, the difference is small, but the loss of performance becomes considerable for increasing λ. The peak value of C_p is only 0.16 compared to 0.18 for the conventional design. An analysis of the flow can readily identify the reason for this loss of performance. Increasing the number of blades increases the reverse moment as well. Closing the passage between the blades leads to a reduction of the airflow entering the system and increases the global drag on the returning blade (Fig. 6.3).
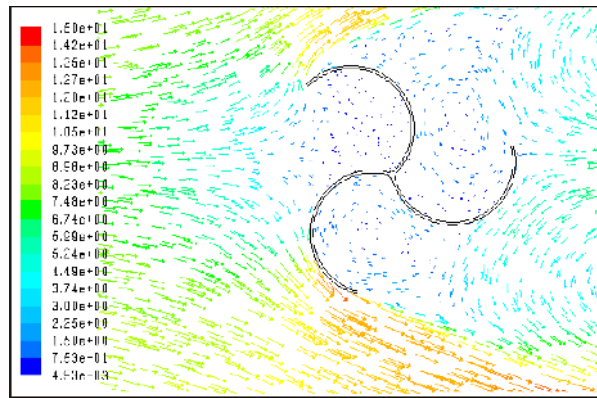
Figure 6.3: Instantaneous velocity vectors around the GW-turbine

6.2.2 Reducing the drag on the returning blade

In order to improve the performance of the GW-turbine, it was proposed to reduce the drag of the returning blade by employing mobile blade sections. In closed position, these mobile parts return back to the standard blade shape. When open, they should lead to a considerable reduction of the drag on the returning blade. This procedure is described schematically in Fig. 6.4.
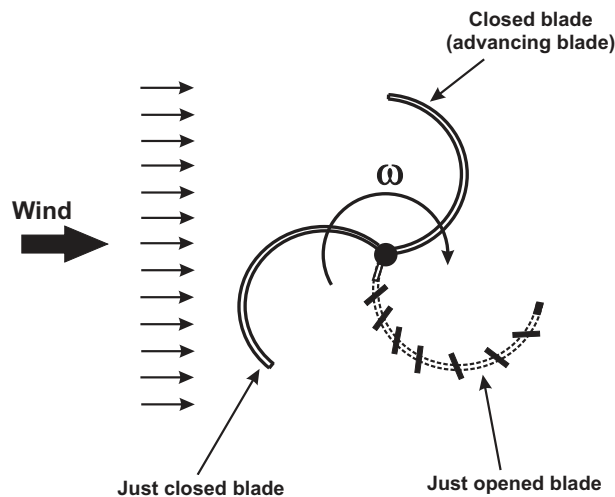
Figure 6.4: Schematic description of the GW-turbine with open returning blade.

The new design with an open returning blade has been investigated numerically for different values of the speed ratio λ. For these computations, the slits are considered to be inclined by 30° (constant value) compared to the local blade direction. The resulting performance has been compared with that of the baseline GW-turbine, as shown in Fig. 6.4. The results show a considerable improvement of the performance

when comparing with the baseline GW-turbine. This improvement is visible both for the torque and for the power coefficient. The gain is directly a consequence of the drag reduction on the returning blade, due to air passing between the slits of this returning blade, as seen in Fig. 6.5. The increase of the power coefficient reaches 0.0843 at $\lambda = 0.8$, which means a relative improvement of performance by almost 36% under such conditions. The GW-turbine with open returning blade is also systematically better than the conventional Savonius turbine. For example, at $\lambda = 0.7$ the relative increase in performance is 25.9%.
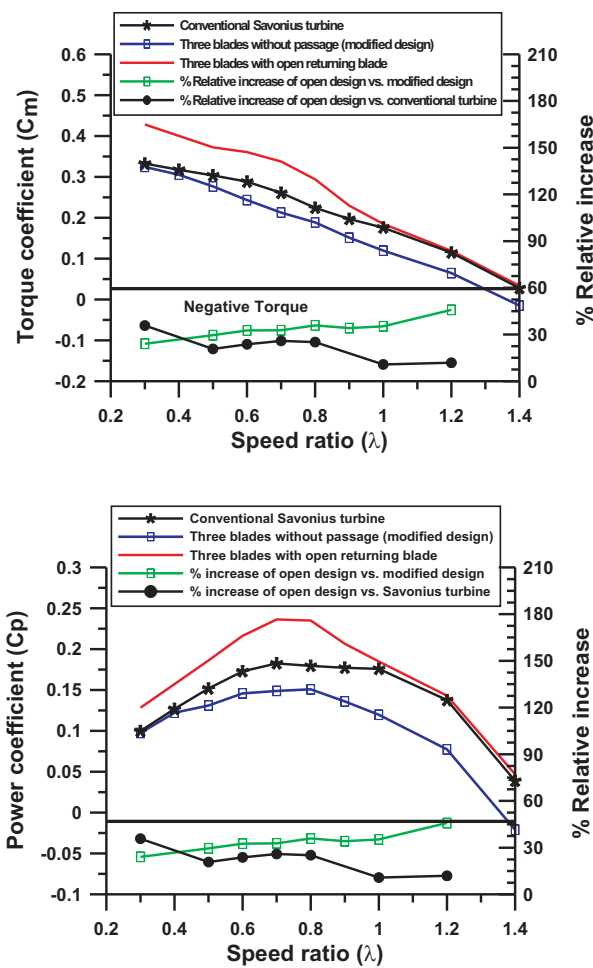
Figure 6.5: Performance comparison between the GW-turbine with or without open returning blade. The performance of the conventional Savonius rotor is also shown for comparison. Top: torque coefficient. Bottom: power coefficient.

Due to the effectiveness of this design, the effect of the slits opening angle on the performance has been investigated. Therefore, nine different angles (from 10° to 90°) have been studied, as shown in Fig. 6.6. From the results for both torque and power coefficients, the best performance for this design is when the slit angle lies between 30°
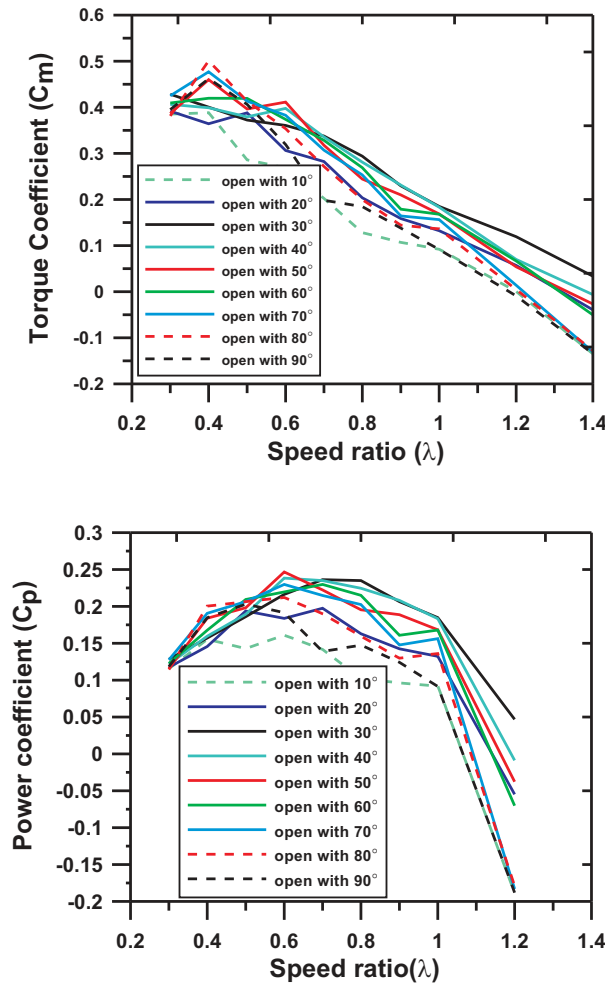
Figure 6.6: Performance of open returning blade turbine for different slit angles. Top: torque coefficient. Bottom: power coefficient.

and 40° considering at effective operating range between $\lambda = 0.6$ to $\lambda = 1.2$, corresponding to practical applications.

6.2.3 Influence of a rounded obstacle plate

In the original concept, a rounded deflector structure is placed in front of two counter-rotating GW-turbines. It is therefore important to check the influence of this deflecting surface on the global system performance. The corresponding geometry is shown schematically in Fig. 6.7.

Figure 6.8 shows a comparison between an isolated GW-turbine and the turbine placed behind the rounded deflector. Here again, it appears unfortunately that the performance is systematically reduced by the deflector. A GW-turbine placed directly in the free flow leads systematically to a higher performance, both in terms of torque
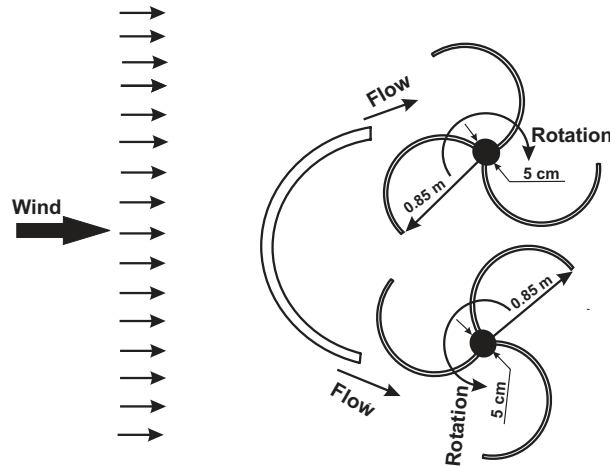
Figure 6.7: Schematic description of the counter-rotating GW-turbine with rounded deflector.

coefficient and of power coefficient. When analyzing the resulting flow field, the decrease in performance can be related to the excessive size and large radius of the planned deflector. As a consequence, the air flow is directed away from the blades instead of entering the system.

6.2.4 Optimization of the blade shape

Both for the conventional Savonius turbine and for the new design, semi-cylindrical blades are considered as a starting condition. Even if such blades are traditionally employed, it has never been demonstrated that such a blade shape leads to an optimal performance. Therefore, an optimization of this shape geometry reconstructed by splines based on three discrete points (Fig. 6.9) has been carried out, moving only one point (p_1).

The mathematical optimization procedure described previously (Genetic Algorithm relying on automated evaluations through CFD) is employed to find the optimal blade shape. This is done for a speed ratio $\lambda = 0.7$, considering an incident wind velocity $U = 10$ m/s, following the literature. This value of λ is retained, since it is known from the literature that it corresponds to the peak power coefficient of the conventional turbine (nominal conditions).

Two degrees of freedom are left simultaneously to the OPAL optimizer: X_1 and Y_1 define the coordinate of the center point of the blades (Fig. 6.9).

In this study, a relatively large domain has been defined for the optimization in the parameter space. The limits of this domain for the two parameters are $(0.32 : 0.675)$ for (X_1/R) and $(-0.294 : 0.294)$ for (Y_1/R), where R is the radius of the original design, kept constant during the optimization.

Finally, the optimization process thus involves simultaneously two parameters (or degrees of freedom): X_1 and Y_1. For each geometrical configuration one single objective
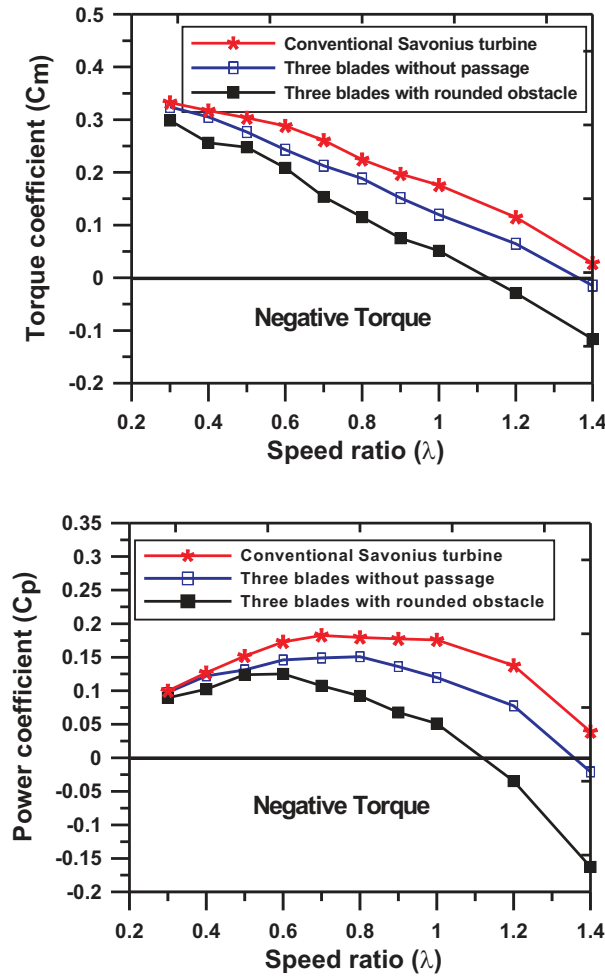
Figure 6.8: Performance comparison between the new concept in free field or placed behind a rounded deflector.

(power output coefficient) is determined by CFD evaluations, and should be maximized by the optimization procedure.

The results presented in Fig. 6.10 indicate that the considered objective is indeed considerably influenced by the two free parameters, X_1 and Y_1. As a whole, 140 different geometrical settings have been evaluated by CFD.

An optimal configuration can readily be identified for $\lambda = 0.7$. This optimum point differs noticeably from the original design and corresponds to the point of coordinate $X_1/R = 0.6315$ and $Y_1/R = -0.0521$ as shown in Fig. 6.10. This optimal condition leads to a power coefficient $C_p = 0.1638$ and a torque coefficient $C_m = 0.2339$.

When compared with the GW-turbine (semi-cylindrical blade shape, Fig. 6.11), the optimal point found by the optimization procedure corresponds simultaneously to an increase of the power coefficient by 0.01487 and of the torque coefficient by 0.02126 at $\lambda = 0.7$. For the power coefficient, this means a relative increase of the performance
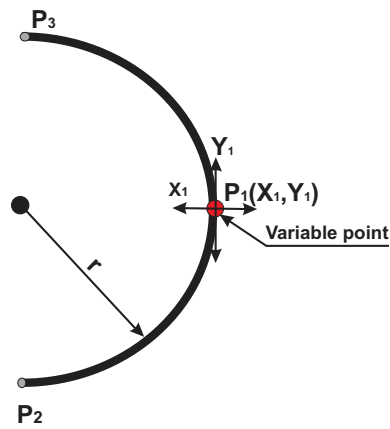
Figure 6.9: Description of the blade shape with 3 discrete points connected by splines.
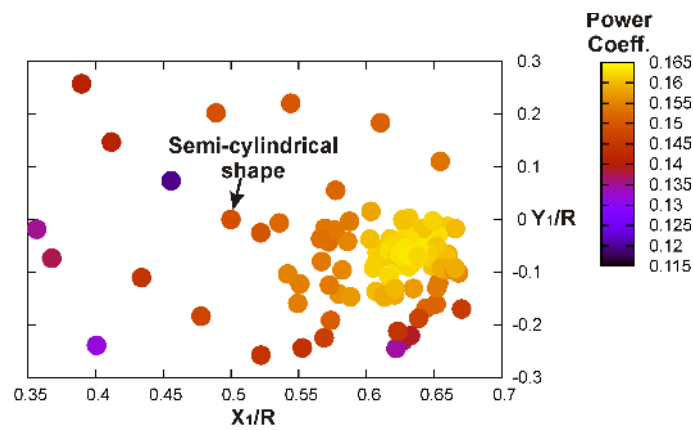
Figure 6.10: The two input parameters of the optimization and the power coefficient.
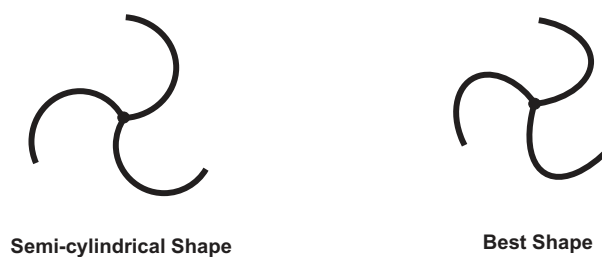
Figure 6.11: The best (right) configuration obtained during the optimization compared to the original GW-turbine (semi-cylindrical shape: left).

by 7.1% compared to the original GW-turbine. Since such turbines must operate also outside of the design conditions, it is now important to check how this gain will change as a function of λ. Therefore, the performance of the obtained optimal configuration

has been computed for the full range of useful λ-values, as shown in Fig. 6.12. The results of the new design with semi-cylindrical blades are also shown for comparison. Figure 6.12 demonstrates that the improvement of power output coefficient is observed at all conditions for intermediate values of λ (in particular between $\lambda = 0.7$ and $\lambda = 1.1$), compared to the semi-cylindrical design. The highest gain in efficiency with the new blade shape is obtained around $\lambda = 1$ and is roughly equal to 15%. For very low ($\lambda < 0.6$) and very high ($\lambda > 1.2$) values of λ, the modified shape is less efficient than the semi-cylindrical one. Therefore, operating at such conditions should be avoided.
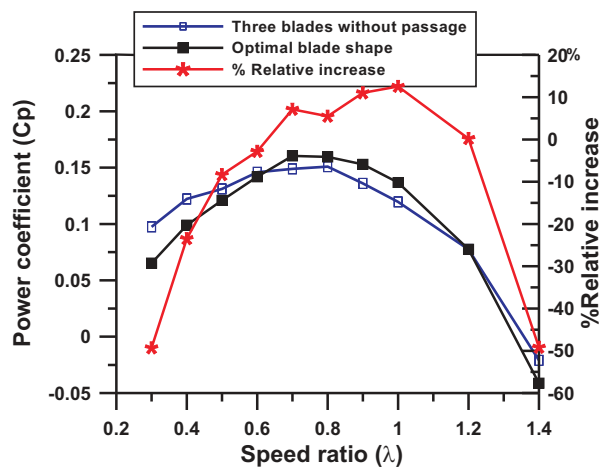
Figure 6.12: Power coefficient of the optimized configuration compared to the GW-turbine as a function of λ.

6.2.5   Conclusions on the GW-turbine

We can summarize all these results as:

- The standard GW-design (three-blade without gap) is less favorable than the conventional Savonius rotor.

- The rounded deflector is much too large in the original design.

- Opening the returning blade leads indeed to a considerable increase of performance. Different opening angles between 10° to 90° have been tested, best values are found between 30° and 40°.

- Similar modifications could possibly lead to even better results for classical Savonius turbines. It is therefore interesting to examine now such configurations, starting with the conventional, three-blade turbine.

6.3   Optimal three-blade Savonius turbine

The conventional, three-blade configuration with gap (Fig. 6.13) of the Savonius rotor has been extensively studied in the past [48]. The corresponding values of C_p and C_m have been determined numerically and sometimes experimentally as a function of the speed ratio λ. This has already been used to validate extensively our numerical procedure by comparison with published results, (see section 5.3.2.2). Published studies have demonstrated that three-blade turbines show considerable drawbacks compared to classical Savonius turbines (two-blade), in particular a lower efficiency. Nevertheless, we will try now to improve the performance of this design through optimization.
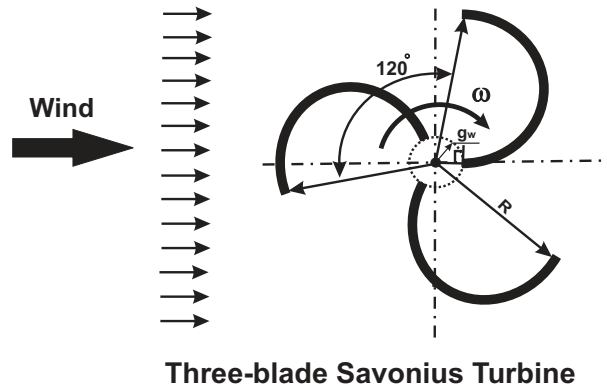
Figure 6.13: Schematic description and main parameters characterizing a conventional Savonius rotor with three blades.

6.3.1   Influence of obstacle plate

Since one of the major advantages of the Savonius turbine is its simplicity and corresponding compactness, robustness and low cost, a modification introducing a high complexity should probably not be retained. Considering the results of the previous studies and of section 3.1.3, some simple guiding or deflecting plate could lead to the best efficiency improvement at the lowest possible cost and complexity. Therefore, we will now investigate numerically the effect of an obstacle shielding partly the returning blade of a Savonius turbine. This part builds on top of a previous investigation [72] considering Savonius turbines with two as well as with three blades. Adding a shielding obstacle should in principle reduce the reverse moment, and as a consequence the total moment of the turbine will be increased, since the total moment is the moment difference between the advancing and the returning blades. Related ideas have already been proposed by other groups in the past [48]. But, at the difference of the previous studies, we are not looking here for a better solution, but directly for the best possible one.

6.3.1.1 Self-starting capability

One important issue associated with wind energy is the self-starting capability of the system. For decentral, low-cost applications as considered here, it is essential to obtain a self-starting system. To investigate this issue, the static torque exerted on a turbine at a fixed angle has been computed by CFD as a function of this angle θ. Figure 6.14 shows the obtained static torque coefficient C_{m_s} obtained for three different positions of the obstacle plate as a function of θ. The experimental results of [48] for the conventional three-blade turbines are also shown for comparison in Fig. 6.14. Due to periodicity, the results are only plotted for θ between 0 and 120°. These computations demonstrate that the obstacle plate has a considerable and mostly positive effect on the static torque coefficient. The obstacle plate improves the self-starting capacity for part of the θ-range. A self-starting capability ($C_{m_s} > 0$) is always obtained in principle at any angle, which is a major advantage.
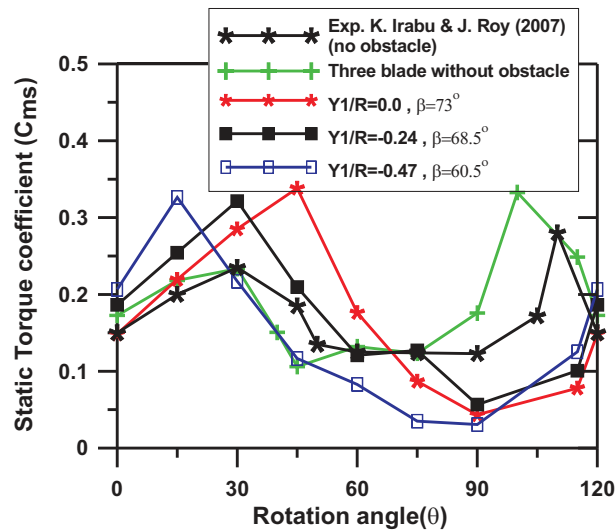
Figure 6.14: Static torque coefficient as a function of the rotor angle θ for three different values of Y_1 choosing $X_1/R = -1.4$ and $X_2/R = -1.76$.

6.3.1.2 Optimization of the obstacle position

The position and the angle of the shielding obstacle will now be optimized. The free design variables considered for the optimization will describe the obstacle position. For this purpose, three parameters are considered (X_1, Y_1 and X_2) which, together with a fixed value for Y_2 are sufficient to fix clearly the geometry of the shielding obstacle (Fig. 6.15). The objective function considers only one output of the simulation, that should be maximized as far as possible: the output power coefficient C_p. The mathematical optimization procedure described previously can be employed to find the optimal position of the obstacle. This is done again for a speed ratio $\lambda = 0.7$, considering a fixed incident wind velocity $U = 10$ m/s.
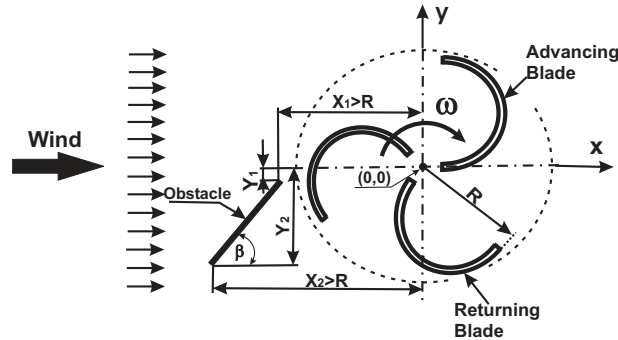
Figure 6.15: Schematic description of the geometry and free optimization parameters X_1, Y_1, X_2 used to modify the position of the shielding obstacle.

As explained previously, three degrees of freedom are left simultaneously to the OPAL optimizer: X_1 and Y_1 define the upper tip of the shielding obstacle; the value X_2 is then sufficient to define the position of the lower tip, since Y_2 is taken constant, with $Y_2/R = -1.177$ (Fig. 6.15). With these three factors, the position of the obstacle is perfectly determined, and the angle β can be deduced as well. In this manner, a truly optimal solution can be obtained considering a large set of possible parameters. Of course, when choosing the parameter space, it must be checked that the shielding obstacle cannot come into direct contact with the rotor ($\| X_1 \| > R$ and $\| X_2 \| > R$), so the acceptable range for the input parameters is shown in Table 6.1. The corresponding positions of the obstacle all lead to configurations that shield partially the returning blade.

Table 6.1: Acceptable range for the input parameters (parameter space)

Parameter	minimum	maximum
X_1/R	-1.88	-1.017
Y_1/R	-0.88	0.0
X_2/R	-1.88	-1.017

In Fig. 6.16 a parallel coordinate representation has been chosen since it is the most popular way to analyze output data from optimization involving several degrees of freedom. Such figures might be at first difficult to understand. Each thin connecting line represents all numerical parameters associated with one specific configuration, where each parameter is associated with its own vertical axis. The first three columns therefore show the value of the three free parameters, $X_1/R, X_2/R$ and Y_1/R; the last column on the right corresponds to the value of the objective function, here the power coefficient C_p. The scale of the first parameter ($X1/R$) is for instance bounded between -1.88 (minimum) and -1.017 (maximum). By following a single line, the reader can therefore determine quantitatively the values of all parameters associated with one configuration. The optimal solution is shown with a thick red line. The results presented in Fig. 6.16 indicate that the considered objective is indeed considerably influenced by the three free

Figure 6.16: Input parameters of the optimization and power coefficient represented using parallel coordinates. The parameters of the optimal configurations are connected with a thick red line. The power coefficient of the conventional three-blade Savonius turbine is shown with a gray circle.

parameters, X_1, Y_1 and X_2. As a whole, 210 different geometrical settings have been evaluated by CFD, requesting 22 days of computing time on a standard PC for the three-blade Savonius turbine. Note that the user-waiting time could be considerably reduced by carrying out the requested CFD in parallel on a PC cluster [132]. Such a parallel procedure, already implemented in OPAL, has not been used in the present case but could reduce the needed time by more than an order of magnitude, as demonstrated in other studies.

The optimal configuration (highest point in the right column in Fig. 6.16, all corresponding parameters being connected by a thick red line) can now readily be identified for $\lambda = 0.7$. The optimum obstacle position, optimum angle β and corresponding optimal power coefficient C_p are listed in Table 6.2.

Table 6.2: Optimal configurations

Design	parameter	value	β	power coeff. C_p
Three-blade Savonius turbine	X_1/R	-1.05632		
	Y_1/R	-0.36912	$(80.52°)$	0.2120
	X_2/R	-1.38162		

When compared with the three-blade Savonius turbines (without shielding obstacle), the optimal point found by the optimization procedure corresponds to an absolute increase of the power coefficient by 0.058 at $\lambda = 0.7$. This means a relative increase of the performance (measured by the power output coefficient) by 27.5%, compared to the conventional three-blade Savonius design without any obstacle.

It is now important to check how this gain would change as a function of λ, since such
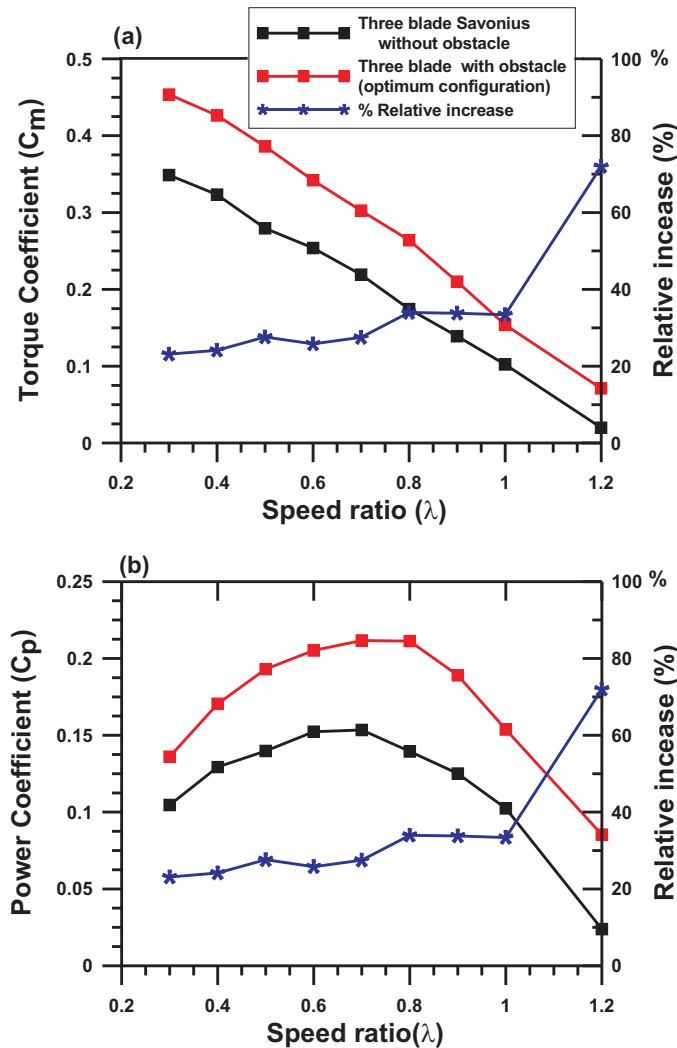
Figure 6.17: Performance of the optimized configuration (red line) compared to the conventional three-blade Savonius turbine without obstacle (black): a: torque coefficient; b: power coefficient. The corresponding relative increase is shown with blue line.

a turbine must be able to work also for off-design conditions. Therefore, the performance of the optimal configurations have been finally computed for the full range of useful λ-values, as shown in Fig. 6.17. This figure demonstrates that the improvement of both torque coefficient and power output coefficient is observed throughout for all values of λ, compared to the conventional three-blade Savonius turbine without obstacle. The absolute gain for C_p increases even slightly with λ at first, the relative increase being highest for the largest values of λ considered in the present study.

6.3.2 Optimal blade shape

In the previous section, the efficiency of the conventional three-blade Savonius turbine has been increased by placing in an optimal manner an obstacle plate shielding the returning blade. The present study now aims at improving further the output power of the three-blade Savonius turbine. In order to achieve this objective, the geometry of the blade shape (skeleton line) is now optimized in presence of the obstacle plate.

Optimization is used here to find the best blade shape while taking into account the obstacle shielding the returning blade in the optimum position. The free design variables considered for the optimization describe the blade skeleton line for a constant blade thickness of 2 mm. For this purpose, six parameters are considered (X_{P1}, Y_{P1}, X_{P2}, Y_{P2}, X_{P3} and Y_{P3}, see Fig. 6.18). The obstacle plate is kept fixed in the optimal position identified in the previous section ($X_1/R = -1.05632$, $Y_1/R = -0.36912$, $X_2/R = -1.38162$ and $Y_2/R = -1.1770$, which leads to an angle $\beta = 80.52°$, see Fig. 6.15). Now, the blade shape of the Savonius turbine will be optimized in order to find the best possible flow conditions. The six shape parameters are sufficient to determine uniquely the geometry of the system, since the obstacle position is fixed.
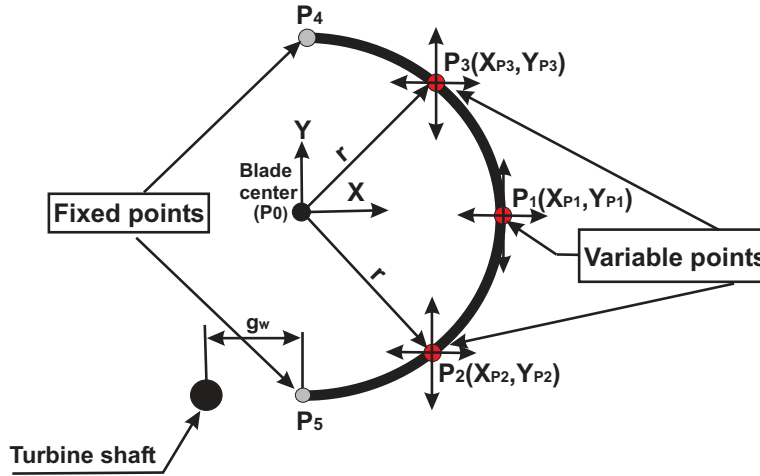
Figure 6.18: Schematic description of the free optimization parameters $X_{P1}, Y_{P1}, X_{P2}, Y_{P2}, X_{P3}$ and Y_{P3} used to modify the blade shape.

Knowing all 5 points, the full profile of the blade is reconstructed using standard splines (Nonuniform rational B-splines, NURBS). The order of a NURBS curve defines the number of nearby control points that influence any given point on the curve. The curve is represented mathematically by a polynomial of degree one less than the order of the curve; this means that the spline order is 5 in our case and the degree of the polynomial is 4. The objective function contains one single output of the simulation, that should be maximized as far as possible: the power coefficient C_p. The parameter space considered in the optimization has been defined as documented in Table 6.3. These domains are selected to prevent any domain overlap along the Y-direction and to keep realistic blade shapes. The reference point of the parameter space is point P_0, which is

the center of the original, semi-cylindrical shape with radius r as shown in Fig. 6.18. During the calculations, a circular turbine shaft is included with a fixed radius R_{sh} computed from $R_{sh}/R = 0.03$.

Table 6.3: Acceptable range for the input parameters (parameter space for blade shape with the obstacle)

Parameter	Minimum allowed	Maximum allowed
X_{P1}/r	0.53	1.47
Y_{P1}/r	-0.24	0.24
X_{P2}/r	0.24	1.2
Y_{P2}/r	-0.94	-0.24
X_{P3}/r	0.24	1.2
Y_{P3}/r	0.24	0.94

The results presented in Fig. 6.19 indicate that the considered objective is again considerably influenced by the six free parameters, X_{P1}, Y_{P1}, X_{P2}, Y_{P2}, X_{P3} and Y_{P3}, and thus by the blade shape. As a whole, 210 different geometrical settings have been evaluated by CFD, requesting one and a half month of total computing time on a standard PC.
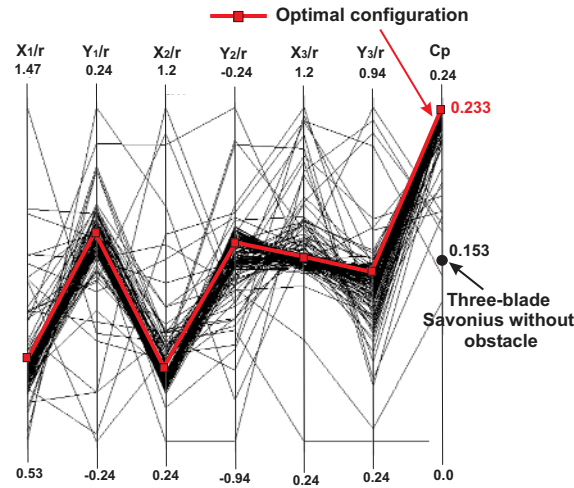
Figure 6.19: Input parameters of the optimization and power coefficient represented using parallel coordinates. The parameters of the optimal configuration are connected with a thick red line. The power coefficient of the conventional three-blade turbine (semi-cylindrical shape) is also shown with a black circle.

The optimal configuration (highest point in the right column in Fig. 6.19, all corresponding parameters being connected by a thick red line) can now readily be identified for $\lambda = 0.7$. The optimum point positions and corresponding optimal power coefficient C_p are listed in Table 6.4.

Table 6.4: Optimal blade shape with the obstacle

X_{P1}/r	Y_{P1}/r	X_{P2}/r	Y_{P2}/r	X_{P3}/r	Y_{P3}/r	Optimal power coeff. C_p
0.7519	0.0307	0.4345	−0.5456	0.6594	0.5464	0.233

At $\lambda = 0.7$ the optimal point found by the optimization procedure corresponds to an absolute increase of the power coefficient by 0.08 compared with the conventional three-blade Savonius turbine, respectively by 0.021 compared with the conventional Savonius rotor (semi-cylindrical blade shape) with obstacle plate. As a whole, this means a relative increase of the performance (measured by the power output coefficient) by 34.3% for the optimum shape with obstacle plate, compared to the conventional three-blade Savonius design without obstacle.

Note that this new shape (Fig. 6.20) is only optimum in combination with the employed obstacle plate. Indeed, the modified shape exploits best the flow redirection induced by the obstacle. As a consequence, the reverse moment is reduced by the shielding obstacle; simultaneously, the modified shape leads to an increase of the positive moment of the advancing blade.
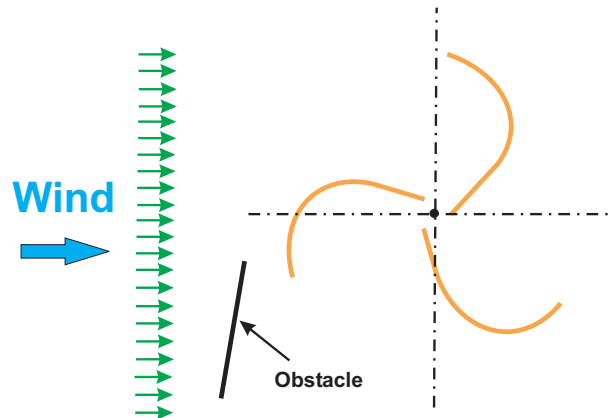
Figure 6.20: Optimum configuration obtained with the optimization procedure.

It is now important to check how this gain would change as a function of λ. Therefore, the performance of the optimal configuration has been finally computed for the full range of useful λ-values, as shown in Fig. 6.21. This figure demonstrates that the improvement of both torque coefficient and power output coefficient is observed throughout for all values of λ, compared to the conventional three-blade Savonius turbine. The absolute gain for C_p and C_m is even higher for lower λ-values. The relative performance increase compared to the conventional three-blade Savonius configuration is always higher than 30% in the effective operating range.
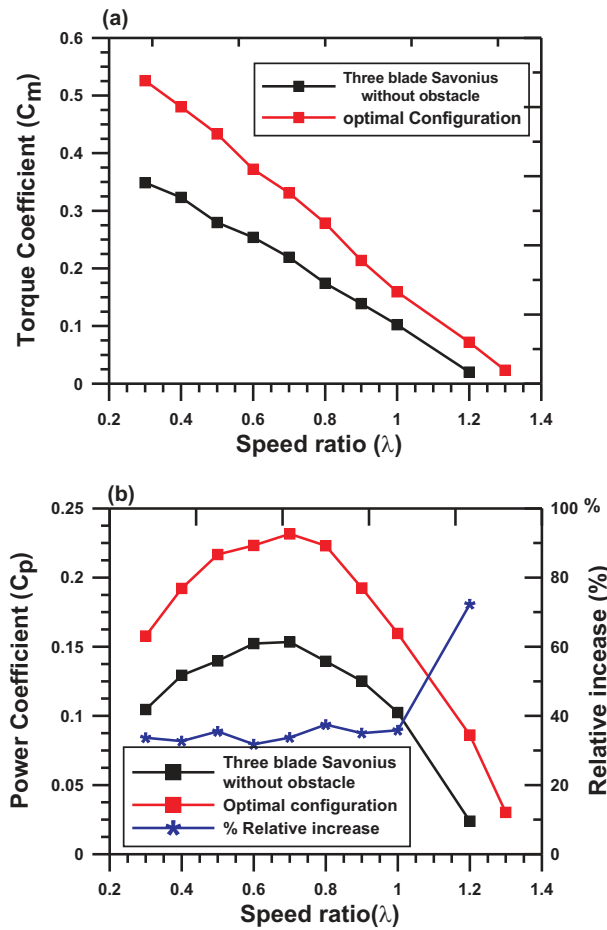
Figure 6.21: Performance of the optimized configuration (red line) compared to the conventional three-blade Savonius turbine (black line): a) torque coefficient; b) power coefficient. The corresponding relative increase compared to the conventional three-blade configuration is shown with blue line.

6.3.3 Optimal three-blade Savonius turbine with guiding plates

After improving the efficiency of the three-blade Savonius turbine by placing appropriately an obstacle shielding the returning blade, the present study aims at investigating and improving further the output power of the three-blade Savonius turbine and improving the static torque, which measures the self-starting capability of the turbine. For this purpose, a modified design is considered, involving simultaneously an obstacle plate shielding the returning blade and a flow deflector (frontal guiding plates). Four geometrical properties are optimized simultaneously: 1) the position of an obstacle shielding the returning blade; 2) the position of a deflector guiding the wind toward the advancing blade; 3) the blade skeleton line and 4) the gap width.

The optimization process thus relies on free design variables that describe the position and angles of the plates, the blade shape (skeleton line) as well as the gap width s
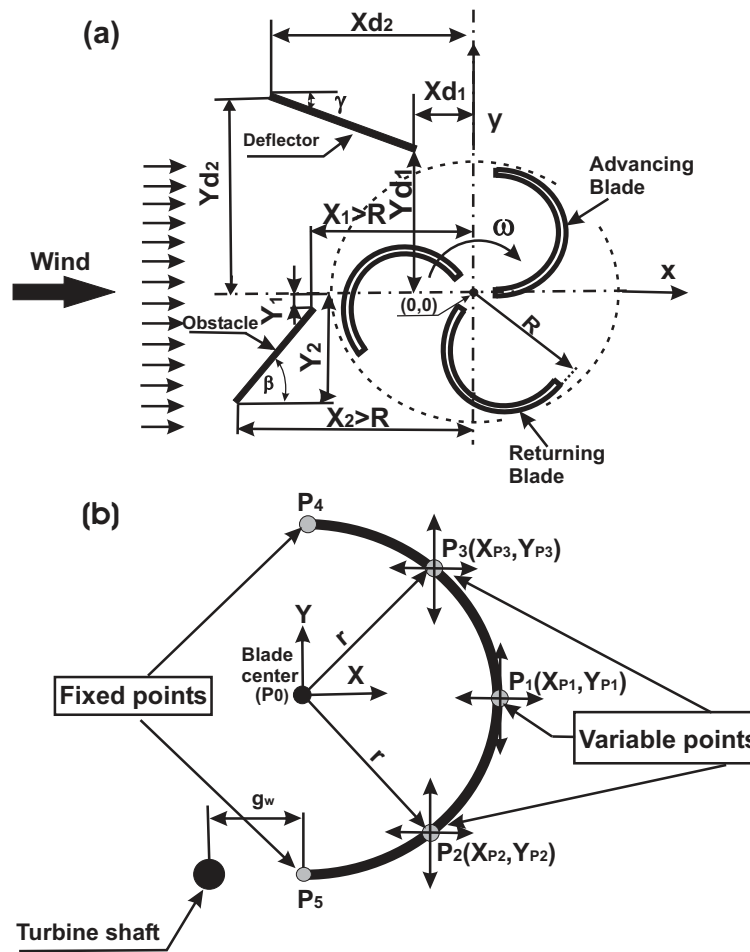
Figure 6.22: Schematic description of the free optimization parameters characterizing a three-blade Savonius rotor : a) plate parameters $(X_1, Y_1, X_2, Y_2, X_{d1}, Y_{d1}, X_{d2}$ and $Y_{d2})$; b) $X_{P1}, Y_{P1}, X_{P2}, Y_{P2}, X_{P3}$ and Y_{P3} used to modify the blade shape; additionally, the gap width g_w.

(Fig. 6.22). At the end, fifteen free parameters are thus considered (X_1, Y_1, X_2, Y_2, X_{d1}, Y_{d1}, X_{d2}, Y_{d2}, X_{P1}, Y_{P1}, X_{P2}, Y_{P2}, X_{P3}, Y_{P3} and g_w). The objective function considers again only one output of the simulation, that should be maximized: the output power coefficient C_p.

The mathematical optimization procedure described previously can now be employed. This is done as usual for a constant speed ratio $\lambda = 0.7$, considering a fixed incident wind velocity $U = 10$ m/s. The parameter space considered in the optimization has been defined as documented in Table 6.5. These domains are selected to prevent any domain overlap along the Y-direction, to keep realistic blade shapes and to cover a wide region for positioning the guiding plates. The reference point of the parameter space for the blade skeleton line is point P_0, which is the center of the original, semi-cylindrical shape with radius r as shown in Fig. 6.22. The reference point for the remaining space

parameters (guiding plates and gap width) is the global center of turbine rotation. During the calculations, a circular turbine shaft is included with a radius R_{sh} computed from $R_{sh}/R = 0.03$.
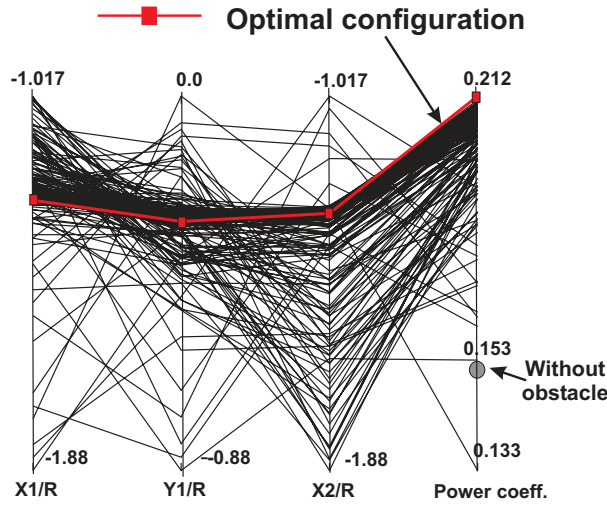

Figure 6.23: Input parameters of the optimization and power coefficient represented using parallel coordinates. The parameters of the optimal configuration are connected with a thick red line. The power coefficient of the conventional three-blade turbine (semi-cylindrical shape) is also shown with a black circle.

The results presented in Fig. 6.23 indicate that the considered objective is indeed considerably influenced by the fifteen free parameters. As a whole, 240 different geometrical settings have been evaluated by CFD, requesting 47 days of total computing time on a standard PC. Relying on parallel computers and possibly carrying out each CFD evaluation again in parallel [132] is clearly necessary when considering three-dimensional problems. Fortunately, this is quite straightforward to implement, so that researchers having access to parallel clusters can solve corresponding problems within an acceptable lapse of time.

The optimal configuration (highest point in the right column in Fig. 6.23, all corresponding parameters being connected by a thick red line) can now readily be identified for $\lambda = 0.7$. The corresponding geometry is shown in Fig. 6.24. The optimum parameter values are listed in Table 6.6.

One instantaneous picture of the velocity field is shown as an example in Fig. 6.25, demonstrating that the employed grid captures all important flow features in the vicinity of the rotor and guiding plates. This is of course a dynamic process, difficult to illustrate in a static figure.

Table 6.5: Acceptable range for the input parameters (parameter space)

Parameter	Minimum allowed	Maximum allowed
Blade shape		
X_{P1}/r	0.53	1.2
Y_{P1}/r	-0.24	0.24
X_{P2}/r	0.24	1.1
Y_{P2}/r	-0.94	-0.24
X_{P3}/r	0.24	1.1
Y_{P3}/r	0.24	0.94
Guiding plates		
X_{1d}/R	-1.2	0.0
Y_{d1}/R	1.1	1.65
X_{2d}/R	-1.88	0.0
Y_{d2}/R	1.76	2.6
X_1/R	-1.88	-1.1
Y_1/R	-0.7	0.0
X_2/R	-1.88	-1.1
Y_2/R	-1.88	-0.7
Gap width		
g_w/R	0.03	0.18
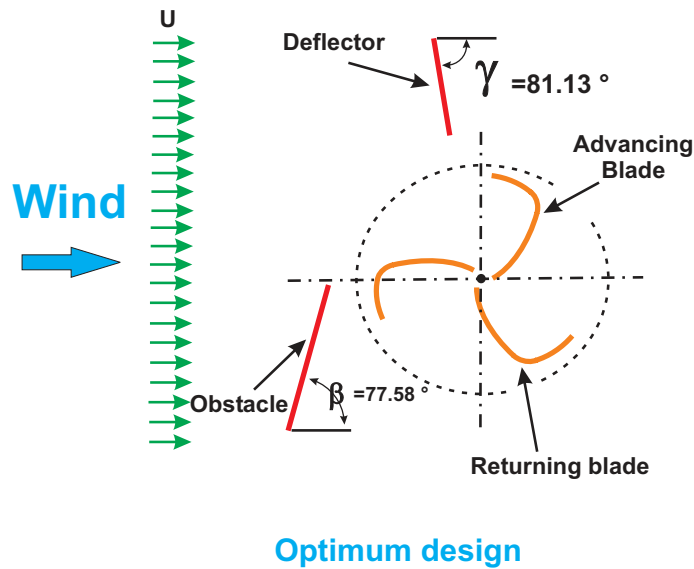
Figure 6.24: Optimum configuration obtained with the optimization procedure.

At $\lambda = 0.7$ the optimal point found by the optimization procedure corresponds to an absolute increase of the power coefficient by 0.207 compared with the conventional three-blade Savonius turbine (semi-cylindrical blade shape). As a whole, this means a relative increase of the performance (measured by the power output coefficient) by 57%

Table 6.6: Optimal configuration

Part	Parameter	Value	Angle
Blade shape	X_{P1}/r	0.6077	-
	Y_{P1}/r	-0.1338	
	X_{P2}/r	0.2735	
	Y_{P2}/r	-0.7136	
	X_{P3}/r	0.7065	
	Y_{P3}/r	0.5901	
Guiding plates	X_{d1}/R	-0.3089	$\gamma = 81.13°$
	Y_{d1}/R	1.436	
	X_{d2}/R	-0.4591	
	Y_{d2}/R	2.388	
	X_1/R	-1.3638	$\beta = 77.58°$
	Y_1/R	-0.1075	
	X_2/R	-1.691	
	Y_2/R	-1.5935	
Gap width	g_w/R	0.0988	-
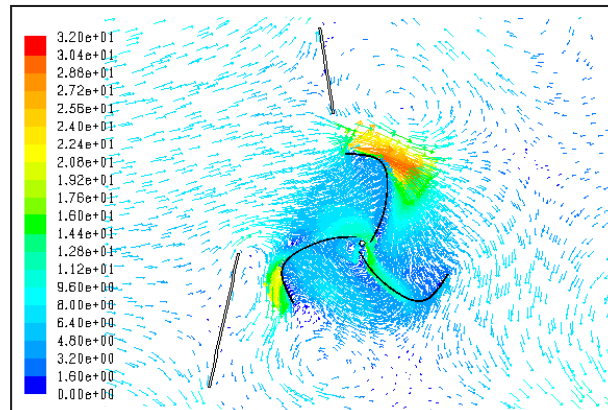
Figure 6.25: Instantaneous velocity vectors magnitude (m/s) around the optimum configuration (zoom) at the design point ($\lambda = 0.7$).

for the optimum design.

The performance of the optimal configuration has been finally computed for the full range of useful λ-values, as shown in Fig. 6.26. This figure demonstrates that the improvement of both torque coefficient and power output coefficient is observed throughout for all values of λ, compared to the conventional three-blade Savonius turbine. The relative performance increase compared to the standard Savonius configuration is always higher than 50% in the usual operating range ($0.6 \leq \lambda \leq 1$), demonstrating again the interest of the optimized configuration.

Figure 6.26: Performance of the optimized configuration (red line) compared to the conventional three-blade Savonius turbine (black line): Top: torque coefficient; Bottom: power coefficient. The corresponding relative increase compared to the standard configuration is shown with blue line.

6.3.3.1 Self-starting capability

For decentralized, low-cost wind-energy applications, it is essential to obtain a self-starting system. To investigate this issue, the static torque exerted on the turbine at a fixed angle has been computed by CFD as a function of this angle θ. Figure 6.27 shows the obtained static torque coefficient C_{ms} for the optimal design compared to the classical three-blade turbine. The experimental results of [48] for a conventional three-blade turbine are also shown for comparison in Fig. 6.27. Due to periodicity, the results are only plotted for θ between 0 and 120°. Compared to the classical turbine, these computations demonstrate that the modifications have a considerable and positive effect on the static torque coefficient, except in a small range ($90° \leq \theta \leq 100°$). There, the static torque coefficient is less than the classical one, but remains strictly positive.

Averaging over all angle positions, C_{ms} is increased by 0.091 for the optimum design.
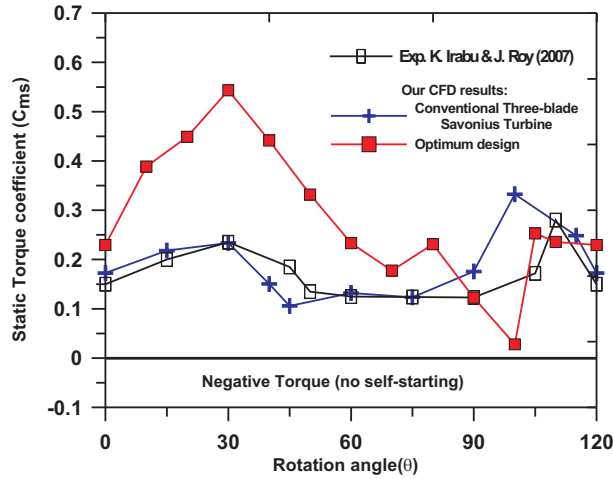
Figure 6.27: Static torque coefficient C_{ms} as a function of the fixed rotor angle θ for the optimal design (filled red squares) compared to the classical three-blade Savonius turbine (blue plus). The experimental results of [48] are also shown for comparison (empty black squares).

6.3.4 Conclusions on three-blade design

It is possible to increase the performance of the conventional three-blade design using optimization by modifying the blade shape and gap width while placing suitable obstacle and deflector plates. However, it is known from the literature that the two-blade design is usual better in terms of power coefficient. Therefore, in a last step, the conventional two-blade design will be optimized along the same lines.

6.4 Optimal two-blade Savonius turbine

In this section, new designs will be step by step investigated and optimized to improve the performance of the conventional two-blade Savonius turbine.

6.4.1 Obstacle plate

To achieve better performance, the position of an obstacle shielding the returning blade of the Savonius turbine and possibly leading to a better flow orientation toward the advancing blade is first optimized (Fig. 6.28).

Adding a shielding obstacle should in principle reduce the reverse moment, and as a consequence the total moment of the turbine will be increased.
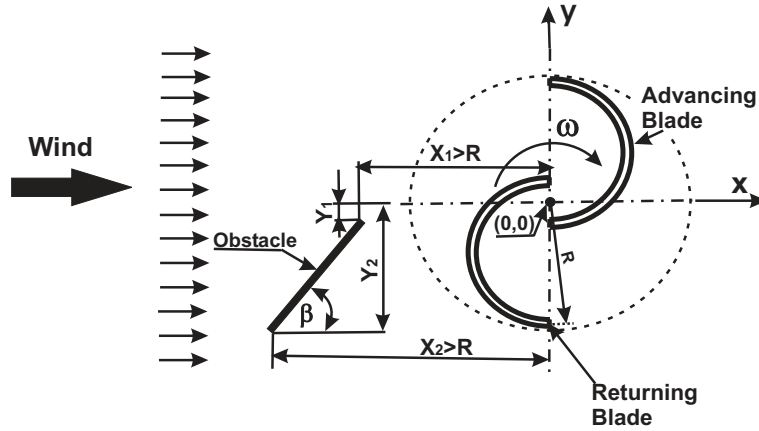
Figure 6.28: Schematic description of the geometry and free optimization parameters X_1, Y_1, X_2 used to modify the position of the shielding obstacle.

6.4.1.1 Self-starting capability

It is essential to obtain a self-starting system. To investigate this issue, the static torque exerted on a turbine at a fixed angle has been computed by CFD as a function of this angle θ. Figure 6.29 shows the obtained static torque coefficient C_{m_s} obtained for three different positions of the obstacle plate as a function of θ. The experimental results of [38] for the conventional turbine are also shown for comparison in Fig. 6.29. Due to periodicity, the results are only plotted for θ between 0 and 180°. These computations demonstrate that the obstacle plate has a considerable and positive effect on the static torque coefficient for the classical configuration. The conventional Savonius turbine shows a very large variation of the static torque coefficient as a function of θ, with negative values around $\theta = 140° - 170°$ (no self-starting). For all investigated positions involving an obstacle, the negative torque region completely disappears, with a minimum value of C_{m_s} higher than 0.07. Apart from that, the evolution as a function of θ is similar to that of the conventional turbine. As a whole, employing an obstacle plate improves noticeably the self-starting properties for the classical configuration. A self-starting capability $(C_{m_s} > 0)$ is always obtained in principle at any angle, which is a major advantage.

6.4.1.2 Optimization

Three degrees of freedom are left simultaneously to the OPAL optimizer: X_1 and Y_1 define the upper tip of the shielding obstacle; the value X_2 is then sufficient to define the position of the lower tip, since Y_2 is taken constant, with $Y_2/R = -1.177$ (Fig. 6.28). With these three factors, the position of the obstacle plate is perfectly determined, and the angle β can be deduced as well.

In a previous study [72], a small range of variation had been defined for the parameter space. Here, a much larger accessible domain has been prescribed, as documented in
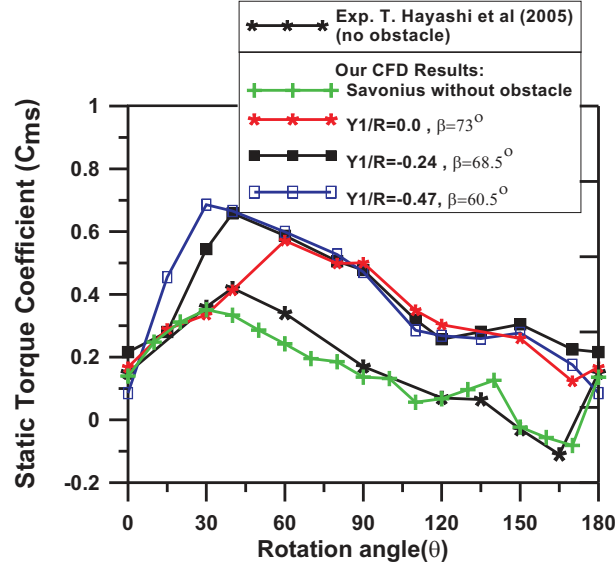
Figure 6.29: Static torque coefficient as a function of the rotor angle θ for three different values of Y_1 choosing $X_1/R = -1.4$ and $X_2/R = -1.76$.

Table 6.7. In this manner, a truly optimal solution can be obtained considering a large set of possible parameters. Of course, when choosing the parameter space, it must be checked that the shielding obstacle cannot come into direct contact with the rotor ($\parallel X_1 \parallel > R$ and $\parallel X_2 \parallel > R$). The corresponding positions of the obstacle all lead to configurations that shield partially the returning blade.

Table 6.7: Acceptable range for the input parameters

Parameter	minimum	maximum
X_1/R	-1.88	-1.017
Y_1/R	-0.88	0.0
X_2/R	-1.88	-1.017

The results presented in Fig. 6.30 indicate that the considered objective is considerably influenced by the three free parameters X_1, Y_1 and X_2. As a whole, 210 different geometrical settings have been evaluated by CFD, requesting 24 days of computing time on a standard PC. The optimal configurations (highest point in the right column in Fig. 6.30, all corresponding parameters being connected by a thick red line) can now be identified for $\lambda = 0.7$. The optimum obstacle position, optimum angle β and corresponding optimal power coefficient C_p are listed in Table 6.8.

When compared with the standard Savonius turbines (without shielding obstacle), the optimal point found by the optimization procedure corresponds to an absolute increase of the power coefficient by 0.068 at $\lambda = 0.7$. This means a relative increase of the performance (measured by the power output coefficient) by 27.3% for the two-blade Savonius turbine, compared to the conventional Savonius design without any obstacle.
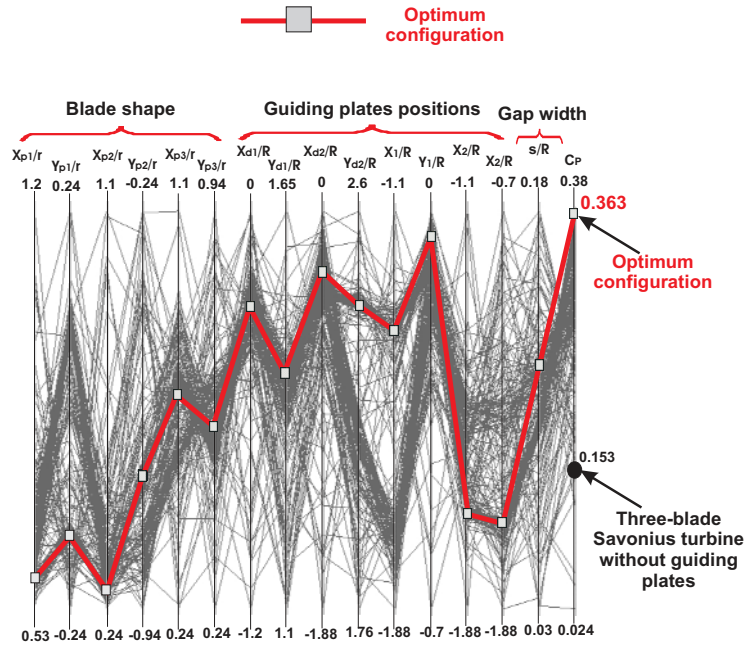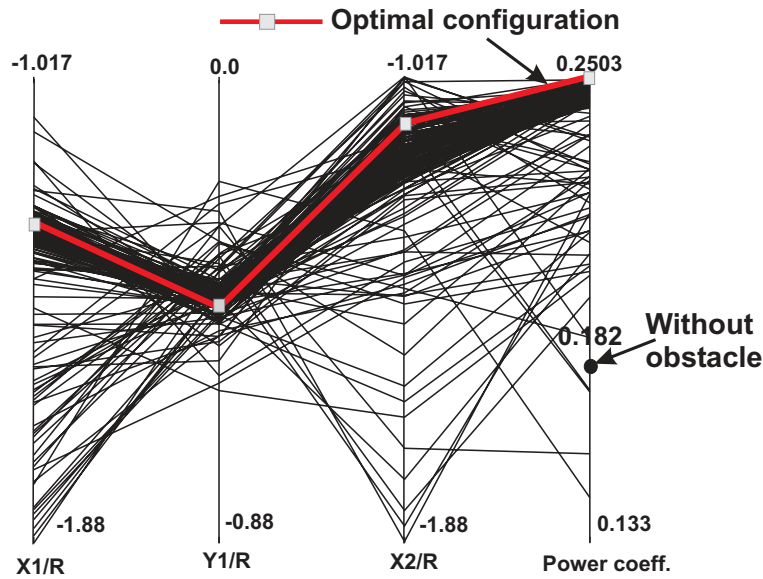
Figure 6.30: Input parameters of the optimization and power coefficient represented using parallel coordinates. The parameters of the optimal configurations are connected with a thick red line. The power coefficient of the conventional turbine is shown with a black circle.

Table 6.8: Optimal configurations (obstacle position and angle)

Design	*parameter*	*value*	β	*power coeff.* C_p
Two-blade Savonius turbine	X_1/R	-1.23830		
	Y_1/R	-0.45390	$(100.83°)$	0.2503
	X_2/R	-1.09993		

Note that we have been at first surprised to obtain an optimal geometry leading to $\beta > 90°$ for the two-blade turbine. After a thorough flow analysis, exemplified in Fig. 6.31, it is possible to understand finally that the flow direction induced by the obstacle at $\beta = 100.83°$ is indeed optimal for the advancing blade in the relative reference frame. Furthermore, for most configurations associated with $\beta < 90°$, the flow behind the shielding obstacle points partly toward the returning blade and thus increases the reverse moment; this effect is reduced for the optimal configuration. The optimal geometry of the shielding obstacle is of course highly dependent on the specific rotor configuration.

6.4.1.3   Off design performance

The performance of the optimal configuration has been finally computed for the full range of useful λ-values, as shown in Figure 6.32 . This figure demonstrate that the improvement of both torque coefficient and power output coefficient is observed throughout for all values of λ, compared to the conventional Savonius turbine without obstacle. The
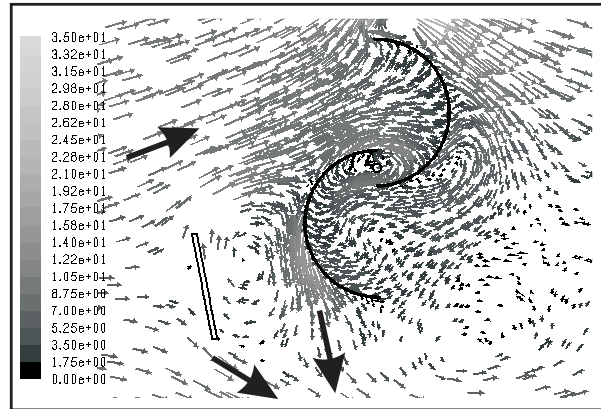
Figure 6.31: Instantaneous flow structure when the advancing blade is in vertical position for the optimal configuration at $\lambda = 0.7$: Zoom on the vicinity of the turbine (full CFD domain is much larger).

absolute gain for C_p increases even slightly with λ at first, the relative increase being highest for the largest values of λ considered in the present study.

6.4.1.4 Practical realization

From the technical point of view, many existing systems already rely on a tail vane for optimal alignment into the wind direction. A similar technical solution would be used for the Savonius turbine using the obstacle. In this manner the orientation of the system can be simply, efficiently and automatically controlled. As a whole, the optimized configuration is only slightly more complex, more expensive and heavier than the original system. Therefore, the improved power and torque coefficients should easily compensate these drawbacks within a short time after installation.

6.4.2 Optimal blade shape with obstacle plate

In the last section, the efficiency of the classical Savonius turbine has been increased by placing in an optimal manner an obstacle plate shielding the returning blade. The study now aims at improving further the output power of the Savonius turbine as well as the static torque, which measures the self-starting capability of the turbine. In order to achieve both objectives, the geometry of the blade shape is now optimized in presence of the obstacle plate. Six free parameters are considered in this optimization process.

6.4.2.1 Optimization

The free design variables considered for the optimization describe the blade skeleton line for a constant blade thickness of 2 mm. For this purpose, six parameters are considered (X_{P1}, Y_{P1}, X_{P2}, Y_{P2}, X_{P3} and Y_{P3}, see Fig. 6.33). The obstacle plate is kept fixed in the
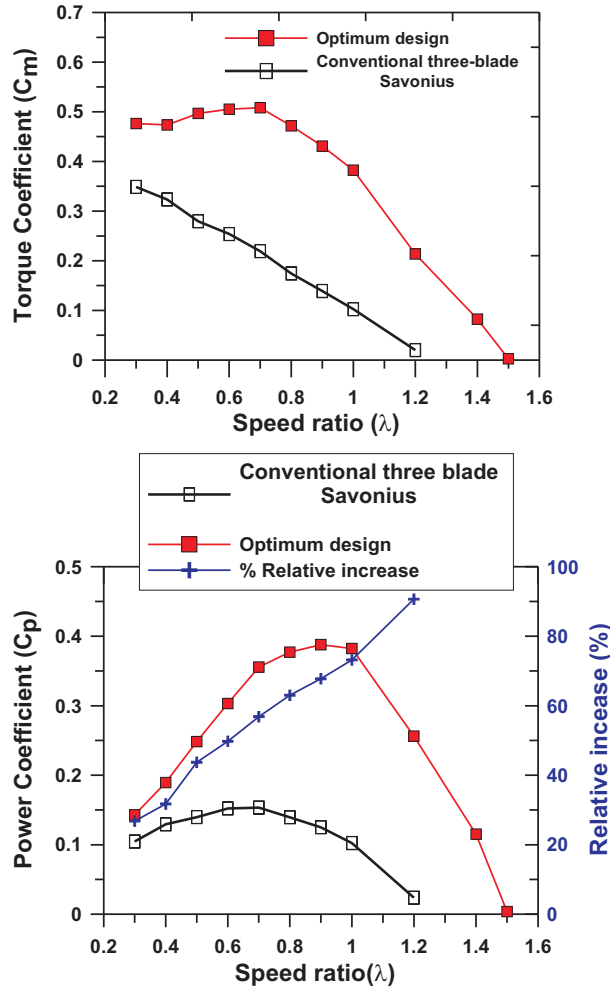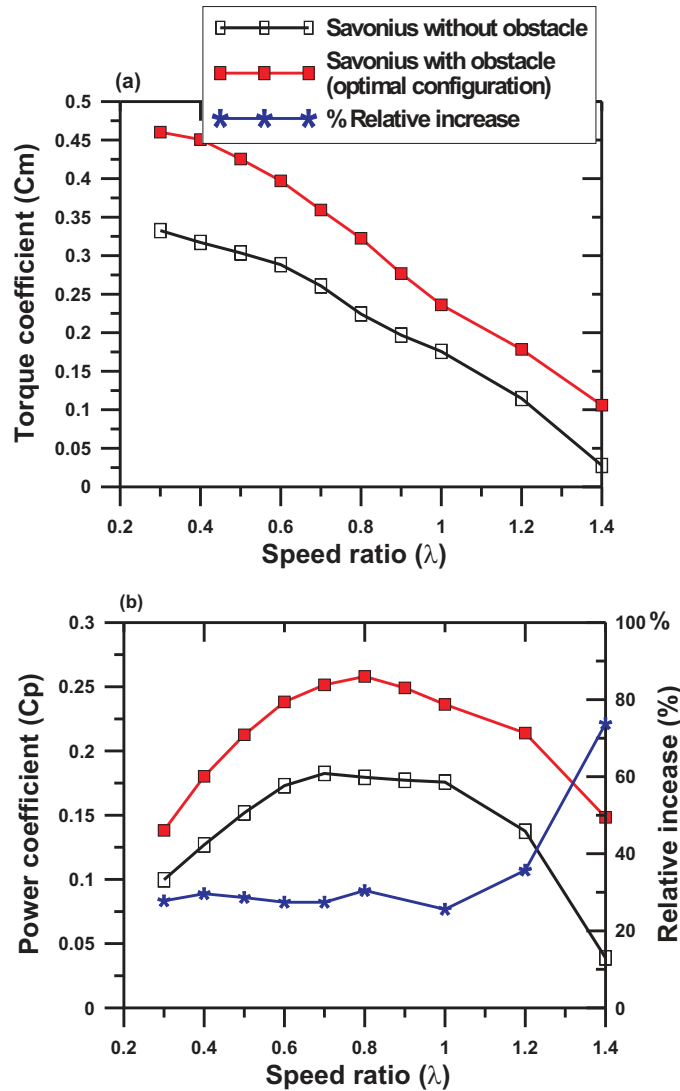
Figure 6.32: Performance of the optimized configuration (red line) compared to the conventional two-blade Savonius turbine without obstacle (black line): a: torque coefficient; b: power coefficient. The corresponding relative increase is shown with blue stars.

optimal position identified in Section 6.4.1 ($X_1/R = -1.2383$, $Y_1/R = -0.4539$, $X_2/R = -1.0999$ and $Y_2/R = -1.1770$, which leads to an angle $\beta = 100.8°$, see Fig. 6.28). The six shape parameters are sufficient to determine uniquely the geometry of the system, since the obstacle position is fixed. The objective function considers only one output of the simulation, that should be maximized as far as possible: the power coefficient C_p.

The parameter space considered in the optimization has been defined as documented in Table 6.9. These domains are selected to prevent any domain overlap along the Y-direction and to keep realistic blade shapes. The reference point of the parameter space is point P_0, which is the center of the original, semi-cylindrical shape with radius r as
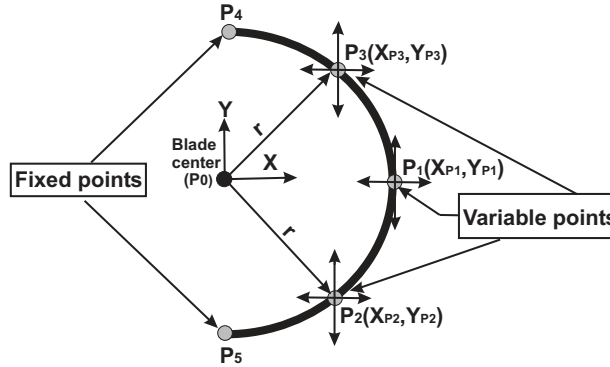
Figure 6.33: *Schematic description of the free optimization parameters* $X_{P1}, Y_{P1}, X_{P2}, Y_{P2}, X_{P3}$ *and* Y_{P3} *used to modify the blade shape.*

shown in Fig. 6.33. During the calculations, a circular turbine shaft is included with a fixed radius R_{sh} computed from $R_{sh}/R = 0.03$.

Table 6.9: Acceptable range for the input parameters for the blade shape

Parameter	Minimum allowed	Maximum allowed
X_{P1}/r	0.53	1.47
Y_{P1}/r	−0.24	0.24
X_{P2}/r	0.24	1.2
Y_{P2}/r	−0.94	−0.24
X_{P3}/r	0.24	1.2
Y_{P3}/r	0.24	0.94

The results presented in Fig. 6.34 indicate that the considered objective is considerably influenced by the six free parameters, X_{P1}, Y_{P1}, X_{P2}, Y_{P2}, X_{P3} and Y_{P3}, and thus by the blade shape. As a whole, 210 different geometrical settings have been evaluated by CFD, requesting one and a half month of total computing time on a standard PC.

The optimal configuration (highest point in the right column in Fig. 6.34, all corresponding parameters being connected by a thick red line) can now be identified for $\lambda = 0.7$. The optimum point positions and corresponding optimal power coefficient C_p are listed in Table 6.10.

Table 6.10: Optimal configuration

X_{P1}/r	Y_{P1}/r	X_{P2}/r	Y_{P2}/r	X_{P3}/r	Y_{P3}/r	Optimal power coeff. C_p
0.6909	0.0386	0.3940	−0.6067	0.6389	0.6357	0.298

At $\lambda = 0.7$ the optimal point found by the optimization procedure corresponds to an absolute increase of the power coefficient by 0.116 compared with the conventional Savonius turbine, respectively by 0.0475 compared with the conventional Savonius rotor

Figure 6.34: Input parameters of the optimization and power coefficient represented using parallel coordinates. The parameters of the optimal shape are connected with a thick red line. The power coefficient of the conventional turbine is shown with a gray circle. The power coefficient of the conventional turbine (semi-cylindrical shape) with obstacle plate is also shown with a black circle.

(semi-cylindrical blade shape) with obstacle plate. As a whole, this means a relative increase of the performance (measured by the power output coefficient) by 38.9% for the optimum shape with obstacle plate, compared to the conventional Savonius design without obstacle.

Note that this new shape (Fig. 6.35) is only optimum in combination with the employed obstacle plate. Indeed, the modified shape exploits best the flow redirection induced by the obstacle. As a consequence, the reverse moment is reduced by the shielding obstacle; simultaneously, the modified shape leads to an increase of the positive moment of the advancing blade.

6.4.2.2 Off design performance

The performance of the optimal configuration has been finally computed for the full range of useful λ-values, as shown in Fig. 6.36. This figure demonstrates that the improvement of both torque coefficient and power output coefficient is observed throughout for all values of λ, compared to the classical Savonius turbine. The absolute gain for C_p and C_m is even higher for lower λ-values. The relative performance increase compared to the standard Savonius configuration is always higher than 30% in the effective operating range.
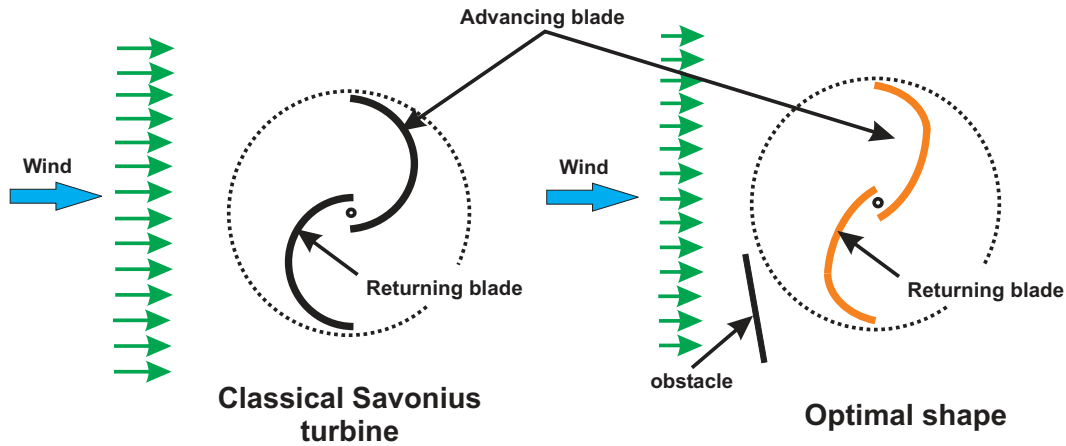
Figure 6.35: Optimum configuration (right) obtained with the optimization procedure compared to the classical Savonius turbine (semi-cylindrical shape: left).

6.4.2.3   Self-starting capability

The static torque exerted on the turbine at a fixed angle has been computed by CFD as a function of this angle θ. Figure 6.37 shows the obtained static torque coefficient C_{ms} obtained for the optimal configuration compared to the classical turbine with obstacle, as a function of θ. The experimental results of [38] for a conventional turbine are also shown for comparison in Fig. 6.37. Compared to the standard Savonius without obstacle plate, these computations demonstrate that the modified blade shape has a considerable and positive effect on the static torque coefficient. In the present, optimal configuration the negative torque region completely disappears, with a minimum value of C_{ms} higher than 0.2. Apart from that, the evolution as a function of θ is similar to that obtained with the conventional shape involving an obstacle plate. A self-starting capability ($C_{ms} > 0$) is always obtained at any angle in both cases, which is a major advantage.

6.4.3   Optimal Savonius turbine with two guiding plates

From the summary of the most important modification proposals listed in Chapter 3, the highest advantage of the Savonius turbine is its robustness. Modifications should not involve an exceedingly complex or expensive design. Therefore, simple guiding plates seem to be the best compromise between the increase of efficiency and the increase of cost and complexity. In the present section we will thus investigate numerically the effect of two combined guiding plates: a deflector plate is employed to obtain the best possible flow conditions for the advancing blade, while an obstacle plate shields partly the returning blade (Fig. 6.38)
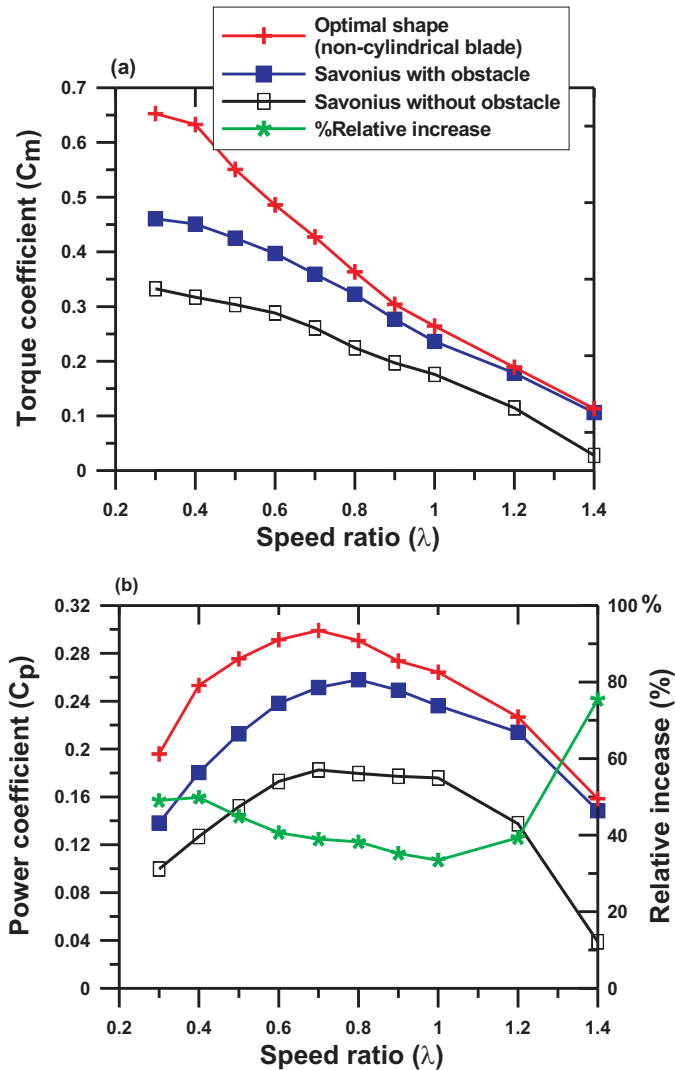
Figure 6.36: Performance of the optimized configuration (red line) compared to the conventional Savonius turbine with and without obstacle plate (blue and black, respectively): a: torque coefficient; b: power coefficient. The corresponding relative increase compared to the standard configuration is shown with green line.

6.4.3.1   Optimization

The optimization work will be carried out for obstacle and deflector simultaneously, with eight free space parameters (X_1, Y_1, X_2, Y_2, X_{d1}, Y_{d1}, X_{d2} and Y_{d2}), which together are sufficient to obtain clearly the position, length and angles of these guiding plates (obstacle and deflector) as shown in see Fig. 6.38. The parameter spaces considered in the optimization have been defined as documented in Table 6.11.

The results in Fig. 6.39 indicate that the considered objective is considerably influenced by the eight free parameters, X_{d1}, Y_{d1}, X_{d2}, Y_{d2}, X_1, Y_1, X_2 and Y_2, and thus by
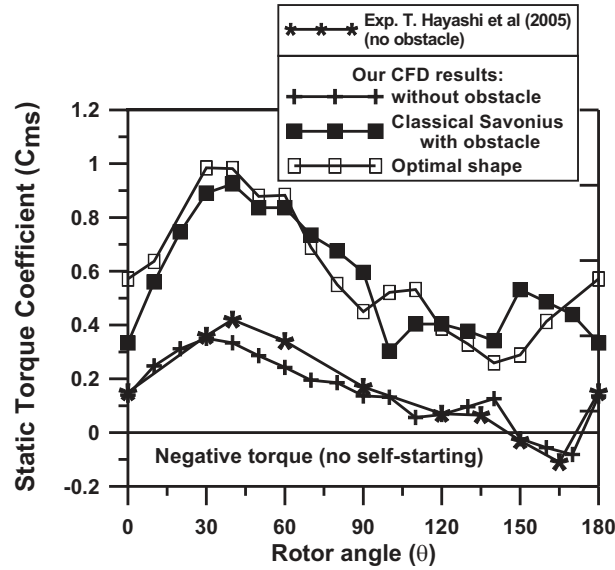
Figure 6.37: Static torque coefficient C_{ms} as a function of the fixed rotor angle θ for the optimal configuration compared to the standard Savonius turbine with and without obstacle plate. For this last case, the experimental results of [38] are also shown for comparison.
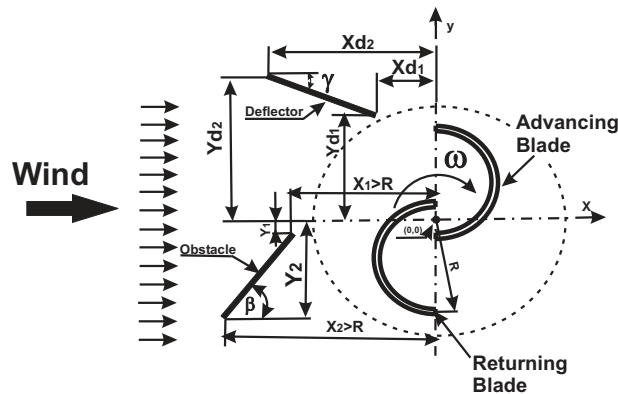
Figure 6.38: Schematic description of the geometry of Savonius turbine with frontal guiding plates.

the positions, angles and lengths of the guiding plates. As a whole, 210 different geometrical settings have been evaluated by CFD, requesting 40 days of total computing time on a standard PC.

The optimum point positions are listed in Table 6.12. These optimum parameters lead to the corresponding angles of 92.35° and 82.15° for obstacle and deflector, respectively and lead also to lengths of the guiding plates $L_o/d = 1.094$ and $L_d/d = 0.782$, as shown in Fig. 6.40.

Table 6.11: Acceptable range for the input parameters (parameter space)

Parameter	Minimum	Maximum
X_{d1}/d	-1.04	0
Y_{d1}/d	0.9	1.87
X_{d2}/d	-1.66	0
Y_{d2}/d	1.3	1.87
X_1/d	-1.66	-0.9
Y_1/d	-0.78	0
X_2/d	-1.66	-0.9
Y_2/d	-1.66	-0.53
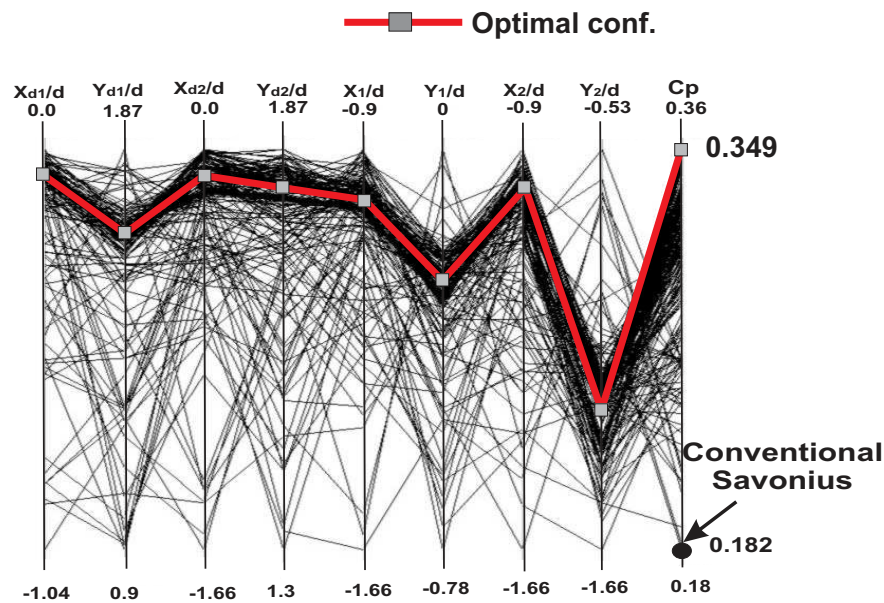
Figure 6.39: Input parameters of the optimization and power coefficient represented using parallel coordinates. The parameters of the optimal design are connected with a thick red line. The power coefficient of the conventional turbine is shown with a black circle.

At $\lambda = 0.7$ the optimal points found by the optimization procedure corresponds to an absolute increase of the power coefficient by 0.167 compared with the conventional Savonius turbine. This means a relative increase of the performance (measured by the power output coefficient) by 47.85% for the optimum design compared to the conventional Savonius design.

6.4.3.2   Off design performance

The performance of the optimal configuration has been next computed for the full range of useful λ-values, as shown in Fig. 6.41. The improvement of both torque coefficient

Table 6.12: Optimum parameters of guiding plates

X_{d1}/d	-0.066981
Y_{d1}/d	1.509671
X_{d2}/d	-0.17377
Y_{d2}/d	2.28434
X_1/d	-1.134209
Y_1/d	-0.286166
X_2/d	-1.0892
Y_2/d	-1.37918
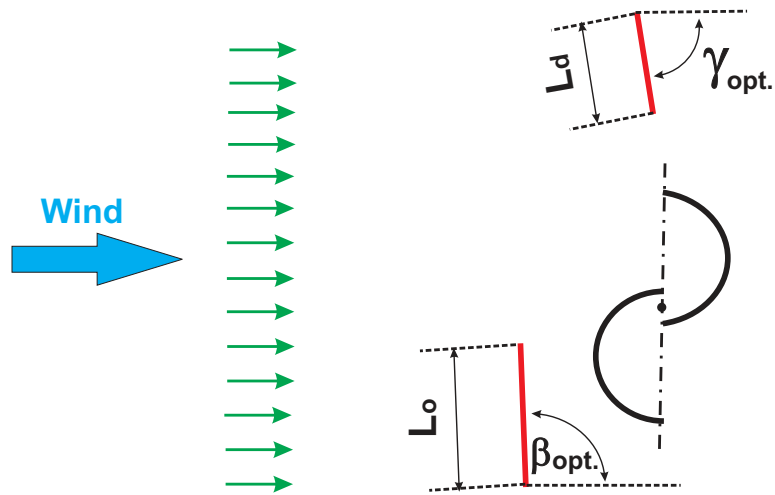
Figure 6.40: Optimum configuration of guiding plates.

and power output coefficient is observed throughout for all values of λ. The absolute gain for C_p and C_m is even higher for lower λ-values. The relative performance increase compared to the standard Savonius configuration is always higher than 35% in the effective operating range.

6.4.3.3 Profiled guiding plates

There is no reason to believe that flat guiding plates are the best choice. Therefore we started an optimization for non-flat guiding plates. Optimization is repeated for obstacle and deflector simultaneously, with fourteen free space parameters describing the optimum shape of both guiding plates. These fourteen parameters (X_{d1}, X_{d2} Y_{d2}, X_{d3}, Y_{d3}, X_{d4}, Y_{d4}, X_1 X_2, Y_2, X_3, Y_3, X_4 and Y_4, while Y_1 and Y_{d1} are constant and taken from the previous section, Table 6.12). Fourteen parameters are sufficient to define clearly the position and shapes of these guiding plates, as shown in Fig. 6.42. The parameter space considered in the optimization has been defined as documented in Table 6.13.

The results are shown in Fig. 6.43. More than 200 different geometrical settings have
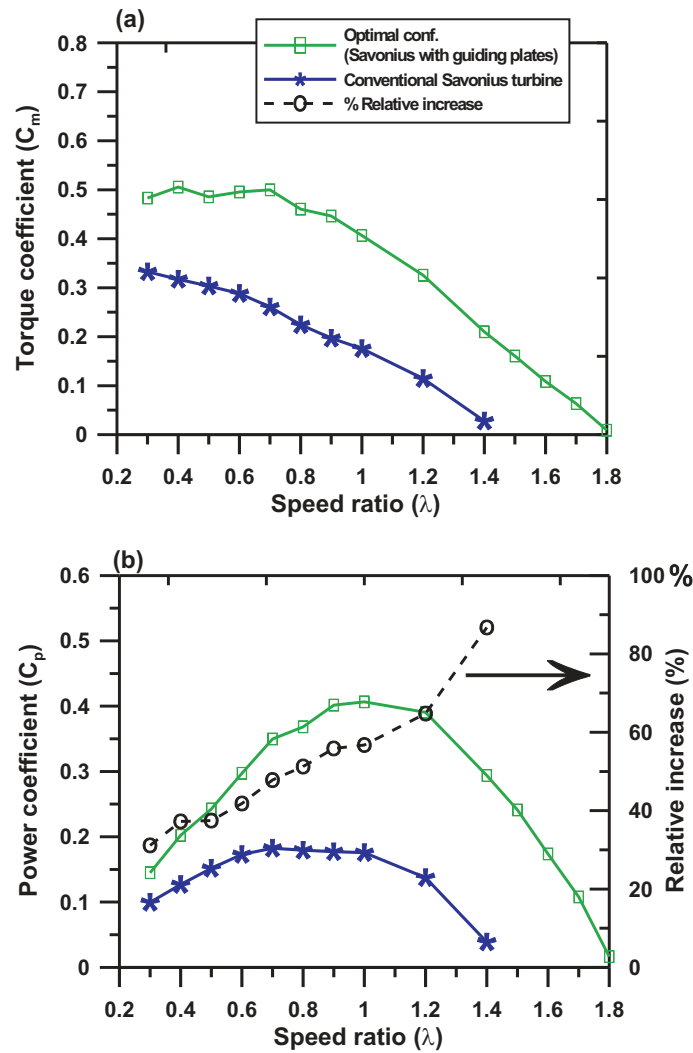
Figure 6.41: Performance of the optimized configuration (green line) compared to the conventional Savonius turbine (blue line): a: torque coefficient; b: power coefficient. The corresponding relative increase compared to the standard configuration is shown with black line.

been evaluated by CFD, requesting 40 days of total computing time on a standard PC. However, by comparison with the results of the flat guiding plates (see Section 6.4.3.1), the difference in power coefficient is only minimal (around $\simeq 0.01$). Therefore, from the manufacturing point of view, the slight improvement in the performance does not compensate the additional complexity, cost and weight of the profiled guiding plates (Fig. 6.44). As a consequence, only flat guiding plates are considered in the final optimization step.
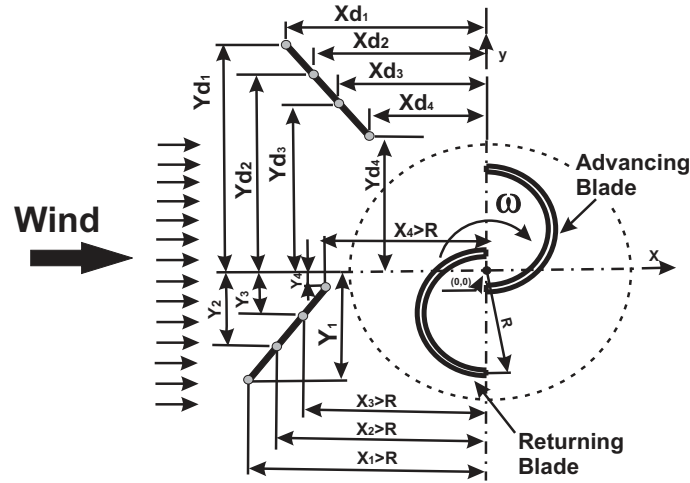
Figure 6.42: Schematic description of the geometry of Savonius turbine with profiled guiding plates.

Table 6.13: Acceptable range for the input parameters (parameter space)

Parameter	Minimum	Maximum
Deflector		
X_{d1}/d	-1.5	0
X_{d2}/d	-1.5	0
Y_{d2}/d	2	2.4
X_{d3}/d	-1.5	0
Y_{d3}/d	1.5	2
X_{d4}/d	-1.5	0
Y_{d4}/d	1.15	1.5
Obstacle		
X_1/d	-1.5	-0.8
X_2/d	-1.5	-1.15
Y_2/d	-1.5	-1
X_3/d	-1.5	-1.15
Y_3/d	-1	-0.5
X_4/d	-1.5	-1.15
Y_4/d	-0.5	0

6.5 Final optimization of Savonius turbine

The optimization steps of increasing complexity described in the previous sections seem very promising. Having now full confidence in the process, a last step involving all characteristic geometrical parameters is now attempted.

The effect of blade shape and guiding plates positions will be incorporated simultaneously during the optimization. In this aggressive optimization work, we will opti-
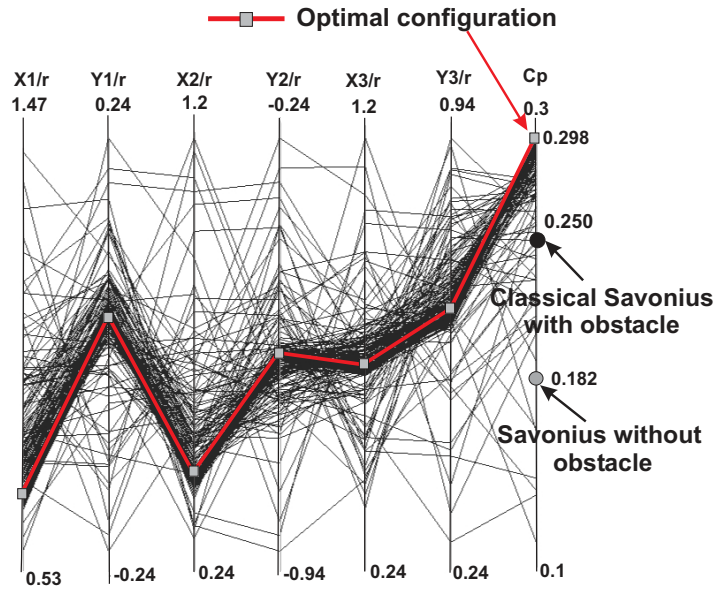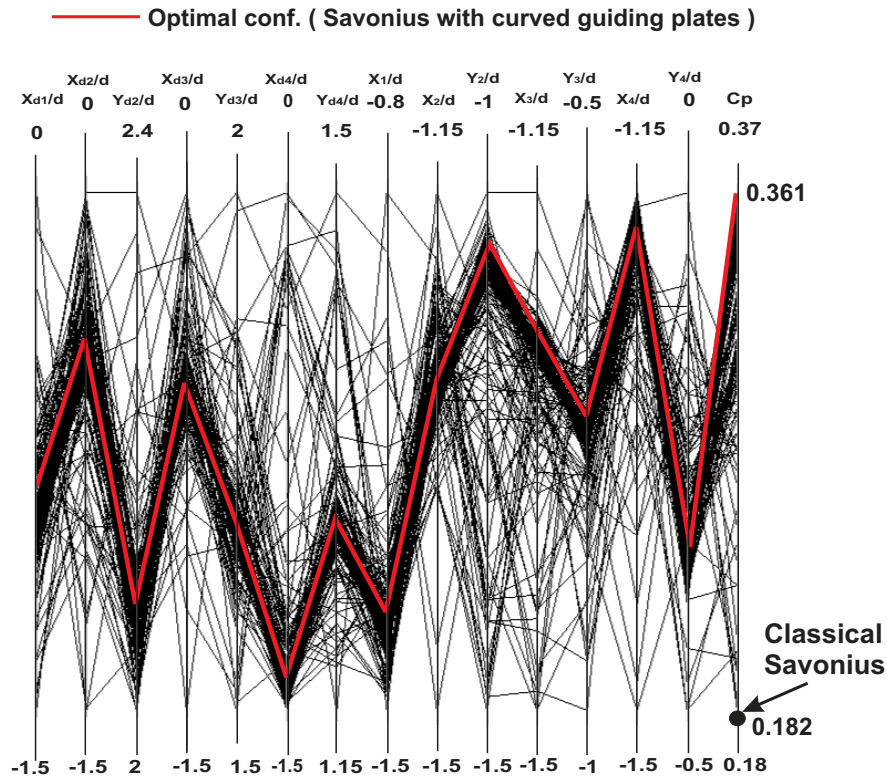
Figure 6.43: Input parameters of the optimization and power coefficient represented using parallel coordinates. The parameters of the optimal designs are connected with a thick red line. The power coefficient of the conventional turbine is shown with a black circle.

mize sixteen parameters simultaneously; eight parameters for both guiding plates (X_1, Y_1, X_2, Y_2, X_{d1}, Y_{d1}, X_{d2} and Y_{d2}, see Fig. 6.45a), considered flat for the reasons explained in the previous section. The blade shape is described by five points, two fixed points (P_4 and P_5) and three movable points (P_1, P_2, P_3). Every point has two coordinates (X_{Pi}, Y_{Pi}) this means we have another six free parameters ($X_{P1}, Y_{P1}, X_{P2}, Y_{P2}, X_{P3}$ and Y_{P3} Fig. 6.45b). Knowing all 5 points, the full profile is reconstructed using standard splines. Another two parameters will taken into consideration for internal spaces of the turbine (a and e see Fig. 6.45c). The objective function considers only one output of the simulation that should be maximized as far as possible: the output power coefficient C_p. The employed optimization parameters have been listed in chapter 5.

The parameter space considered in the optimization has been defined as documented in Table 6.14.

Optimization results are shown in Fig. 6.46. 310 different geometrical settings have been evaluated by CFD, requesting two and a half months of total computing time on a standard PC for this ambitious analysis.

The optimal configuration (highest point in the right column in Fig. 6.46, all corresponding parameters being connected by a thick red line) can now readily be identified
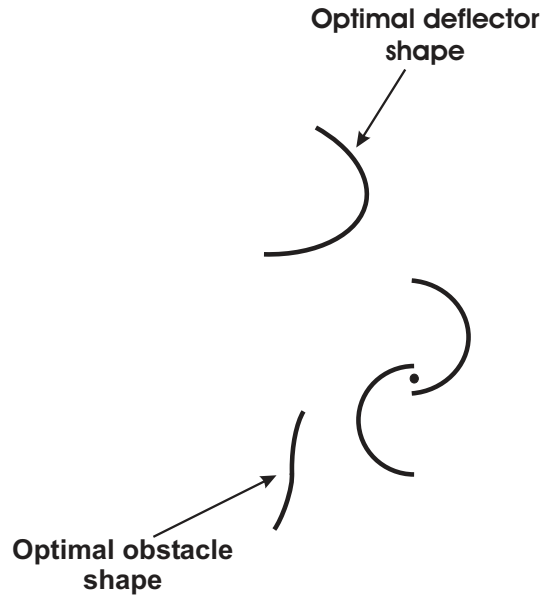
Figure 6.44: Optimum configurations of curved guiding plates.

Table 6.14: Acceptable range for the input parameters (parameter space)

Parameter	Minimum	Maximum
Blade shape		
X_{P1}/r	0.53	1.47
Y_{P1}/r	−0.24	0.24
X_{P2}/r	0.24	1.2
Y_{P2}/r	−0.94	−0.24
X_{P3}/r	0.24	1.2
Y_{P3}/r	0.24	0.94
Guiding plates		
X_{d1}/d	−1.04	0
Y_{d1}/d	0.9	1.87
X_{d2}/d	−1.66	0
Y_{d2}/d	1.3	1.87
X_1/d	−1.66	−0.9
Y_1/d	−0.78	0
X_2/d	−1.66	−0.9
Y_2/d	−1.66	−0.53
Internal spaces		
a/d	−0.09	0.18
e/d	0.05	0.28

for $\lambda = 0.7$. The optimum parameters are listed in Table 6.15, leading to the correspond-
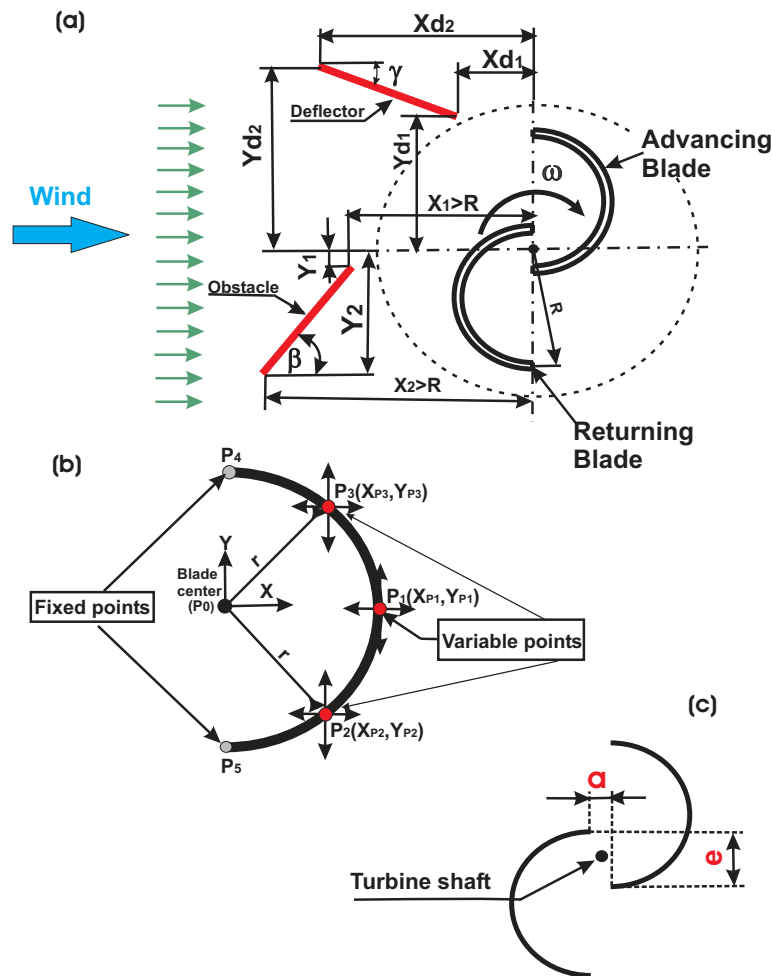
Figure 6.45: Schematic description of the geometry and free optimization parameters.

ing angles of 90.41° and 94.13° for obstacle and deflector, respectively. The lengths of the guiding plates are $L_o/d = 0.7597$ and $L_d/d = 1.048$, as shown in Fig. 6.47.

Note that this new shape (Fig. 6.47) is only optimum in combination with the employed guiding plates. Indeed, the modified shape exploits best the flow redirection induced by the guiding plates. As a consequence, the reverse moment is reduced by the shielding obstacle and the flow redirected by the deflector to the advancing blade; simultaneously, the modified shape leads to an increase of the positive moment of the advancing blade.

One instantaneous picture of the flow field (pressure, velocity magnitude and velocity vectors) is shown as an example in Fig. 6.48 for the finally optimized design and for the classical semi-cylindrical turbine with guiding plates, demonstrating that the employed CFD captures all important flow features in the vicinity of the rotor and guiding plates. This is of course a dynamic process, difficult to illustrate in a static figure. The pressure difference obtained for the optimal design is much larger, explaining the better
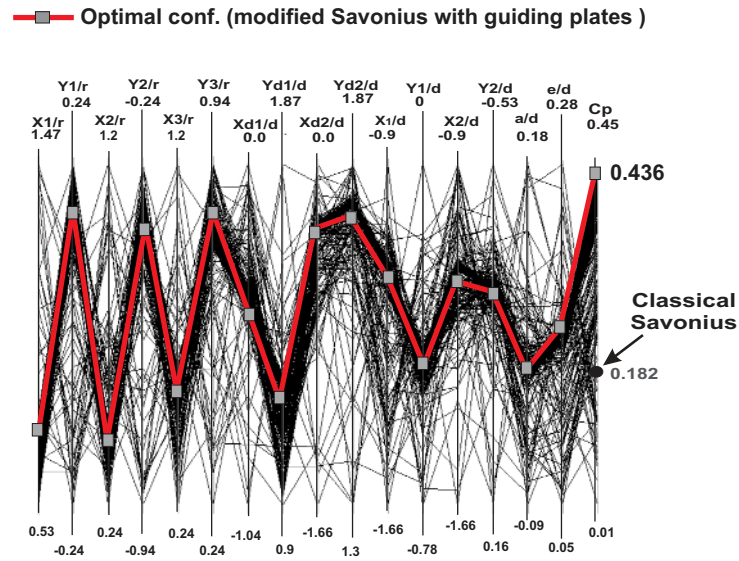
Figure 6.46: Input parameters of the optimization and power coefficient represented using parallel coordinates. The parameters of the optimal design are connected with a thick red line. The power coefficient of the conventional turbine is shown with a black circle.

Table 6.15: Optimum configurations

Blade shape	
X_{P1}/r	0.54822
Y_{P1}/r	0.19762
X_{P2}/r	0.34849
Y_{P2}/r	-0.37885
X_{P3}/r	0.54593
Y_{P3}/r	0.770346
Guiding plates	
X_{d1}/d	-0.41882
Y_{d1}/d	1.24505
X_{d2}/d	-0.3433
Y_{d2}/d	2.29074
X_1/d	-1.2828
Y_1/d	-0.4037
X_2/d	-1.27654
Y_2/d	-1.16339
Internal spaces	
a/d	-0.00635
e/d	0.18286
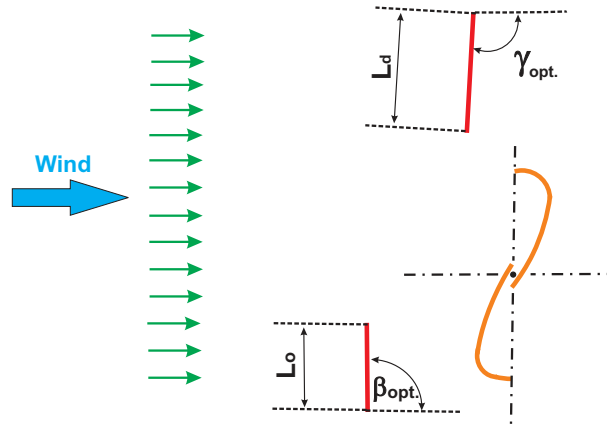
Figure 6.47: Optimum design of Savonius turbine with guiding plates.

performance.

6.5.1   Off design performance

It is now important to check how this gain would change as a function of λ, since such a turbine must be able to work also for off-design conditions. Therefore, the performance of the optimal configuration has been finally computed for the full range of useful λ-values, as shown in Fig. 6.49. This figure demonstrates that the improvement of both torque coefficient and power output coefficient is observed throughout for all values of λ, compared to the conventional Savonius turbine. The absolute gain for C_p and C_m is even higher for lower λ-values. The relative performance increase compared to the standard Savonius configuration is always higher than 40% in the effective operating range.

6.5.2   Self-starting capability

To investigate the self-starting capability of the system, the static torque exerted on a turbine at a fixed angle has been computed by CFD as a function of this angle θ. Figure 6.50 shows the obtained static torque coefficient C_{ms} obtained for the optimal configuration compared to the classical turbine, as a function of θ. The experimental results of [38] for a conventional turbine are again shown for comparison. Compared to the classical Savonius, these computations demonstrate that the new design has a considerable and positive effect on the static torque coefficient. For the optimal configuration the negative torque region completely disappears, with a minimum value of C_{ms} of about 0.2. A self-starting capability ($C_{ms} > 0$) is always obtained at any angle in both cases, which is an essential property.

Pressure distribution

Velocity vector distribution

Velocity distribution
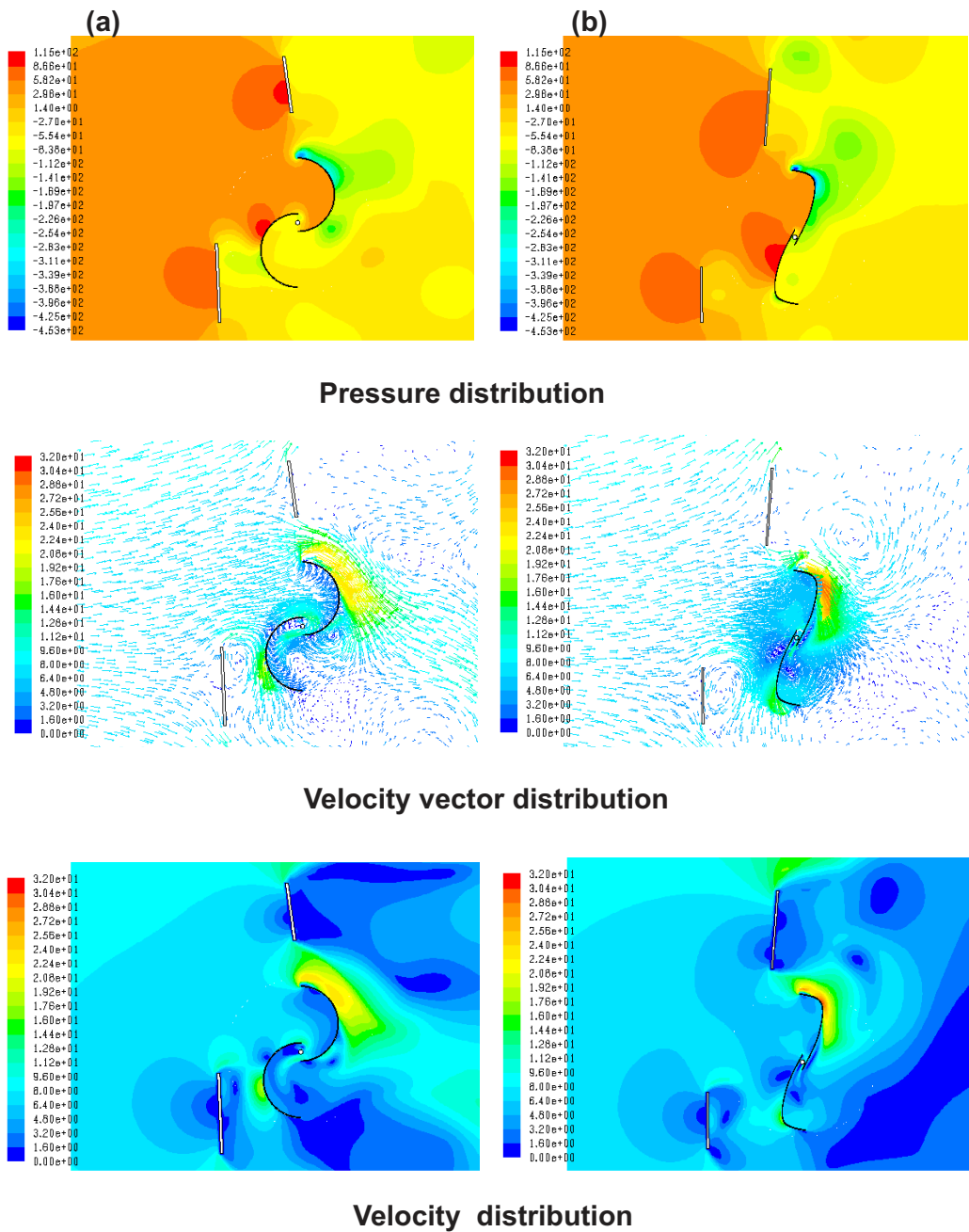
Figure 6.48: Instantaneous flow fields around optimum configurations (zoom) at the design point ($\lambda = 0.7$), static pressure (Pa), velocity and velocity vector magnitudes (m/s); a) classical Savonius with optimal guiding plates, b) optimal Savonius with optimal guiding plates. Note that the color scales are identical to facilitate comparisons.
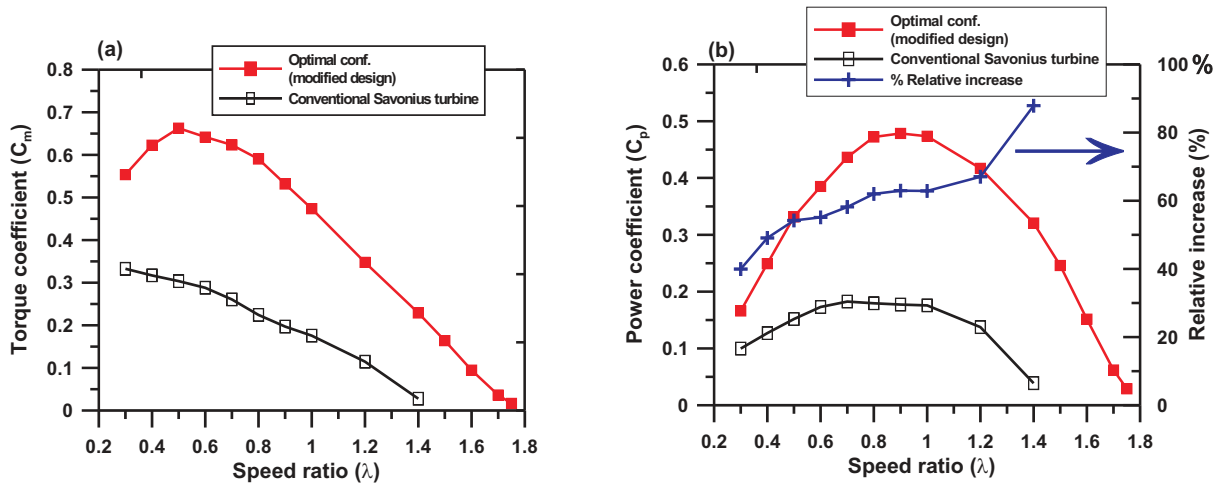
Figure 6.49: Performance of the optimized configuration (red line) compared to the conventional Savonius turbine (black line): a: torque coefficient; b: power coefficient. The corresponding relative increase compared to the classical configuration is shown with blue line.
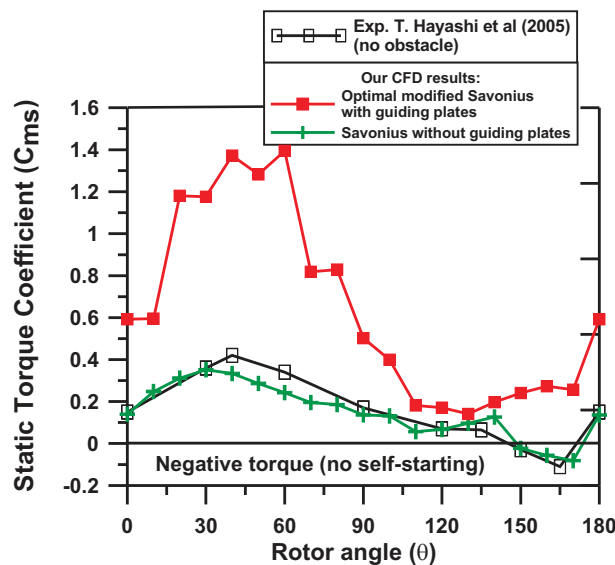
Figure 6.50: Static torque coefficient C_{ms} as a function of the fixed rotor angle θ for the optimal configuration compared to the conventional Savonius turbine. For this last case, the experimental results of [38] are also shown for comparison.

6.6 Preliminary experimental tests in wind-tunnel

It is now important to check the CFD results experimentally. Therefore, we have constructed two small models for Savonius turbine, one model for the conventional two-

blade Savonius and an other for the optimized shape with shielding obstacle. The main objective of this work is to check that the optimized design is superior to the original design.

**Installation of Savonius turbine
at the test section**

Figure 6.51: Model installation with open wind tunnel.

The wind tunnel operates with open or closed test section. The maximum flow rate for open test section is 40 m/s (Fig. 6.51). When closed, velocity up to nearly 60 m/s is possible. The setting of the load is carried out by a brake handle, fine-tuned by a screw. To get the torque / speed curve, the signal of the torque sensor was transmitted to a computer, which also is used to control the wind speed of the wind tunnel. The software used for both tasks is LabView.

Five test series were run for each rotor design. Before each measurement the off set of the torque sensor was set to zero. The model has been submitted to increasing wind speed, self-starting, until a nominal wind speed of 20 m/s was achieved. Once the rotor speed reaches a constant value, the load was progressively increased. Then, output torque and rotation speed of the rotor have been recorded at every load to get performance curves for the two designs.

First results (Fig. 6.52) indeed show increased power coefficient and torque coefficient for the optimized design.

Technical difficulties (limited accuracy of the torque meter, vibrations of the set-up, rapid wear of the employed brake) have prevented up to now a more thorough comparison.

6.7 Conclusions on Savonius turbine

The conventional Savonius turbine is a promising concept for small-scale wind-energy systems, but suffers from a poor efficiency. Therefore, the major objective of the present
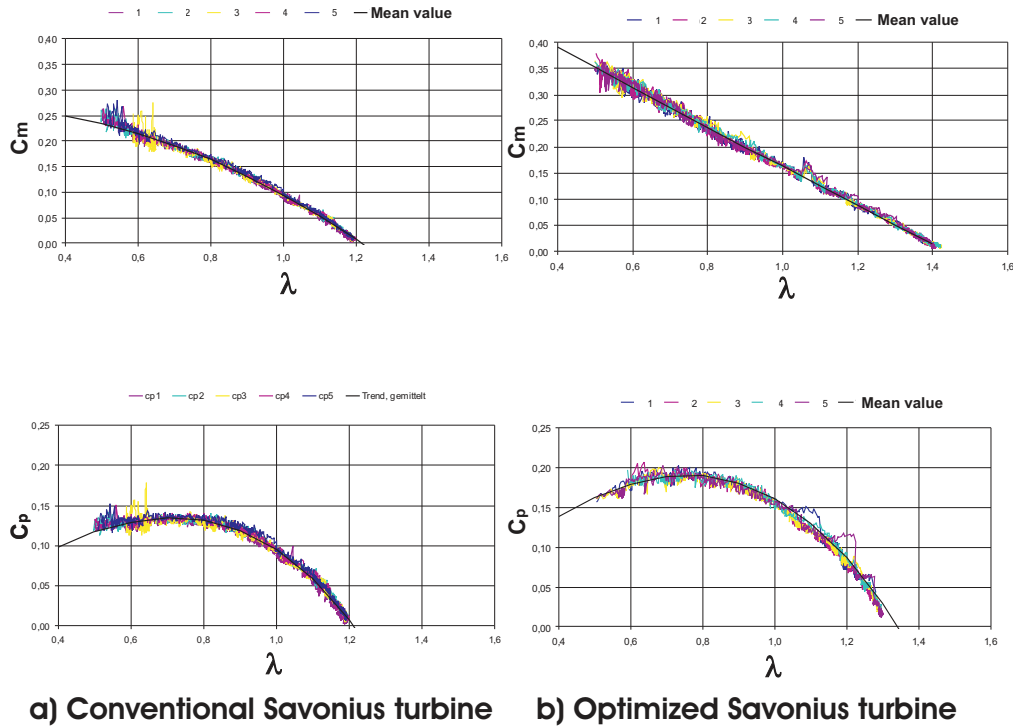
Figure 6.52: Selected experimental results [64] a) conventional Savonius turbine; b) Optimized design.

study was to identify an optimal design, leading to higher values of the power coefficient and of the static torque, thus obtaining a higher efficiency and better self-starting capability. For this purpose, many designs have been successively introduced and optimized in this chapter.

- **Three-blade Savonius turbine**

  After some preliminary steps, all the geometrical parameters are simultaneously taken into consideration during optimization. Therefore, the blade shape, position and angles of the guiding plates and gap width have been optimized in a fully automatic manner, in order to obtain the best possible performance, as measured by the power coefficient C_p. The optimization relies on evolutionary algorithms, while all geometrical configurations are evaluated by CFD. This optimization procedure is able to identify considerably better configurations than the conventional three-blade Savonius turbine. The best one leads in particular to a relative increase of the power output coefficient by 57% at $\lambda = 0.7$. A performance gain of at least 25% is found for the full operating range of the conventional design. At the same time, the operating range is extended up to $\lambda = 1.5$. A peak power coefficient of $C_p \simeq 0.39$ is obtained for $\lambda = 0.9$. This positive effect is also observed for the torque coefficient. The optimal design still ensures self-starting capability for all rotating angles.

- **Two-stage Savonius turbine**
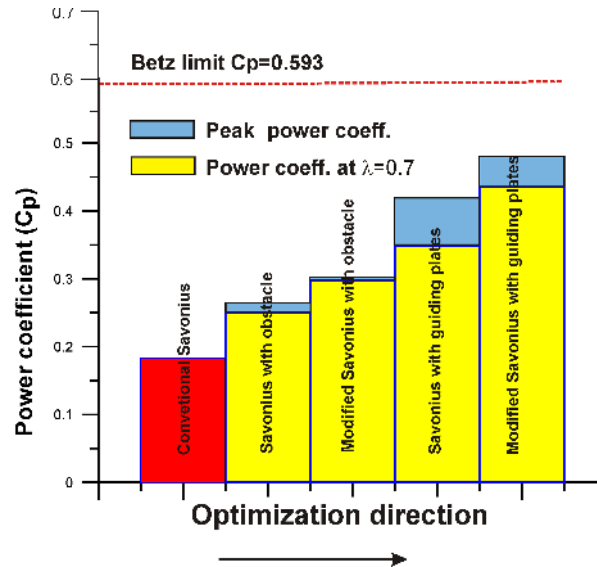
Figure 6.53: Successive optimization steps for the two-blade Savonius turbine.

Here again, preliminary steps have been followed by an optimization involving all important parameters. This optimization procedure is able to identify a tremendously better configuration than the conventional Savonius turbine, leading in particular to a relative increase of the power output coefficient by 58% at $\lambda = 0.7$. A performance gain of at least 35% is found for the full conventional operating range ($0.3 \leq \lambda \leq 1.4$). The optimal design shows a much larger range and still delivers power at $\lambda = 1.7$. This positive effect is also observed for the torque coefficient. The optimal design furthermore leads to self-starting capability at any angle, at the difference of the conventional Savonius. Therefore, this optimal configuration appears indeed to be very promising for low-power wind energy generation in urban areas.

The successive steps of the optimization are documented in Fig. 6.53. At $\lambda = 0.7$, the power coefficient has been increased from $C_p \simeq 0.18$ to $C_p \simeq 0.44$ thanks to optimization. For the best design, a peak C_p of 0.48 is obtained for $\lambda = 0.9$, approaching Betz' limit.

As a whole, and supporting previous findings from the literature, the two-blade design appears superior to the three-blade configuration in terms of low weight, cost, as well as efficiency and operating range. Self-stating capabilities are similar, with only a very slight advantage for the three-blade design. Therefore, the optimized two-blade configuration should indeed be very useful to supplement wind energy conversion.

Chapter 7

Wells turbine: Concurrent optimization

7.1 Introduction

Wells turbine is a self-rectifying air flow turbine employed to convert the pneumatic power of the air stream induced by an Oscillating Water Column into mechanical energy. Standard Wells turbines have several well-known disadvantages: a very low tangential force, leading to a low power output from the turbine; a high undesired axial force; usually a low aerodynamic efficiency and a limited range of operation due to stall. All the theoretical and experimental investigations listed in the section 3.2.3 only considered the performance of Wells turbines using standard symmetric airfoils of type NACA 00XX. As an illustration, Fig. 7.1 shows NACA 0015 and NACA 0021. Most investigations pertaining to Wells turbines have considered NACA 0012, NACA 0015, NACA 0018 and NACA 0021 (e.g., [73, 81, 91, 93]). The formula for the shape of a NACA 00XX foil, with "XX" being replaced by the percentage of maximum thickness to chord length c, is

$$y = \frac{ct}{0.2}\left[0.2969\sqrt{\frac{x}{c}} - 0.126\left(\frac{x}{c}\right) - 0.3517\left(\frac{x}{c}\right)^2 + 0.2843\left(\frac{x}{c}\right)^3 - 0.1015\left(\frac{x}{c}\right)^4\right] \quad (7.1)$$

where x is the position along the chord from 0 to c, y is the half-thickness at a given value of x (centerline to external surface), and t is the maximum half-thickness as a fraction of the chord (so that 100 t gives a half of the last two digits in the NACA 4-digit denomination). Both monoplane and two-plane Wells turbines are considered in the literature and show different advantage and drawbacks. As a consequence, it is interesting to optimize both designs separately, starting with the simple configuration.

7.2 Optimal monoplane Wells turbine

Reference investigations indicated that NACA 0021 airfoil profiles (21% thickness) lead to the best performance for conventional monoplane Wells turbines [93]. There is nev-
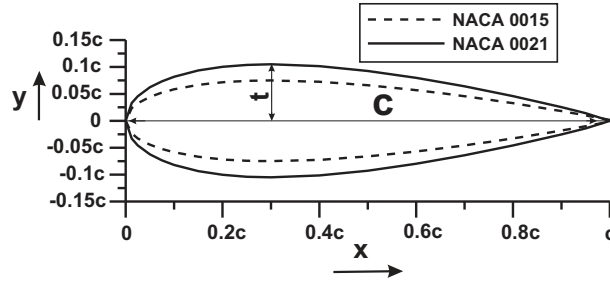
Figure 7.1: Standard airfoils NACA 0015 and NACA 0021.

ertheless no proof that NACA profiles, as defined by Eq. 7.1, automatically lead to the best possible performance. An alternative geometry might be much better, in particular for such very specific applications. As a consequence, the present section now concentrates on the optimization of a symmetric airfoil shape, leading to the best possible performance of a Wells turbine (i.e., maximal tangential force coefficient and efficiency). Due to the complexity of the underlying optimization procedure, this first study considers only monoplane Wells turbines (the original design) and a constant turbine solidity ($s = 0.67$, as proposed by [110]), while taking into account the mutual interaction effect between the blades.
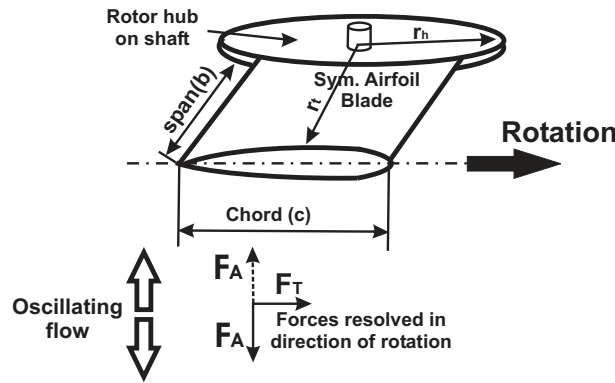
Figure 7.2: Axial and tangential forces acting on a Wells turbine.

In the present section, the free design variables considered for the optimization will be the shape of the blade using a constant solidity ($s = zc/[\pi r_t(1 + h)]$) where h is the ratio between hub radius r_h and tip radius r_t (Fig. 7.2). The objective function contains simultaneously two outputs of the simulation, that should both be maximized as far as possible: the tangential force coefficient C_T; and the turbine efficiency η, which is inversely proportional to the axial force coefficient, and is defined for a negligible density change as:

$$\eta = \frac{F_T\, u_t}{\Delta p_0\, Q} \qquad (7.2)$$

with Q the volumetric flow-rate through the turbine. For configurations involving concurrent objectives, Evolutionary Algorithms are particulary robust and have therefore been used in the present study. The employed optimization parameters are listed in Table 5.1.

7.2.1 Optimization of airfoil shape

After having checked the accuracy of an individual evaluation relying on CFD as described in section 5.3.2.3, it is now possible to start the optimization procedure. As explained previously, only symmetric blades are considered in what follows, based on the profile NACA 0021 for a first guess.

To illustrate the optimization, a fixed angle of incidence $\alpha = 8°$ (flow coefficient $\phi = 0.14$) is considered. Twenty-two free parameters are varied simultaneously by the OPAL optimizer, explaining the difficulty of the process. In the present case the outer boundary of the airfoil (or airfoil shape) is constructed with thirteen points; two fixed points (P_1 and P_{13}) and eleven variable points (P_2, P_3, P_4, P_5, P_6, P_7, P_8, P_9, P_{10}, P_{11} and P_{12}) as shown in Fig. 7.3. Knowing the exact position of these 13 points, the full profile is finally reconstructed for one face of the airfoil using standard splines (Nonuniform rational B-splines, NURBS). The order of a NURBS curve defines the number of nearby control points that influence any given point on the curve. The curve is represented mathematically by a polynomial of degree one less than the order of the curve; this means that the spline order is 13 in our case. Then, the obtained face is mirrored to obtain the full symmetric airfoil. Every point P_2 to P_{12} has two coordinates (X_{pi}, Y_{pi}), where $i = 2 \dots 12$. The parameter space considered in the optimization has been defined as documented in Table 7.1 and illustrated in Fig. 7.3. The corresponding parameter spaces have been selected to cover all usual NACA 00XX, while avoiding collisions between reference points and keeping acceptable geometries. The reference point is point $P_1(0,0)$, origin of the cartesian coordinate system.
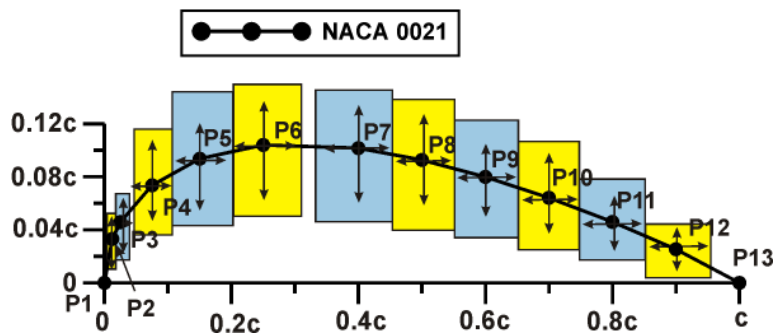
Figure 7.3: Allowed parameter space for the moving points P_2 to P_{12}.

Table 7.1: Parameter space for the moving points P_2 to P_{12} for monoplane Wells turbine.

Point	Parameter	Minimum	Maximum	Point	Parameter	Minimum	Maximum
P_2	X_{P2}/c	0.01	0.015	P_8	X_{P8}/c	0.45	0.55
	Y_{P2}/c	0.023	0.043		Y_{P8}/c	0.043	0.143
P_3	X_{P3}/c	0.015	0.035	P_9	X_{P9}/c	0.55	0.65
	Y_{P3}/c	0.025	0.066		Y_{P9}/c	0.039	0.11
P_4	X_{P4}/c	0.05	0.1	P_{10}	X_{P10}/c	0.65	0.75
	Y_{P4}/c	0.034	0.11		Y_{P10}/c	0.034	0.094
P_5	X_{P5}/c	0.1	0.2	P_{11}	X_{P11}/c	0.75	0.85
	Y_{P5}/c	0.043	0.143		Y_{P11}/c	0.026	0.066
P_6	X_{P6}/c	0.2	0.3	P_{12}	X_{P12}/c	0.85	0.95
	Y_{P6}/c	0.054	0.154		Y_{P12}/c	0.015	0.035
P_7	X_{P7}/c	0.35	0.45				
	Y_{P7}/c	0.052	0.152				

As a whole, the optimization process thus involves twenty two parameters (or degrees of freedom) X_{pi} and Y_{pi} with $i = 2 \ldots 12$ and two objectives (efficiency and tangential force coefficient) that should be simultaneously maximized in a concurrent manner.

The results presented in Figs. 7.4(a) and 7.4(b) indicate that the two considered objectives are indeed considerably influenced by the airfoil shape. Figure 7.4(a) shows all evaluation results. As a whole, 615 different configurations have been finally tested by the optimizer, leading to 15 days of total computing time on a standard PC. In Fig. 7.4(a) the performance of the standard airfoil NACA 0021 (tangential force coefficient and efficiency $(C_T, \eta) = (0.1163;\ 0.5109)$) is also plotted for comparison. Globally, the two considered objectives are not fully concurrent but increase simultaneously, which is not a complete surprise since the tangential force appears on the numerator in Eq. 7.2 defining the efficiency.

When considering now only the best configurations of Fig. 7.4(a), located in the upper-right corner (marked by a red square in dashed line), a more complex picture appears, as documented in Fig. 7.4(b). For the last percent of performance improvement, the two objectives (tangential force coefficient and efficiency) become indeed slightly concurrent and cannot be optimized simultaneously. Two optimal conditions are finally found: Point A, $(C_{T_A}, \eta_A) = (0.1325; 0.5187)$ (highest tangential force); and Point B, $(C_{T_B}, \eta_B) = (0.1281; 0.5197)$ (highest efficiency). By analyzing in detail the resulting geometries and considering daily engineering purposes, the increase in tangential force coefficient (higher power output) appears to be more significant and valuable than the very slightly increased efficiency. Therefore, the most interesting point is globally Point A with $(C_{T_A}, \eta_A) \approx (0.1325;\ 0.519)$.

The results of the optimization process can be usefully visualized in a different manner using parallel coordinates (Fig. 7.5). Here again, the performance of the standard airfoil NACA 0021 is also plotted for comparison, close to the middle of the parameter space (thick dashed blue line). Figures 7.5(a) and 7.5(b) indicate by parallel coordinates
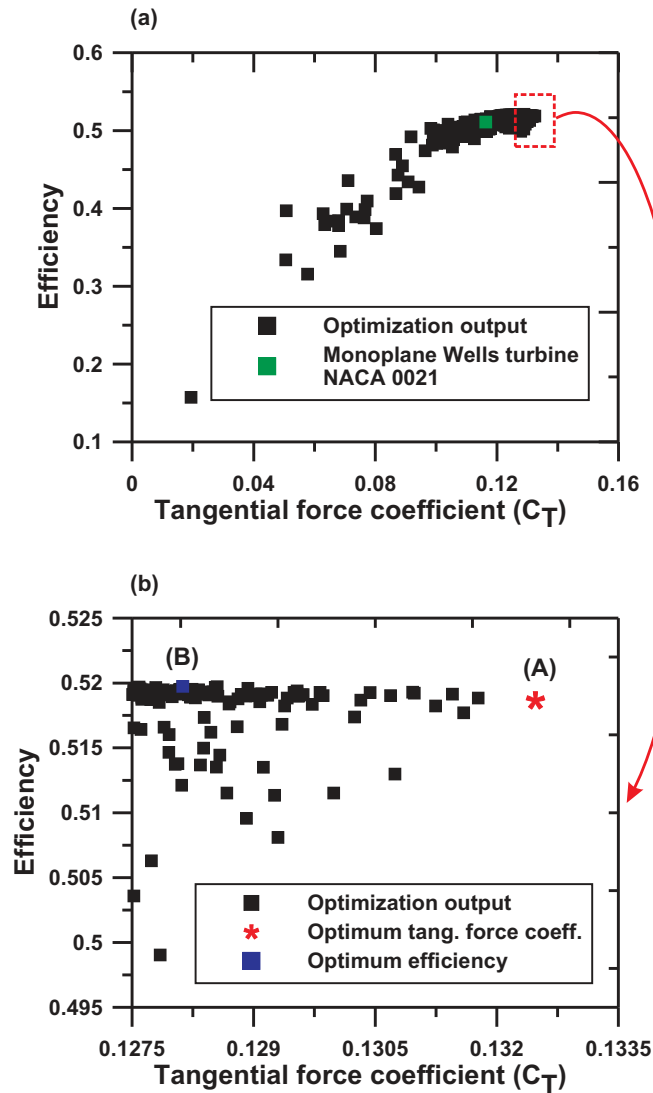
Figure 7.4: Objectives of the optimization; a) for all computed configurations b) for the best configurations (i.e., zoom on the upper-right part (red square) of a).

the X and Y coordinates of the eleven moving points $(P_2 \dots P_{12})$, together with the two objectives. This figure demonstrates that very different shapes have been evaluated on the way toward the optimal solution. The optimum configuration (Point A) is indicated by a thick red line.

It can be seen that the optimal airfoil shape leads only to a slightly higher efficiency (+0.78%) compared to the standard airfoil (NACA 0021). However, the tangential force coefficient C_T is at the same time increased by 0.0162. This means a relative increase of 12.2% for the present flow coefficient, equal to 0.14.

The geometrical parameters corresponding to the optimal shape are listed in Table 7.2. The resulting shape of the optimal airfoil in comparison with the standard
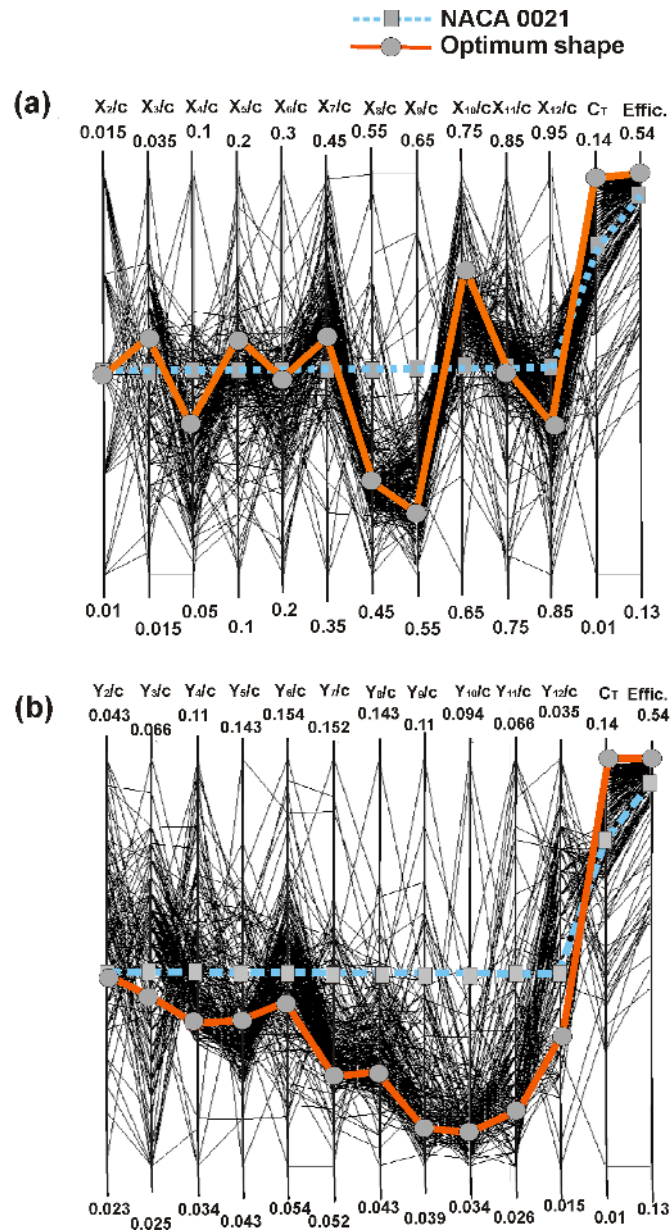
Figure 7.5: Input parameters of the optimization and objectives represented using parallel coordinates. The parameters of the optimal shape are connected with a thick red line. The standard design (NACA 0021) is shown with a thick dashed blue line; a) X-coordinates of the variable points $(P_2 \ldots P_{12})$; b) Y-coordinates of the variable points $(P_2 \ldots P_{12})$.

NACA 0021 is shown in Fig. 7.6. Knowing all points P_1 to P_{13}, the full profile is again reconstructed using standard splines of order 13. Nevertheless, a simple polynomial description of this profile would be helpful for practical purposes. An excellent fit (average

Table 7.2: Optimum shape parameters for monoplane Wells turbine

Point	Parameter	Value	Point	Parameter	Value
P_2	X_{P2}/c	0.0124947	P_8	X_{P8}/c	0.469922
	Y_{P2}/c	0.033155		Y_{P8}/c	0.0666932
P_3	X_{P3}/c	0.0269924	P_9	X_{P9}/c	0.56625
	Y_{P3}/c	0.045006		Y_{P9}/c	0.0493063
P_4	X_{P4}/c	0.0678583	P_{10}	X_{P10}/c	0.723109
	Y_{P4}/c	0.0608499		Y_{P10}/c	0.037401
P_5	X_{P5}/c	0.155326	P_{11}	X_{P11}/c	0.798623
	Y_{P5}/c	0.078402		Y_{P11}/c	0.0315091
P_6	X_{P6}/c	0.248998	P_{12}	X_{P12}/c	0.8891079
	Y_{P6}/c	0.0877814		Y_{P12}/c	0.0214618
P_7	X_{P7}/c	0.405838			
	Y_{P7}/c	0.0751153			

residual error of 0.38%) has been obtained with following polynomial description:

$$\frac{Y}{c} = A\left(\frac{X}{c}\right)^5 + B\left(\frac{X}{c}\right)^4 + D\left(\frac{X}{c}\right)^3 + E\left(\frac{X}{c}\right)^2 + H\left(\frac{X}{c}\right) + K \qquad (7.3)$$

with the constants A to H listed in Table 7.3. Furthermore, this polynomial removes any possible oscillations of the profile shape induced by the spline description.

Table 7.3: Polynomial coefficients of optimal airfoil shape (best fit)

A	B	D	E	H	K
1.6958588	-5.4277515	6.560073	-3.737973	0.898334	0.01409362
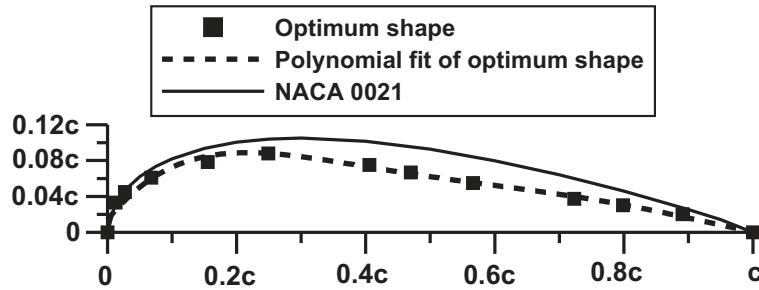
Figure 7.6: Comparison between the original profile NACA 0021 (solid line), the optimal airfoil shape described by splines (black squares showing the position of the control points) and the corresponding polynomial fit (Eq. 7.3, dashed line).

7.2.2 Off design performance

It is important to check how the gain induced by the new airfoil shape would change as a function of the flow coefficient ϕ, since such a turbine must be able to work also for off-design conditions. Therefore, the performance of the optimal shape has been finally computed for the full range of useful ϕ-values, as shown in Fig. 7.7. These results demonstrate that the improvement of tangential force coefficient is observed throughout for all values of ϕ, compared to the conventional turbine based on standard airfoils NACA 0021. The absolute gain for C_T increases even slightly with ϕ. The relative increase is higher than 8.8% throughout the useful operating range, with an average gain of 11.3% (Fig. 7.7a). At the same time the efficiency of the optimized shape is always higher than for the conventional design, the difference being lower for large flow coefficients. The corresponding gain varies between 0.2% and up to 3.2%, with an average increase of 1% (Fig. 7.7b). No significant difference is observed in Fig. 7.7 between the performance of the exact profile described by splines and the associated polynomial fit (Eq. 7.3).

7.3 Optimal two-stage Wells turbine with non-symmetric airfoils

In this section we investigate extensively the potential of non-symmetric airfoil blades to improve the tangential force and efficiency associated to a two-stage Wells turbine. Since these two stages are mirrored, the system stays globally symmetric, as requested. Non-symmetric blades could perhaps allow to increase considerably the power output from the turbine and the global efficiency of the system.

All published results concerning the flow field around a Wells turbine rotor indicate that a considerable amount of exit kinetic energy is lost with the swirl component of the flow velocity, at least in the absence of guide vanes (see Section 3.2.3). This kinetic energy can be partly recovered by using a second stage of blades. Two-stage Wells turbine have been already investigated experimentally and theoretically [21, 61, 66, 80, 107], but considering only symmetric airfoils. The present work concentrates on a modified, two-stage Wells turbine constructed from non-symmetric airfoils based initially on NACA 2421. The two stages are mirrored to keep the global symmetry of the turbine as shown in Fig. 7.8.

The performance of the two-stage rotor is modified by mutual aerodynamic interferences due to the proximity of the two planes. The upstream rotor affects the performance of the downstream rotor by producing a deflection of the air stream. Therefore, the gap between the two rotors is an important parameter to control performance. Using numerical optimization, the solidity and the shape of the non-symmetric airfoils will be optimized in this section.
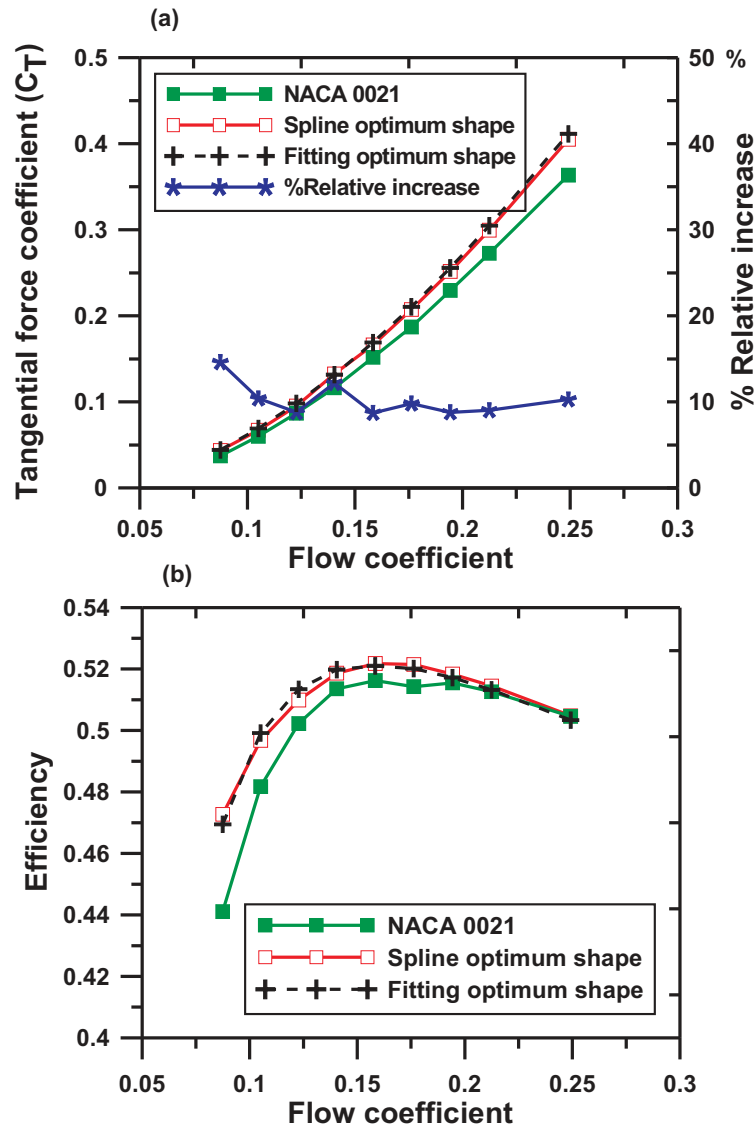
Figure 7.7: Performance of the spline optimal configuration (red line), fitting optimal one (black cross) compared to the conventional Wells turbine relying on the NACA 0021 profile (green line). The corresponding relative increase is shown with blue line; a) tangential force coefficient; b) efficiency.

7.3.1 Optimal airfoil shape without mutual interactions

In order to assess the potential of non-symmetric airfoils, a first optimization is carried out without mutual interactions between the blades. To illustrate the process, a fixed angle of incidence $\alpha = 12°$ (flow coefficient $\phi = 0.21$) is considered. Two degrees of freedom are left to the OPAL optimizer: the thickness factors y_1 for the upper side of the airfoil and y_2 for the lower side (see Fig. 7.8). These two factors are constrained by the user between 0.2 and 1.6, so that considerable variations are still allowed (both
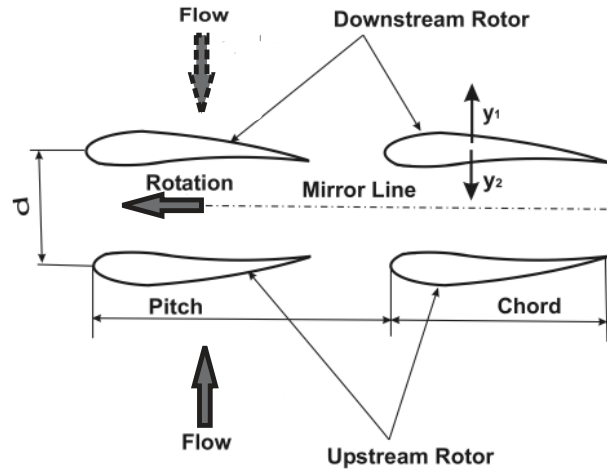
Figure 7.8: Two-stage Wells turbine based on non-symmetric airfoils

for increasing and decreasing thickness). All blades of both rotors are always modified simultaneously and the two rotors are still mirrored to preserve the global symmetry of the turbine. As a whole, the optimization process thus involves only two parameters y_1 and y_2 and two objectives (efficiency and tangential force coefficient) that should be simultaneously maximized in a concurrent manner.

The optimal point found in this first study, corresponds to the scaling factors $y_1 = 1.22966$ (23% thickening) for the upper face and $y_2 = 1.1795$ (18% thickening) for the lower face. The resulting shape of the optimal airfoil in comparison with the standard one is shown in Fig. 7.9.
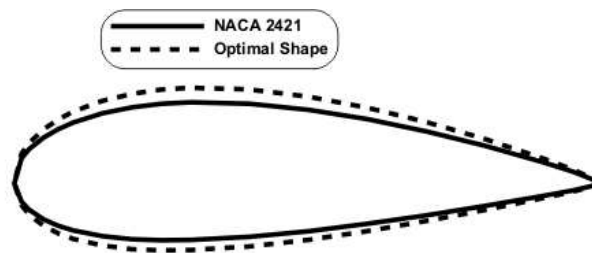
Figure 7.9: Comparison between the optimal shape of the airfoil and the original profile NACA 2421

When compared with the baseline case (NACA 2421) the optimal point corresponds simultaneously to a relative improvement of the efficiency by 2.1% and of the tangential force coefficient by almost 6%, demonstrating the interest of non-symmetric airfoils. However, mutual interactions could modify these results and must now be taken into

account.

7.3.2 Optimal airfoil shape with mutual interactions

7.3.2.1 Mutual interactions effect

The present section describes the optimization of the airfoil shape considering mutual interactions between the blades. A Wells turbine consisting of two mirrored airfoil stages is considered again. Mirroring is needed to keep the global symmetry of the system, as requested when using power from an Oscillating Water Column. But, in order to increase system efficiency, non-symmetric blades are considered. The influence of the mutual interactions between the blades building one plane (perpendicular to the main flow direction) are considered extensively in what follows.

The results of the previous section indicated that non-symmetric airfoils are better than symmetric ones. However, these results have been obtained neglecting any interactions between the blades. The validity of these first results is therefore questionable, since the performance of the two-stage Wells turbine is affected by mutual aerodynamic interaction between the blades in a single plane. This aerodynamic interaction results from the wakes produced by the preceeding blades and is a function of the angle of incidence of the air flow as well as of the solidity of the blades.

In the past, the influence of the mutual interaction between blades has been studied using wind-tunnel measurements or simple theoretical correlations relying on potential flow analysis and singularity theory for flat plate aerofoils in cascade [86]. According to such studies, the correlation factor m describing the ratio between the lift coefficient considering the interaction and the coefficient of an isolated flat plate is given by:

$$m = \left(\frac{2B}{\pi c}\right) \tan\left(\frac{\pi c}{2B}\right) \tag{7.4}$$

where c is the blade chord length and B is the pitch between the blades.

In this section, the interaction effect of the modified Wells turbine is investigated numerically in a systematic manner. The axial and tangential force coefficients normalized by the corresponding coefficients obtained for an isolated blade (single airfoil) have been computed for a constant gap ratio $G = 1$ (Fig. 7.10). The results demonstrate that both the normalized tangential and axial force coefficients increase exponentially with the solidity s due to the growing influence of wake effects. Increasing the tangential force is a positive aspect, but an increasing axial force is of course a major drawback.

The efficiency of the modified Wells turbine decreases very rapidly when increasing the solidity due to high losses, as shown in Fig. 7.11b. As the same time, the tangential force coefficient increases with the solidity (Fig. 7.11a).

This decrease in efficiency can be explained by the fact that the losses near the turbine hub are considerably higher than near the turbine tip, because the flow passage at the tip is much wider than the flow passage near the hub for a standard rectangular blade shape as shown in Fig. 7.12a. Therefore, we suggest to replace the rectangular shape of the blades by a trapezoidal shape as shown in Fig. 7.12b. This trapezoidal
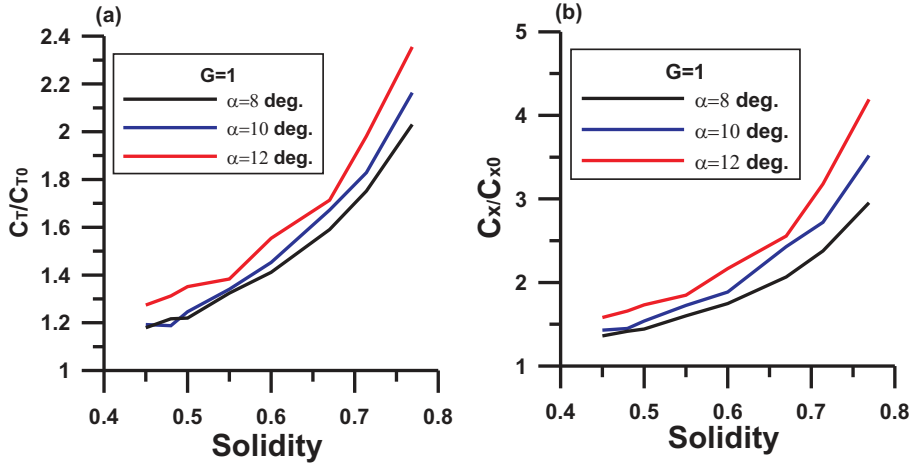
Figure 7.10: Impact of mutual interaction between blades in the same plane on a) tangential force (left) and b) axial force (right), as a function of the solidity.
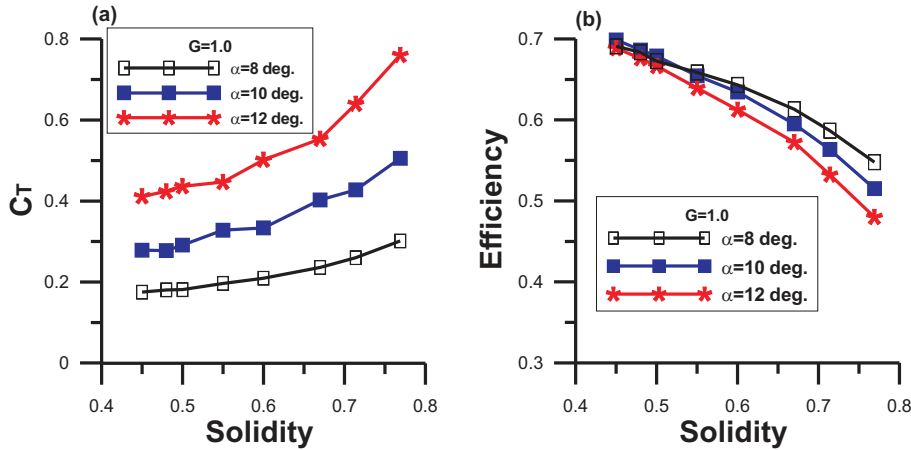
Figure 7.11: Impact of solidity on the two-stage Wells turbine performance considering the tangential force coefficient (a: left figure) and the turbine efficiency (b: right figure).

shape leads to the same passage at both hub and tip, and consequently such blades should give globally a better efficiency along the blade span (iso-performance blade). The best conditions should be obtained when the ratio between hub radius and tip radius equals the ratio between hub chord and tip chord:

$$\left(\frac{R_h}{R_t}\right) = \left(\frac{c_h}{c_t}\right) \tag{7.5}$$

Checking the performance of this modified design would unfortunately require three-dimensional CFD which are beyond reach when coupled with an optimizer. Therefore, this issue is left for future studies.
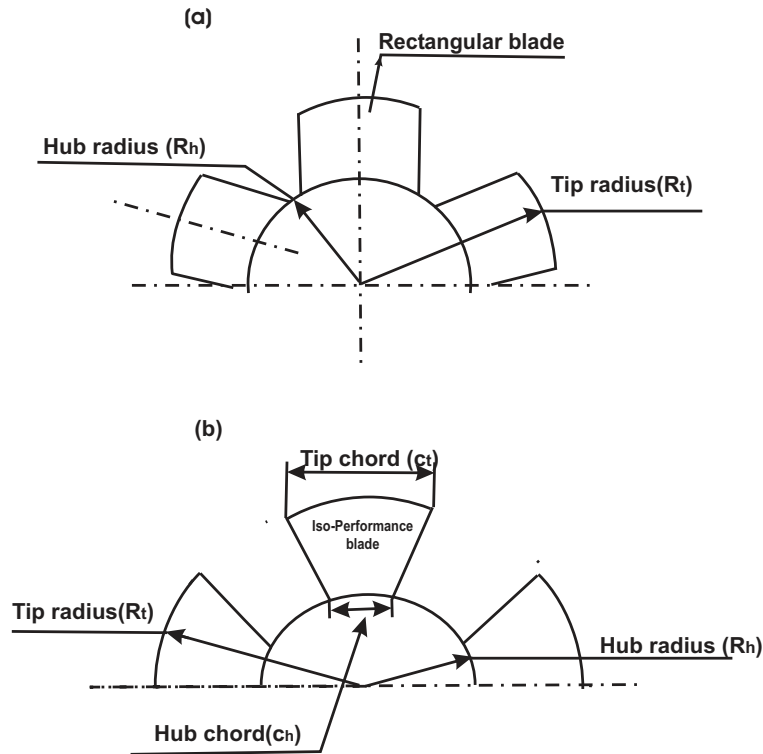
Figure 7.12: Projected shape of the turbine; a) Conventional turbine b) Suggestion of iso-performance turbine.

7.3.2.2 Optimization

Starting from NACA 2421, the present section concentrates on the optimization of a non-symmetric airfoil shape, leading to the best possible performance (as usual, maximal tangential force coefficient and efficiency) of a two-stage Wells turbine. A constant turbine solidity ($s = 0.67$, as proposed by [110]) and a constant gap between the rotors $G = d/c = 1.0$ are again considered, while taking into account the mutual interaction effect between the blades (see previous section). In the present case the outer boundary of the airfoil is constructed with thirty four points; two fixed points (P_0 and P_{17}) and thirty two variable points (sixteen variable points for every face of the airfoil, $P_1, P_2, P_3, P_4, P_5, P_6, P_7, P_8, P_9, P_{10}, P_{11}, P_{12}, P_{13}, P_{14}, P_{15}$ and P_{16} for upper face, $P_{18}, P_{19}, P_{20}, P_{21}, P_{22}, P_{23}, P_{24}, P_{25}, P_{26}, P_{27}, P_{28}, P_{29}, P_{30}, P_{31}, P_{32}$ and P_{33} for lower face) as shown in Fig. 7.13. Knowing the exact position of these 34 points, the full profile is reconstructed for each face of the airfoil using standard splines (NURBS). The parameter space considered in the optimization has been defined as documented in Table 7.4 and illustrated in Fig. 7.13. The corresponding parameter spaces have been selected to cover all usual NACA airfoils, while avoiding collisions between reference points and keeping acceptable geometries. The reference point is point $P_0(0,0)$, origin of the cartesian coordinate system.

Table 7.4: Parameter space for the moving points P_1 to P_{16} for upper face and P_{18} to P_{33} for lower face

Point	Parameter	Minimum	Maximum	Point	Parameter	Minimum	Maximum
P_1	X_{P1}/c	0.006	0.018	P_{18}	X_{P18}/c	0.006	0.018
	Y_{P1}/c	0.03	0.06		Y_{P18}/c	-0.03	-0.016
P_2	X_{P2}/c	0.018	0.032	P_{19}	X_{P19}/c	0.018	0.032
	Y_{P2}/c	0.03	0.07		Y_{P19}/c	-0.04	-0.025
P_3	X_{P3}/c	0.032	0.06	P_{20}	X_{P20}/c	0.032	0.06
	Y_{P3}/c	0.05	0.07		Y_{P20}/c	-0.055	-0.035
P_4	X_{P4}/c	0.06	0.08	P_{21}	X_{P21}/c	0.06	0.08
	Y_{P4}/c	0.07	0.13		Y_{P21}/c	-0.06	-0.045
P_5	X_{P5}/c	0.08	0.13	P_{22}	X_{P22}/c	0.08	0.13
	Y_{P5}/c	0.08	0.14		Y_{P22}/c	-0.076	-0.055
P_6	X_{P6}/c	0.13	0.17	P_{23}	X_{P23}/c	0.13	0.17
	Y_{P6}/c	0.1	0.15		Y_{P23}/c	-0.08	-0.06
P_7	X_{P7}/c	0.17	0.23	P_{24}	X_{P24}/c	0.17	0.23
	Y_{P7}/c	0.11	0.16		Y_{P24}/c	-0.08	-0.06
P_8	X_{P8}/c	0.23	0.27	P_{25}	X_{P25}/c	0.23	0.27
	Y_{P8}/c	0.11	0.17		Y_{P25}/c	-0.08	-0.06
P_9	X_{P9}/c	0.27	0.35	P_{26}	X_{P26}/c	0.27	0.35
	Y_{P9}/c	0.12	0.18		Y_{P26}/c	-0.075	-0.06
P_{10}	X_{P10}/c	0.35	0.45	P_{27}	X_{P27}/c	0.35	0.45
	Y_{P10}/c	0.12	0.17		Y_{P27}/c	-0.07	-0.055
P_{11}	X_{P11}/c	0.45	0.55	P_{28}	X_{P28}/c	0.45	0.55
	Y_{P11}/c	0.11	0.16		Y_{P28}/c	-0.06	-0.045
P_{12}	X_{P12}/c	0.55	0.65	P_{29}	X_{P29}/c	0.55	0.65
	Y_{P12}/c	0.1	0.15		Y_{P29}/c	-0.055	-0.035
P_{13}	X_{P13}/c	0.65	0.75	P_{30}	X_{P30}/c	0.65	0.75
	Y_{P13}/c	0.08	0.13		Y_{P30}/c	-0.04	-0.025
P_{14}	X_{P14}/c	0.75	0.85	P_{31}	X_{P31}/c	0.75	0.85
	Y_{P14}/c	0.06	0.09		Y_{P31}/c	-0.03	-0.016
P_{15}	X_{P15}/c	0.85	0.93	$P32$	X_{P32}/c	0.85	0.93
	Y_{P15}/c	0.03	0.06		Y_{P32}/c	-0.014	-0.01
P_{16}	X_{P16}/c	0.93	0.98	P_{33}	X_{P33}/c	0.93	0.98
	Y_{P16}/c	0.01	0.04		Y_{P33}/c	-0.009	-0.006

The results are presented in Fig. 7.14. As a whole, 615 different configurations have been tested by the optimizer, leading to 18 days of total computing time on a standard PC. In Fig. 7.14a the performance of the standard airfoil NACA 2421 (tangential force coefficient and efficiency (C_T, η)=(0.2074;0.4453)) is also plotted for comparison. Globally, the two considered objectives are not fully concurrent but increase simultaneously. When considering now only the best configurations of Fig. 7.14, located in the upper-right corner (marked by a red square), a more complex picture appears, as
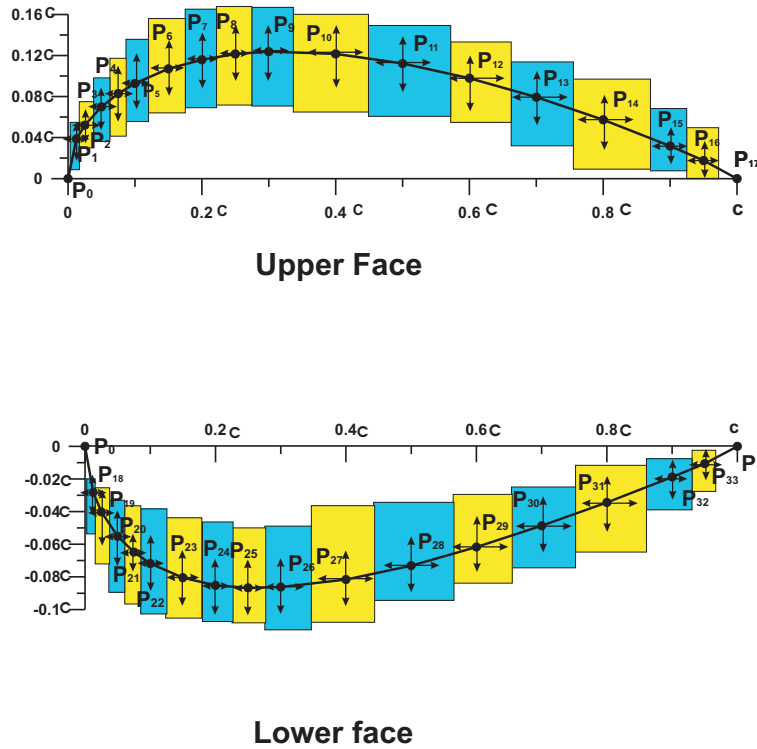
Figure 7.13: Allowed parameter space for the moving points.

in previous cases, with slightly concurrent objectives. Two optimal conditions are finally found: Point A, $(C_T, \eta) = (0.2247; 0.4482)$ (highest tangential force); and Point B, $(C_T, \eta) = (0.2212; 0.4506)$ (highest efficiency). As usual, the increase in tangential force coefficient (higher power output) appears to be more significant and valuable than the very slightly increased efficiency.

Therefore, the most interesting point is globally Point A with $(C_T, \eta) \simeq (0.225; 0.448)$. The results of the optimization process can be also visualized using parallel coordinates (Fig. 7.15). Figure 7.15a indicates by parallel coordinates the X and Y coordinates of the eleven moving points of upper face $(P_1 \ldots P_{16})$, together with the two objectives, while Fig. 7.15b shows by parallel coordinates the X and Y coordinates of the eleven moving points of lower face $(P_{18} \ldots P_{33})$, with the same two objectives.

This figure demonstrates that very different shapes have been evaluated on the way toward the optimal solution. The optimum configuration (Point A) is indicated by a thick red line. It can be seen that the optimal airfoil shape leads only to a slightly higher efficiency (+0.5%) compared to the standard airfoil (NACA 2421). However, the tangential force coefficient C_T is at the same time increased by 0.017, i.e., a relative increase of more than 7.7% for the present flow coefficient, equal to 0.14. The geometrical parameters corresponding to the optimal shape are listed in Table 7.5.

The resulting shape of the optimal airfoil in comparison with the standard NACA 2421 is shown in Fig. 7.16. Knowing all points P_0 to P_{33}, the full profile is again
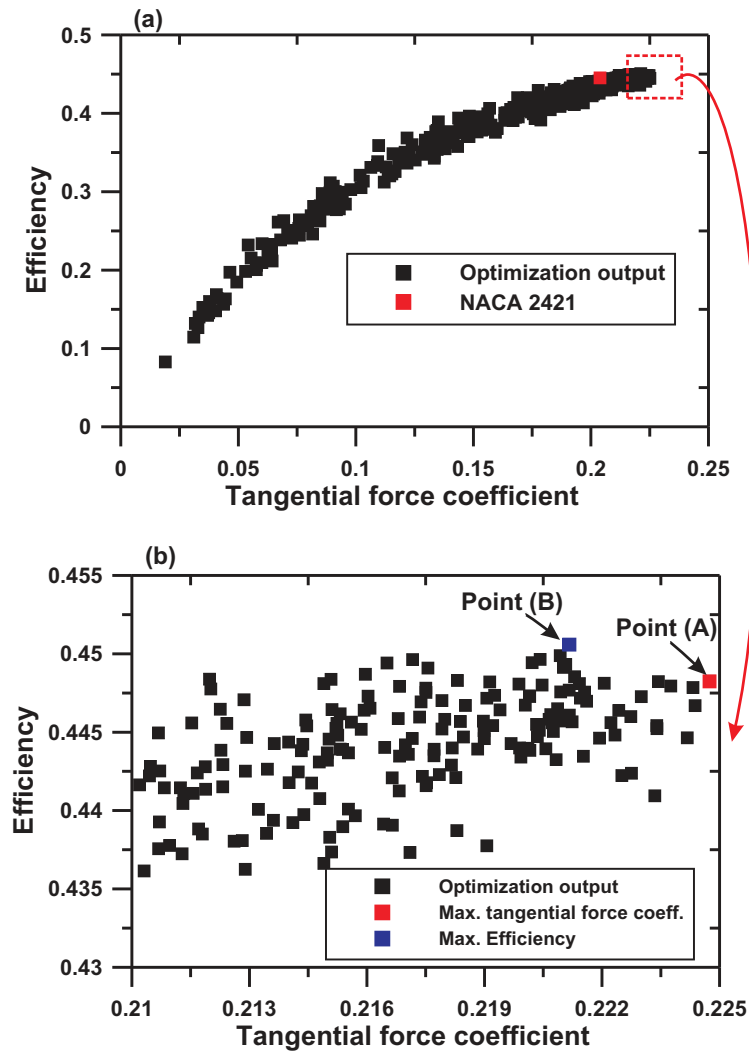
Figure 7.14: Objectives of the optimization: a) for all computed configurations; b) for the best configurations, i.e., zoom on the upper-right part (red square) of (a).

reconstructed using standard splines. Nevertheless, a simple polynomial description of these profiles is helpful for practical purposes. An excellent fit (average residual error of 0.3%) has been obtained using Eq. 7.3

with the constants A to H listed in Table 7.6 for the upper face and the lower face.

7.3.2.3 Off design performance

The results shown in Fig. 7.17 demonstrate that the improvement of tangential force coefficient is observed throughout for all values of ϕ, compared to the non-symmetric turbine based on standard airfoils NACA 2421, with an average increase of 5.5%. At the same time the efficiency of the optimized shape is slightly higher than the standard airfoil design. The corresponding gain varies between 0.2% and 0.7%, with an average

Figure 7.15: Input parameters of the optimization and objectives represented using parallel coordinates. The parameters of the optimal shape are connected with a thick red line.

Figure 7.16: Comparison between the original profile NACA 2421 (solid line) and the optimal airfoil shape (dashed line), considering mutual interaction between the blades.

Table 7.5: Optimum shape parameters for two-stage Wells turbine with non-symmetric airfoils

Point	Parameter	Value	Point	Parameter	Value	Point	Parameter	Value
P_1	X_{P1}/c	0.01129	P_{12}	X_{P12}/c	0.5748	P_{24}	X_{P24}/c	0.18961
	Y_{P1}/c	0.0405		Y_{P12}/c	0.125		Y_{P24}/c	-0.0653
P_2	X_{P2}/c	0.02179	P_{13}	X_{P13}/c	0.68696	P_{25}	X_{P25}/c	0.2485
	Y_{P2}/c	0.0527		Y_{P13}/c	0.09814		Y_{P25}/c	-0.06995
P_3	X_{P3}/c	0.0377	P_{14}	X_{P14}/c	0.7556	P_{26}	X_{P26}/c	0.3229
	Y_{P3}/c	0.06611		Y_{P14}/c	0.07551		Y_{P26}/c	-0.06117
P_4	X_{P4}/c	0.06938	P_{15}	X_{P15}/c	0.8759	P_{27}	X_{P27}/c	0.3846
	Y_{P4}/c	0.0928		Y_{P15}/c	0.0386		Y_{P27}/c	-0.0602
P_5	X_{P5}/c	0.1169	P_{16}	X_{P16}/c	0.9365	P_{28}	X_{P28}/c	0.5078
	Y_{P5}/c	0.1229		Y_{P16}/c	0.0149		Y_{P28}/c	-0.0584
P_6	X_{P6}/c	0.1372	P_{18}	X_{P18}/c	0.0096	P_{29}	X_{P29}/c	0.559
	Y_{P6}/c	0.1302		Y_{P18}/c	-0.02274		Y_{P29}/c	-0.0464
P_7	X_{P7}/c	0.1795	P_{19}	X_{P19}/c	0.0196	P_{30}	X_{P30}/c	0.6882
	Y_{P7}/c	0.1345		Y_{P19}/c	-0.03159		Y_{P30}/c	-0.0327
P_8	X_{P8}/c	0.247	P_{20}	X_{P20}/c	0.0577	P_{31}	X_{P31}/c	0.8019
	Y_{P8}/c	0.1351		Y_{P20}/c	-0.0453		Y_{P31}/c	-0.0219
P_9	X_{P9}/c	0.2783	P_{21}	X_{P21}/c	0.0689	P_{32}	X_{P32}/c	0.862
	Y_{P9}/c	0.1417		Y_{P21}/c	-0.0514		Y_{P32}/c	-0.0121
P_{10}	X_{P10}/c	0.3936	P_{22}	X_{P22}/c	0.1069	P_{33}	X_{P33}/c	0.9508
	Y_{P10}/c	0.1353		Y_{P22}/c	-0.0633		Y_{P33}/c	-0.0073
P_{11}	X_{P11}/c	0.5205	P_{23}	X_{P23}/c	0.1478			
	Y_{P11}/c	0.1334		Y_{P23}/c	-0.0709			

Table 7.6: Polynomial coefficients of optimal airfoil shape (best fit) for two-stage non-symmetric airfoil Wells turbine considering mutual interaction between the blades (upper and lower face)

Face	A	B	D	E	H
Upper face	-1.31571	3.19739	-2.9773	1.06296	0.02429
Lower face	0.88881	-2.18127	1.8927	-0.58341	-0.014714

increase of 0.3% (Fig. 7.17b).

This optimization study considers the largest number of free optimization parameters (64) ever considered in our group. By analyzing the results we observed that the resulting Pareto frontier was relatively irregular and poorly populated.

The presented results should therefore be considered with caution. It is probably better to keep a lower number of free parameters in association with concurrent optimization problems. For this reason, the next section considers only symmetric profiles, that might be described with much fewer control points while keeping a larger parameter space.
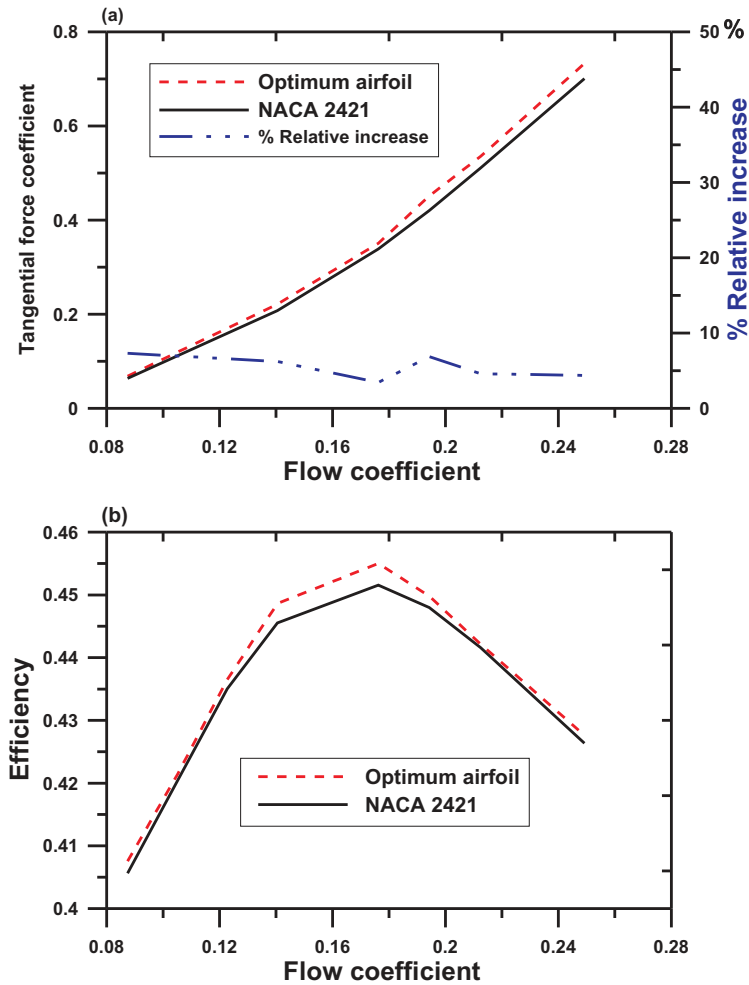
Figure 7.17: Performance of the optimal configuration (red line), compared to the non-symmetric two-stage Wells turbine relying on the NACA 2421 profile (black line). The corresponding relative increase is shown with blue line; a) tangential force coefficient; b) efficiency.

7.4 Optimal two-stage Wells turbine with symmetric airfoils

The present section finally concentrates on the optimization of a symmetric airfoil shape, leading to the best possible performance (i.e., maximal tangential force coefficient and efficiency) for a two-stage Wells turbine. A constant turbine solidity ($s = 0.67$)) and a constant gap between the rotors $G = d/c = 1.0$ (Fig. 7.18) are again considered, while taking into account the mutual interaction effect between the blades.
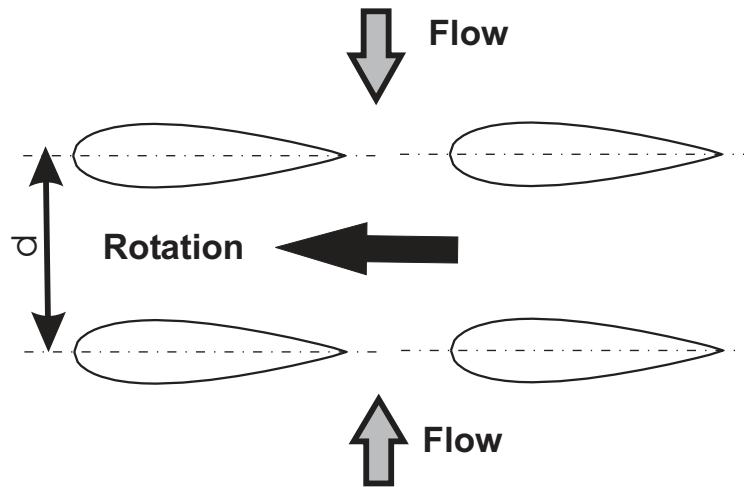
Figure 7.18: Two-stage Wells turbine with symmetric airfoils NACA 0021.

7.4.1   Optimization of airfoil shape

The blade shape is now constructed with thirteen points, two fixed points (P_1 and P_{13}) and eleven variable points ($P_2, P_3, P_4, P_5, P_6, P_7, P_8, P_9, P_{10}, P_{11}$ and P_{12}) as shown in Fig. 7.19. Knowing the exact position of these 13 points, the full profile is finally reconstructed for one face of the airfoil using standard splines. Figure 7.20a shows all
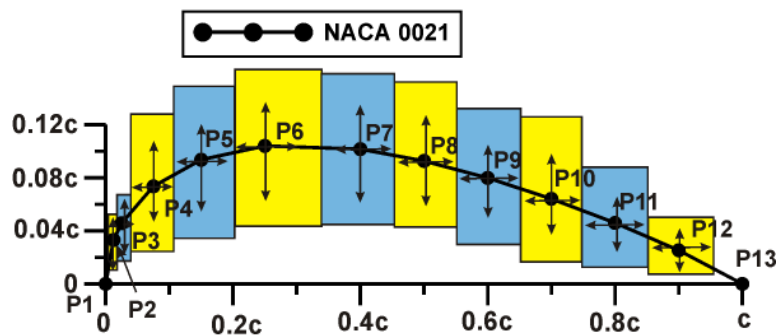
Figure 7.19: Allowed parameter space for the moving points.

evaluation results. As a whole, 615 different configurations have been finally tested by the optimizer, leading to 17 days of total computing time on a standard PC. In Fig. 7.20a the performance of the standard airfoil NACA 0021 (tangential force coefficient and efficiency $(C_T, \eta){=}(0.2104; 0.4351)$) is also plotted for comparison. Globally, the two considered objectives are not fully concurrent but increase simultaneously. When considering now only the best configurations of Fig. 7.20, located in the upper-right corner (marked by a red circle), a more complex picture appears, as documented in

Figure 7.20b. For the last percent of performance improvement, the two objectives (tangential force coefficient and efficiency) become again slightly concurrent and cannot be optimized simultaneously. Two optimal conditions are finally found: Point A, (C_T, η)= (0.2489;0.4430) (highest tangential force); and Point B, (C_T, η)= (0.2384;0.4450) (highest efficiency). Here again, the increase in tangential force coefficient (higher power output) appears to be more significant and valuable than the very slightly increased efficiency.
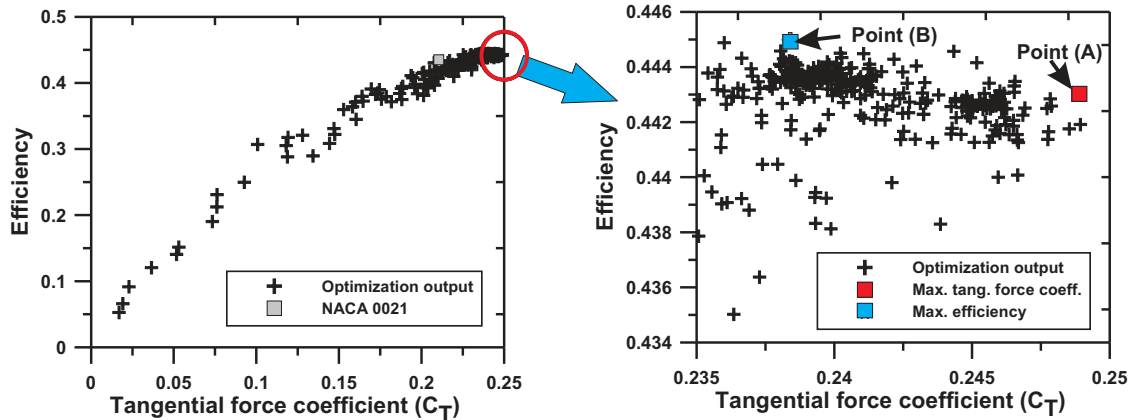
Figure 7.20: Objectives of the optimization: a) for all computed configurations; b) for the best configurations, i.e., zoom on the upper-right part (red circle) of (a).

Therefore, the most interesting point is Point A with $(C_T, \eta) \approx (0.249;0.443)$. The results of the optimization process can be also visualized using parallel coordinates (Fig. 7.21). Here again, the performance of the standard airfoil NACA 0021 is also plotted for comparison (thick dashed blue line).

The optimum configuration (Point A) is indicated by a thick red line. It can be seen that the optimal airfoil shape leads only to a slightly higher efficiency (+0.8%) compared to the standard airfoil (NACA 0021). However, the tangential force coefficient C_T is at the same time increased by 0.0385, i.e., a relative increase of more than 15% for the present flow coefficient, equal to 0.14. The geometrical parameters corresponding to the optimal shape are listed in Table 7.7.

The resulting shape of the optimal airfoil in comparison with the standard NACA 0021 is shown in Fig. 7.22. Knowing all points P1 to P13, the full profile is again reconstructed using standard splines of order 13. A polynomial description of this profile would be helpful for practical purposes. An excellent fit (average residual error of 0.16%) has been obtained using again Eq. 7.3 with the constants A to H listed in Table 7.8.

7.4.1.1   Off design performance

The results shown in Fig. 7.23 demonstrate that the improvement of tangential force coefficient is observed throughout for all values of ϕ, compared to the conventional
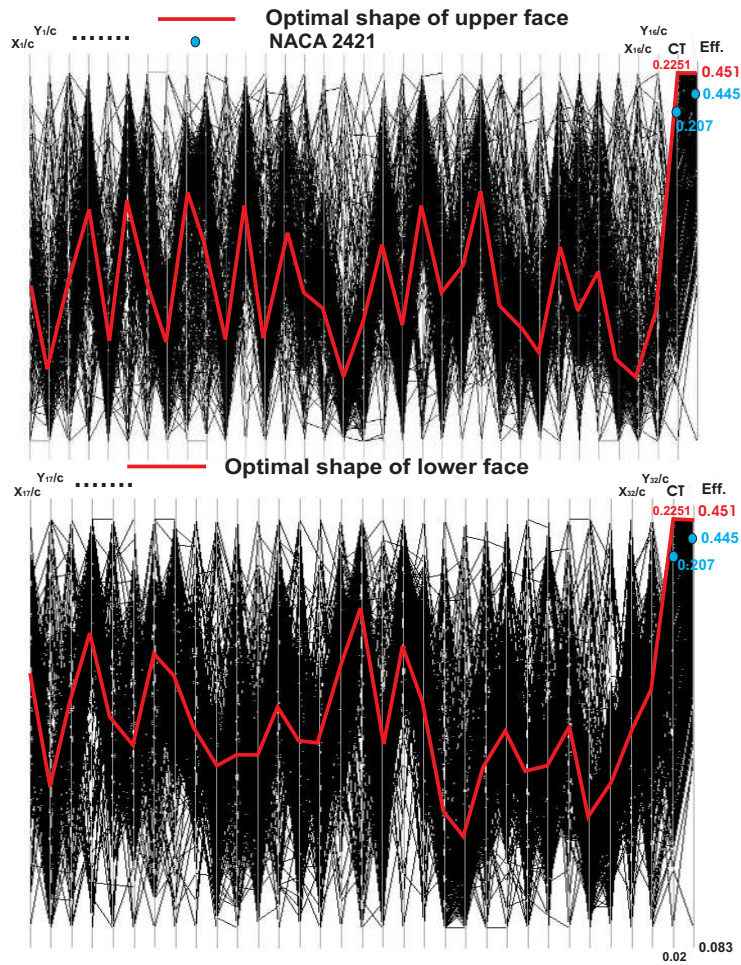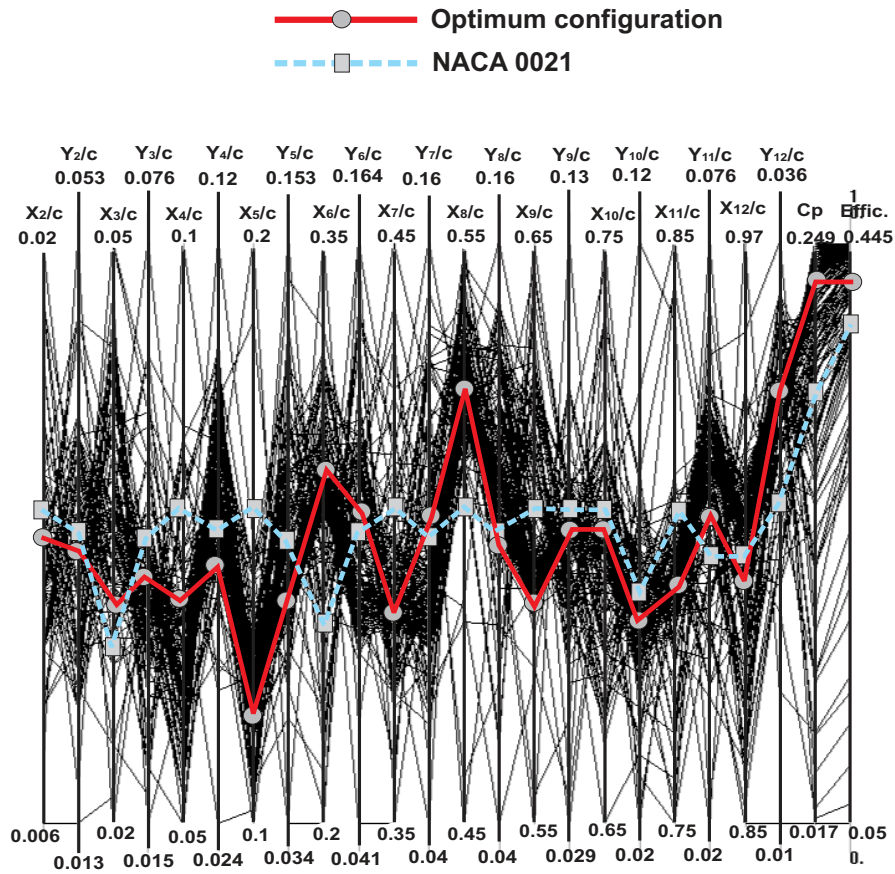
Figure 7.21: Input parameters of the optimization and objectives represented using parallel coordinates. The parameters of the optimal shape are connected with a thick red line. The standard design (NACA 0021) is shown with a thick dashed blue line.
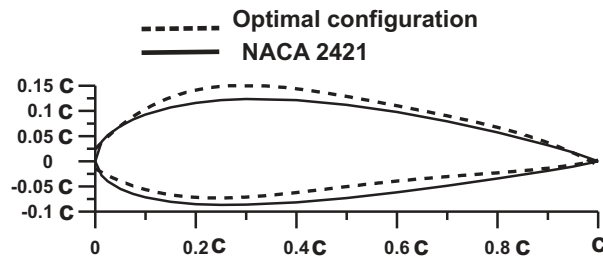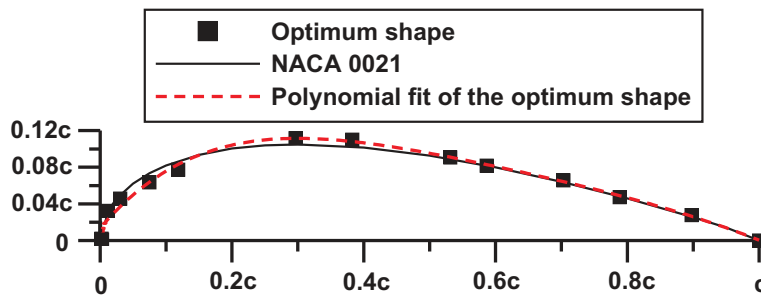

Figure 7.22: Comparison between the original profile NACA 0021 (solid line), the polynomial optimal airfoil shape (red line) and optimal shape by splines (black square).

turbine based on standard airfoils NACA 0021. The absolute gain for C_T increases even slightly with ϕ. The relative increase is higher than 10% throughout the useful operating

Table 7.7: Optimum shape parameters for two-stage Wells turbine

Point	Parameter	Value	Point	Parameter	Value
P_2	X_{P2}/c	0.01188	P_8	X_{P8}/c	0.53128
	Y_{P2}/c	0.03242		Y_{P8}/c	0.090718
P_3	X_{P3}/c	0.03056	P_9	X_{P9}/c	0.58674
	Y_{P3}/c	0.0458		Y_{P9}/c	0.08169
P_4	X_{P4}/c	0.0746	P_{10}	X_{P10}/c	0.70306
	Y_{P4}/c	0.0636		Y_{P10}/c	0.065626
P_5	X_{P5}/c	0.11839	P_{11}	X_{P11}/c	0.78848
	Y_{P5}/c	0.07726		Y_{P11}/c	0.047259
P_6	X_{P6}/c	0.29647	P_{12}	X_{P12}/c	0.89755
	Y_{P6}/c	0.111736		Y_{P12}/c	0.027875
P_7	X_{P7}/c	0.3825			
	Y_{P7}/c	0.11015			

Table 7.8: Polynomial coefficients of optimal airfoil shape (best fit) for two-stage Wells turbine with symmetric airfoils

A	B	D	E	H	K
0.5233101	-2.1617185	3.357793	-2.588445	0.8563828	0.01314256

range, with an average gain of 12% (Fig. 7.23a). At the same time the efficiency of the optimized shape is higher than the conventional design for $\phi < 0.18$; the difference disappears for large flow coefficients due to stall. The corresponding gain varies between 0.5% and 2%, with an average increase of 0.6% (Fig. 7.23b).

7.5 Conclusions on Wells turbine

As discussed previously, standard Wells turbines have several well-known disadvantages: low tangential force, high (undesired) axial force; low aerodynamic efficiency and limited range of operation. In the present work we have shown the potential of CFD-based optimization to improve the tangential force induced by monoplane and two-stage Wells turbines. Two concurrent objectives (efficiency and tangential force coefficient) have been maximized in a concurrent manner. The optimization relied on Genetic Algorithms, all geometrical configurations being evaluated in an automatic manner by CFD, taking into account the influence of the mutual interaction between the blades.

- **Monoplane Wells turbine**

  In this case, only symmetric airfoils can be considered. Due to the importance of the airfoil shape, a mathematical optimization procedure has been carried out considering simultaneously up to twenty-two free parameters.

 This optimization procedure is able to identify a considerably better configuration
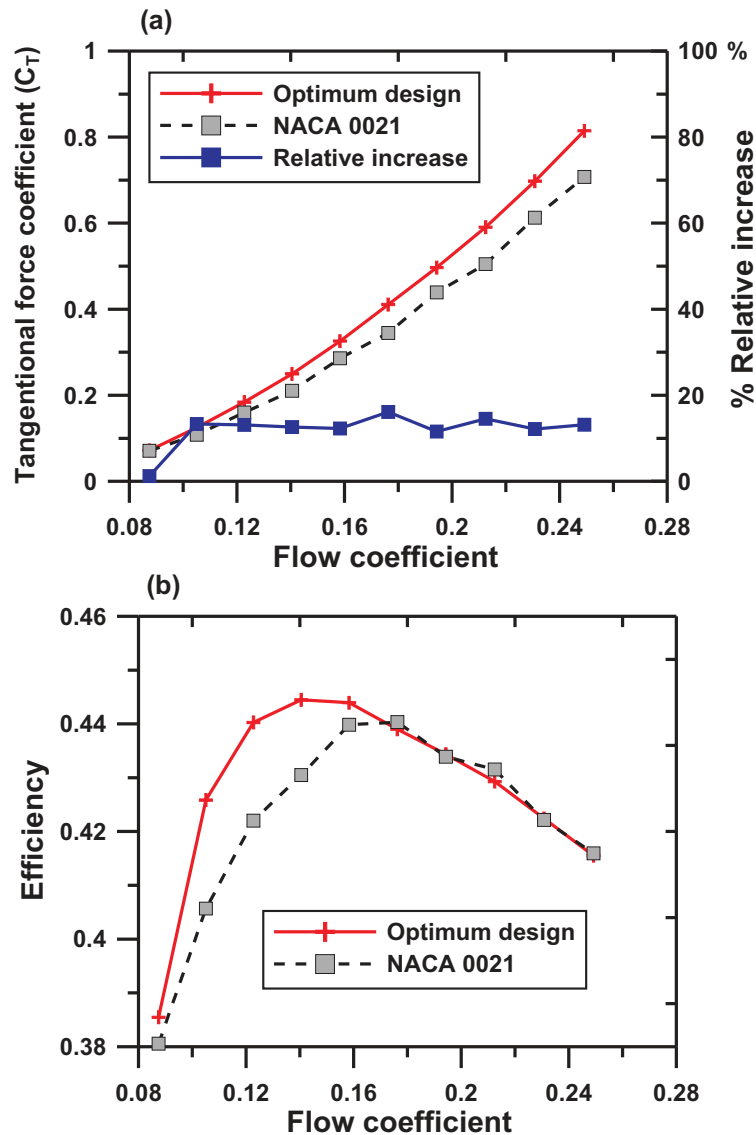
Figure 7.23: Performance of the optimal configuration (red line), compared to the conventional two-stage Wells turbine relying on the NACA 0021 profile (gray squares). The corresponding relative increase is shown with blue line; a) tangential force coefficient; b) efficiency.

than the standard design relying on NACA 0021. A relative increase of the tangential force coefficient exceeding 8.8% (as a mean, 11.3%) is obtained for the full operating range. At the same time, the efficiency improves also by at least 0.2% and up to 3.2% (as a mean, 1%).

- **Two-stage Wells turbine with non-symmetric airfoils**

Then, the aerodynamic performance of a modified two-stage Wells turbine consist-
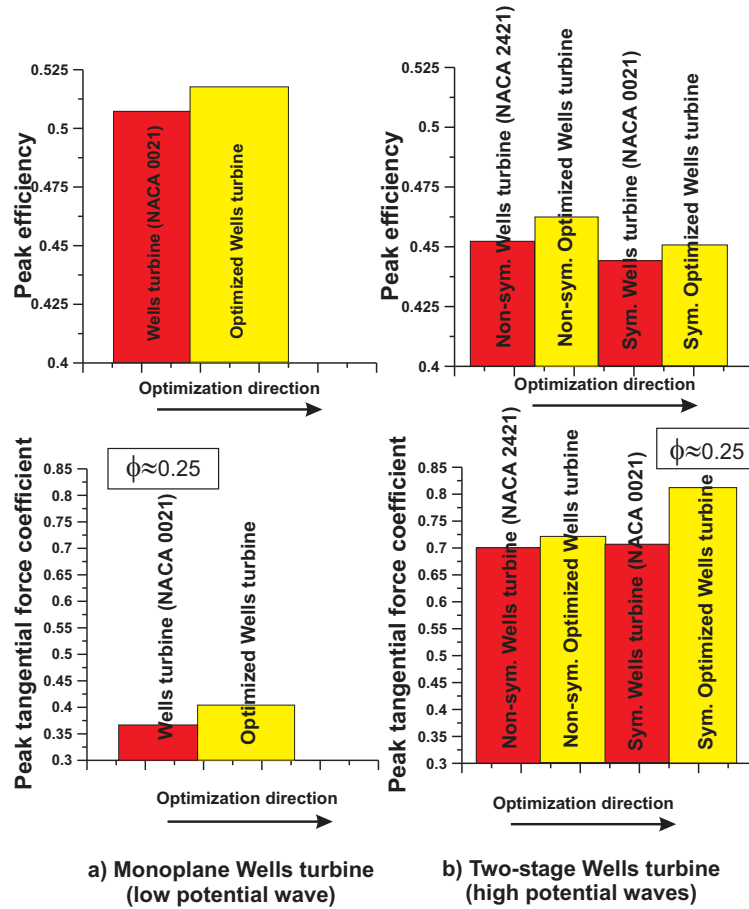
Figure 7.24: Successive optimization steps for the monoplane and two-stage Wells turbines.

ing of non-symmetric airfoils has been optimized. The two stages are mirrored, so that the system globally stays symmetric. Mutual interaction effects between the blades are taken in account. An aggressive mathematical optimization procedure has been carried out considering simultaneously sixty-four free parameters. This optimization procedure is able to identify a better configuration than the standard design (NACA 2421). It can be seen that the optimal airfoil shape leads only to a slightly higher efficiency compared to the standard airfoil (NACA 2421). The relative increase of the tangential force coefficient is however 6.2% at $\phi = 0.14$, with an average increase of 5.5% along the operating range. The gain in efficiency varies between 0.2% and 0.7%, with an average increase of 0.3%.

- **Two-stage Wells turbine with symmetric airfoils**

Finally, two-stage Wells turbines consisting of classical, symmetric airfoils have been considered. Optimization has been carried out considering twenty-two free parameters. This optimization procedure is again able to find a considerably better

configuration than the standard design (NACA 0021). The absolute gain for C_T increases even slightly with the flow coefficient. The relative increase is higher than 10% throughout the useful operating range, with an average gain of 12%. At the same time the efficiency of the optimized shape is higher than the conventional design for a flow coefficient $\phi \leq 0.18$. The corresponding gain varies between 0.5% and 2%, with an average increase of 0.6%.

As a whole, and supporting previous findings from the literature, the monoplane design appears clearly superior to the two-stage design in terms of efficiency. At $\phi = 0.14$, the efficiency of the optimized monoplane turbine exceeds $\eta \simeq 52\%$, compared to $\eta \simeq 45\%$ for optimized two-stage design (Fig. 7.24). The tangential force coefficient of the two-stage design is approximately twice the monoplane one, keeping in mind that the two-stage design needs higher potential waves to operate (see section 2.3.1). The two-stage Wells turbine consisting of symmetric airfoils is found better than the two-stage design consisting of non-symmetric airfoils in terms of tangential force coefficient with only minor difference in efficiency (Fig. 7.24).

Finally, we can conclude that these optimized Wells turbine configurations should help indeed to improve wave energy conversion.

Chapter 8

Conclusions and Outlook

In this thesis, two important systems allowing energy generation from renewable sources (Savonius turbine: wind; Wells turbine: sea waves) have been optimized by Genetic Algorithms, evaluating the performance by Computational Fluid Dynamics. After many new development, check, and validation steps, the optimization process can be carried out in a fully automatic manner allowing to explore efficiently a variety of configurations. Concerning the process, the main findings are as follows:

- An optimization requires typically one month of computing time on a single PC. While acceptable for research purposes, this is too long for industrial needs, highlighting the need for parallel computing. Fortunately, GAs are ideally suited for parallelization. Furthermore, it must be kept in mind that only two-dimensional geometries have been considered here. For 3D cases, parallel optimization is a clear must, even for academic research.

- It is possible to optimize considering a large number of design parameters. Up to 64 such free parameters have been employed in this work. This is, however, the maximum number that can be reasonably considered with the present algorithm. For concurrent optimization, GA works better for only 10 to 30 parameters and improvements are needed before considering, say, 100 variables.

- Concurrent optimization involving several objectives is also possible but leads to additional issues. In particular, it is usually necessary to involve additional criteria in the final decision process, when Pareto fronts are encountered.

Concerning engineering results:

- The performance of the original Savonius turbine could be tremendously increased, with an extraordinary peak C_p of about 0.48 compared to 0.18 for the original system (Fig. 8.1). A patent has been submitted for this configuration.

- In a similar but somewhat less impressive manner, the tangential force coefficient and efficiency of the original Wells turbine could be improved, typically by 12% for the tangential force coefficient and 1% for efficiency. Though limited, this gain

is already highly interesting for practical purposes and discussions with possible industrial partners are running.
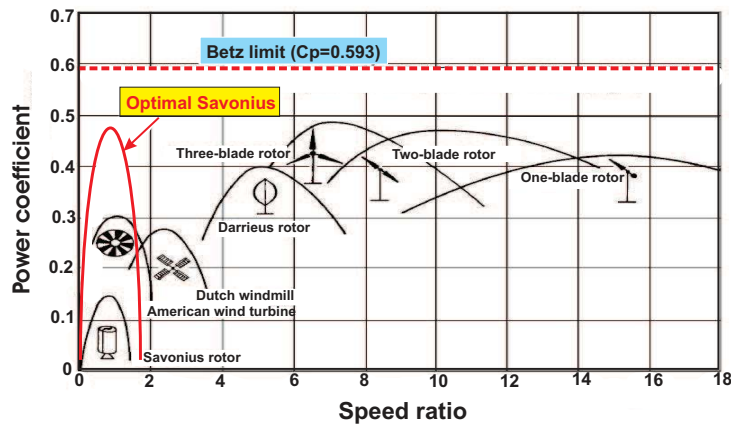
Figure 8.1: Power coefficients of wind rotors of different designs including newly developed, optimal Savonius turbine.

8.1 Suggestions for further research

The present study introduced optimized designs with superior performance for Savonius and Wells turbines. However, a full experimental verification of the findings is needed:

- Wind tunnel or urban wind measurements should be carried out for the optimal Savonius turbine.

- Experimental measurements should be carried out as well for the optimal Wells turbine considering an oscillating flow.

Concerning methodology:

- Fully parallel optimization involving parallel CFD should be implemented as a future standard.

- Improvements in the algorithm are needed to consider many parameters in a concurrent optimization.

- The performance of GA could be improved by coupling with other alternatives like particle swarm or surface responce techniques, allowing to reduce the numbers of (very costly) evaluations.

Bibliography

[1] B. D. Altan and M. Atýlgan. The use of a curtain design to increase the performance level of Savonius wind rotors. *Renewable Energy*, 35(4):821–829, 2008.

[2] A. Antoniou and L. Wu-Sheng. *Practical Optimization, Algorithms and Engineering Applications*. Springer Science+Business Media, LLC, New York, USA, 2007.

[3] V. Bellucci, B. Schuermans, D. Nowak, P. Flohr, and C. O. Paschereit. Thermoacoustic modeling of a gas turbine combustor equipped with acoustic dampers. *Journal of Turbomachinery*, 127(2), 2005.

[4] D. Benghrib, A. Ahram, and L. Bchir. Description of the vortex formation on a Savonius rotor in a water channel. *Comptes Rendus de l'Academie de Sciences - Serie IIb: Mecanique, Physique, Chimie, Astronomie*, 326(8):495–500, 1998.

[5] R. Bhattacharyya and M. E. McCormick. Wave Energy Conversion. *Elsevier Ocean Engineering Series*, 6(7):1–187, 2003.

[6] C. B. Boake, T. J. T. Whittaker, M. Folley, and H. Ellen. Overview and initial operational experience of the LIMPET wave energy plant. Proceedings of the International Offshore and Polar Engineering Conference, Kitakyushu, Japan, 586-594, 2002.

[7] P. Boccotti. Comparison between a U-OWC and a conventional OWC. *Ocean Engineering*, 34(5-6):799–805, 2007.

[8] A. Brito-Melo, L.M.C. Gato, and A.J.N.A. Sarmento. Analysis of Wells turbine design parameters by numerical simulation of the OWC performance. *Ocean Engineering*, 29(1):1463–1477, 2002.

[9] S. M. Camporeale, M. Torresi, G. Pascazio, and B. Fortunato. A 3D unsteady analysis of a Wells turbine in a sea-wave energy conversion device. American Society of Mechanical Engineers, International Gas Turbine Institute, Turbo Expo, Atlanta, Georgia, USA, GT2003-38715, 2003.

[10] A. Chauvin and D. Benghrib. Drag and lift coefficients evolution of a Savonius rotor. *Experiments in Fluids*, 8(1-2):118–120, 1989.

[11] REN21 Steering Committee. Renewables global status report 2007. *RENE21 Renewable Energy policy Network for the 21st century*, pages 1–54, 2007.

[12] REN21 Steering Committee. Renewables global status report 2009 update. *RENE21 Renewable Energy policy Network for the 21st century*, pages 1–32, 2009.

[13] R. Curran and L. M. C. Gato. Aerodynamic losses incurred by the Wells turbine. Proceedings of the International Offshore and Polar Engineering Conference, Los Angeles, California, USA, (1):58-65, 1996.

[14] R. Curran and L. M. C. Gato. The energy conversion performance of several types of Wells turbine designs. *Proceedings of the Institution of Mechanical Engineers, Part A: Journal of Power and Energy*, 211(2):133–145, 1997.

[15] R. Curran, R. S. Raghunathan, T. P. Stewart, and T. J. T. Whittaker. Matching a Wells turbine to the Islay oscillating water column wave power converter. Proceedings of the International Conference on Offshore Mechanics and Arctic Engineering - OMAE 1, Copenhagen, Denmark, Part A, 147-154, 1995.

[16] R. Curran, T. P. Stewart, and T. J. T. Whittaker. Design synthesis of oscillating water column wave energy converters: Performance matching. *Proceedings of the Institution of Mechanical Engineers, Part A: Journal of Power and Energy*, 211(6):489–505, 1997.

[17] R. Curran, T. J. T. Whittaker, S. Raghunathan, and W. C. Beattie. Performance prediction of contra-rotating Wells turbines for wave energy converter design. *Journal of Energy Engineering*, 124(2):35–52, 1998.

[18] R. Curran, T. J. T. Whittaker, S. Raghunathan, and W. C. Beattie. Performance prediction of contrarotating Wells turbines for wave energy converter design. *Journal of Energy Engineering*, 124(2):35–52, 1998.

[19] K. DaeHo, L. MinJeong, J. Won-Hyouk, and U. Krewer. Non-isothermal dynamic modelling and optimization of a direct methanol fuel cell. *Journal of Power Sources*, 180(1):71–83, 2008.

[20] R. A. Van den Braembussche. Numerical optimization for advanced turbomachinery design. In D. Thévenin and G. Janiga, editors, *Optimization and Computational Fluid Dynamics*, Berlin, Heidelberg, 2008. Springer-Verlag.

[21] T. S. Dhanasekaran and M. Govardhan. Computational analysis of performance and flow investigation on Wells turbine for wave energy conversion. *Journal of Renewable Energy*, 30(14):2129–2147, 2005.

[22] A. F. D. O. Falca and R. J. A. Rodrigues. Stochastic modelling of OWC wave power plant performance. *Applied Ocean Research*, 24(2):59–71, 2002.

[23] M. S. U. K. Fernando and V. J. Modi. A numerical analysis of the unsteady flow past bluff bodies. *Computational Mechanics*, 6(1):11–34, 1990.

[24] M. Folley, R. Curran, and T. Whittaker. Comparison of LIMPET contra-rotating Wells turbine with theoretical and model test predictions. *Ocean Engineering*, 33(8-9):1056–1069, 2006.

[25] M. Folley and T. Whittaker. The effect of plenum chamber volume and air turbine hysteresis on the optimal performance of oscillating water columns. Proceedings of the International Conference on Offshore Mechanics and Arctic Engineering, Halkidiki, Greece, (2):493-498, 2005.

[26] EU-Japan Centre for Industrial Cooperation Seminar Report 2008. The future of energy: Shell energy scenarios to 2050. *Climate Change, Environment and Energy seminar series*, (4):1–59, 2008.

[27] N. Fujisawa. On the torque mechanism of Savonius rotors. *Wind Engineering and Industrial Aerodynamics*, 40(3):277–292, 1992.

[28] N. Fujisawa. Velocity measurements and numerical calculations of flow fields in and around Savonius rotors. *Wind Engineering and Industrial Aerodynamics*, 59(1):39–50, 1996.

[29] N. Fujisawa and F. Gotoh. Visualization study of the flow in and around a Savonius rotor. *Experiments in Fluids*, 12(6):407–412, 1992.

[30] N. Fujisawa and F. Gotoh. Experimental study on the aerodynamic performance of a Savonius rotor. *Solar Energy Engineering, Transactions of the ASME*, 116(3):148–152, 1994.

[31] N. Fujisawa, Y. Taguchi, T. Satoh, T. Uemura, K. Nagaya, and S. Ikai. Investigation of flow field inside a Savonius rotor by image processing technique with conditional sampling. *Nippon Kikai Gakkai Ronbunshu, B Hen/Transactions of the Japan Society of Mechanical Engineers, Part B*, 59(567):3519–3523, 1993.

[32] L. M. C. Gato and A. F. D. O. Falcao. Aerodynamics of the Wells turbine: control by swinging rotor-blades. *International Journal of Mechanical Sciences*, 31(6):425–434, 1989.

[33] L. M. C. Gato and A. F. d. O. Falcao. Performance of the Wells turbine with a double row of guide vanes. *JSME International Journal, Series 2: Fluids Engineering, Heat Transfer, Power, Combustion, Thermophysical Properties*, 33(2):265–271, 1990.

[34] L. M. C. Gato, A. F. d. O. Falcao, N. H. C. Pereira, and R. M. R. J. Pereira. Design of wells turbine for OWC wave power plant. Proceedings of the First International Offshore and Polar Engineering Conference, Colorado, USA, (1):380-384, 1991.

[35] E. D. Glandt, M. T. Klein, and T. E. Edgar. *Optimization of chemical processes.* McGraw-Hill, New York, USA, 2001.

[36] R. Gupta, A. Biswas, and K. K. Sharma. Comparative study of a three-bucket Savonius rotor with a combined three-bucket Savonius-three-bladed Darrieus rotor. *Renewable Energy*, 33(9):1974–1981, 2008.

[37] E. Hau. *Renewable Energy, Fundamental, Technology, Applications and Economics.* Springer-Verlag, Berlin, Heidelberg, 2006.

[38] T. Hayashi, Y. Li, and Y. Hara. Wind tunnel tests on a different phase three-stage Savonius rotor. *JSME International Journal, Series B: Fluids and Thermal Engineering*, 48(1):9–16, 2005.

[39] T. Hayashi, Y. Li, and Y. Hara. Wind tunnel tests on a different phase three-stage Savonius rotor. *JSME International Journal, Series B: Fluids and Thermal Engineering*, 48(1):9–16, 2005.

[40] R. Hilbert, G. Janiga, R. Baron, and D. Thévenin. Multiobjective shape optimization of the flow around a heat exchanger using parallel genetic algorithms. *International Journal of Heat and Mass Transfer*, 49:2567–2577, 2006.

[41] H. Holttinen, H. P. Meibom, A. G. Orths, B. Lange, M. O'Malley, J. O. Tande, A. Estanqueiro, E. Gomez, L. Söder, G. Strbac, J. C. Smith, and F. V. Hulle. Impacts of large amounts of wind power on design and operation of power systems, results of IEA collaboration. Proceeding of 14th Kassel Symposium on Energy Systems Technology, Kassel, Germany, 7-24, 2009.

[42] http://www.scienceonline.co.uk/energy/renewable energy.html. Renewable energy resources. *last accessed April 2010.*

[43] M. D. Huda, M. A. Selim, A. K. M. S. Islam, and M. Q. Islam. Performance of an S-shaped Savonius rotor with a deflecting plate. *RERIC International Energy Journal*, 14(1):25–32, 1992.

[44] M. Inoue, K. Kaneko, T. Setoguchi, and H. Hamakawa. Air turbine with self-pitch-controlled blades for wave power generator (estimation of performance by model testing). *JSME International Journal, Series B: Fluids and Thermal Engineering*, 32(1):19–24, 1989.

[45] M. Inoue, K. Kaneko, T. Setoguchi, and S. Raghunathan. Starting and running characteristics of biplane Wells turbine. Proceedings of the 5th International Symposium on Offshore Mechanics and Arctic Engineering, Tokyo,Japan, 604-609, 1986.

[46] M. Inoue, K. Kaneko, T. Setoguchi, and S. Raghunathan. The fundamental characteristics and future of Wells turbine for wave power generator. *Journal of Science of Machines*, 39:275–280, 1987.

[47] M. Inoue, K. Kenji, T. Setoguchi, and F. Koura. Hysteretic characteristics of Wells turbine in reciprocating flow. *Nippon Kikai Gakkai Ronbunshu, BHen/Transactions of the Japan Society of Mechanical Engineers,Part B.*, 53(496):3699–3704, 1997.

[48] K. Irabu and J. N. Roy. Characteristics of wind power on Savonius rotor using a guide-box tunnel. *Experimental Thermal and Fluid Science*, 32(2):580–586, 2007.

[49] K. Ishimatsu, T. Shinohara, K. Kage, and T. Okubayashi. Numerical simulation for Savonius rotors (effects of shed vortices on running performance). *Nippon Kikai Gakkai Ronbunshu, B Hen/Transactions of the Japan Society of Mechanical Engineers, Part B*, 61(581):12–17, 1995.

[50] K. Ishimatsu, T. Shinohara, and F. Takuma. Numerical simulation for Savonius rotors (running performance and flow fields). *Nippon Kikai Gakkai Ronbunshu, B Hen/Transactions of the Japan Society of Mechanical Engineers, Part B*, 60(569):154–160, 1994.

[51] S. A. K. M. Islam, Q. M. Islam, A. C. Mandal, and M. M. Razzaque. Aerodynamic characteristics of a stationary Savonius rotor. *RERIC International Energy Journal*, 15(2):125–136, 1993.

[52] G. Janiga and D. Thévenin. Reducing the CO emissions in a laminar burner using different numerical optimization methods. *Journal of Power and Energy*, 221(5):647–655, 2007.

[53] M. Kaltschmitt, W. Streicher, and A. Wiese. *Renewable Energy, Technology and Environment Economics.* Springer-Verlag, Berlin, Heidelberg, 2007.

[54] M. A. Kamoji, S. B. Kedare, and S. V. Prabhu. Experimental investigations on modified Savonius rotor. *Collection of Technical Papers - AIAA Applied Aerodynamics Conference*, 1:768–780, 2007.

[55] K. Kaneko, T. Setoguchi, H. Hamakawa, and M. Inoue. Biplane axial turbine for wave power generator. *International Journal of Offshore and Polar Engineering*, 1(2):122–128, 1991.

[56] K. Kaneko, T. Setoguchi, and S. Raghunathan. Self-rectifying turbines for wave energy conversion. Proceedings of the First International Offshore and Polar Engineering Conference, Colorado, USA, (1):385-392, 1991.

[57] T. Kim, Y. Lee, I. Park, T. Setoguchi, and C. Kang. Numerical analysis for unsteady flow characteristics of the Wells turbine. Proceedings of 12th the International Offshore and Polar Engineering Conference, Kitakyushu, Japan, 694-699, 2002.

[58] T. Kim, M. Takao, T. Setoguchi, K. Kaneko, and M. Inoue. Performance comparison of turbines for wave power conversion. *International Journal of Thermal Sciences*, 40(7):681–689, 2001.

[59] T. H. Kim, T. Setoguchi, Y. Kinoue, K. Kaneko, and M. Inoue. Hysteretic characteristics of Wells turbine for wave power conversion. *Proceedings of the International Offshore and Polar Engineering Conference*, 2002.

[60] T. H. Kim, T. Setoguchi, M. Takao, K. Kaneko, and S. Santhakumar. Study of turbine with self-pitch-controlled blades for wave energy conversion. *International Journal of Thermal Sciences*, 41(1), 2002.

[61] Y. Kinoue, T. H. Kim, T. Setoguchi, M. Mohammad, K. Kaneko, and M. Inoue. Hysteretic characteristics of monoplane and biplane Wells turbine for wave power conversion. *Energy Conversion and Management*, 45(9-10):1617–1629, 2004.

[62] Y. Kinoue, T. Setoguchi, T. Kim, K. Kaneko, and M. Inoue. Mechanism of hysteretic characteristics of Wells turbine. *Nippon Kikai Gakkai Ronbunshu, B Hen/Transactions of the Japan Society of Mechanical Engineers, Part B*, 69(679):610–616, 2003.

[63] H. Lee, J. Kim, Y. Lee, T. Setoguchi, and C. Kang. Numerical analysis of flow characteristics in a Wells turbine for wave power conversion. Proceedings of the 10th International Offshore and Polar Engineering Conference, Seattle, USA, 427-433, 2000.

[64] M. Lind. *Experimental Investigation of a modified Savonius Turbine.* Studienarbeit Thesis, LSS-S01/10, Univ. of Magdeburg, 2010.

[65] J. Makower, R. Pernick, and C. Wilder. Clean energy trends 2009. *Clean Edge, 1-22, 2009.*

[66] M. Mamun, Y. Kinoue, T. Setoguchi, K. Kaneko, and Y. Lee. Hysteretic characteristics of biplane Wells turbine in a deep stall condition. Proceedings of the 15th International Offshore and Polar Engineering Conference, Seoul, Korea, (1):523-529, 2005.

[67] M. V. Mark and W. Dürrschmidt. Electricity from renewable energy sources. *Federal Ministry for the Environment, Nature Conservation and Nuclear Safety (BMU)*, Berlin - Germany:1–44, 2009.

[68] J. Menet. A double-step Savonius rotor for local production of electricity: A design study. *Renewable Energy*, 29(11):1843–1862, 2004.

[69] J. Menet. Aerodynamic behaviour of a new type of slow-running VAWT. *Wind Energy Proceedings of the Euromech Colloquium*, Springer,(43):235–240, 2007.

[70] J. Menet and B. Nachida. Increase in the Savonius rotors efficiency via a parametric investigation. *European Wind Energy Conference EWEA*, Aerodynamics and Aeroacoustics, 2004.

[71] J. Menet, L. Valdés, and B. Ménart. A comparative calculation of the wind turbines capacities on the basis of the $L - \sigma$ criterion. *Renewable Energy*, 22(4):491–506, 2001.

[72] M. H. Mohamed, G. Janiga, E. Pap, and D Thévenin. Optimal performance of a Savonius turbine using an obstacle shielding the returning blade. Ninth International Congress of Fluid Dynamics and Propulsion ASME-ICFDP9, ICFDP9-EG-249, Alexandria, Egypt, 2008.

[73] M.H. Mohamed. Aerodynamic performance of the Wells turbine used in the sea wave conversion. *Master's Thesis, Helwan University, Cairo, Egypt*, 2003.

[74] M.H Mohamed, G. Janiga, and D. Thévenin. Performance optimization of a modified Wells turbine using non-symmetric airfoil blades. American Society of Mechanical Engineers, International Gas Turbine Institute, Turbo Expo, Berlin, Germany, GT2008-50815, (6):2481-2488, 2008.

[75] I. G. Morrison and C. A. Greated. Oscillating water column modeling. *Proceedings of the Coastal Engineering Conference*, (1):502–511, 1993.

[76] C. O. Paschereit, B. Schuermans, and D. Büche. Combustion process optimization using evolutionary algorithm. American Society of Mechanical Engineers, International Gas Turbine Institute, Turbo Expo, Atlanta, Georgia, USA, GT2003-38393, (2):281-291, 2003.

[77] G. Pechlivanoglou, S. Fuehr, C. N. Nayeri, and C. O. Paschereit. The effect of distributed roughness on the power performance of wind turbines. American Society of Mechanical Engineers, International Gas Turbine Institute, Turbo Expo, Glasgow, UK, GT2010-23258, 2010.

[78] G. Pechlivanoglou, J. Wagner, C. N. Nayeri, and C. O. Paschereit. Active aerodynamic control of wind turbine blades with high deflection flexible flaps. 48th AIAA Aerospace Sciences Meeting, Orlando, Florida, USA, (AIAA 2010-644), 2010.

[79] M. Powalko, A. G. Orths, and P. B. Eriksen. Grid operation supported by wind farms: The Danish experience. Proceeding of 14th Kassel Symposium Energy Systems Technology, Kassel, Germany, 63-71, 2009.

[80] S. Raghunathan. Prediction of performance of biplane Wells turbine. Proceedings of the Third International Offshore and Polar Engineering Conference, Singapore, (1):167-171, 1993.

[81] S. Raghunathan. A methodology for Wells turbine design for waves energy conversion. *Proceedings - IMechE: A, Journal of Power and Energy*, 209(A3):221–232, 1995.

[82] S. Raghunathan. The Wells air turbine for wave energy conversion. *Progress in Aerospace Sciences*, 31(4):335–386, 1995.

[83] S. Raghunathan and W. C. Beattie. Aerodynamic performance of contra-rotating Wells turbine for wave energy conversion. *Proceedings of the Institution of Mechanical Engineers, Part A: Journal of Power and Energy*, 210(6):431–447, 1996.

[84] S. Raghunathan, R. Curran, and T. J. T. Whittaker. Performance of the Islay Wells air turbine. *Proceedings of the Institution of Mechanical Engineers, Part A: Journal of Power and Energy*, 209(1):55–62, 1995.

[85] S. Raghunathan, T. Setoguchi, and K. Kaneko. The effect of inlet conditions on the performance of Wells turbine. USA, Proceedings of the ASME Fluids Engineering Conference, 87-FE2, 1987.

[86] S. Raghunathan, T. Setoguchi, and K. Kaneko. Some techniques to improve the operation range of the Wells turbine for wave power generator. *JSME International Journal, Series B: Fluids and Thermal Engineering*, 32(1):71–77, 1989.

[87] S. Raghunathan, T. Setoguchi, and K. Kaneko. Some techniques to improve the operation range of the Wells turbine for wave power generator. *JSME International Journal, Series B: Fluids and Thermal Engineering*, 32(1):71–77, 1989.

[88] S. Raghunathan, T. Setoguchi, and K. Kaneko. Aerodynamics of monoplane Wells turbine- a review. Proceedings of the First International Offshore and Polar Engineering Conference, Colorado, USA, (1):370-379, 1991.

[89] S. Raghunathan and C. P. Tan. Performance of the Wells turbine at starting. *AIAA Journal (Journal of Energy)*, 6(6):430–431, 1982.

[90] S. Raghunathan and C. P. Tan. Aerodynamic performance of a Wells air turbine. *Journal of Energy*, 7(3):226–230, 1983.

[91] S. Raghunathan and C. P. Tan. The effect of blade profile on the performance of Wells turbine. *International Journal of Heat and Fluid Flow*, 6:17–22, 1985.

[92] S. Raghunathan, C. P. Tan, and O. O. Ombaka. Performance of the Wells self-rectifying air turbine. *Aeronautical Journal*, 89(890):369–379, 1985.

[93] S. Raghunathan, C. P. Tan, and N. A. J. Wells. Wind tunnel tests on airfoil in tandem cascade. *AIAA Journal*, 19(11):1490–1492, 1981.

[94] M. J. Rajkumar and U. K. Saha. Valve-aided twisted Savonius rotor. *Wind Engineering*, 30(3):243–254, 2006.

[95] M. J. Rajkumar, U. K. Saha, and D. Maity. Simulation of flow around and behind a Savonius rotor. *International Energy Journal*, 6(2):83–90, 2005.

[96] A. Ravindran, K. M. Ragsdell, and G. V. Reklaitis. *Engineering optimization: methods and applications.* John Wiley & Sons, Inc., New Jersey, USA, 2006.

[97] T. Setoguchi S. Raghunathan and K. Kaneko. Aerodynamic of monoplane Wells turbine - A review. *International Journal of Offshore and Polar Engineering*, 4(1):68–75, 1994.

[98] U. K. Saha and M. J. Rajkumar. On the performance analysis of Savonius rotor with twisted blades. *Renewable Energy*, 31(11):1776–1788, 2006.

[99] T. Setoguchi, K. Kaneko, M. Takao, and M. Inoue. Air turbine with self-pitch-controlled blades for wave energy conversion. Proceedings of the 6 th International Offshore and Polar Engineering Conference, Los Angeles, California, USA, (1):70-74, 1996.

[100] T. Setoguchi, T. Kim, K. Kaneko, M. Takao, Y. Lee, and M. Inoue. Air turbine with staggered blades for wave power conversion. *International Journal of Offshore and Polar Engineering*, 13(4):316–320, 2003.

[101] T. Setoguchi, T. H. Kim, K. Kaneko, M. Takao, Y. W. Lee, and M. Inoue. Air turbine with staggered blades for wave power conversion. Proceedings of the International Offshore and Polar Engineering Conference, Kitakyushu, Japan, 662-667, 2002.

[102] T. Setoguchi, T. W. Kim, M. Takao, A. Thakker, and S. Raghunathan. The effect of rotor geometry on the performance of a Wells turbine for wave energy conversion. *International Journal of Ambient Energy*, 25(3):137–150, 2004.

[103] T. Setoguchi, Y. Kinoue, T. H. Kim, K. Kaneko, and M. Inoue. Hysteretic characteristics of Wells turbine for wave power conversion. *Renewable Energy*, 28(13):2113–2127, 2003.

[104] T. Setoguchi, Y. Kinoue, M. Mohammad, K. Kaneko, and M. Takao. Unsteady flow phenomena of Wells turbine in deep stall condition. Proceedings of the International Offshore and Polar Engineering Conference, Toulon, France, (1):266-271, 2004.

[105] T. Setoguchi, S. Santhakumar, M. Takao, T. H. Kim, and K. Kaneko. Effect of guide vane shape on the performance of a wells turbine. *Renewable Energy*, 1:1–15, 2001.

[106] T. Setoguchi, S. Santhakumar, M. Takao, T. H. Kim, and K. Kaneko. A modified Wells turbine for wave energy conversion. *Renewable Energy*, 28(1):79–91, 2003.

[107] T. Setoguchi and M. Takao. Current status of self rectifying air turbines for wave energy conversion. *Energy Conversion and Management*, 47(15-16):2382–2396, 2006.

[108] T. Setoguchi, M. Takao, K. Itakura, M. Mohammad, K. Kaneko, and A. Thakker. Effect of rotor geometry on the performance of Wells turbine. Proceedings of the International Offshore and Polar Engineering Conference, Honolulu, Hawaii, USA, (1):374-381, 2003.

[109] T. Setoguchi, M. Takao, K. Kaneko, and M. Inoue. Effect of guide vanes on the performance of a Wells turbine for wave energy conversion. Proceedings of the International Offshore and Polar Engineering Conference, Honolulu, Hawaii, (1):83-88, 1997.

[110] T. Setoguchi, M. Takao, K. Kaneko, and M. Inoue. Effect of guide vanes on the performance of a Wells turbine for wave energy conversion. *International Journal of Offshore and Polar Engineering*, 8(2):155–160, 1998.

[111] T. Setoguchi, M. Takao, K. Kaneko, and M. Inoue. Effect of guide vanes on the performance of a Wells turbine for wave energy conversion. *International Journal of Offshore and Polar Engineering*, 8(2):155–160, 1998.

[112] T. Setoguchi, M. Takao, E. Kinoue, K. Kaneko, and M. Inoue. Comparative study of performances of turbines for wave power conversion. Proceedings of the International Offshore and Polar Engineering Conference, Seattle, USA, (4):351-357, 2000.

[113] T. Shih, W. W. Liou, A. Shabbir, Z. Yang, and J. Zhu. A new k-ϵ eddy viscosity model for high Reynolds number turbulent flows. *Computers and Fluids*, 24(3):227–238, 1995.

[114] S. N. Sivanandam and S. N. Deepa. *Introduction to Genetic Algorithms*. Springer-Verlag, Berlin, Heidelberg, 2008.

[115] L. Söder, L. Hofmann, A. G. Orths, H. Holttinen, Y. H. Wan, and A. Tuohy. Experience from wind integration in some high penetration areas. *IEEE Transactions on Energy Conversion*, 22(2):4–12, 2007.

[116] M. Suzuki. Design method of guide vane for Wells turbine. *Journal of Thermal Science*, 15(2):126–131, 2006.

[117] M. Suzuki and C. Arakawa. Guide vanes effect of Wells turbine for wave power generator. Proceedings of the Ninth International Offshore and Polar Engineering Conference, Brest, France, (1):162-168, 1999.

[118] M. Suzuki, C. Arakawa, and T. Tagori. Fundamental studies on Wells turbine for wave power generator (1st report, the effect of solidity, and self-starting). *Bulletin of the JSME*, 27(231):1925–1931, 1984.

[119] M. Takao, Y. Kinoue, T. Setoguchi, K. Kaneko, and S. Nagata. Improvement of Wells turbine performance by means of end plate. *Nihon Kikai Gakkai Ronbunshu, B Hen/Transactions of the Japan Society of Mechanical Engineers, Part B*, 72(10):2381–2385, 2006.

[120] M. Takao, T. Setoguchi, K. Kaneko, and M. Inoue. Air turbine with self-pitch controlled blades for wave energy conversion. *International Journal of Offshore and Polar Engineering*, 7(4):308–312, 1997.

[121] M. Takao, T. Setoguchi, K. Kaneko, and M. Inoue. Effect of guide vanes on the performance of a Wells turbine. *Nippon Kikai Gakkai Ronbunshu, B Hen/Transactions of the Japan Society of Mechanical Engineers, Part B*, 63:577–582, 1997.

[122] M. Takao, T. Setoguchi, T. H. Kim, K. Kaneko, and M. Inoue. The performance of Wells turbine with 3D guide vanes. Proceedings of the International Offshore and Polar Engineering Conference, Seattle, USA, (4):381-386, 2000.

[123] M. Takao, T. Setoguchi, Y. Kinoue, and K. Kaneko. Effect of end plates on the performance of a Wells turbine for wave energy conversion. *Journal of Thermal Science*, 15(4):319–323, 2006.

[124] M. Takao, T. Setoguchi, Y. Kinoue, and K. Kaneko. Wells turbine with end plates for wave energy conversion. *Ocean Engineering*, 34(11-12):1790–1795, 2007.

[125] M. Takao, T. Setoguchi, Y. Kinoue, K. Kaneko, and S. Nagata. Improvement of Wells turbine performance by means of end plate. Proceedings of the International Offshore and Polar Engineering Conference, San Francisco, California, USA, (1):480-484, 2006.

[126] M. Takao, A. Thakker, R. Abdulhadi, and T. Setoguchi. Effect of blade profile on the performance of large-scale Wells turbine. Proceedings of the International Offshore and Polar Engineering Conference, Toulon, France, (1):272-276, 2004.

[127] M. Takao, A. Thakker, R. Abdulhadi, and T. Setoguchi. Effect of blade profile on the performance of large-scale Wells turbine. *International Journal of Sustainable Energy*, 25(1):53–61, 2006.

[128] S. Tan, Y. Shimizu, and K. Kikuyama. Experimental studies on a Savonius rotor with casing. *Nippon Kikai Gakkai Ronbunshu, B Hen/Transactions of the Japan Society of Mechanical Engineers, Part B*, 63(611):2356–2363, 1997.

[129] A. Thakker, P. Frawley, and E. S. Bajeet. CA9: Analysis of a stall-resistant aerofoil in view of wave power conversion. Proceedings of the International Offshore and Polar Engineering Conference, Stavanger, Norway, (1):614-619, 2001.

[130] A. Thakker, P. Frawley, and E. S. Bajeet. Numerical analysis of Wells turbine performance using a 3D Navier-Stokes explicit solver. Proceedings of the International Offshore and Polar Engineering Conference, Stavanger, Norway, (1):604-608, 2001.

[131] A. Thakker, P. Frawley, and E. S. Bajeet. Performance simulation on CA9 Wells turbine rotor using a 3D Navier-Stokes explicit solver. *Proceedings of the fourth European Conference on Turbomachinery*, 2001.

[132] D. Thévenin and G. Janiga. *Optimization and Computational Fluid Dynamics.* Springer-Verlag, Berlin, Heidelberg, 2008.

[133] T Thorpe. An overview of wave energy technologies: status, performance and costs. wave-energy.net. Retrieved 2008-10-13.

[134] J. W. Twidell and A. D. Weir. *Renewable Energy Resources.* ELBS/E. & F.N. Spon, London, UK, 1987.

[135] M. Webster and L. M. C. Gato. Effect of rotor blade shape on the performance of the Wells turbine. Proceedings of the International Offshore and Polar Engineering Conference, Brest, France, (1):169-173, 1999.

[136] M. Webster and L. M. C. Gato. The effect of rotor blade sweep on the performance of the Wells turbine. *International Journal of Offshore and Polar Engineering*, 9(3):233–239, 1999.

[137] P. White, M. Webster, A. Thakker, and M. O'Dowd. Utilization of CFD to study an oscillating water column. Proceedings of the International Offshore and Polar Engineering Conference, Honolulu, Hawaii, USA, (1):70-76, 1997.

[138] T. J. T. Whittaker and S. McIlwaine. Shoreline wave power experience with the Islay prototype. Proceedings of the First International Offshore and Polar Engineering Conference, Colorado, USA, (1):393-397, 1991.

[139] H. Yu. *Numerical investigation of a rotating system using OpenFOAM.* Master's Thesis, LSS-M02/09, Univ. of Magdeburg, 2009.

[140] Z. Yu. Self-starting process simulation of Wells turbine in regular and irregular oscillating air flows. *China Ocean Engineering*, 4(4):469–476, 1990.

[141] Z. Yu and H. Maeda. Optimal matching design method of the Wells turbine with the air chamber in an oscillating air flow. *Journal of Hydrodynamics*, 3(2), 1991.

[142] J. Zarinchang and A. Sabzevari. Variable geometry Savonius windmill: modeling and wind tunnel testing. *Modelling, simulation and control. B*, 56(1):57–64, 1994.

********* Curriculum Vitae *********

Name:	Mohamed Hassan Ahmed Mohamed
Date of Birth:	Juli 15, 1974; in Cairo, Egypt
Nationality:	Egyptian
Status:	Married, two Children
Address:	Coswiger Str. 8,
	D-39114 Magdeburg, Germany
E-mail:	mohamed.mohamed@st.ovgu.de
	moh75202@yahoo.de

Education:

1989 - 1992	Secondary School Certificate, Cairo, Egypt.
1992 - 1997	B.Sc. in Mechanical Power Engineering, Faculty of Engineering -Mattria Helwan University, Cairo, Egypt.
1998 - 1999	Military service.
1999 - 2001	Postgraduate courses for M.Sc. Faculty of Engineering-Mattria, Helwan University, Cairo, Egypt.
2001 - 2003	M.Sc. in Mechanical Power Engineering, Helwan University, Cairo, Egypt.
2003 - 2005	Postgraduate courses for Ph.D. Faculty of Engineering-Mattria, Helwan University, Cairo, Egypt.
Aug. 2007 - till Now	Works towards Ph.D. degree at Institut für Strömungstechnik & Thermodynamik, Lehrstuhl Strömungsmechanik & Strömungstechnik (ISUT/LSS), Otto-von-Guericke-University Magdeburg, Germany.

Work Experience:

1999 - 2003	Demonstrator in Dept. of Mechanical Power Engineering, Faculty of Engineering-Mattria, Helwan University, Cairo, Egypt.
2003 - 2007	Assistant lecturer in Dept. of Mechanical Power Engineering, Faculty of Engineering-Mattria, Helwan University, Cairo, Egypt.
Aug. 2007 - till Now	PhD student and Assistant lecturer in Turbomachines, Chair of Fluid Dynamics and Technical Flows, Otto-von-Guericke University Magdeburg, Germany.

Magdeburg, 4. October 2010
M. H. Mohamed

Related Publications

The presented thesis is partly based on the following publication in international reviewed journals and conferences:

1. <u>**Mohamed, M.H.**</u>, Janiga, G., Pap, E. and Thévenin, D., **Multi-Objective Optimization of the Airfoil Shape of Wells Turbine used for Wave Energy Conversion.** Energy, 36(1):438-446, 2011.

2. <u>**Mohamed, M.H.**</u>, Janiga, G., Pap, E. and Thévenin, D., **Optimal Blade Shape of a Modified Savonius Turbine Using an Obstacle Shielding the Returning Blade.** Energy Conversion and Management, 52(1):236-242, 2011.

3. <u>**Mohamed, M.H.**</u>, Janiga, G., Pap, E. and Thévenin, D., **Optimization of Savonius turbines using an obstacle shielding the returning blade.** Renewable Energy, 35(11):2618-2626, 2010.

4. <u>**Mohamed, M.H.**</u>, and Thévenin, D.: **Performance optimization of a Savonius Turbine Considering Different Shapes for Frontal Guiding Plates.** In: 10th Int. Congress of Fluid Dynamics ASME-ICFD10, EG-3026, Cairo, Egypt, 2010.

5. <u>**Mohamed, M.H.**</u>, Janiga, G., Pap, E. and Thévenin, D.: **Optimal performance of a modified three-blade Savonius turbine using frontal guiding plates.** In: ASME Turbo Expo Conference, Glasgow, Scotland, GT2010-22538, 2010.

6. <u>**Mohamed, M.H.**</u>, Janiga, G. and Thévenin, D.: **Airfoil shape optimization of a two-stage Wells turbine.** In: microCAD10 International Scientific Conference, (Bikfalvi, P., Ed.), Miskolc, Hungary, ISBN 978-963-661-910-7, 51-56, 2010.

7. <u>**Mohamed, M.H.**</u>, Janiga, G. and Thévenin, D.: **Airfoil shape optimization of a two-stage Wells turbine.** In: proc. Magdeburg-Miskolc Interuniversity Cooperation (50 Year Cooperation), (Bikfalvi, P., Ed.), Miskolc, Hungary, ISBN 978-963-661-924-4, 99-104, 2010.

8. <u>**Mohamed, M.H.**</u>, Janiga, G., Pap, E. and Thévenin, D.: **Optimal performance of a Savonius turbine using guiding plates.** In: Conference on Modelling Fluid Flow (the 14th International Conference on Fluid Flow Technologies), (Vad, J., Ed.), Budapest, Hungary, ISBN 978-963-420-987-4, 871-878, 2009.

9. <u>**Mohamed, M.H.**</u>, Janiga, G., Pap, E. and Thévenin, D.: **Optimal shape of a modified Wells turbine considering mutual interaction between the blades.** In: First International Conference of Energy Engineering ICEE-1, Aswan, Egypt, 2008.

10. **Mohamed, M.H.**, Janiga, G., Pap, E. and Thévenin, D.: **Optimal performance of a Savonius turbine using an obstacle shielding the returning blade.** In: 9th Int. Congress of Fluid Dynamics and Propulsion ASME-ICFDP9, Alexandria, Egypt, 249/1-249/9, 2008.

11. **Mohamed, M.H.**, Janiga, G. and Thévenin, D.: **Performance optimization of a modified Wells turbine using non-symmetric airfoil blades.** In: ASME Turbo Expo Conference, Berlin, Germany, GT2008-50815, 2481-2488, 2008.